Physics of Atomic Nuclei, Vol. 64, No. 1, 2001, pp. 1–8. Translated from Yadernaya Fizika, Vol. 64, No. 1, 2001, pp. 3–10.

NUCLEI
Experiment

Investigation of the Spectra of Neutrons Originating from ^{238}U Fission Induced by 5.0- and 13.2-MeV Neutrons

A. M. Trufanov, G. N. Lovchikova, M. I. Svirin, A. V. Polyakov, V. A. Vinogradov, V. D. Dmitriev[1)], and G. S. Boikov[1)]

Institute of Physics and Power Engineering, pl. Bondarenko 1, Obninsk, Kaluga oblast, 249020 Russia

Received December 23, 1999; in final form, April 20, 2000

Abstract—The spectra of neutrons accompanying ^{238}U fission induced by 5.0- and 13.2-MeV primary neutrons are measured by the time-of-flight method. This investigation of fission-neutron spectra supplements previous measurements performed at the different primary energies of 2.9, 14.7, 16.0, and 17.7 MeV. The shape of the neutron spectrum at 13.2 MeV is similar to the shape of the neutron spectra for the primary energy of 14.7 MeV and higher. A calculation of the spectra within a conventional approach reproduces the shape of the observed distributions only at primary energies in excess of 2 MeV. In relation to a theoretical description, the experimental distributions for low primary energies show an anomalously high yield of soft neutrons. © *2001 MAIK "Nauka/Interperiodica".*

1. INTRODUCTION

The present article reports on a further step in a series of studies initiated at the Khlopin Radium Institute (St. Petersburg) and then continued in cooperation with the Institute of Physics and Power Engineering (Obninsk) that are devoted to measurement of the spectra $N(E, E_n)$ of neutrons accompanying the fission of heavy actinide nuclei. Initially, the spectra of neutrons were measured for two characteristic primary-neutron energies of E_n = 2.9 (an energy value below the emission-fission threshold) and 14.7 MeV (an energy value above this threshold) [1]. It was found that the shape of the fission-neutron spectra changes as soon as the primary-neutron energy becomes higher than the $(n, n'f)$ threshold, in which case the fission process appears to be of an emission character. At the primary energy of 14.7 MeV, these changes manifest themselves in a characteristic increase in the yield of neutrons in two regions of secondary-neutron energies: as a maximum in the high-energy section of the spectrum and as an ascending branch in its low-energy section. At secondary-neutron energies below 2 MeV, the latter leads to a sizable excess of neutrons in relation to what emerges from the calculations on the basis of the statistical model. The latest investigations at the Institute of Physics and Power Engineering were focused on the region of emission nuclear fission at primary-neutron energies above 14 MeV [2, 3]. Both in the hard and in the soft section of neutron spectra, the investigations reported in [2, 3] confirmed the above features, which were observed previously in [1] and which distinguish these spectra from those at the primary-neutron energy of E_n = 2.9 MeV, where only (n, f) reactions can occur. It was clear from the outset that the above distinction in the hard section of the spectrum is associated with nonequilibrium neutron emission in the decay of an excited fissile nucleus. In order to explain the excess of soft neutrons accompanying the emission fission of nuclei, it was assumed in [4] that neutrons may originate not only from a fissile nucleus and from fully accelerated fragments but also from nonaccelerated fragments. Since this assumption was based on data that were far from extensive, additional experimental and theoretical investigations aimed at establishing the emission from nonaccelerated fragments were necessary for obtaining deeper insights into the mechanism of neutron emission.

In this article, we present new experimental results obtained by measuring the spectra of neutrons from ^{238}U fission induced by primary neutrons with energies of 5.0 ± 0.01 and 13.2 ± 0.2 MeV. These neutron energies extend the energy range over which we previously studied the differential yield of neutrons from the reaction ^{238}U$(n, xn'f)$.

Measurement of the spectra of neutrons from ^{238}U fission induced by 5.0-MeV primary neutrons is an important supplement to the only neutron spectrum that was measured by the same method at the primary energy of 2.9 MeV and which was used as a reference in a comparison with all neutron spectra measured by the present authors in emission fission at the primary energies of 14.7, 16.0, and 17.7 MeV.

There is yet another reason why the energy distributions of neutrons originating from the reaction ^{238}U$(n, xn'f)$ at a primary neutron energy of 13.2 MeV are of interest. Since these distributions are determined almost exclusively by the relevant reactions (n, f) and $(n, n'f)$ and since emission spectra measured at higher

[1)] Khlopin Radium Institute, St. Petersburg, 198021 Russia.

primary energies receive a contribution from the reaction $(n, 2n'f)$ as well, there arises the possibility of clarifying the effect of neutrons from the reaction $(n, 2n'f)$ on the character of the emission spectra; on this basis, we can also verify the assumption made in theoretically calculating the spectra of fission neutrons that takes into account the nonequilibrium mechanism only at the first step of the emission cascade, treating all other steps in terms of purely evaporation processes.

At the chosen energy value, the spectra of fission neutrons can be calculated with smaller uncertainties, so that a comparison with experimental data can be more reliable and informative here.

2. DESCRIPTION OF THE EXPERIMENT

A detailed account of methodological questions concerning measurements of fission-neutron spectra was given elsewhere [1–3]; for this reason, we only describe briefly the basic units of the experimental facility used in the present study.

Our experiment was conducted in a neutron beam from the KG-2.5 cascade generator installed at the Institute of Physics and Power Engineering (Obninsk) by harnessing the reactions $T(d, n)^4He$ at $E_d = 600$ keV and $D(d, n)^3He$ at $E_d = 1.9$ MeV to obtain neutrons with initial energies of 5.0 ± 0.1 and 13.2 ± 0.2, respectively. Exposed to these neutrons were tritium–titanium targets on a copper substrate and deuterium–titanium targets, the thicknesses of the active layer being 1.1 and 1.6 mg/cm^2 for the former and the latter, respectively. The average current of deuterons was 5 or 25 μA for tritium or deuteron targets, respectively. The energy distributions of secondary neutrons were measured by a time-of-flight spectrometer in the energy range 0.25–13.0 MeV. A fission-fragment detector; a neutron detector featuring complex, combined shielding; and electronics that made it possible to run the experiment and control the acquisition, accumulation, and sampling of experimental data in the memory of a PC were the basic units of the spectrometer used.

A multilayer flow-through ionization chamber that contained layers of fissile ^{238}U and which was developed and manufactured at the Khlopin Radium Institute [1] served as the fission-fragment detector. The chamber consisted of four sections, each being connected to an individual wideband preamplifier. One of the sections—a monitoring one—contained two one-sided targets from the substance featuring the spontaneously fissile isotope ^{252}Cf uniformly distributed over its thickness (2 mg/cm^2). This made it possible to determine the efficiency of the neutron detector and to perform relative measurements by using the spectrum of neutrons from the spontaneous fission of ^{252}Cf as a reference. In the remaining three sections, ^{238}U layers 2 mg/cm^2 in thickness and 100 mm in diameter were deposited onto both sides of an aluminum substrate (electrode) 0.05 mm thick. There were 20 electrodes in the fission chamber, and the total weight of the fissile sample was 5.5 g. Pure (99.99%) methane was used as a flow-through gas in the fission chamber. The efficiency of fission-fragment detection was about 70% (for more details on the features of the fission chamber, the reader is referred to [2]).

A stilbene single crystal 63 mm in diameter and 39 mm in height connected to a FEU-30 phototube served as the detector of neutrons. This detector was equipped with dedicated combined shielding that was manufactured from monolithic paraffin containing an admixture of ^6LiH, lead, and iron and which was supplemented with copper attachments on the side of the source of neutrons. This ensured a considerable reduction of the background from photons and scattered neutrons. In order to reduce the background of photons, we also employed the scheme of n–γ separation according to the pulse shape, the suppression factor being about 70 at the neutron-detection threshold approximately equal to 0.2 MeV.

The spectrum of fission neutrons was measured over a flight base of 1.7 m at an angle of 90° with respect to the beam of primary neutrons. The absolute efficiency of the neutron detector was determined in the range 0.25–13 MeV with respect to the spectrum of neutrons from the spontaneous fission of ^{252}Cf (the shape of this spectrum was taken to be identical to that in [5]).

In measuring the spectra of fission neutrons, an all-wave detector, which was virtually insensitive to photons and which was arranged at an angle of 45° with respect to the deuteron-beam direction at a distance of 4 m from the target, was used to monitor the neutron beam. The electronics of the spectrometer was implemented in the CAMAC standard. In order to record simultaneously the neutron time-of-flight spectra from all four sections of the chamber, one time analog-to-digital converter was used in the spectrometer, whereby systematic uncertainties associated with the nonlinearity and with the temperature drift of the converter were considerably reduced. The stability of the electronics and detector performance was monitored by the shape and the position (on the time scale) of the γ peak from the spontaneous fission of ^{252}Cf occurring in the ionization chamber.

3. SPECTRA OF PROMPT FISSION NEUTRONS ($E_n = 5.0$ MeV)

3.1. Shape of the Spectra of Fission Neutrons in (n, f) Reactions

Frequently, the experimental spectra of neutrons originating from both spontaneous and induced fission are analyzed in terms of the Maxwell distribution

$$N_M(E, T) = 2(E/(\pi T^3))^{1/2} \exp(-E/T), \qquad (1)$$

in which case the mean energy of emitted neutrons is given by

$$\bar{E} = (3/2)T. \qquad (2)$$

The spectrum described by expression (1) has the required energy dependence, but it is difficult to validate it theoretically. In any case, it should be recalled that the parameter T is not the temperature in the same sense as in the Weisskopf and Le Couteur formulas. Expression (1), which depends on only one parameter T, can be considered as a convenient parametrization of experimental data, for example, in constructing a systematics of $\bar{E}$ values.

From the estimate that is presented in [5] and which relies on extensive experimental data and on the results of theoretical calculations, it follows that the spectrum $N(E)$ of neutrons from the spontaneous fission of ^{252}Cf may deviate from (1) quite sizably. These deviations can be taken into account in terms of the shape function

$$\mu(E) = N(E)/N_{\mathrm{M}}(E, T), \tag{3}$$

where

$$T = \frac{2}{3}\bar{E} = \frac{2}{3}\int_0^\infty EN(E)dE.$$

For ^{252}Cf, the estimate from [5] yields $T = 1.420 \pm 0.001$ MeV. Figure 1 displays the function $\mu(E)$ according to [5] and the form

$$\mu(E) = A\exp(B_0 + B_1x + B_2x^2)\frac{1 + B_3E}{1 + B_3E_2}, \qquad x = \ln(E/E_0), \tag{4}$$

which we proposed as an approximation of this function. In (4), we have set $A = 1.0265$, $E_0 = 2.65$ MeV, and $E_2 = 8.5$ MeV and determined the parameters B_i by fitting experimental data for three intervals of neutron energies. The results are as follows: (i) $B_0 = 6.711 \times 10^{-4}$, $B_1 = 3.5 \times 10^{-2}$, $B_2 = 4.5 \times 10^{-3}$, and $B_3 = 0$ for $E \le E_1 = 2.46$ MeV; (ii) $B_0 = 0$, $B_1 = 1.7 \times 10^{-2}$, $B_2 = -1.162 \times 10^{-1}$, and $B_3 = 0$ for $E_1 \le E \le E_2$; and (iii) $B_0 = 0$, $B_1 = 1.7 \times 10^{-2}$, $B_2 = -1.162 \times 10^{-2}$, and $B_3 = -1.2 \times 10^{-2}$ MeV^{-1} for $E > E_2$ [$x = \ln(E_2/E_0)$].

The same figure also shows the spectrum of neutrons originating from the fission-chamber section that contains ^{252}Cf and which is used in implementing the relative method in our measurements. With the aid of this method, the induced fission of the nuclide being investigated and the well-understood spontaneous fission of ^{252}Cf can be studied under very similar conditions.

An alternative expression for the spectrum of neutrons can be obtained by using the relation of the evaporation model in the fragment c.m. frame, that is, the Le Couteur formula

$$n(\varepsilon)d\varepsilon = \frac{1}{\Gamma(n+1)\theta^{n+1}}\varepsilon^n\exp(-\varepsilon/\theta)d\varepsilon, \tag{5}$$

where $n = 1$ and $\theta = \tau_1$ for single emission and $n = 5/11 \approx 1/2$ and $\theta = (11/12)\,\tau_1$ for multiparticle emission, τ_1 being the temperature of the residual nucleus (fragment) upon the emission of the first neutron. In rescaling the neutron distribution (5) from the c.m. frame to the laboratory frame with allowance for the contribution of the complementary fragment and under the assumption that the complementary fragments are identical, we arrive at an expression that leads, upon integration with respect to the neutron emission angle relative to the line along which the fragments fly apart, to the well-known Watt formula

$$N_{\mathrm{W}}(E, \omega, \theta) = (\pi\omega\theta)^{-1/2}\exp(-(\omega + E)/\theta)\sinh(2\sqrt{\omega E}/\theta). \tag{6}$$

In Eq. (6), the parameter ω represents the mean kinetic energy of fission fragments per nucleon, while θ—to be distinguished from T in (1)—is sometimes referred to as the effective temperature. This effective temperature is related to the mean energy of the spectrum by the equation

$$\bar{E} = \omega + 3\theta/2. \tag{7}$$

The traditional description assuming that fully accelerated fragments appear as a source of neutrons and that the emission process follows the pattern predicted by the evaporation model complies well with experimental data both in the shape of the spectra and in the spatial correlation between neutrons and fission fragments. This is so not only in the case of nuclear fission induced by thermal neutrons but also in the case of induced fission, at least in the region of the first plateau ($E_n \le 6$ MeV).

For ^{252}Cf, a fit to the estimate from [5] in terms of expression (6) leads to the values of $\theta = 1.185$ MeV and $\omega = 0.343$ MeV.

For this case, the expression

$$\bar{N}_{\mathrm{W}}(E, \theta, \omega) = \frac{1}{2}[N_{\mathrm{W}}(E, \theta, C_L\omega) + N_{\mathrm{W}}(E, \theta, C_H\omega)], \tag{8}$$

the arithmetic mean of two Watt spectra for a light (L) fragment and the complementary heavy fragment (H), which was obtained by Froner [6] in the approximation specified by the equalities $\theta_L = \theta_H = \theta$, $\bar{\nu}_L = \bar{\nu}_H$, $\omega_L = C_L\omega$, and $\omega_H = C_H\omega$, where the constants $C_L = 2A_H^2/(A_L^2 + A_H^2)$ and $C_H = 2 - C_L$ are determined by the momentum-conservation law, with the ratio $A_L/A_H = 108/144 = 3/4$ being the most probable mass splitting, yields $\theta = 1.170$ MeV and $\omega = 0.364$ MeV. These values are in excellent agreement with estimates presented in [6] ($\theta = 1.174 \pm 0.08$ MeV, $\omega = 0.361 \pm 0.014$ MeV). The above results for ω are at odds with the estimate $\omega \approx 0.75$ MeV quoted in [7]. This discrepancy is due to many simplifying assumptions made in deriving expression (6). Figure 1 also shows the results obtained by fitting the Watt distribution in (8) to experimental data on ^{252}Cf. This distribution reproduces basic trends

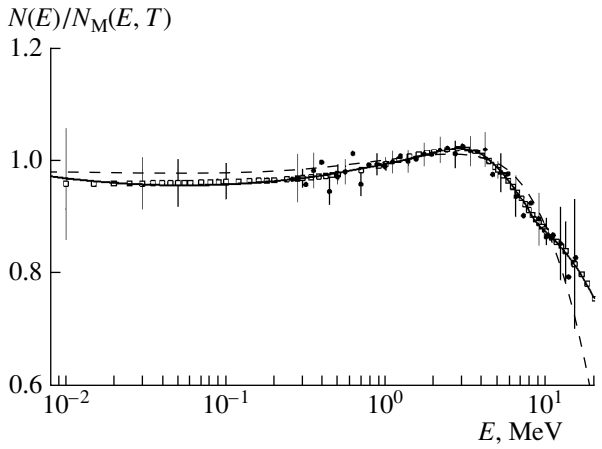

Fig. 1. Ratio of the spectrum of prompt neutrons from the spontaneous fission of ^{252}Cf, $N(E)$, to the Maxwell spectrum $N_M(E, T)$ at T = 1.42 MeV: (open squares) estimate from [5], (closed circles) spectrum of the ^{252}Cf section of the fission chamber, (solid curve) fit to data from [5] in terms of relation (4), and (dashed curve) fit to data from [5] in terms of the Watt relation.

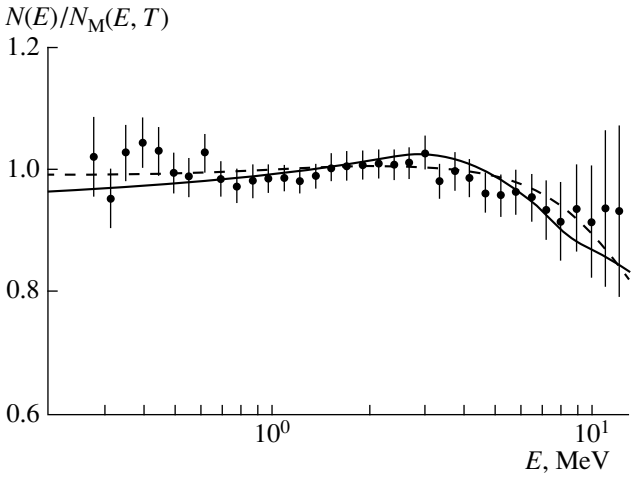

Fig. 2. Ratio of the spectrum of prompt neutron from ^{238}U fission induced by 5-MeV neutrons to the Maxwell distribution $N_M(E, T)$ at T = 1.353 MeV. Points represent experimental data obtained in this study. The notation for the curves is identical to that in Fig. 1.

of the deviation of the spectrum measured for ^{252}Cf from the Maxwell spectrum—that is, it contains information about the shape function $\mu(E)$. For $\omega \longrightarrow 0$, the Watt formula reduces to the Maxwell formula.

For ^{238}U fission induced by 5-MeV neutrons, experimental results and a fit to them are displayed in Fig. 2 in the form of the ratio of the spectrum being studied to the Maxwell distribution at T = 1.353 MeV. The parameter value was obtained by fitting the ratio

$$N(E) = N_M(E, T)\mu(E) \quad (9)$$

to experimental data in the neutron-energy range E = 0.5–12.28 MeV, where $\mu(E)$ is determined by expression (4) with the parameters B_i set to the values deduced from the spectrum for ^{252}Cf. In just the same way as at E_n = 2.9 MeV [8], the behavior of the deviation of the measured spectrum from the relevant Maxwell distribution is similar to that for neutrons from spontaneous fission. This result is not independent, however, since it is determined by the assumption that is made in relative measurements and which concerns the shape of the reference spectrum. In studying the spontaneous fission of actinides, the authors of [9, 10] determined the efficiency of the neutron detector and calibrated the energy scale of the time-of-flight spectrometer by using various reactions like H(n, n') scattering, T(p, n)^{3}He, and ^{9}Be(d, n)^{10}B; that is, they did not assume any a priori information about the function $\mu(E)$. The measured spectra also show a deviation from the Maxwell distribution; therefore, there is every reason to believe that the deviations being discussed are of a universal character and that they can be taken into account by introducing a correction to the distribution in (1). The Watt distribution in Fig. 2 corresponds to the parameter values of θ = 1.169 MeV and ω = 0.265 MeV.

For the relevant distributions in (1), (6), and (9), Table 1 quotes the parameter values, which confirm the conclusion that, if the spectra of fission neutrons have been measured over a sufficiently broad energy interval, it makes no difference which form of approximation—that in (1) or that in (6)—is used to determine the mean energy of neutrons from a fit to the experimental distributions: the distinction between the $\bar{E}$ values in the two cases under consideration does not exceed 0.01 versus the mean value of 2.02 MeV as obtained for all $\bar{E}$ values quoted in Table 1—this is less than the experimental uncertainty equal to 0.03 MeV. Apart from statistical errors, the experimental uncertainty includes (i) the error associated with a finite width of the secondary-neutron-energy range studied here, (ii) the error

Table 1. Fitted parameters of the spectrum of neutrons originating from ^{238}U fission induced by 5-MeV neutrons

E_{min}–E_{max}, MeV	$N_M(E, T)$ (1)			$N_M(E, T)\,\mu(E)$ (9)			$N_W(E, \theta, \omega)$ (6)			
	T, MeV	$\bar{E}_{expt}$, MeV	χ^2	T, MeV	$\bar{E}_{expt}$, MeV	χ^2	ω, MeV	θ, MeV	$\bar{E}_{expt}$, MeV	χ^2
0.28–12.27	1.341	2.012	0.40	1.349	2.024	0.32	0.228	1.191	2.015	0.34
0.50–12.27	1.342	2.013	0.37	1.353	2.030	0.50	0.265	1.169	2.019	0.27

that stems from extrapolating the measured spectrum $N_{exp}(E)$ by using the Maxwell distribution at energies E below the boundary energy E_{min} equal to the energy threshold of the neutron detector, and (iii) the errors in the corrections introduced.

The general trend in the behavior of $\bar{E}$ is as follows: the smallest value corresponds to expression (1), while the largest one results from a fit in terms of expression (9). The same is true for the spectrum of neutrons from ^{252}Cf fission: $\bar{E}$ = 2.096, 2.121, and 2.13 MeV for (1), (6) or (8), and (9), respectively.

Table 2 displays a sample of mean-energy values for the spectrum under study and the experimental errors in them. The first value was found on the basis of a fit in terms of expressions (1), (6), and (9) as a mean over all $\bar{E}$ values from Table 1. The second value was determined directly from the observed spectrum $N(E)$ by evaluating the integral

$$\bar{E} = \int_0^\infty EN(E)dE, \qquad (10)$$

the contribution from neutrons with energies below the detection threshold $0 < E \le E_{thr} = 0.2$ MeV being taken into account via an extrapolation from E_{thr} to zero with the aid of the Maxwell distribution.

In Table 2, we present the mean energies $\bar{E}_{exp}$ obtained from the measured spectra of fission neutrons. Also given are $\bar{E}$ values that take into account a correction for the angular correlation between secondary and primary neutrons (see [1]), which arises owing to a strong angular anisotropy of fragment emission and to a strong angular correlation between the direction of motion of postfission neutrons and the direction of motion of fission fragments. For the eventual value of the mean neutron energy $\bar{E}$, we took 2.03 ± 0.03 MeV. Table 2 also quotes the $\bar{E}$ values corresponding to the compilations from [7, 11].

The fission-neutron spectrum obtained in the present study is shown in Fig. 3, along with the estimated spectrum from the ENDF/B-VI library, which was composed on the basis of the Madland–Nix model [12], and with the spectrum calculated by Merten with the aid of the FINESSE code [13]. As can be seen from the figure, the results of the FINESSE calculations are in better agreement with experimental data than with the ENDF/B-VI estimate. The calculated spectrum from ENDF/B-VI underestimates the contribution of neutrons both in the low-energy region $E < 1$ MeV and in the region of high energies.

3.2. Experimental Ratio R(E, E_n)

In just the same way as in our preceding studies devoted to measurements of fission-neutron spectra,

Table 2. Mean energies of neutrons originating from ^{238}U fission induced by 5-MeV neutrons

Sample of $\bar{E}$	$\bar{E}_{expt}$, MeV	$\bar{E}$, MeV
$\bar{E}$ according to Table 1	2.02 ± 0.03	2.03 ± 0.03
$\bar{E}$ according to Eq. (10)	2.01 ± 0.03	2.02 ± 0.03
Accepted value	2.02 ± 0.03	2.03 ± 0.03
Systematics from [7]	2.054	$\bar{\nu}_f$ = 3.024
Systematics from [11]	2.063	$\bar{\nu}_f$ = 3.024

the experimental results for the primary neutron energy of E_n = 5.0 MeV are displayed in Fig. 4*b* as the ratio of the spectrum of prompt neutrons originating from ^{238}U fission to the spectrum of neutrons from the spontaneous fission of ^{252}Cf,

$$R(E, E_n) = \frac{N_U(E, E_n)}{N_{Cf}(E)}. \qquad (11)$$

The spectra in question are normalized as

$$\int_0^\infty N_U(E, E_n)dE = \int_0^\infty N_{Cf}(E)dE = 1, \qquad (12)$$

where the contribution of neutrons with energies E below E_{thr} = 0.2 MeV is taken into account. As was indicated above, this representation of our experimental results makes it possible to avoid many uncertainties like those that are associated with the precision achieved in calibrating the energy scale of the spectrometer or with the energy dependence of the neutron-detector efficiency. For this purpose, measurements for the induced fission of the isotope being studied and the

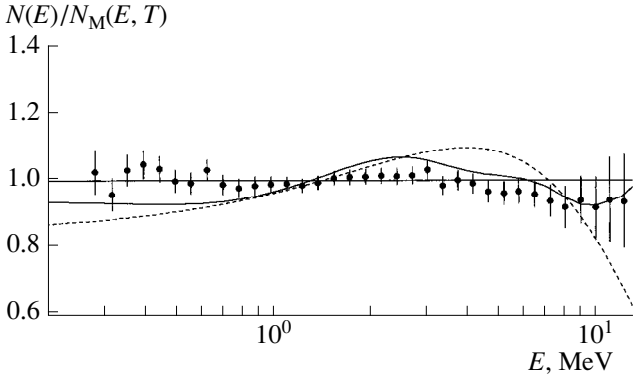

Fig. 3. Measured spectrum of neutrons from ^{238}U fission induced by 5-MeV neutrons (points) along with the results of the calculations based on the FINESSE code (solid curve) and with the estimate from the ENDF/B-VI library (dashed curve). All neutron spectra are presented in the form of the ratio to the Maxwell distribution at T = 1.353 MeV.

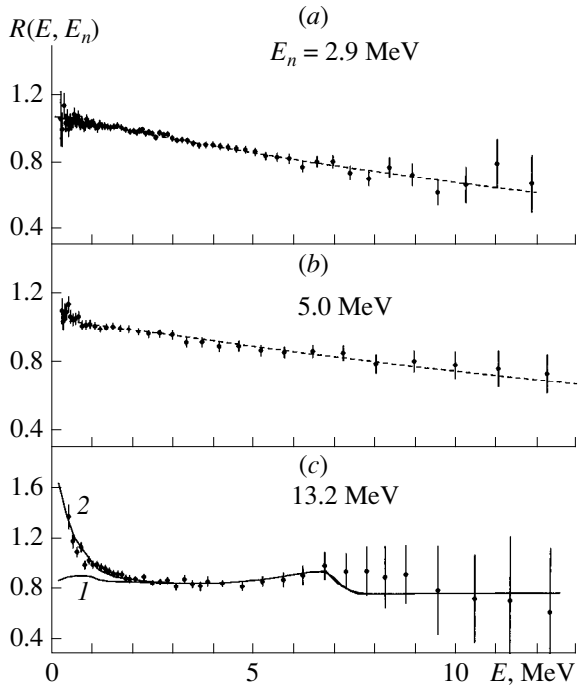

Fig. 4. Ratio $R(E, E_n)$ of the fission-neutron spectrum for the reaction $^{238}U(n, xn'f)$ to the spectrum of neutrons from the spontaneous fission of ^{252}Cf. Points represent experimental data of this study. The solid curves in Fig. 4*c* depict the results of the calculations (*1*) without and (*2*) with allowance for neutron emission from nonaccelerated fragments. The dashed curves in Figs. 4*a* and 4*b* correspond to the ratio of the Maxwell distributions at T_U = (*a*) 1.232 and (*b*) 1.353 MeV for T_{Cf} = 1.42 MeV in either case.

well-understood spontaneous fission of ^{252}Cf were performed simultaneously under conditions as similar as possible. Figure 4*a* shows experimental results obtained at the primary neutron energy of E_n = 2.9 MeV [1]. The dashed curves in Figs. 4*a* and 4*b* represent the ratios of the Maxwell distributions for ^{238}U and ^{252}Cf at the values of the temperature T that are indicated in the caption under the corresponding figure,

$$R_M(E, E_n) = \frac{N_M^U(E, E_n)}{N_M^{Cf}}. \quad (13)$$

It can be seen that, at E_n = 2.9 and 5.0 MeV, both the observed and the approximating ratio [$R(E, E_n)$ and $R_M(E, E_n)$, respectively] behave as nearly linear functions of the secondary-neutron energy. This implies that the observed neutron spectrum is similar in shape to the Maxwell distribution and that the slope is determined by the difference of the temperatures obtained from the neutron spectra for the ^{252}Cf nucleus and the ^{238}U nucleus being studied.

4. SPECTRA OF EMISSION-FISSION NEUTRONS (E_n = 13.2 MeV)

For the incident-neutron energy of E_n = 13.2 MeV, the experimental energy dependence of the ratio $R(E, E_n) = N_U(E, E_n)/N_{Cf}(E)$ is shown in Fig. 4*c*. It differs markedly from the simple, nearly linear dependences $R(E, E_n)$ observed at the primary-neutron energies of E_n = 2.9 and 5.0 MeV, featuring a maximum at high energies of emitted neutrons, which is due to the contribution from a nonequilibrium mechanism of excited-nucleus decay—this mechanism leads to a much harder spectrum of emitted neutrons. If we compare experimental data that are presented in the form of the ratio $R(E, E_n)$ and which were obtained in [2, 3] at higher incident-neutron energies (in excess of 14 MeV) with similar results of the present study, it becomes clear that the peak on top of the high-energy tail of the spectrum due to the nonequilibrium component of prefission neutrons is much less pronounced in the present case. The observed shift of the high-energy peak in $R(E, E_n)$ along the scale of the emitted-neutron energy E in response to a reduction of incident-neutron energy from $E_n >$ 14 MeV to 13.2 MeV, together with a decrease in the peak height, indicates once again that the physical interpretation of the effect has been chosen correctly, since the contribution of the nonequilibrium component of prefission neutrons becomes less pronounced with decreasing primary neutron energy.

At low energies of emitted neutrons (E < 2 MeV), the ratio $R(E, E_n)$ shows another feature of emission fission, the presence of an anomalously soft neutron component, which manifests itself as an excess of the observed distribution over the distribution computed on the basis of the statistical model.

Smooth curves in Fig. 4*c* represent the results of a theoretical calculation based on the statistical model. All inputs that were used in describing the experimental spectra of neutrons accompanying the emission fission of ^{238}U nuclei irradiated with 14.7-, 16.0-, and 17.7-MeV neutrons and which include basic relations of statistical theory and of the preequilibrium-decay model, level densities, and the mechanism of postfission-neutron emission were described in detail elsewhere [4]. Preliminary theoretical estimates obtained on the basis of the relations from that study reveal that the low-energy anomaly can also be observed at primary neutron energies E_n in excess of $E_{thr} \approx 9$ MeV. With the aim of testing the potential of the model in predicting measurable results, we have applied the previous approach to measure the neutron spectrum at the primary neutron energy of E_n = 13.2 MeV, which is closer to the threshold energy E_{thr} than any energy value studied thus far.

The calculated spectrum was represented as the sum of the contributions from prefission neutrons, neutrons from fully accelerated fragments (postfission-neutron spectrum), and neutrons from nonaccelerated fragments; that is,

$$\frac{d\bar{\nu}_c(E, E_n)}{dE} = \frac{d\bar{\nu}_{pre}(E, E_n)}{dE} + \frac{d\bar{\nu}_{faf}(E, E_n, \beta T_x)}{dE} + \frac{d\bar{\nu}_{naf}(E, E_n, C)}{dE}. \quad (14)$$

The prefission-neutron spectrum $d\bar{\nu}_{pre}(E, E_n)/dE$ was calculated as the sum of the spectrum of coincidence between first-chance neutrons and events of ^{238}U fission ($d\bar{\nu}_{pre,1}/dE$) and the spectrum of coincidence of second- and third-chance neutrons and events of ^{237}U fission ($d\bar{\nu}_{pre,2}/dE$, $d\bar{\nu}_{pre,3}/dE$) [4]. The contribution of the last two to $d\bar{\nu}_{pre}/dE$ is much less than the contribution of the first since the fraction of the third-chance cross section—that is, $\sigma_{f,237}$—in the total fission cross section σ_f at the primary neutron energy of 13.2 MeV is extremely small. Because of the contribution from the nonequilibrium mechanism of neutron emission at the first step of the emission chain, the component $d\bar{\nu}_{pre,1}/dE$ has a harder shape of the distribution than the evaporation component.

The postfission-neutron spectrum $d\bar{\nu}_{faf}/dE$ (in other words, the differential multiplicity of neutrons from fully accelerated fragments), as given by the second term in the expression on the right-hand side of (14), is represented in the form

$$\frac{d\bar{\nu}_{faf}}{dE} = \alpha\sum_{x=0}^{2}\bar{\nu}_{f,A-x}N_M(E, \beta T_x)\frac{\sigma_{f,A-x}}{\sigma_f}. \qquad (15)$$

The values of x = 0, 1, and 2, which stand for the numbers of neutrons emitted prior to the fission event, correspond to the chain of fissile nuclei ^{239}U, ^{238}U, and ^{237}U. The quantity $\bar{\nu}_{f,A-x}$ determines the mean multiplicity of neutrons emitted from the fully accelerated fragments originating from the fission of $A - x$ nuclei (A = 239). The partial fission cross sections $\sigma_{f,A-x}$, which represent the contributions of individual chances to the total fission cross section σ_f, are determined from an analysis of this total cross section as a function of the primary neutron energy on the basis of statistical theory and the exciton model of preequilibrium cascade. The contribution of the x = 2 component to expression (15) is very small. The constant α is introduced to ensure a fit to experimental data and to compensate for the error in describing $\bar{\nu}_{f,A-x}$. This error can be removed from our analysis since the description in question is based on an extrapolation of the systematics of $\bar{\nu}_f(E_n)$ from [14] to the region E_n > 6 MeV. Since similar uncertainties stem from the use of the systematics of $T(E_n)$ from [7], we introduced the constant β to implement variations of T_x within $|\Delta T_x/T_x| < 3\%$.

A method that can be used to compute the spectrum of neutrons from nonaccelerated fragments, $d\bar{\nu}_{naf}(E, E_n, C)/dE$, was described in detail elsewhere [4]. The parameter C specifies the excitation-energy fraction that the compound nucleus transfers to internal degrees of freedom of fully developed fragments by the instant of their separation. By varying the parameter C, which determines the hardness of the spectrum and the yield of soft neutrons from nonaccelerated fragments, we were able to describe the experimental spectrum in the low-energy region E < 2 MeV. The characteristic fitted values of the parameters involved are quoted in [4].

Experimental data and the results of the calculations by formula (14) are shown in Fig. 4*c* in the form of the ratio

$$R(E, E_n) = \frac{N(E, E_n)}{N_{Cf}(E)} = \frac{d\bar{\nu}_c(E, E_n)/dE}{\bar{\nu}(E_n)N_{Cf}(E)}, \qquad (16)$$

where $\bar{\nu}(E_n)$ stands for the experimental mean values of the integrated neutron yield, while $N_{Cf}(E)$ is the spectrum of neutrons from the spontaneous fission of ^{252}Cf (a normalization to unity is assumed here for this spectrum). If, in accordance with the traditional approach, postfission neutrons are taken to be emitted only from fully accelerated fragments, we can see an excess of soft neutrons in relation to the results of the calculations based on the statistical model (curve *1*). Upon additionally taking into account neutron emission from nonaccelerated fragments, good agreement between experimental data and the results of the calculations is achieved over almost the entire energy range (curve *2*), including the low-energy section. At one value of the coefficient C, C = 0.53, a unified description of the soft component was obtained both for the neutron spectra studied previously at E_n = 14.7, 16.0, and 17.7 MeV [2] and for the spectrum measured in the present study at E_n = 13.2 MeV.

Thus, the emergence of a low-energy anomaly (excess of soft neutrons) in the spectra measured at the high primary-neutron energies of E_n = 13.2, 14.7, 16.0, and 17.7 MeV and its absence at the low energies of E_n = 2.9 and 5.0 MeV (see [1]) could be explained on the basis of the proposed model.

Immediately from the measured spectrum $N_{exp}(E, E_n)$, we have determined the mean energy of fission neutrons by using the relation

$$\bar{E}_{exp}(E_n) = \int_0^\infty EN_{exp}(E, E_n)dE. \qquad (17)$$

At energies E below the boundary energy E_{min} equal to the energy threshold of the neutron detector, the measured spectrum $N_{exp}(E, E_n)$ was supplemented with an extrapolation according to the dependence in (1).

The resulting mean energy $\bar{E}_{exp}(E_n)$ was then corrected for the effect of the angular correlation between the secondary and primary neutrons, which is due to a highly anisotropic angular distribution of the direction along which the fragments fly apart and to a strong angular correlation between this direction and the direction of postfission-neutron emission. The relevant correction was estimated in just the same way as in [2]. For ^{238}U, our eventual result for the mean neutron energy at E_n = 13.2 MeV is 1.97 ± 0.04 MeV.

5. CONCLUSION

For ^{238}U fission induced by primary neutrons of energies 5.0 and 13.2 MeV, which are of importance for obtaining deeper insight into the mechanism of fission-neutron emission, the spectra of prompt neutrons have been measured for the first time. For this fissile nuclear species, the experimental energy dependences of the ratios $R(E, E_n)$ of the neutron spectra being studied to the corresponding spectrum of neutrons from the spontaneous fission of ^{252}Cf show the same special features as those that were found in analogous measurements at primary energies of 2.9 and 14.7 MeV [1]. The ratios $R(E, E_n)$ measured at $E_n = 5.0$ MeV have a form similar to that determined previously at $E_n = 2.9$ MeV. The shape of the spectrum at $E_n = 13.2$ MeV is similar to the shape of the spectra for $E_n > 14$ MeV. As to the calculation of the spectrum within the traditional approach, it reproduces the shape of the observed distribution only in the energy region above 2 MeV. In the low-energy region, the experimental distribution exhibits an anomalously high yield of soft neutrons in relation to the theoretical description. Upon the inclusion of the third neutron source (emission from nonaccelerated fragments), the calculated curves prove to be in good agreement with experimental data over the entire neutron-energy range studied here.

REFERENCES

1. G. S. Boĭkov, V. D. Dmitriev, G. A. Kudyaev, *et al.*, Yad. Fiz. **53**, 628 (1991) [Sov. J. Nucl. Phys. **53**, 392 (1991)].
2. G. N. Smirenkin, G. N. Lovchikova, A. M. Trufanov, *et al.*, Yad. Fiz. **59**, 1934 (1996) [Phys. At. Nucl. **59**, 1865 (1996)].
3. G. N. Smirenkin, G. N. Lovchikova, A. M. Trufanov, *et al.*, Preprint No. 2439, FÉI (Institute of Physics and Power Engineering, Obninsk, 1995).
4. M. I. Svirin, G. N. Lovchikova, and A. M. Trufanov, Yad. Fiz. **60**, 818 (1997) [Phys. At. Nucl. **60**, 727 (1997)].
5. W. Mannhart, IAEA-TECDOK-410 (IAEA, Vienna, 1987) p. 158.
6. F.H. Froner, IAEA-TECDOC-483 (IAEA, Vienna, 1988), p. 160.
7. J. Terrell, in *Proceedings of the Symposium on the Physics and Chemistry of Fission, Salzburg, 1965* (IAEA, Vienna, 1965), Vol. 11, p. 3.
8. G. S. Boĭkov, V. D. Dmitriev, M. I. Svirin, and G. N. Smirenkin, Yad. Fiz. **57**, 2126 (1994) [Phys. At. Nucl. **57**, 2047 (1994)].
9. P. J. Johansson and B. Holmqvist, Nucl. Sci. Eng. **62**, 695 (1977).
10. B. I. Starostov, A. F. Semenov, and V. N. Nefedov, Vopr. At. Nauki Tekh., Ser.: Yad. Konstanty, No. 3, 16 (1985).
11. R. J. Howerton and R. Doyas, Nucl. Sci. Eng. **46**, 414 (1971).
12. D. G. Madland and J. R. Nix, Nucl. Sci. Eng. **81**, 213 (1982).
13. D. Seeliger *et al.*, INDC (GDR)-057 (IAEA, Vienna, 1990).
14. R. J. Howerton, Nucl. Sci. Eng. **62**, 438 (1977).

Translated by A. Isaakyan

Physics of Atomic Nuclei, Vol. 64, No. 1, 2001, pp. 103–106. From Yadernaya Fizika, Vol. 64, No. 1, 2001, pp. 106–109.

ELEMENTARY PARTICLES AND FIELDS
Theory

Lepton-Flavor-Violating Pion Decay $\pi^+ \longrightarrow \mu^-\nu_\mu e^+e^+$ and $SU(3)_C \otimes SU(3)_L \otimes U(1)_N$ Model*

Hoang Ngoc Long[1), **]

Universität Bielefeld, Universitätstrasse 25, D 33615 Bielefeld, Germany

Received December 15, 1999

Abstract—Within the minimal $SU(3)_C \otimes SU(3)_L \otimes U(1)_N$ model, the lepton-flavor-violating decay $\pi^+ \longrightarrow \mu^-\nu_\mu e^+e^+$ is calculated without directly invoking lepton mixing. The branching ratio for this rare pion-decay mode is found to be much smaller than the current experimental upper limit. If the anomalous interactions are discarded, this result coincides with the result of the previous calculation. © *2001 MAIK "Nauka/Interperiodica".*

At present, neutrinos are presumably massive and mixed as is indicated by various experiments: SuperKamiokande [1] and others [2]. This significant deviation from the Standard Model (SM) calls for its extension. Models based on the $SU(3)_C \otimes SU(3)_L \otimes U(1)_N$ (3 3 1) gauge group [3, 4] are among the most popular in such extensions of the SM. The SM assumes lepton-flavor-number conservation, and its observed violation would be a clear indication of new physics. In the (3 3 1) models, the lepton-flavor number is not conserved, and these models have motivated a variety of dedicated sensitive searches for rare modes of muon and kaon decays and for neutrino oscillations [5]. It is known that the muon system is one of the best places to seek lepton-flavor violation, compared with the others. The "wrong" muon decay $\mu^- \longrightarrow e^-\nu_e\bar{\nu}_\mu$ is widely used to set a lower bound on the singly charged bilepton mass ($M_Y \geq 230$ GeV) [6].

In this study, we pay attention to the lepton-flavor-violating pion decay $\pi^+ \longrightarrow \mu^-\nu_\mu e^+e^+$. The upper limit on its branching ratio is given by $R \leq 1.6 \times 10^{-6}$ at a 90% C.L. [7, 8]. By assuming lepton mixing or horizontal interactions, the above decay was studied theoretically in [9]. However, this decay may be described by the minimal (3 3 1) model in a simple manner without directly invoking lepton mixing.

To start, we first give some basic elements of the model (for more details, see [10]). Three lepton components of each family are in one triplet,

$$f_L^a = (\nu_L^a, l_L^a, (l^c)_L^a)^T,$$

where $a = 1, 2, 3$ is the family index. Under $SU(3)_L$, two of the three quark families transform as an antitriplet and one family transforms as a triplet,

$$Q_{iL} = \begin{pmatrix} d_{iL} \\ -u_{iL} \\ D_{iL} \end{pmatrix}, \quad i = 1, 2, \quad Q_{3L} = \begin{pmatrix} u_{3L} \\ d_{3L} \\ T_L \end{pmatrix}.$$

The right-handed quarks are singlets under $SU(3)_L$. The exotic quarks T and D_i have electric charges of +5/3 and –4/3, respectively.

There are five new gauge bosons: the Z' boson and the charged bileptons with lepton numbers $L = \pm 2$, which are identified as follows: $\sqrt{2}Y_\mu^- = W_\mu^4 - iW_\mu^5$ and $\sqrt{2}X_\mu^{--} = W_\mu^6 - iW_\mu^7$; their couplings to leptons are given by [11]

$$\mathcal{L}_l^{CC} = -\frac{g}{2\sqrt{2}}[\bar{\nu}\gamma^\mu(1-\gamma_5)C\bar{l}^T Y_\mu^- - \bar{l}\gamma^\mu\gamma_5 C\bar{l}^T X_\mu^{--} + \text{h.c.}]. \quad (1)$$

The interactions among the charged vector fields with quarks are

$$\mathcal{L}_q^{CC} = -\frac{g}{\sqrt{2}}[(\bar{u}_{3L}\gamma^\mu d_{3L} + \bar{u}_{iL}\gamma^\mu d_{iL})W_\mu^+ + (\bar{T}_L\gamma^\mu d_{3L} + \bar{u}_{iL}\gamma^\mu D_{iL})X_\mu^{++} + (\bar{u}_{3L}\gamma^\mu T_L - \bar{D}_{iL}\gamma^\mu d_{iL})Y_\mu^- + \text{h.c.}]. \quad (2)$$

It should be noted that the vector currents coupled to X^{--} and X^{++} vanish owing to Fermi statistics, and the exotic quarks interact with ordinary ones only via the bileptons and non-SM Higgs bosons.

The current experimental lower bound on the exotic-quark mass is 200 GeV [12], while the lower bound on the bilepton mass is in the range of 300 GeV.

* This article was submitted by the author in English.

1) On leave of absence from Institute of Physics, NCST, P.O. Box 429, Bo Ho, Hanoi, 10000 Vietnam.

** e-mail: HoangNgocLong@cern.ch

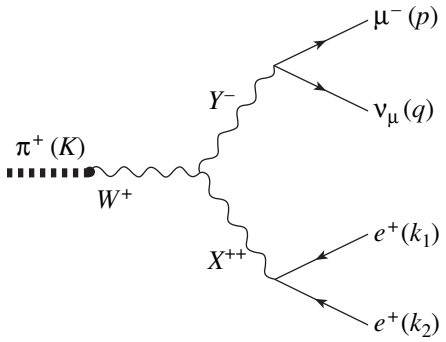

Fig. 1. Feynman diagram for the decay $\pi^+(K) \longrightarrow \mu^-(p)\nu_\mu(q)e^+(k_1)e^+(k_2)$ in the (3 3 1) model.

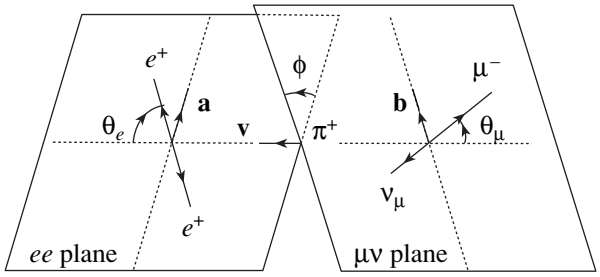

Fig. 2. Illustration of the angles θ_e, θ_μ, and ϕ.

To deal with the above process, we also need the couplings of the bileptons X and Y to the SM weak vector boson W. In the notation adopted in [13], it is $CWXY = \dfrac{g}{\sqrt{2}}$.

We start now with the decay

$$\pi^+(K) \longrightarrow \mu^-(p)\nu_\mu(q)e^+(k_1)e^+(k_2), \tag{3}$$

where the letters in parentheses stand for particle momenta. We assume that the Higgs bosons responsible for lepton-flavor-violating interactions, as well as the exotic quarks, are much heavier than the SM W boson. Hence, the contributions from the exotic quarks and non-SM Higgs bosons are suppressed. With new gauge bosons carrying lepton number $L = 2$, the process in (3) can be described simply by the Feynman diagram in Fig. 1.

For low momentum transfers ($q^2 \ll m_W^2, M_X^2, M_Y^2$), as is the case here, the matrix element for this process is found to be

$$\begin{aligned}\mathcal{M}_{fi} &= 2\frac{G_F^2 f_\pi m_W^2}{M_X^2 M_Y^2}[-(P+K)_\beta K_\gamma + (K+L)_\gamma K_\beta \\ &+ (-L+P)Kg_{\beta\gamma}]\bar{u}_{\nu_\mu}(q)\gamma^\beta(1-\gamma_5) \\ &\times C\bar{u}_\mu^T(p)v_e^T(k_1)C\gamma^\gamma\gamma_5 v_e(k_2),\end{aligned} \tag{4}$$

where the following combinations of four vectors are introduced:

$$\begin{gathered}P = k_1 + k_2, \quad Q = k_1 - k_2, \quad L = p + q, \\ N = p - q, \quad K = P + L.\end{gathered} \tag{5}$$

The squared matrix element is given by

$$\begin{aligned}|\mathcal{M}_{fi}|^2 &= 128\frac{G_F^4 f_\pi^2 m_W^4}{M_X^4 M_Y^4}C_{\beta\gamma}C_{\beta'\gamma'} \\ &\times [p^\beta q^{\beta'} + p^{\beta'}q^\beta - g^{\beta\beta'}(p\cdot q) + i\varepsilon^{\beta\beta' mn}p_m q_n] \\ &\times [k_1^\gamma k_2^{\gamma'} + k_1^{\gamma'}k_2^\gamma - g^{\gamma\gamma'}(k_1\cdot k_2 - m_e^2)],\end{aligned} \tag{6}$$

where the notation $C_{\beta\gamma} \equiv [-(P+K)_\beta K_\gamma + (K+L)_\gamma K_\beta + (-L+P)Kg_{\beta\gamma}]$ is used.

In order to describe the kinematics of the decay, we introduce the following vectors: **v**, a unit vector along the direction of flight of the dipositron in the π^+ rest frame (Σ_π); **a**, a unit vector along the projection of the e^+ 3-momentum in the e^+e^+ c.m. frame (Σ_{2e}) perpendicular to **v**; and **b**, a unit vector along the projection of the μ^- 3-momentum in the $\mu^-\nu_\mu$ c.m. frame ($\Sigma_{\mu\nu}$) perpendicular to **–v**. The kinematics of this decay is then similar to that in [14], which is described in terms of five variables. These are $s_e \equiv P^2$, $s_\mu \equiv L^2$, and three angles: (i) θ_e, the angle of e^+ in Σ_{2e} with respect to the dipositron line of flight in Σ_π; (ii) θ_μ, the angle of μ^- in $\Sigma_{\mu\nu}$ with respect to the $\mu\nu_\mu$ line of flight in Σ_π; and (iii) ϕ, the angle between the plane formed by the positrons in Σ_π and the corresponding plane formed by μ^- and ν_μ. The angles θ_e, θ_μ, and ϕ are shown in Fig. 2.

The width with respect to the pion decay (3) is then written as

$$\begin{aligned}d\Gamma &= \left(\frac{1}{2}\right)\frac{1}{2^{14}\pi^6 m_\pi^3} \\ &\times \sum_{\text{spins}}|\mathcal{M}_{fi}|^2(1-z_\mu)\sigma_e X ds_e ds_\mu d(\cos\theta_e)d(\cos\theta_\mu)d\phi.\end{aligned} \tag{7}$$

In Eq. (7), (1/2) is a statistical factor indicating that there are two (identical) positrons in the final state [15]. With the above definitions, we have the scalar products

$$\begin{gathered}Q^2 = 4m_e^2 - s_e, \quad N^2 = 2m_\mu^2 - s_\mu, \quad K^2 = m_\pi^2, \\ LN = m_\mu^2, \quad PL = \frac{1}{2}(m_\pi^2 - s_e - s_\mu), \\ PN = z_\mu PL + (1-z_\mu)X\cos\theta_\mu, \quad QL = \sigma_e X\cos\theta_e, \\ QN = z_\mu QL + \sigma_e(1-z_\mu)PL\cos\theta_e\cos\theta_\mu \\ -(s_e s_\mu)^{1/2}\sin\theta_e\sin\theta_\mu\cos\phi, \\ d \equiv \varepsilon^{\mu\nu\alpha\beta}L_\mu N_\nu P_\alpha Q_\beta \\ = -(s_e s_\mu)^{1/2}\sigma_e(1-z_\mu)X\sin\theta_e\sin\theta_\mu\sin\phi,\end{gathered} \tag{8}$$

where

$$z_\mu \equiv \frac{m_\mu^2}{s_\mu}, \quad \sigma_e \equiv \left(1 - \frac{4m_e^2}{s_e}\right)^{1/2}, \quad X \equiv ((PL)^2 - s_e s_\mu)^{1/2},$$

and m_e, m_μ, and m_π stand for the masses of the electron, the muon, and the pion, respectively. The ranges of the variables are

$$\begin{aligned} 4m_e^2 \le s_e \le (m_\pi - m_\mu)^2, \\ m_\mu^2 \le s_\mu \le (m_\pi - \sqrt{s_e})^2, \\ 0 \le \theta_e, \quad \theta_\mu \le \pi, \quad 0 \le \phi \le 2\pi. \end{aligned} \tag{9}$$

It should be noted that the imaginary part of $|\mathcal{M}_{fi}|^2$ associated with the pseudotensor d is linear in $\sin\phi$—that is, there are no terms like $Q \cdot Nd$; hence, it will be removed after integration with respect to the angle ϕ. As a result, we find that the decay width is real, as it must.

Integrations with respect to the angles can be carried out analytically by using the Mathematica system for analytic computations. Numerical integrations with respect to the effective masses squared s_e and s_μ are performed by employing the Monte Carlo routine VEGAS [16]. Upon going over to dimensionless parameters $x_e = \frac{s_e}{m_\pi^2}$ and $y_\mu = \frac{s_\mu}{m_\pi^2}$, we obtain the decay width

$$\Gamma(\pi^+ \longrightarrow \mu^- \nu_\mu e^+ e^+) = \frac{G_F^4 f_\pi^2 m_W^4 m_\pi^{11} N}{256\pi^6 M_X^4 M_Y^4}, \tag{10}$$

where N is numerically evaluated at $N = 6.17 \times 10^{-6}$.

We recall that the main (99.987%) mode of π^+ decay is well known:

$$\begin{aligned} \Gamma(\pi^+ \longrightarrow \mu^+ \nu_\mu) \\ = \frac{G_F^2 f_\pi^2 m_\mu^2}{8\pi m_\pi^3}(m_\pi^2 - m_\mu^2)^2 \simeq 2.63 \times 10^{-17}\ \text{GeV}. \end{aligned} \tag{11}$$

From (10) and (11), we obtain the branching ratio

$$\begin{aligned} R_\pi = \frac{\Gamma(\pi^+ \longrightarrow \mu^- \nu_\mu e^+ e^+)}{\Gamma(\pi^+ \longrightarrow \mu^+ \nu_\mu)} \\ = \frac{6.17 \times 10^{-6} G_F^2 m_W^4 m_\pi^{14}}{32\pi^5 M_X^4 M_Y^4 m_\mu^2 (m_\pi^2 - m_\mu^2)^2} \simeq \\ \simeq 4.97 \times 10^{-18} \frac{1}{M_X^4\ [\text{GeV}] M_Y^4\ [\text{GeV}]}. \end{aligned} \tag{12}$$

Setting $M_X \simeq M_Y \simeq 120$ GeV as a lower limit obtained from the LEP data analysis [17], we arrive at $R_\pi \sim 2.3 \times 10^{-34}$. This value is much smaller than the current experimental upper limit, but it coincides with the previous theoretical evaluation without anomalous interactions included [8]. This raises the question about the mechanism of the large lepton-flavor-violating pion-decay mode. However, it is worth mentioning that experimental data on R_π decrease with time—for example, the 1988 data were $R_\pi \le 8 \times 10^{-6}$, while the 1998 data are $R_\pi \le 1.6 \times 10^{-6}$. We assume that, by adding contributions from diagrams featuring the exotic quarks and Higgs bosons, the situation will be modified but not improved too much.

Our calculation can be analogously applied to the lepton-flavor-violating kaon decay $K^+ \longrightarrow \mu^- \nu_\mu e^+ e^+$, which has an experimental branching ratio of $R_K \le 2.0 \times 10^{-8}$. However, the main decay mode $K^+ \longrightarrow \mu^+ \nu_\mu$ only has a branching ratio of 69.51%, instead of 99.987% in the π^+ case considered here.

In summary, we have considered the lepton-flavor-violating pion decay without directly invoking lepton mixing. Our result is twenty-eight orders of magnitude smaller than the current experimental upper limit. This conclusion is not expected to be modified too much upon the inclusion of the contributions from the exotic quarks and Higgs bosons. Hence, the mechanism of the large lepton-flavor-violating pion-decay mode remains a mystery.

ACKNOWLEDGMENTS

I am grateful to Prof. D. Schildknecht for stimulating remarks and to S. Dittmaier for a consultation on the Monte Carlo routine VEGAS. This work was initiated when I was at LAPTH, Annecy, France. I am indebted to G. Belanger and F. Boudjema for a consultation on the decay kinematics and a numerical calculation. Thanks are also due to P. Aurenche and the Theory Group at LAPP and Bielefeld University for kind hospitality.

This work was supported by a DAAD grant.

REFERENCES

1. Y. Fukuda *et al.*, Phys. Lett. B **433**, 9 (1998); Phys. Rev. Lett. **81**, 1562 (1998); T. Kajita, in *Proceedings of the XVIII International Conference on Neutrino Physics and Astrophysics, Takayama, Japan, June 1998.*
2. S. M. Bilenky, C. Giunti, and W. Grimus, hep-ph/9812360; Prog. Part. Nucl. Phys. **43**, 1 (1999).
3. F. Pisano and V. Pleitez, Phys. Rev. D **46**, 410 (1992); P. H. Frampton, Phys. Rev. Lett. **69**, 2889 (1992); R. Foot, O. F. Hernández, F. Pisano, and V. Pleitez, Phys. Rev. D **47**, 4158 (1993).
4. R. Foot, H. N. Long, and Tuan A. Tran, Phys. Rev. D **50**, R34 (1994); H. N. Long, Phys. Rev. D **54**, 4691 (1996); J. C. Montero, F. Pisano, and V. Pleitez, Phys. Rev. D **47**, 2918 (1993).
5. M. M. Guzzo, H. Nunokawa, O. L. G. Peres, *et al.*, IPT-P.057/99; hep-ph/9908308.
6. E. D. Carlson and P. H. Frampton, Phys. Lett. B **283**, 123 (1992); H. Fujii, S. Nakamura, and K. Sasaki, Phys. Lett. B **299**, 342 (1993); H. N. Long and T. Inami, hep-

ph/9902475; Phys. Rev. D **61**, 075002 (2000); Y. Kuno and Y. Okada, KEK-TH 639; hep-ph/9909265.

7. Particle Data Group (R. M. Barnett *et al.*), Eur. Phys. J. C **3**, 1 (1998); Phys. Lett. B **204**, 1 (1988).
8. V. A. Baranov *et al.*, Yad. Fiz. **54**, 1298 (1991) [Sov. J. Nucl. Phys. **54**, 790 (1991)].
9. V. D. Laptev, in *Program of Experimental Investigations at the Meson Factory of the Institute of Nuclear Research of the USSR Academy of Sciences* (Moscow, 1984), p. 145.
10. D. Ng, Phys. Rev. D **49**, 4805 (1994).
11. P. H. Frampton and D. Ng, Phys. Rev. D **45**, 4240 (1992).
12. P. Das, P. Jain, and D. W. McKay, hep-ph/9808256; Phys. Rev. D **59**, 055011 (1999).
13. T. Ishikawa, T. Kaneko, K. Kato, *et al.*, GRACE Manual, KEK Report 92-19 (1993); H. N. Long and T. Inami, hep-ph/9902475; Phys. Rev. D **61**, 075002 (2000).
14. A. Pais and S. B. Treiman, Phys. Rev. **168**, 1858 (1968); N. Cabibbo and A. Maksymovicz, Phys. Rev. B **137**, 438 (1965); Erratum: **168**, 1926 (1968); J. Bijnens, Nucl. Phys. B **337**, 635 (1990).
15. C. Quigg, *Gauge Theories of the Strong, Weak, and Electromagnetic Interactions* (Benjamin, 1983); T.-P. Cheng and L.-F. Li, *Gauge Theory of Elementary Particle Physics* (Oxford Univ. Press, New York, 1984); Q. Ho-Kim and X. Y. Pham, *Elementary Particles and Their Interactions: Concepts and Phenomena* (Springer-Verlag, Berlin, 1998).
16. G. P. Lepage, J. Comput. Phys. **27**, 192 (1978).
17. P. Frampton, Int. J. Mod. Phys. A **13**, 2345 (1998).

Physics of Atomic Nuclei, Vol. 64, No. 1, 2001, pp. 107–119. Translated from Yadernaya Fizika, Vol. 64, No. 1, 2001, pp. 110–122.

ELEMENTARY PARTICLES AND FIELDS
Theory

QCD String in Mesons and Baryons

D. S. Kuzmenko* and Yu. A. Simonov**

Institute of Theoretical and Experimental Physics, Bol'shaya Cheremushkinskaya ul. 25, Moscow, 117259 Russia

Received July 10, 2000

Abstract—The distributions of fields generated by static $Q\bar{Q}$ and QQQ sources are calculated analytically within the bilocal approximation of the method of vacuum correlation functions. At large distances between the quarks, the fields assume a clear-cut stringlike shape. The main contribution to the string comes from the longitudinal component of the chromoelectric field. The contribution of the transverse chromoelectric field is below 3% of the contribution from the longitudinal component. A baryonic string has a *Y*-like shape with a deep well in the region of the string-junction position. Field distributions are considered for a quark–diquark configuration and in the case of three quarks occurring on a straight line. The interaction potential is calculated for three quarks residing at the vertices of an equilateral triangle. © *2001 MAIK "Nauka/Interperiodica".*

1. INTRODUCTION

The distributions of fields within a string connecting static $Q\bar{Q}$ sources were repeatedly investigated in lattice calculations by using either connected [1–3] or disconnected [4, 5] probing plaquettes. Later on, such investigations were performed for configurations in the Abelian projection [6]. The analytic calculations performed by Rueter and Dosch and Dosch *et al.* [7] for disconnected probes treated within the model of a Gaussian stochastic vacuum (by the method of vacuum correlation functions [8, 9]) revealed that, in the distribution of the field strength tensor, there is a string structure of the same type as that which was found in lattice calculations. It was shown, however, that, in contrast to a disconnected probe, a connected one makes it possible to obtain the distribution of each field component individually.

A comparison of lattice data [1] both in magnitude and in direction with analytic predictions obtained within the method of vacuum correlation functions was drawn in [2]. This comparison compellingly demonstrated a satisfactory agreement for all distributions. In particular, the lattice result according to which the longitudinal electric field decreases with increasing distance from the string axis (string profile) is described very well by the contribution of the lowest (bilocal) correlation function [2]. It should be emphasized that the form of the field correlation function, which is specified by the scalar form factors D and D_1 [8], appears as an input in the method of vacuum correlation functions. For each of these two, lattice data [10] yield an exponential with a slope of $T_g \simeq 0.2$ fm. Dominance of a bilocal correlation function (sometimes, this situation is said to be described by the Gaussian stochastic model of the QCD vacuum) was demonstrated in [11] by precisely calculating the static potential for a $Q\bar{Q}$ Wilson loop on a lattice in various representations of the $SU(3)$ group. The analysis of data reported in [11] that was performed in [12] confirmed that the contribution from the Gaussian stochastic model saturates about 99% of the static $Q\bar{Q}$ potential. These results furnish sufficient motivation for studying field distributions in terms of the lowest bilocal correlation function.

For static $Q\bar{Q}$ and QQQ systems, we calculate here field distributions in the bilocal approximation of the method of vacuum correlation functions by using connected probing plaquettes. It will be shown that the main contribution to string formation comes from the longitudinal component of the chromoelectric field. In the case of three quarks occurring at the vertices of an equilateral triangle, the string has a *Y*-like shape with a deep well in the region of the string-junction position. We consider field distributions in a quark–diquark configuration and in the case of three quarks situated on a straight line. In addition, we calculate the interaction potential for three quarks occurring at the vertices of an equilateral triangle. A minimum in the field distribution near the string junction hinders the growth of the interaction potential at small quark separations.

Some of the results set forth below were quoted in [13].

The present article is organized as follows. In Section 2, we derive analytically the distributions of the longitudinal and the transverse field component in the $Q\bar{Q}$ system and determine the contribution of the function D_1 to the longitudinal field component at various quark–antiquark distances. In the same section, we also present distributions of the total field, taking into account perturbative one-gluon exchange. In Section 3, we obtain analytically the distribution of the field of

* e-mail: kuzmenko@heron.itep.ru
** e-mail: simonov@heron.itep.ru

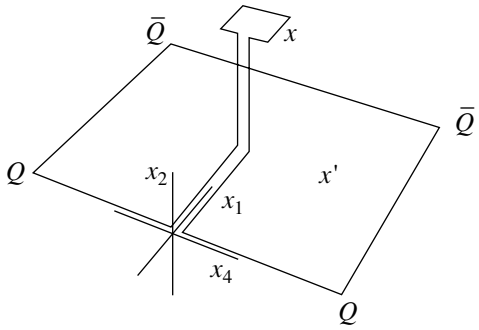

Fig. 1. Connected probe for the $Q\bar{Q}$ system.

three quarks for various configurations of these quarks. For the case of three quarks residing at the vertices of an equilateral triangle, we also construct the field distribution with allowance for one-gluon exchange. In Section 4, we calculate the potential of quark interaction in a baryon. In Section 5, we summarize our results and discuss their possible physical implications.

2. DISTRIBUTIONS IN A MESON

We will calculate field distributions with the aid of gauge-invariant construction $\rho_{\mu\nu}(x)$ formed by a probing plaquette $P_{\mu\nu}(x)$ and the Wilson loop W, which are related by parallel transporters Φ. In the following, this construction, which does not possess Lorentz invariance, is referred to as a connected probe (see Fig. 1). By definition, we have

$$\rho_{\mu\nu}(x) = \frac{\langle W^{\alpha}_{\beta}(x_0)\Phi^{\beta}_{\gamma}(x_0, x)(P_{\mu\nu}(x))^{\gamma}_{\delta}(\Phi^{+})^{\delta}_{\alpha}(x, x_0)\rangle}{\langle W\rangle} - 1, \quad (1)$$

where

$$W = \frac{1}{N_c}\mathrm{tr}\,P\exp\left(ig\oint_C A^a_\mu t^a dz_\mu\right), \quad (2)$$

$$(P_{\mu\nu}(x))^{\alpha}_{\beta} = (P\exp iga^2 F^a_{\mu\nu}(x)t^a)^{\alpha}_{\beta}, \quad (3)$$

$$\Phi^{\alpha}_{\beta}(x, y) = \left(P\exp ig\int_y^x A^a_\mu t^a dz_\mu\right)^{\alpha}_{\beta}, \quad (4)$$

and $W^{\alpha}_{\beta}(x_0)$ stands for an exponential ordered along the contour C of the Wilson loop with a discontinuity at the point $x_0 = (0, 0, 0, 0)$. The contour C lies in the (1 4) plane and represents a rectangle of dimensions $R \times T$ (the quarks are static). The surface S bounded by the contour has the coordinates $x' = (x'_1, x'_2, x'_3, x'_4)$, where $0 \le x'_1 \le R$, $x'_2 = x'_3 \equiv 0$, and $-T/2 \le x'_4 \le T/2$. The probing plaquette $P_{\mu\nu}(x)$ of dimensions $a \times a$ is oriented in the $(\mu\ \nu)$ plane. It occurs at the point $x = (x_1, x_2, x_3, x_4)$, where x_1 is the coordinate of the probe along the string direction, x_2 is the distance from the probe to the string axis, and $x_3 = x_4 \equiv 0$. In the limit of small plaquette dimensions a, it follows from the expansion of expression (3) in terms of a^2 that the connected probe is proportional to the field strength at the point x:

$$\rho_{\mu\nu}(x) = iga^2\frac{\langle W^{\alpha}_{\beta}\Phi^{\beta}_{\gamma}(F^a_{\mu\nu}(x)t^a)^{\gamma}_{\delta}(\Phi^{+})^{\delta}_{\alpha}\rangle}{\langle W\rangle} + O(a^4). \quad (5)$$

With the aid of the connected probe, we can therefore change the components of the color field that is generated by a quark–antiquark pair and which is not distorted by a probing plaquette in the limit of small a. We will evaluate the connected probe (1) in the bilocal approximation of the method of vacuum correlation functions, where only the contribution of bilocal correlation functions is retained in the expansion of the Wilson loop in the field $F_{\mu\nu}$. Let us express the Wilson loop in terms of $F_{\mu\nu}$ with the aid of the non-Abelian Stokes theorem as

$$W = \frac{1}{N_c}\exp\left(ig\int_S F_{\mu\nu}(x, z_0)d\sigma_{\mu\nu}(x)\right), \quad (6)$$

where

$$F_{\mu\nu}(x, z_0) = \Phi(z_0, x)F_{\mu\nu}(x)\Phi(x, z_0). \quad (7)$$

Averaging the Wilson loop over vacuum fields in the bilocal approximation, we arrive at

$$\begin{aligned}\langle W\rangle &= \left\langle \frac{1}{N_c}\mathrm{tr}\left(1 + ig\int_S F_{\mu\nu}(x, z_0)d\sigma_{\mu\nu}(x)\right.\right.\\ &\left. -\frac{g^2}{2}\int_S\int_S d\sigma_{\mu\nu}(x)d\sigma_{\rho\sigma}(x')F_{\mu\nu}(x)\Phi(x, x')\right.\\ &\left.\left.\times F_{\rho\sigma}(x')\Phi(x', x) + \ldots\right)\right\rangle = 1 - \frac{g^2}{2}\int_S\int_S d\sigma_{\mu\nu}(x)\\ &\times d\sigma_{\rho\sigma}(x')\frac{1}{N_c}\mathrm{tr}\langle F_{\mu\nu}(x)\Phi(x, x')F_{\rho\sigma}(x')\Phi(x', x)\rangle + \ldots\\ &\approx \exp\left(-\frac{g^2}{2}\int_S\int_S d\sigma_{\mu\nu}(x)d\sigma_{\rho\sigma}(x')\right.\\ &\left.\times\frac{1}{N_c}\mathrm{tr}\langle F_{\mu\nu}(x)\Phi(x, x')F_{\rho\sigma}(x')\Phi(x', x)\rangle\right).\end{aligned} \quad (8)$$

In the bilocal approximation, we have obtained a double surface integral. The surface of the connected probe, S_ρ, is formed by the surface of the Wilson loop, S, and the plaquette surface S_P, $S_\rho = S + S_P$. Let us

apply Eq. (8) to S_ρ. The double integral in (8) can then be represented as the sum of three terms,

$$\iint_{S_\rho S_\rho} = \iint_{S\,S} + 2\iint_{S\,S_P} + \iint_{S_P S_P}. \tag{9}$$

In the bilocal-approximation expression for the connected probe, the first term in (9) is canceled by the double integral in the denominator, while the third term vanishes in the limit of small a; that is, we have

$$\rho_{\mu\nu}(x) \simeq \frac{\exp\left(-\frac{1}{2}\iint_{S_\rho S_\rho}\right)}{\exp\left(-\frac{1}{2}\iint_{S\,S}\right)} - 1 \tag{10}$$

$$= \exp\left(-\iint_{S\,S_P} - \frac{1}{2}\iint_{S_P S_P}\right) - 1 = -\iint_{S\,S_P} + O(a^4),$$

where

$$-\iint_{S\,S_P} \equiv \rho^{\text{biloc}}_{\mu\nu}(x) \equiv -a^2\int_S d\sigma_{\rho\sigma}(x') \times \frac{g^2}{N_c}\mathrm{tr}\langle F_{\rho\sigma}(x')\Phi(x', x)F_{\mu\nu}(x)\Phi(x, x')\rangle \tag{11}$$

(in performing integration over the plaquette surface, no summation over the orientations of the surface is implied).

In the following, the mean (color-singlet) field at the point x will be defined in the bilocal approximation as

$$\langle F_{\mu\nu}(x)\rangle_{Q\bar{Q}} \equiv -\frac{1}{a^2}\rho^{\text{biloc}}_{\mu\nu}(x) = \int_S d\sigma_{\rho\sigma}(x')\frac{g^2}{N_c}\mathrm{tr}\langle F_{\rho\sigma}(x')\Phi(x', x)F_{\mu\nu}(x)\Phi(x, x')\rangle. \tag{12}$$

Within the method of vacuum correlation functions, it is proposed to parametrize bilocal correlation functions in terms of the scalar form factors D and D_1 as (see the second reference in [8])

$$\frac{g^2}{N_c}\mathrm{tr}\langle F_{\rho\sigma}(x')\Phi(x', x)F_{\mu\nu}(x)\Phi(x, x')\rangle = (\delta_{\rho\mu}\delta_{\sigma\nu} - \delta_{\rho\nu}\delta_{\sigma\mu})(D(h^2) + D_1(h^2)) + (h_\mu h_\rho\delta_{\nu\sigma} - h_\mu h_\sigma\delta_{\nu\rho} - h_\rho h_\nu\delta_{\mu\sigma} + h_\nu h_\sigma\delta_{\mu\rho})\frac{\partial D_1(h^2)}{\partial h^2} \equiv D_{\rho\sigma,\mu\nu}(h), \tag{13}$$

where $h \equiv x - x'$. In lattice calculations, it was shown [10] that, at large distances, either form factor has the form of an exponential with a slope of $T_g \simeq 0.2$ fm:

$$D(h^2) = D(0)\exp(-\mu|h|),$$
$$D_1(h^2) = D_1(0)\exp(-\mu|h|), \tag{14}$$
$$D_1(0) \simeq D(0)/3, \quad \mu \simeq 1\ \text{GeV}; \quad T_g \equiv 1/\mu.$$

Following [2], we will use the functions D and D_1 in the form (14) at all distances.

The values of $(\rho\ \sigma) = (1\ 4)$ on the right-hand side of Eq. (12) are determined by the orientation of the Wilson loop; therefore, the parametrization in (13) reduces to

$$D_{14,\,i4}(h) = \delta_{1i}(D(h^2) + D_1(h^2)) + (h_1h_i + h_4^2\delta_{1i})\frac{\partial D_1(h^2)}{\partial h^2}, \tag{15}$$

$$D_{14,\,ik}(h) = (h_k h_4\delta_{i1} - h_i h_4\delta_{k1})\frac{\partial D_1(h^2)}{\partial h^2}, \tag{16}$$

where $i, k = 1, 2, 3$; it can be shown that relations (15) and (16) determine, respectively, the chromoelectric and the chromomagnetic field components, $\langle\mathbf{E}(x)\rangle_{Q\bar{Q}}$ and $\langle\mathbf{B}(x)\rangle_{Q\bar{Q}}$.

Let us now show that $\langle E_1(x)\rangle_{Q\bar{Q}}$ and $\langle E_2(x)\rangle_{Q\bar{Q}}$ are the only nonzero field components. Indeed, we have $D_{14,\,34}(h) \equiv 0$ in Eq. (15) since $h_3 \equiv x_3 - x_3' \equiv 0$; therefore, $\langle E_3(x)\rangle_{Q\bar{Q}} \equiv \langle F_{34}(x)\rangle_{Q\bar{Q}} \equiv 0$ in Eq. (12) as well. Expression (16) for $D_{14,\,ik}(h)$ is antisymmetric in $h_4 \equiv -x_4'$; therefore, we obtain $\int_S d\sigma_{\rho\sigma}(x') = \int_0^R dx_1'\int_{-T/2}^{T/2} dx_4'$ upon the integration in (12) over the measure $\langle\mathbf{B}(x)\rangle_{Q\bar{Q}} \equiv 0$.

The expressions for $\langle E_1(x)\rangle_{Q\bar{Q}}$ and $\langle E_2(x)\rangle_{Q\bar{Q}}$ are given by

$$\langle E_1(x)\rangle_{Q\bar{Q}} = \int_0^R dx_1'\int_{-T/2}^{T/2} dx_4'\left(D(h^2) + D_1(h^2) + (h_1^2 + h_4^2)\frac{\partial D_1(h^2)}{\partial h^2}\right), \tag{17}$$

$$\langle E_2(x)\rangle_{Q\bar{Q}} = \int_0^R dx_1'\int_{-T/2}^{T/2} dx_4' h_1h_2\frac{\partial D_1(h^2)}{\partial h^2}. \tag{18}$$

Upon performing integration in (17) and (18), we arrive at

$$\langle E_1(x)\rangle_{Q\bar{Q}} = \frac{D(0)}{3}\left\{\int_0^{\frac{R}{2}+\left|x_1-\frac{R}{2}\right|} (7K_1(\mu\sqrt{a'^2 + x_2^2})\right.$$

$$\times\sqrt{a'^2+x_2^2}-\mu K_0(\mu\sqrt{a'^2+x_2^2})a'^2)da'$$
$$+\int_0^{\frac{R}{2}-\left|x_1-\frac{R}{2}\right|}(7K_1(\mu\sqrt{a'^2+x_2^2})\sqrt{a'^2+x_2^2}$$
$$-\mu K_0(\mu\sqrt{a'^2+x_2^2})a'^2)da'\Bigg\}, \quad (19)$$

$$\langle E_2(x)\rangle_{Q\bar{Q}} = \frac{x_2 D(0)}{3}\Bigg\{K_1\Bigg(\mu\sqrt{\left(\frac{R}{2}+\left|x_1-\frac{R}{2}\right|\right)^2+x_2^2}\Bigg)$$
$$\times\sqrt{\left(\frac{R}{2}+\left|x_1-\frac{R}{2}\right|\right)^2+x_2^2}\,\mathrm{sgn}\Big(x_1-\frac{R}{2}\Big)$$
$$-K_1\Bigg(\mu\sqrt{\left(\frac{R}{2}-\left|x_1-\frac{R}{2}\right|\right)^2+x_2^2}\Bigg) \quad (20)$$
$$-\sqrt{\left(\frac{R}{2}-\left|x_1-\frac{R}{2}\right|\right)^2+x_2^2}\,\mathrm{sgn}\Big(x_1-\frac{R}{2}\Big)\Bigg\},$$

where K_0 and K_1 are Macdonald functions.

Presented immediately below are the expressions for the individual contributions of D and D_1 to $\langle E_1(x)\rangle_{Q\bar{Q}}$. We have

$$\langle E_1(x_1,x_2)\rangle^D_{Q\bar{Q}} \equiv \int_0^R dx_1'\int_{-T/2}^{T/2}dx_4' D(h^2)$$
$$= 2D(0)\Bigg\{\int_0^{\frac{R}{2}+\left|x_1-\frac{R}{2}\right|}K_1(\mu\sqrt{a'^2+x_2^2})\sqrt{a'^2+x_2^2}da' \quad (21)$$
$$+\int_0^{\frac{R}{2}-\left|x_1-\frac{R}{2}\right|}K_1(\mu\sqrt{a'^2+x_2^2})\sqrt{a'^2+x_2^2}da'\Bigg\},$$

$$\langle E_1(x_1,x_2)\rangle^{D_1}_{Q\bar{Q}}$$
$$\equiv\int_0^R dx_1'\int_{-T/2}^{T/2}dx_4'\Bigg(D_1(h^2)+(h_1^2+h_4^2)\frac{\partial D_1(h^2)}{\partial h^2}\Bigg)$$
$$= \frac{D(0)}{3}\Bigg\{\int_0^{\frac{R}{2}+\left|x_1-\frac{R}{2}\right|}(K_1(\mu\sqrt{a'^2+x_2^2})\sqrt{a'^2+x_2^2} \quad (22)$$
$$-\mu K_0(\mu\sqrt{a'^2+x_2^2})a'^2)da'$$
$$+\int_0^{\frac{R}{2}-\left|x_1-\frac{R}{2}\right|}(K_1(\mu\sqrt{a'^2+x_2^2})\sqrt{a'^2+x_2^2}$$
$$-\mu K_0(\mu\sqrt{a'^2+x_2^2})a'^2)da'\Bigg\},$$

where $D(0)$ is fitted to the $Q\bar{Q}$-string tension $\sigma = 0.9$ GeV/fm. In the bilocal approximation of the method of vacuum correlation functions, these two quantities are related by the equation

$$\sigma = \pi D(0)/\mu^2 \quad (23)$$

[see the comment after Eq. (49) below].

In the leading order in α_s, the perturbative interaction is determined by one-gluon exchange between the quarks. In just the same way as in the Abelian case (QED), this leads to the emergence of the Coulomb field

$$\mathbf{E}^{\mathrm{coul}} = C_F\alpha_s\Big(\frac{\mathbf{r}_1}{r_1^3}-\frac{\mathbf{r}_2}{r_2^3}\Big), \quad (24)$$

where $\mathbf{r}_1$ is the end-to-end vector from the quark to the probe, while $\mathbf{r}_2$ is the analogous vector from the antiquark to the probe. Since the $Q\bar{Q}$ system is in the $SU(3)$-singlet state, there arises the Casimir operator $C_F = \mathrm{tr}\,t^a t^a = 4/3$. The value of $e = 4\alpha_s/3 = 0.295$ was determined from a fit to the results of lattice calculations for the $Q\bar{Q}$ potential in terms of the Cornell potential $V_{\mathrm{Corn}} = -e/R + \sigma R$ (see the review article of Bali [14] and references therein).

Figures 2*a*–5*a* display the distributions $\langle E_1(x_1, x_2)\rangle^2_{Q\bar{Q}}$ for the quark–antiquark distances $R = T_g$, $5T_g$, $10T_g$, and $30T_g$. It can be seen that, from $5T_g$, a string of characteristic shape is stretched between the quark and the antiquark. For the same distances, Figs. 2*b*–5*b* show the distributions of the total field with allowance for perturbative one-gluon exchange,

$$(\mathbf{E}^{\mathrm{tot}}_{Q\bar{Q}}(x_1,x_2))^2 \equiv (E_1^{\mathrm{coul}}+\langle E_1\rangle_{Q\bar{Q}})^2+(E_2^{\mathrm{coul}})^2. \quad (25)$$

We can see that perturbative one-gluon exchange is dominant at distances of $T_g \simeq 0.2$ fm.

Figure 6 depicts the distribution $\langle E_2(x_1, x_2)\rangle^2_{Q\bar{Q}}$ at $R = T_g$ and $30T_g$. From this figure, it is obvious that E_2 makes no contribution to the string. In the region of distances from the quark and the antiquark about $\sim T_g$, E_2 is less than 3% of the field strength in the string, decreasing fast with increasing distances.

Figure 7 presents $x_1 = R/2$ (transverse) sections of the distributions plotted in Figs. 2*a*–5*a*. The profiles of

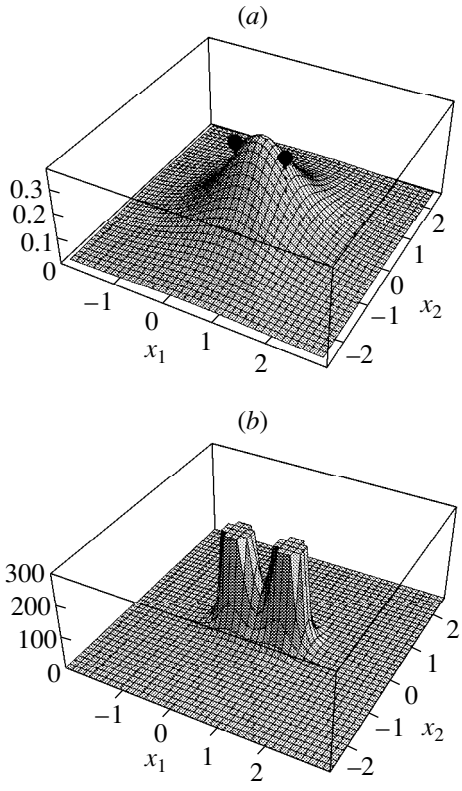

Fig. 2. Distributions (*a*) $\langle E_1(x_1, x_2)\rangle^2_{Q\bar{Q}}$ and (*b*) $(\mathbf{E}^{\text{tot}}_{Q\bar{Q}}(x_1, x_2))^2$ (in GeV^2/fm^2). Here and in Figs. 3–9, x_1 and x_2 are measured in T_g units. The quark–antiquark distance was taken to be $R = T_g$. The quark and antiquark positions are shown by points.

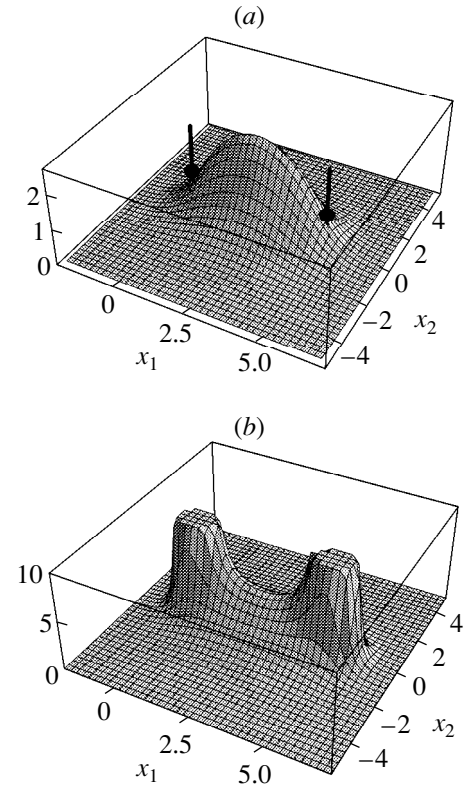

Fig. 3. As in Fig. 2, but for $R = 5T_g$, with the quark and antiquark positions being shown by points with vertical bars.

the $R = 10T_g$ and $30T_g$ strings nearly coincide—for $R \gtrsim 10T_g$, the string has an invariable saturated shape. At the midpoint of the saturated string, the field strength is $E^{\text{sat}} = 1.8$ GeV/fm. The saturated-string thickness is $\delta x^{\text{sat}} = 2.2T_g$ [according to the definition of δx^{sat}, $E_1^2(R/2, \delta x^{\text{sat}}/2) = 1/2(E^{\text{sat}})^2$].

Figure 8 displays the $x_2 = 0$ (longitudinal) section of the $R = 30T_g$ string. The field strength grows fast in the region from $-3T_g$ to $3T_g$, reaching a long plateau at $E_1 = E^{\text{sat}}$. The same figure also shows the total field that was calculated with allowance for perturbative one-gluon exchange and which decreases monotonically for $x_1 > 0$, reaching a plateau at $x_1 \simeq 5T_g$; this field grows in the region $25T_g < x_1 < 30T_g$ and has no inflection points over the entire region $0 < x_1 < R$.

For $R = T_g$ and $30T_g$, Fig. 9 shows the distribution $\langle E_1(x_1, x_2)\rangle^{D_1}_{Q\bar{Q}}$ of the contribution from the function D_1 (22). In just the same way as E_2, $E_1^{D_1}$ does not contribute to the string. In the region of distances from the

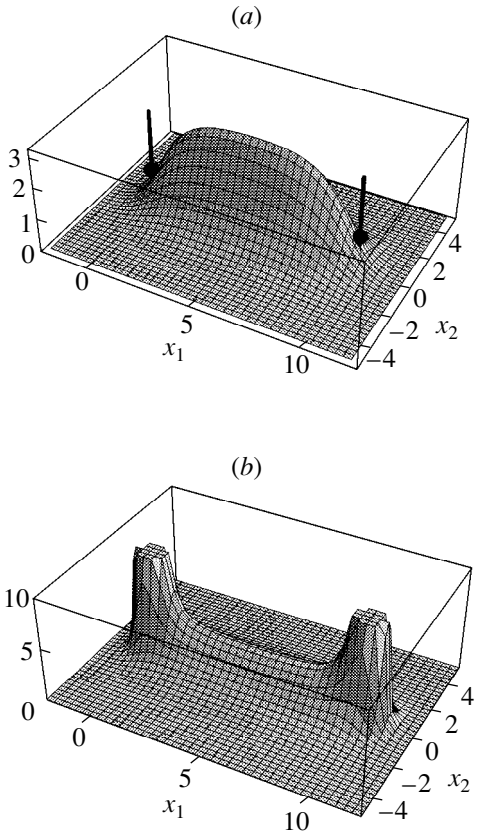

Fig. 4. As in Fig. 3, but for $R = 10T_g$.

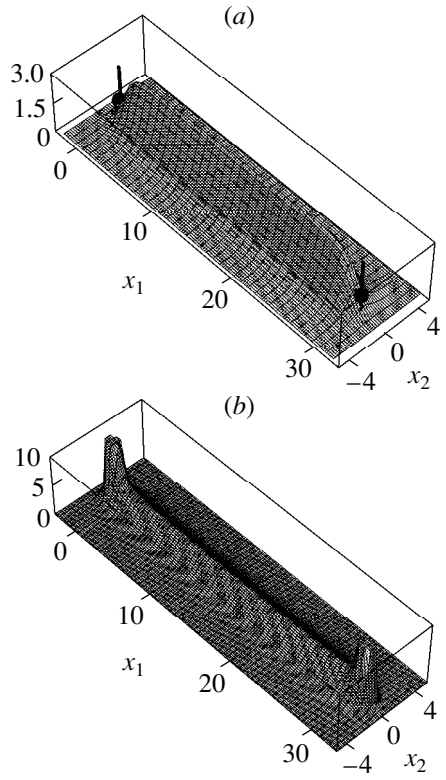

Fig. 5. As in Fig. 3, but for $R = 30T_g$.

quark and the antiquark about T_g, $E_1^{D_1}$ is less than 3% of the field strength in the string, decreasing fast with distance. Two symmetric distributions that correspond to two integrals in (22) are formed near the quark and the antiquark. At $R = T_g$, they are superimposed, with the result that the total distribution has a maximum at zero. At $R = 30T_g$, there arises a zero-field region in between these distributions, which are antisymmetric under the reflection $x_1 \longrightarrow -x_1$ with respect to the points $x_1^0 = 0$ and $x_1^0 = R$ for the quark and the antiquark, respectively.

3. FIELD DISTRIBUTIONS IN BARYONS

Let us first consider three quarks occurring at the vertices of an equilateral triangle. The contour of the baryonic Wilson loop $W^{(3Q)}$ consists of the string-junction trajectory and three contours C_Γ, $\Gamma = A, B, C$, that are formed by the quark trajectories (see Fig. 10). The position of the string junction is determined by the condition requiring that the contour surface be minimal. In Fig. 10, three petals of the contour converge at angle of $2\pi/2$, forming the Mercedes star. A color-singlet object is constructed from the loop by using fully antisymmetric tensors as follows:

$$W^{(3Q)} = \frac{1}{3}\epsilon_{\alpha\beta\gamma}\Phi^{\alpha}_{\alpha'}(C_A)\Phi^{\beta}_{\beta'}(C_B)\Phi^{\gamma}_{\gamma'}(C_C)\epsilon^{\alpha'\beta'\gamma'}. \quad (26)$$

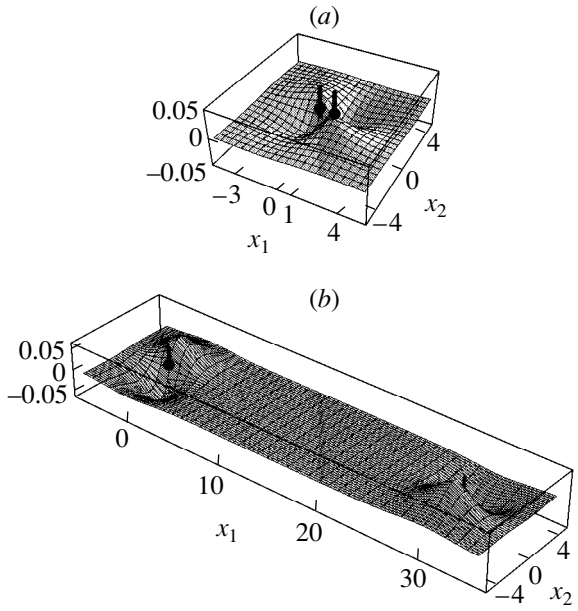

Fig. 6. Distribution $\langle E_2(x_1, x_2)\rangle_{Q\bar{Q}}$ (in GeV/fm) for $R =$ (*a*) T_g and (*b*) $30T_g$. The quark and antiquark positions are shown by points with vertical bars.

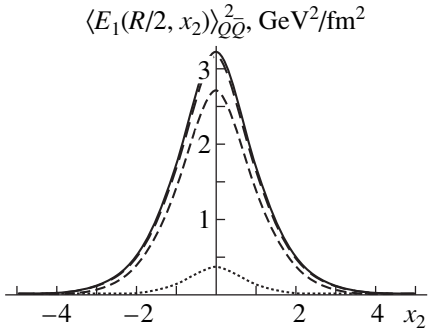

Fig.7. Profile of the transverse section of the $Q\bar{Q}$ string, $\langle E_1(R/2, x_2)\rangle^2_{Q\bar{Q}}$, for $R =$ (dotted curve) T_g, (short dashes) $5T_g$, (long dashes) $10T_g$, and (solid curve) $30T_g$. At distances R about $10T_g$, the string reaches saturation: the string profile for $R = 10T_g$ is virtually coincident with that for $R = 30T_g$.

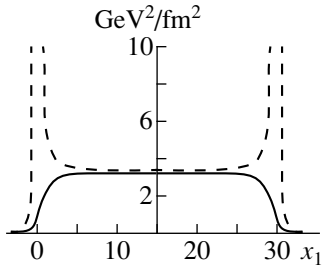

Fig. 8. Profile of the longitudinal section of the $Q\bar{Q}$ string, $\langle E_1(x_1, 0)\rangle^2_{Q\bar{Q}}$, and distribution $(\mathbf{E}^{\text{tot}}_{Q\bar{Q}}(x_1, 0))^2$ obtained with allowance for perturbative one-gluon exchange (solid and dashed curve, respectively; $R = 30T_g$).

With the aid of parallel transporters, the probing plaquette is connected to the contour C_A at the point x^0 ($x_1^0 = x_4^0 = 0$, $x_3^0 = R$); $x_2 \equiv 0$ for the entire construction of the connected probe.

In expression (12) for the mean field in the bilocal approximation of the method of vacuum correlation functions, we must perform summation over all three surfaces A, B, and C; that is,

$$\langle F_{\mu\nu}(x)\rangle_{3Q} = \sum_{\Gamma = A, B, C} \int_{\Sigma_\Gamma} d\sigma^\Gamma_{\rho\sigma}(x') \times \frac{g^2}{N_c}\mathrm{tr}\langle F_{\rho\sigma}(x')\Phi(x', x)F_{\mu\nu}(x)\Phi(x, x')\rangle, \quad (27)$$

where Σ_Γ stands for the area of the corresponding surface, $\Sigma_\Gamma = R \times T$. Upon introducing, in the (x_1, x_3) plane, the direction vectors $\mathbf{n}^A = (0, 1)$, $\mathbf{n}^B = (\sqrt{3}/2, -1/2)$, and $\mathbf{n}^C = (-\sqrt{3}/2, -1/2)$, we perform integration in (27) over the surfaces:

$$d\sigma^\Gamma_{\rho\sigma}(x')F_{\rho\sigma}(x') = d\sigma^\Gamma_{i4}(x')F_{i4}(x') = n_i^\Gamma E_i(l'\mathbf{n}^\Gamma, x_4')dl'dx_4'. \quad (28)$$

As a result, we obtain

$$\langle F_{\mu\nu}(x)\rangle_{3Q} = \sum_\Gamma n_i^\Gamma \int_0^R dl' \int_{-T/2}^{T/2} dx_4' D_{i4,\mu\nu}(l'\mathbf{n}^\Gamma - \mathbf{x}, x_4' - x_4). \quad (29)$$

In the ensuing calculations, we will take into account only the contribution of D; as was shown in the preceding section, this contribution determines the string shape. From (29), (15), and (14), we then obtain

$$\langle E_3(x_1, x_3)\rangle_{3Q} = D(0)\int_0^R dl' \int_{-T/2}^{T/2} dx_4' \times \left[\exp\left(-\mu\sqrt{x_1^2 + (x_3 - l')^2 + x_4'^2}\right) - \frac{1}{2}\exp\left(-\mu\sqrt{\left(x_1 - \frac{\sqrt{3}}{2}l'\right)^2 + (x_3 + l'/2)^2 + x_4'^2}\right) - \frac{1}{2}\exp\left(-\mu\sqrt{\left(x_1 + \frac{\sqrt{3}}{2}l'\right)^2 + (x_3 + l'/2)^2 + x_4'^2}\right)\right], \quad (30)$$

$$\langle E_1(x_1, x_3)\rangle_{3Q} = D(0)\int_0^R dl' \int_{-T/2}^{T/2} dx_4' \times \left[\frac{\sqrt{3}}{2}\exp\left(-\mu\sqrt{\left(x_1 - \frac{\sqrt{3}}{2}l'\right)^2 + (x_3 + l'/2)^2 + x_4'^2}\right) - \frac{\sqrt{3}}{2}\exp\left(-\mu\sqrt{\left(x_1 + \frac{\sqrt{3}}{2}l'\right)^2 + (x_3 + l'/2)^2 + x_4'^2}\right)\right]. \quad (31)$$

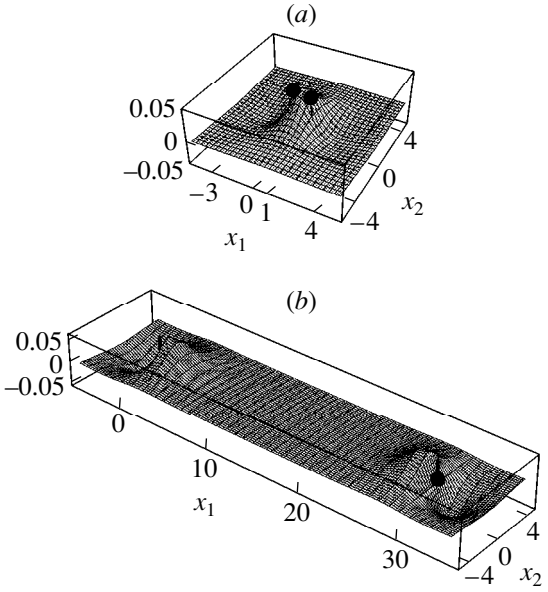

Fig. 9. Contribution of the form factor D_1 to $\langle E_1(x_1, x_2)\rangle_{Q\bar{Q}}$ in (GeV/fm) for $R = (a)\ T_g$ and $(b)\ 30T_g$. The quark and antiquark positions are shown by points with vertical bars.

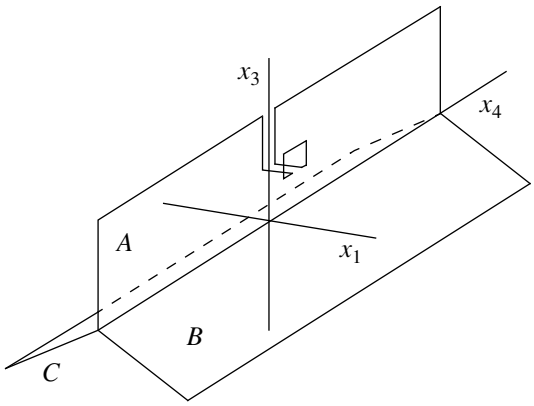

Fig. 10. Connected probe for the QQQ system.

As can be seen from the above expressions, the baryonic string can be represented as a superposition of a mesonic string $\langle E_1(x_3, x_1)\rangle^D_{Q\bar{Q}}$ (21) and the same string rotated through $2\pi/3$ and $4\pi/3$; that is,

$$\langle E_3(x_1, x_3)\rangle_{3Q} = \langle E_1(x_3, x_1)\rangle^D_{Q\bar{Q}} - \frac{1}{2}\langle E_1(x_3', x_1')\rangle^D_{Q\bar{Q}} - \frac{1}{2}\langle E_1(x_3'', x_1'')\rangle^D_{Q\bar{Q}}, \quad (32)$$

$$\langle E_1(x_1, x_3)\rangle_{3Q} = \frac{\sqrt{3}}{2}\langle E_1(x_3', x_1')\rangle^D_{Q\bar{Q}} - \frac{\sqrt{3}}{2}\langle E_1(x_3'', x_1'')\rangle^D_{Q\bar{Q}}, \quad (33)$$

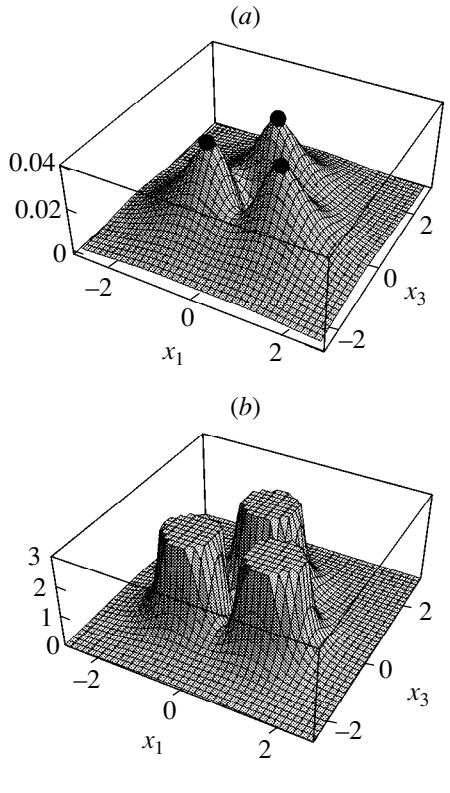

Fig. 11. Distributions (*a*) $\langle \mathbf{E}(x_1, x_3)\rangle^2_{3Q}$ and (*b*) $(\mathbf{E}^{\mathrm{tot}}_{3Q}(x_1, x_3))^2$ (in GeV^2/fm^2) for three quarks occurring at the vertices of an equilateral triangle. The distance from each quark to the string junction is $R = T_g$. The positions of the quarks are denoted by points. Here and in the figures that follow, x_1 and x_3 are measured in T_g units.

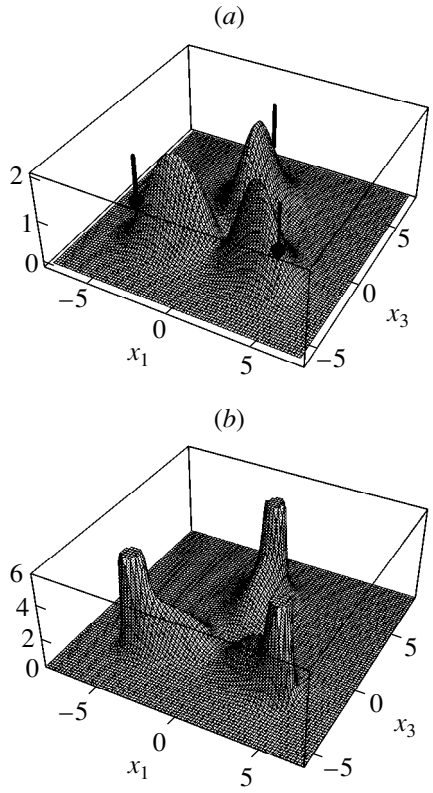

Fig. 12. As in Fig. 11, but for $R = 5T_g$, with the quark positions being shown by points with vertical bars.

where

$$x_1' = -\frac{1}{2}x_1 - \frac{\sqrt{3}}{2}x_3, \quad x_3' = \frac{\sqrt{3}}{2}x_1 - \frac{1}{2}x_3;$$
$$x_1'' = -\frac{1}{2}x_1 + \frac{\sqrt{3}}{2}x_3, \quad x_3'' = -\frac{\sqrt{3}}{2}x_1 - \frac{1}{2}x_3. \tag{34}$$

For $R = T_g$, $5T_g$, $10T_g$, and $30T_g$, Figs. 11*a*–13*a* and 14 display the squared-field distributions

$$\langle \mathbf{E}(x_1, x_3)\rangle^2_{3Q} = \langle E_1(x_1, x_3)\rangle^2_{3Q} + \langle E_3(x_1, x_3)\rangle^2_{3Q}. \tag{35}$$

A feature peculiar to all distributions is that there is a deep well in the region of the string junction. At the very junction point, the field vanishes since, by virtue of the symmetry of the three-quark system, there is no specific direction at this point. Off the well, the baryonic string is formed by three mesonic strings going from the three quarks to the string junction. It should be noted that, if the mesonic strings are saturated off the well region, the distribution in the string-junction region retains symmetry even at different distances from the quarks to the junction.

The distributions in Figs. 11*b*–13*b* and 15 were obtained by supplementing $\langle \mathbf{E}(x_1, x_3)\rangle^2_{3Q}$ with the perturbative-one-gluon-exchange Coulomb field

$$\mathbf{E}^{\mathrm{coul}}_{3Q} = -\frac{C_F\alpha_s}{2}\left(\frac{\mathbf{r}_1}{r_1^3} + \frac{\mathbf{r}_2}{r_2^3} + \frac{\mathbf{r}_3}{r_3^3}\right), \tag{36}$$

where $\mathbf{r}_i$ is the distance from the ith quark to the probe. The factor $C_F/2$ arises upon the contraction of antisymmetric tensors in the Wilson loop (26); that is,

$$\frac{1}{3!}\epsilon_{\alpha\beta\gamma}\epsilon_{\alpha\sigma\tau}t^a_{\beta\sigma}t^a_{\gamma\tau} = -\frac{1}{6}\mathrm{tr}(t^a t^a) = -\frac{C_F}{2}, \tag{37}$$

where $C_F = 4/3$ is the Casimir operator; $C_F\alpha_s = 0.295$ [see the explanation after Eq. (24)]. The total field is given by

$$\mathbf{E}^{\mathrm{tot}}_{3Q} = \langle \mathbf{E}\rangle_{3Q} + \mathbf{E}^{\mathrm{coul}}_{3Q}. \tag{38}$$

In Fig. 11*b*, the total field is at least two orders of magnitude greater than the nonperturbative field component (Fig. 11*a*) over the entire region considered here. Figure 12 shows half of the string, that which issues from the Coulomb peak. In Figs. 13*b* and 15, the Coulomb field changes only the shape of the string end, not affecting the remaining part of the string.

For the strings depicted in Figs. 11*a*–13*a* and 14, Fig. 16 displays the $x_1 = 0$ (longitudinal) sections along

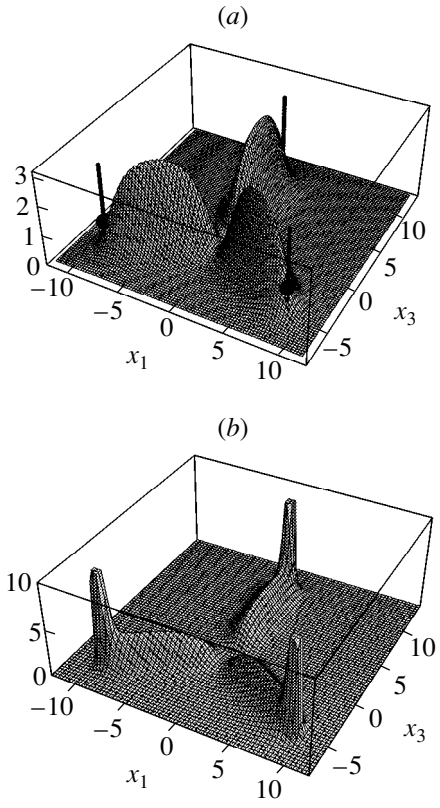

Fig. 13. As in Fig. 12, but for $R = 10T_g$.

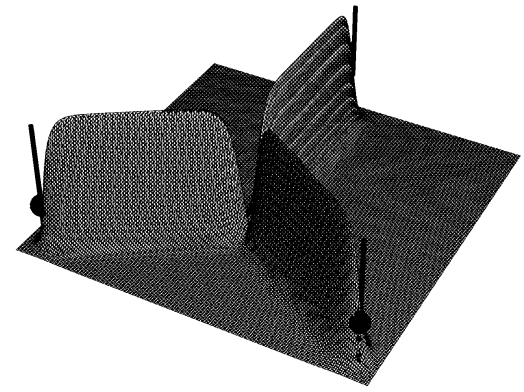

Fig. 14. As in Fig. 12*a*, but for $R = 30T_g$.

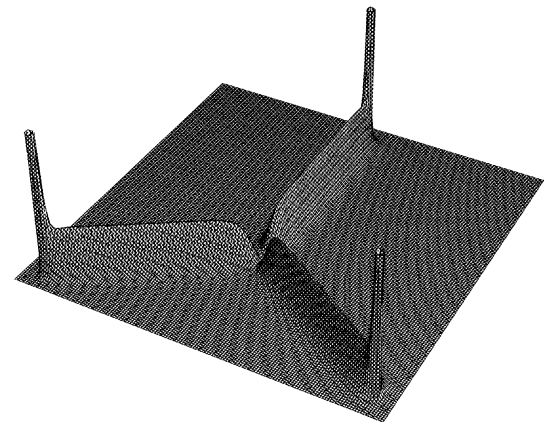

Fig. 15. As in Fig. 12*b*, but for $R = 30T_g$.

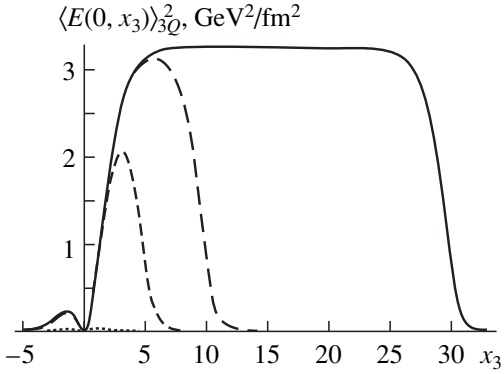

Fig. 16. Profile of the QQQ string, $\langle E(0, x_3)\rangle^2_{3Q}$, for quarks occurring at the vertices of an equilateral triangle at a distance R for the string junction. The dotted curve, short dashes, long dashes, and the solid curve represent data corresponding to $R = T_g$, $5T_g$, $10T_g$, and $30T_g$, respectively.

the x_3 axis. For $R \geq 5T_g$, the shape of the well is independent of the interquark distance. At $R \geq 10T_g$, the string is saturated; its longitudinal section grows for $0 \leq x_3 \leq 6T_g$ from zero to $(E^{\text{sat}})^2$ and then reaches a plateau. In the region of negative x_3 values, this section grows over the segment $0 \leq |x_3| \leq 1.25T_g$ from zero to 0.25 GeV^2/fm^2 and then decreases fast as $|x_3|$ increases from $1.25T_g$ to $5T_g$. We determine the well radius R_{well} as that which satisfies the equation $E^2(0, R_{\text{well}}) = (E^{\text{sat}})^2/2$. From the data in Fig. 16, we then obtain $R_{\text{well}} = 1.75T_g$.

Let us now consider a quark–diquark configuration in which two quarks are situated quite closely to each other, but they are both far off the third quark. We assume that these quarks occur at the vertices of an isosceles triangle whose base is much smaller than the lateral sides. The shortest path along which a string is formed consists of three straight segments connecting the quarks with the string junction, where they meet at an angle of $2\pi/3$, forming a Mercedes star. We denote by R_{QQ} the length of the two short segments and by R_Q the length of the long segment. In expression (29) for the field distribution, we will now perform integration with respect to dl' from 0 to R_Q for $\Gamma = A$ and from 0 to R_{QQ} for $\Gamma = B, C$. In Eqs. (32) and (33), we additionally introduce indices corresponding to the integration limits; that is,

$$\langle E_3(x_1, x_3)\rangle_{Q-QQ} = \langle E_1(x_3, x_1)\rangle^{D, R_Q}_{Q\bar{Q}} - \frac{1}{2}\langle E_1(x_3', x_1')\rangle^{D, R_{QQ}}_{Q\bar{Q}} - \frac{1}{2}\langle E_1(x_3'', x_1'')\rangle^{D, R_{QQ}}_{Q\bar{Q}}, \quad (39)$$

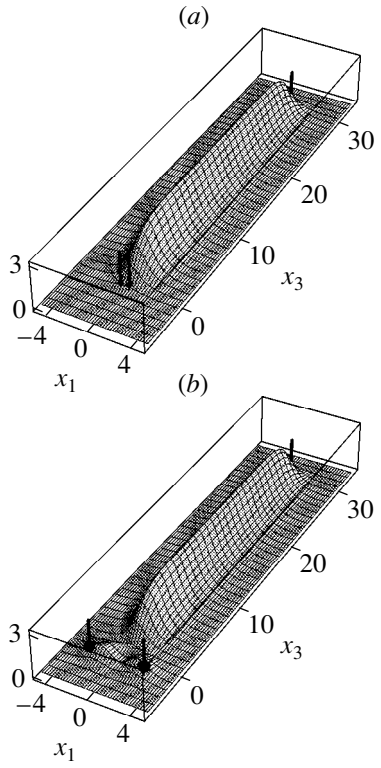

Fig. 17. Distribution $\langle \mathbf{E}(x_1, x_3)\rangle^2_{Q-QQ}$ (in GeV^2/fm^2) for a quark–diquark configuration at two values of the distance from each quark of the diquark to the string junction: R_{QQ} = (*a*) $0.5T_g$ and (*b*) $3T_g$. In either case, the distance from the third quark to string junction is $R_Q = 30T_g$. The quark positions are shown by points with vertical bars.

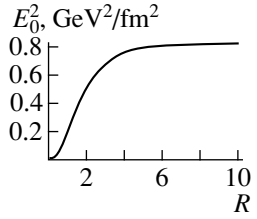

Fig. 18. Squared mesonic-string field at the origin, E_0^2 [see Eq. (21)], as a function of the quark–antiquark distance R measured in T_g units.

$$\langle E_1(x_1, x_3)\rangle_{Q-QQ} = \frac{\sqrt{3}}{2}\langle E_1(x_3', x_1')\rangle^{D, R_{QQ}}_{Q\bar{Q}} - \frac{\sqrt{3}}{2}\langle E_1(x_3'', x_1'')\rangle^{D, R_{QQ}}_{Q\bar{Q}}. \quad (40)$$

Figure 17 shows the distributions

$$\langle \mathbf{E}(x_1, x_3)\rangle^2_{Q-QQ} = \langle E_1(x_1, x_3)\rangle^2_{Q-QQ} + \langle E_3(x_1, x_3)\rangle^2_{Q-QQ} \quad (41)$$

for $R_Q = 30T_g$ and for R_{QQ} = (*a*) $0.5T_g$ and (*b*) $3T_g$. We can see a mesonic string at $R_{QQ} = 0.5T_g$ (compare with Fig. 5*a*) and a baryonic string with a well in the string-junction region at $R_{QQ} = 3T_g$. It is of interest to investigate the transition from one regime to another. According to (39) and (40), the field strength at zero is determined by the difference of the strengths of the fields at zero that are generated by the mesonic strings of lengths R_Q and R_{QQ}. The strength of the field (21) associated with a mesonic string of length R at the origin is given by

$$E_0(R) = \frac{2\sigma}{\pi}\int_0^{R/T_g} K_1(x)x\,dx. \quad (42)$$

This function grows linearly from zero at small R and approaches the asymptotic value $E_{\text{asymp}} = \sigma$ in the region $R > 4T_g$. The dependence $E_0^2(R)$ is depicted in Fig. 18.

We define the radius corresponding to the transition of a baryonic string into a mesonic one, $R_{\text{bar}\to\text{mes}}$, as that which satisfies the condition $E_0^2(R_{\text{bar}\to\text{mes}}) = E^2_{\text{asymp}}/2$. From the data in Fig. 18, we find that $R_{\text{bar}\to\text{mes}} = 1.5T_g$. At $R_{QQ} > R_{\text{bar}\to\text{mes}}$, the string of the quark–diquark configuration has a typical baryonic shape featuring a well in the string-junction region (Fig. 17*b*), while, in the region $R_{QQ} < R_{\text{bar}\to\text{mes}}$, it undergoes a transition into a mesonic string (Fig. 17*a*).

Let us now consider the case where the quarks lie on a straight line, the distances between them being R_1 and R_2. As in the preceding cases, the position of the string junction is determined from the condition requiring that the string length be minimal. For the quark arrangement being considered, the string length is minimal when the string junction occurs at the same point as the quark situated between the other two; obviously, this minimal length is equal to the sum of the distances from the extreme quarks to the central one. The contour of the Wilson loop lies in the (1 4) plane. Further proceeding in just the same way as at the beginning of this section, we introduce two direction vectors $\mathbf{n}_1 = (-1, 0)$ and $\mathbf{n}_2 = (1, 0)$ in the (1 3) plane and obtain

$$\langle E_3(x_1, x_3)\rangle_{3Ql} \equiv 0, \quad (43)$$

$$\langle E_1(x_1, x_3)\rangle_{3Ql} = -\int_0^{R_1} dl' \int_{-T/2}^{T/2} dx_4' D_{14,14}(-l' - x_1, -x_3, x_4') + \int_0^{R_2} dl' \int_{-T/2}^{T/2} dx_4' D_{14,14}(l' - x_1, -x_3, x_4') = -\langle E_1(-x_1, x_3)\rangle^{D, R_1}_{Q\bar{Q}} + \langle E_1(x_1, x_3)\rangle^{D, R_2}_{Q\bar{Q}}. \quad (44)$$

The distributions $\langle E_1(x_1, x_3)\rangle^2_{3Ql}$ are shown in Fig. 19*a* for $R_1 = R_2 = 15T_g$ and in Fig. 19*b* for $R_1 = 10T_g$ and $R_2 = 20T_g$. Since the two mesonic strings that form the distribution both have saturated profiles, the field is zero at the string-junction point $x_1 = 0$.

4. POTENTIAL OF QUARK INTERACTION IN A BARYON

In this section, we consider static quarks occurring at the vertices of an equilateral triangle at a distance R from the string-junction point.

Since the Wilson loop is a Green's function for the three-quark system, it determines the potential of quark interaction in a baryon:

$$V^{(3Q)}(R) = -\lim_{T\to\infty}\frac{1}{T}\ln\langle W^{(3Q)}(R, T)\rangle. \qquad (45)$$

In order to obtain the potential in the bilocal approximation, the surface integrals of bilocal correlation functions are summed over the surfaces of the contour of the Wilson loop. Performing integration over the surfaces in just the same way as in calculating the mean field for baryons, we then arrive at

$$-\ln\langle W^{(3Q)}(R, T)\rangle = \frac{1}{2}\sum_{a,b=A,B,C}\int\limits_{\Sigma_a}\int\limits_{\Sigma_b} d\sigma^a_{\mu\nu}(x)d\sigma^b_{\rho\sigma}(x')$$
$$\times\frac{g^2}{N_c}\mathrm{tr}\langle F_{\mu\nu}(x)\Phi(x, x')F_{\rho\sigma}(x')\Phi(x', x)\rangle$$
$$= \frac{3}{2}\sum_{\substack{a=A\\ b=A,B,C}} n^a_i n^b_k\int_0^R\int_0^R dl dl'\int_{-T/2}^{T/2}\int_{-T/2}^{T/2} dx_4 dx'_4 \qquad (46)$$
$$\times D_{i4,k4}(l\mathbf{n}^a - l'\mathbf{n}^b, x_4 - x'_4).$$

In the last equality, we have made use of the fact that the contour of the Wilson loop possesses the symmetry property

$$\sum_{a,b=A,B,C} = 3\sum_{\substack{a=A\\ b=A,B,C}}. \qquad (47)$$

As in the preceding section, we take into account only the contribution of the form factor D to the potential. The result then has the form

$$V^{(3Q)}(R) = \lim_{T\to\infty}\frac{3}{2}\frac{D(0)}{T}\int_0^R\int_0^R dl dl' \qquad (48)$$
$$\times\int_{-T/2}^{T/2}\int_{-T/2}^{T/2} dx_4 dx'_4\left\{\exp\left(-\mu\sqrt{(l-l')^2 + (x_4 - x'_4)^2}\right)\right.$$
$$\left. - \exp\left(-\mu\sqrt{\frac{3}{4}l'^2 + (l + l'/2)^2 + (x_4 - x'_4)^2}\right)\right\}.$$

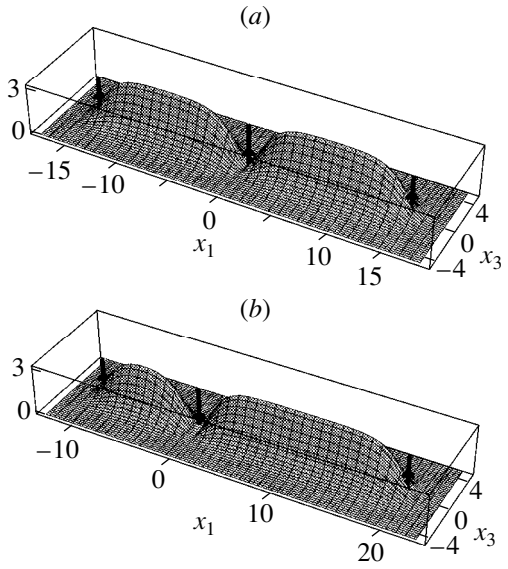

Fig. 19. Distribution $\langle E_1(x_1, x_3)\rangle^2_{3Ql}$ (in GeV^2/fm^2) for three quarks occurring on a straight line at (*a*) $R_1 = R_2 = 15T_g$ and (*b*) $R_1 = 10T_g$ and $R_2 = 20T_g$. The quark positions are shown by points with vertical bars.

We will refer to the first exponential in Eq. (48) as a diagonal one [since it is obtained at $a = b = A$ in (46)] and to the second exponential as an off-diagonal one [since it is obtained at $a = A$ and $b = B, C$ in (46)]. Upon integration, we arrive at

$$V^{(3Q)}(R) = \frac{6\sigma\mu^2}{\pi}\left\{R\int_0^R dl l K_1(\mu l)\right.$$
$$-\frac{1}{\mu^3}(2 - (\mu R)^2 K_2(\mu R)) - \frac{1}{2}\int_0^R dl\int_0^R dl' \qquad (49)$$
$$\left.\times\sqrt{\frac{3}{4}l'^2 + (l + l'/2)^2}K_1\left(\mu\sqrt{\frac{3}{4}l'^2 + (l + l'/2)^2}\right)\right\}.$$

For $D(0)$, we have used here the normalization condition (23).

The first two terms on the right-hand side of Eq. (49) are obtained from the diagonal exponential in (48), while the third term stems from the off-diagonal exponential. At distances satisfying the condition $R \gg T_g$, the first term leads to a linear potential with a slope equal to 3σ, while the second term appears to be a small correction to it (at large values of R, we have $12\sigma T_g/\pi$ for the second term). The third term shows an ascending behavior, substantially affecting the growth of the potential up to values close to $R \simeq 3T_g$; at greater values of R, it flattens out, however. This term arises as the result of the well at the center of the baryonic string. We note that the third term is absent in the case of a mesonic string and that the potential of the quark–anti-

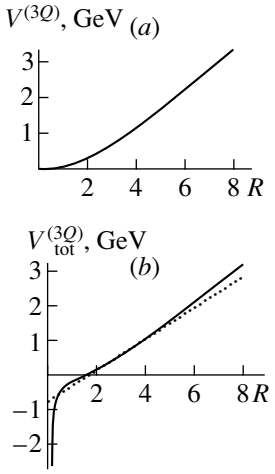

Fig. 20. (*a*) Three-quark-interaction potential $V^{(3Q)}(R)$ and (*b*) total potential $V^{(3Q)}_{\text{tot}}(R)$ calculated with allowance for perturbative one-gluon exchange. The dashed line is tangential to the curve. The quantity R is measured in T_g units.

quark interaction at large distances, $V^{(Q\bar{Q})} = \sigma R$, where σ is expressed in terms of $D(0)$ via relation (23), is one-third of the first term in (49).

The behavior of the potential $V^{(3Q)}(R)$ is illustrated in Fig. 20*a*. In the region $0 \le R \le 6T_g$, the slope of the tangent $\sigma'(R) \equiv \dfrac{dV}{dR}(R)$ grows from zero to 3σ. Off this region, the baryonic string can be represented everywhere, apart from the radius value corresponding to the well, as the sum of three mesonic strings (compare Figs. 8 and 16). Figure 20*b* displays the total potential $V^{(3Q)}_{\text{tot}}(R)$ including perturbative one-gluon exchange and having the form

$$V^{(3Q)}_{\text{tot}}(R) = -\frac{C_F\alpha_s}{2}\sum\frac{1}{r_{ij}} + V^{(3Q)}(R) = -\frac{\sqrt{3}}{2}\frac{C_F\alpha_s}{R} + V^{(3Q)}(R), \quad (50)$$

where $r_{ij} = R\sqrt{3}$ is the distance between the quarks, the sum is taken over three distances, and $C_F\alpha_s = 0.295$ [see comments to Eqs. (24) and (36)]. In the figure, we can see that the potential has a dip, which is associated with the occurrence of the well at the center of the baryonic string.

Let us now compare our results with the results of lattice calculations for the baryon potential (see the survey of Bali [14] and reference therein) where the potential of the interaction of three quarks situated at the vertices of an equilateral triangle was approximated by the sum of the Coulomb and a linear potential (that is, by the Cornell potential) in the region $0.055 \le R \le 0.71$ fm. This resulted in determining the slope of the linear potential to be 2.6σ, a value that is equal to that which we obtained for the slope of the tangent σ' to $V^{(3Q)}(R)$ at $R = 3.5T_g$. Thus, a decrease in the potential of quark interaction because of the well at the center of a baryonic string, an effect that was found in our calculations, is close to a similar effect in lattice calculations.

5. CONCLUSION

With the aid of a connected probe, we have calculated the distributions of the fields for $Q\bar{Q}$ and QQQ systems by using the lowest (Gaussian) field correlation functions. Since the contribution of the Gaussian correlation function saturates 99% of the static $Q\bar{Q}$ potential (see [11, 12]), there is every reason to believe that higher correlation functions will not change the pattern of the distributions significantly.

By investigating fields with a connected probe, we have been able to determine the distribution specified by the orientation of the probe and to distinguish between the chromoelectric and chromomagnetic field components associated with this orientation. We can see that the main contribution to string formation comes from the longitudinal component of the chromoelectric field. The contribution of the transverse component is less than 3% of the contribution of the longitudinal component. The transverse and the longitudinal component are determined by the form factor D and the form factor D_1, respectively. The contribution of the form factor D_1 to the longitudinal component does not reach 3% of its value. At distances greater than $10T_g$, the string profile is saturated, ceasing to vary. The thickness of the saturated string is $2.2T_g$. For the $Q\bar{Q}$, our results agree with the results presented in [1–3]. The distribution of the total field also agrees with data obtained by studying the $Q\bar{Q}$ field with a disconnected probe [4, 5].

The pattern of a baryonic string has been obtained here for the first time. Around the string junction, there arises a deep well in the distribution of the electric field. At the very string-junction point, the field vanishes by virtue of the symmetry of the distribution. The well, which severely suppresses quark fields near the center of a heavy baryon, has a radius of $1.75T_g$. For the quark–diquark configuration, we have found that the radius corresponding to the transition from a baryonic to a mesonic string is $1.5T_g$. For three quarks lying on a straight line, it has been shown that, at the point where the central quark resides, the field vanishes at large distances between the quarks.

Since the same Wilson loop for the QQQ configuration is used for light quarks as well [15], the physical implications of the well can be observed both in heavy and in light hadrons. One of the implications is illustrated in Fig. 20, where the nonperturbative part of the potential grows very slowly at small values of R, so that

the asymptotic slope is reached only at very large distances. Therefore, the effective slope for the ground baryon states may be 10–20% less than that which complies with the relativistic quark model of the baryons [16] and with recent lattice calculations for the static QQQ potential [14].

It should be noted that the vanishing of the field at the QQQ string junction was obtained by analyzing each component of the field individually with a connected probe. Fluctuations of the field measured by a disconnected probe can be present at this point.

ACKNOWLEDGMENTS

This work was supported in part by the Russian Foundation for Basic Research (project nos. 00-02-17836 and 00-15-96786).

REFERENCES

1. A. Di Giacomo, M. Maggiore, and S. Olejnik, Phys. Lett. B **236**, 199 (1990); Nucl. Phys. B **347**, 441 (1990).
2. L. Del Debbio, A. Di Giacomo, and Yu. A. Simonov, Phys. Lett. B **332**, 111 (1994).
3. P. Cea and L. Cosmai, Phys. Rev. D **52**, 5152 (1995).
4. Ch. Schlichter, G. S. Bali, and K. Schilling, Nucl. Phys. B (Proc. Suppl.) **42**, 273 (1995); Phys. Rev. D **51**, 5165 (1995).
5. R. W. Haymaker, V. Singh, Y. Peng, and J. Wosiek, Phys. Rev. D **53**, 389 (1996).
6. Ch. Schlichter, G. S. Bali, and K. Schilling, Nucl. Phys. B (Proc. Suppl.) **63**, 519 (1998); Prog. Theor. Phys. Suppl. **131**, 645 (1998).
7. M. Rueter and H. G. Dosch, Z. Phys. C **66**, 245 (1995); H. G. Dosch, O. Nachtmann, and M. Rueter, Preprint HD-THEP-95-12; hep-ph/9503386.
8. H. G. Dosch, Phys. Lett. B **190**, 177 (1987); H. G. Dosch and Yu. A. Simonov, Phys. Lett. B **205**, 399 (1988); Yu. A. Simonov, Nucl. Phys. B **307**, 512 (1988).
9. Yu. A. Simonov, Usp. Fiz. Nauk **166**, 337 (1996) [Phys. Usp. **39**, 313 (1996)].
10. M. Campostrini, A. Di Giacomo, and G. Mussardo, Z. Phys. C **25**, 173 (1984); A. Di Giacomo and H. Panagopoulos, Phys. Lett. B **285**, 133 (1992); A. Di Giacomo, E. Meggiolaro, and H. Panagopoulos, Nucl. Phys. B **483**, 371 (1997).
11. G. S. Bali, Nucl. Phys. (Proc. Suppl.) **83**, 422 (2000).
12. Yu. A. Simonov, Pis'ma Zh. Éksp. Teor. Fiz. **71**, 187 (2000) [JETP Lett. **71**, 127 (2000)]; hep-ph/0001244; V. I. Shevchenko and Yu. A. Simonov, Phys. Rev. Lett. **85**, 1811 (2000).
13. D. S. Kuzmenko and Yu. A. Simonov, Phys. Lett. B (in press); hep-ph/0006192.
14. G. S. Bali, Preprint HUP-EP-99-67; hep-ph/0001312.
15. Yu. A. Simonov, Phys. Lett. B **228**, 413 (1989); M. Fabre de la Ripelle and Yu. A. Simonov, Ann. Phys. (N.Y.) **212**, 235 (1991); B. O. Kerbikov and Yu. A. Simonov, Phys. Rev. D **62**, 093016 (2000).
16. S. Capstick and N. Isgur, Phys. Rev. D **34**, 2809 (1986).

Translated by A. Isaakyan

Physics of Atomic Nuclei, Vol. 64, No. 1, 2001, pp. 120–131. Translated from Yadernaya Fizika, Vol. 64, No. 1, 2001, pp. 123–134.

ELEMENTARY PARTICLES AND FIELDS
Theory

Charm Hadroproduction within k_T-Factorization Approach

M. G. Ryskin*, A. G. Shuvaev, and Yu. M. Shabelski[1), ***]**

Petersburg Nuclear Physics Institute, Russian Academy of Sciences, Gatchina, 188350 Russia

Received September 30, 1999; in final form, March 2, 2000

Abstract—In the problem of describing heavy-quark production in high-energy hadron collisions, a comparison is made between the theoretical status and numerical predictions of two approaches, the traditional parton model in the leading order (LO) and the k_T-factorization approach. Basic assumptions underlying relevant calculations are discussed. A very simple gluon structure function and a fixed coupling constant are chosen for the calculations in order to highlight distinctions associated with the use of nonidentical matrix elements in these two approaches. It is shown that, in the k_T-factorization approach, formal LO calculations performed with allowance for the Sudakov form factor include many terms usually treated as next-to-leading-order (NLO) contributions of the traditional parton model (or even contributions next to NLO ones, NNLO). © *2001 MAIK "Nauka/Interperiodica".*

1. INTRODUCTION

Investigation of heavy-quark production in high-energy hadron collision provides a clue to the internal structure of hadrons.

Quantum chromodynamics (QCD) is the universally adopted theory of quark and gluon interactions. A description of hard hadronic processes in terms of QCD is possible only with the aid of phenomenology that reduces hadron interactions to interactions between partons—for example, within the formalism of hadron structure functions. Within this framework, cross sections for hard processes in hadron–hadron interactions are represented as the convolution of parton distributions in colliding hadrons with the cross section that describes the elementary partonic subprocess and which is determined by the square of the matrix element computed within perturbative QCD.

A few phenomenological approaches to calculating cross sections for hard processes have been described in the literature.

The collinear approximation of QCD, also known as the parton model, is the most popular and technically advanced approach. The underlying assumptions of the model are the following: (i) All interacting particles are taken to be on their mass shells. (ii) The transverse momenta of initial partons are equal to zero. As to the cross sections in question, they are averaged over two transverse polarizations of initial gluons. The virtualities of the initial partons are taken into account only through the parton densities (structure functions) calculated in the leading-logarithm approximation (LLA) by using the Dokshitzer–Gribov–Lipatov–Altarelli–Parisi (DGLAP) evolution equation and experimental data. The cross sections for QCD subprocesses are usually calculated in the leading or in the next-to-leading order (LO and NLO) [1–5]. In such calculations, the transverse momenta of initial partons are disregarded in the matrix elements for the relevant subprocesses. This approach represents a direct analogy of the Weizsäcker–Williams approximation in QED. It provides a satisfactory description of data on the total cross sections for the production of heavy quarks and on single-particle distributions of product heavy quarks (more precisely, of hadrons containing these quarks). However, neither data on the azimuthal correlations of a heavy-quark pair [6] nor the measured distributions with respect to the total transverse momentum of the product pair [7]—these are quantities that are controlled by the transverse momenta of initial partons—are reproduced within the approach being discussed [8, 9].

The simplest way to take into account the transverse momenta of initial partons in order to describe correctly the correlations of heavy quarks was proposed in [7]; it consists in shifting at random the final transverse momenta, but this procedure was not validated theoretically. The shift of the scale $\Lambda_{\rm QCD}$ ($\langle k_T\rangle \sim 300$ MeV) seems quite natural because of the possible effect of confining forces at large distances, but values of $\langle k_T\rangle \sim 1$ GeV, or still higher values, should have had an explanation within perturbative QCD. Mean values of such a shift seem to depend on the primary energy, on the kinematical domain, and on some other similar factors. Upon introducing the above shift, it would be rather difficult to describe simultaneously longitudinal- and transverse-momentum distributions [10].

Calculations including the transverse momenta of initial partons can also be implemented within the so-

[1)] Abdus Salam International Centre for Theoretical Physics, Strada Costiera 11, PO Box 586, I-34014 Trieste, Italy, and Petersburg Nuclear Physics Institute, Russian Academy of Sciences, Gatchina, 188350 Russia.

* e-mail: ryskin@thd.pnpi.spb.ru

** e-mail: shuvaev@thd.pnpi.spb.ru

*** shabelsk@thd.pnpi.spb.ru

called k_T-factorization approach [11–15] or within the theory of semihard processes [16–19]. Relevant Feynman diagrams are then evaluated with allowance for the virtualities and polarizations of initial partons. It is well known that, at high primary energies, the main contribution to heavy-quark production comes from gluon–gluon interaction. In the region of small x, there are no grounds to disregard the transverse momenta of initial gluons, q_{1T} and q_{2T}, against the masses and transverse momenta of heavy quarks. Since the matrix elements that are calculated for the relevant subprocesses within the approach being discussed are very complicated in relation to those within the standard parton model, we treat them only in the LO approximation. At the same time, a significant part—maybe, even a major part—of NLO corrections (and a part of corrections of order next to NLO, which are further referred to as NNLO corrections) are associated with the contribution of nonzero transverse momenta of initial partons, so that such corrections have already been included in the LO contributions within the k_T-factorization approach. Thus, we can hope that, in the k_T-factorization approach, NLO, NNLO, etc., corrections will be modest, which will render it more efficient.

Nonintegrated parton distributions are not determined by the derivatives of the relevant structure functions exclusively [16]—they also involve doubly logarithmic (Sudakov) form factors, as was discussed in detail elsewhere [20] (see also Section 3 of the present article). In the Feynman gauge, a doubly logarithmic contribution emerges from diagrams where a soft gluon (in contrast to the parton-model diagram in Fig. 1*a*) embraces the hard-interaction block, as is exemplified in Fig. 1*b*.

As the primary energy is increased, the momentum fraction x carried by partons involved in a hard interaction decreases on average. When a greater number of gluons is emitted, a parton acquires a sufficiently high transverse momentum k_T, whence it becomes clear why large shifts in k_T are required in the parton model in order to describe high-energy data.

Presently, it is obvious that the k_T-factorization approach is self-consistent and that its predictions are in reasonably good agreement both with experimental data and with the predictions of the collinear approximation in the cases where this approximation is applicable. At the same time, a detailed numerical analysis of hard processes within the k_T-factorization approach has not yet been performed.

The predictions of all phenomenological approaches greatly depend on the form of quark and gluon structure functions. Information about these functions comes primarily from HERA data, but next to nothing is known about them in the region of very small x ($x < 10^{-4}$). At the same time, this region makes a dominant contribution to heavy-quark production at high energies,[2)] and the applicability of the existing sets of structure functions at small x is questionable (see the relevant discussion in [21]).

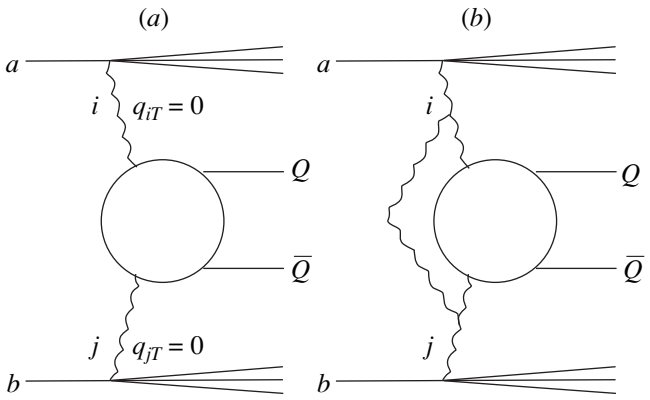

Fig. 1. Heavy-quark production in (*a*) the leading-order parton model and in (*b*) the k_T-factorization approach that takes into account the Sudakov form factor T (see also the relevant discussion in Section 3).

The main objective of the present study is to compare the results obtained within the standard parton model and within the k_T-factorization approach and to clarify the reasons behind the distinctions between their predictions. We begin by recalling the formalism for either approach and then present numerical results. For the sake of clarity, we consider very high energies, including the unrealistic case of $\sqrt{s}$ = 1000 TeV, and represent the structure function for a gluon in a nucleon in a form as simple as is possible.

2. PARTON-MODEL APPROXIMATION

In the standard parton model, the cross section for the production of two heavy quarks in a collision of two hadrons a and b is represented in the factorized form [22]

$$d\sigma(ab \longrightarrow Q\bar{Q}) = \sum_{ij}\int dx_i dx_j G_{a/i}(x_i, \mu_F) \times G_{b/j}(x_j, \mu_F) d\hat{\sigma}(ij \longrightarrow Q\bar{Q}), \quad (1)$$

where $G_{a/i}(x_i, \mu_F)$ and $G_{b/j}(x_j, \mu_F)$ are the structure functions for partons i and j in the colliding hadrons, μ_F is the factorization point of normalization, and $d\hat{\sigma}(ij \longrightarrow Q\bar{Q})$ is the subprocess cross section computed within perturbative QCD. This cross section can written as the sum of the LO and the NLO contribution; that is,

$$d\hat{\sigma}(ij \longrightarrow Q\bar{Q}) = \frac{\alpha_s^2(\mu_R)}{m_Q^2}(f_{ij}^{(0)} + 4\pi\alpha_s(\mu_R)[f_{ij}^{(1)} + \bar{f}_{ij}^{(1)}\ln(\mu^2/m_Q^2)]), \quad (2)$$

[2)] By way of example, we indicate that, in the case of charm production (m_c = 1.4 GeV), the product x_1x_2 for two gluons (the quantities x_1 and x_2 are both variables of integration) is equal to 4×10^{-8} at the LHC energy ($\sqrt{s}$ = 14 TeV).

where μ_R is the renormalization point of normalization and where it is assumed that $\mu_F = \mu_R = \mu$. The functions $f_{ij}^{(0)}$, $f_{ij}^{(1)}$, and $\bar{f}_{ij}^{(1)}$ depend only on the variable

$$\rho = \frac{4m_Q^2}{\hat{s}}, \quad \hat{s} = x_i x_j s_{ab}. \tag{3}$$

Expression (1) corresponds to the processes depicted schematically in Fig. 1*a*. At small x, the main contribution to the cross section comes from the fusion of initial gluons, $i = j = g$.

The uncertainties of a conceptual character that emerge in numerical results are associated with unknown values of the normalization points μ_F and μ_R,[3)] as well with unknown values of the heavy-quark masses. The values of these normalization points must be both on the order of the maximal hardness in the process, but it remains unclear which values must be used, m_Q, $m_T = \sqrt{m_Q^2 + p_T^2}$, or $\hat{s}$. These uncertainties are not expected to be great, since the dependences on the parameters are of a logarithmic character. Nonetheless, the uncertainties at currently available energies are numerically large because of insufficiently large values of the *c*- and the *b*-quark mass (see, for example, [7]).

The collinear approximation presents yet another problem in the parton model. The transverse momenta of initial partons, q_{iT} and q_{jT}, are assumed to be equal to zero (Fig. 1*a*), while their virtualities are taken into account only through the structure functions—the cross section $d\hat{\sigma}(ij \longrightarrow Q\bar{Q})$ is taken to be independent of the virtualities. Naturally, these assumptions greatly simplify the calculations.

The commonly accepted NLO parton model in the collinear approximation provides an accurate description of single-particle distributions and total cross sections for heavy-quark production. At the same time, its predictions are in a glaring contradiction with data on azimuthal correlations and on the distributions with respect to the total transverse momentum of the product heavy-quark pair. The reason for this is quite obvious. Let us consider the fusion of two partons with transverse momenta q_{1T} and q_{2T} into a $Q\bar{Q}$ pair whose constituents have transverse momenta p_{1T} and p_{2T}. In the LO parton model, we have $q_{1T} + q_{2T} = p_{1T} + p_{2T} = 0$, so that the distribution with respect to the transverse momentum of the quark pair, $p_{\text{pair}} = p_{1T} + p_{2T}$, coincides with the distribution with respect to the total transverse momentum of initial partons, appearing to be $\delta(p_{\text{pair}})$ in the LO parton model. Here, the NLO correction is numerically modest, since the p_T single-particle distributions in the LO and in the NLO approximation are very similar in shape [3, 23]; therefore, the eventual (NLO + LO) distribution with respect to the total transverse momentum of a heavy-quark pair differs only slightly from a delta function, but this is at odds with available data [7–9].

It was shown in [7] that the commonly adopted NLO parton model is capable of describing data on azimuthal correlations and on the distributions with respect to the transverse momentum of the product heavy-quark pair if one assumes from the outset that the colliding partons initially possess a comparatively high transverse momentum k_T^{kick} of about 1 GeV. Suppose that, in the collinear approximation, the total transverse momentum of the pair in the NLO is $\mathbf{p}_T(Q\bar{Q})$. For each event, the pair is shifted in the transverse direction with the result that its transverse momentum becomes $\mathbf{p}_T(Q\bar{Q}) + \mathbf{k}_T(1) + \mathbf{k}_T(2)$. The vectors $\mathbf{k}_T(1)$ and $\mathbf{k}_T(2)$, which are the transverse momenta of the initial partons, are chosen at random, their absolute values being distributed as

$$\frac{1}{N}\frac{dN}{dk_T^2} = \frac{1}{\langle k_T^2 \rangle}\exp(-k_T^2/\langle k_T^2 \rangle). \tag{4}$$

There is, however, no theoretical substantiation of this method.

A general phenomenological expression describing the production of a heavy-quark pair can be represented as[4)] the convolution of the initial transverse-momentum distributions $I(q_{1T})$ and $I(q_{2T})$ with the squared modulus of the matrix element; that is,

$$\sigma_{\text{QCD}}(Q\bar{Q}) \propto \int d^2q_{1T}d^2q_{2T}I(q_{1T})I(q_{2T}) \times |M(q_{1T}, q_{2T}, p_{1T}, p_{2T})|^2. \tag{5}$$

There are two possibilities here:

(i) The important values of the transverse momenta of initial partons are much less than the transverse momenta of the product heavy quarks, $q_{iT} \ll p_{iT}$.

(ii) All the transverse momenta are on the same order of magnitude, $q_{iT} \sim p_{iT}$.

In the first case, both initial distributions $I(q_{iT})$ can be replaced by $\delta(q_{iT})$ with the result that expression (5) reduces to that in the collinear approximation; that is,

$$\sigma_{\text{coll}}(Q\bar{Q}) \propto |M(0, 0, p_{1T}, p_{2T})|^2, \tag{6}$$

which is in perfect analogy with the Weizsäcker–Williams approximation in QED.

[3)]The dependence of the results on the normalization points must vanish upon summation of all orders of perturbation theory. Sometimes, it is argued that a strong (weak) dependence of the LO or the NLO results on the normalization points implies a large (small) contribution of higher order diagrams, but this is generally incorrect. A strong or a weak dependence of the LO or the NLO results on the normalization points only implies a similar dependence of higher order contributions, which can be either numerically large or numerically small.

[4)]All factors immaterial for the present discussion are omitted here for the sake of simplicity.

In the second case, there are no grounds to expect a priori that the Weizsäcker–Williams approximation would yield accurate results; nevertheless, these results are quite reasonable in some cases.

The k_T^{kick} method [7], which was discussed above, takes effectively into account the transverse momenta of the initial partons. It relies on an expression that can be symbolically written in the form

$$\sigma_{\text{kick}}(Q\bar{Q}) \propto I(q_{1T})I(q_{2T}) \otimes |M(0, 0, p_{1T}, p_{2T})|^2 \quad (7)$$

and which differs from the general expression (5) in that the values $\langle k_T^2 \rangle$ in (4) must be different in different processes (for example, when the product heavy quarks have comparatively low p_T and when they have very high p_T), since the matrix element does not involve the transverse momenta q_{iT}. The reason is that, in the general expression (5), $I(q_{iT})$ decreases at high q_{iT}^2 as a power-law function with a comparatively small exponent (see the next section)—that is, at a comparatively low rate—whence it follows that the q_{iT}^2 dependence of the matrix element proves to be more important.

3. HEAVY-QUARK PRODUCTION IN THE k_T-FACTORIZATION APPROACH

Let us now consider an alternative approach, that in which the transverse momenta of initial gluons in the low-x region arise owing to the diffusion of transverse parton momenta in the evolution process. This diffusion is described by the function $\varphi(x, q^2)$, which governs the distribution of gluons characterized by a given value of the hadron-longitudinal-momentum fraction x and a given value of the virtuality q^2. In the low-x region, the function $\varphi(x, q^2)$ is approximately given by the derivative of the conventional gluon structure function. Generally, it is a function of three variables, x, q_T, and q^2, but the dependence on q_T at a fixed value of q^2 is rather weak. This is because, for $x \ll 1$, $q_T^2 \approx -q^2$ in the LLA, in accordance with the q^2 dependence of the structure functions. Because scaling is violated in QCD, $\varphi(x, q^2)$ for realistic structure functions increases with decreasing x, so that ever larger values of q_T become operative in numerical calculations.

A precise result for the q_T distribution of gluons can in principle be found from the evolution equation, which is now nonlinear, in contrast to what occurs in the parton model, owing to parton interactions at low x. The result of the LO calculation of q_T distributions of gluons that was performed in [24] on the basis of Balitsky–Fadin–Kuraev–Lipatov (BFKL) theory differs from our $\varphi(x, q^2)$ by 10 to 15%.

Let us now consider expression (5) with a matrix element that takes into account the polarizations of gluons and their virtualities. Since the form of this matrix element is much more complicated than that in the parton model, we will consider only the LO contribution to the subprocess $gg \longrightarrow Q\bar{Q}$ (see Fig. 2); at low x, this contribution saturates a dominant part of the cross section. The upper and the lower ladder block represent the two-dimensional gluon distributions $\varphi(x_1, q_1^2)$ and $\varphi(x_2, q_2^2)$. Within the standard DGLAP scheme, these distributions at low x are defined as [16]

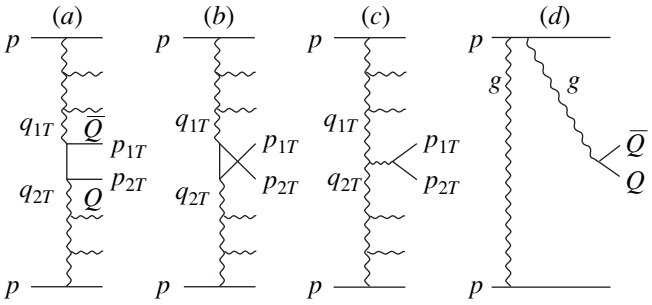

Fig. 2. (*a–c*) Leading-order QCD diagrams for heavy-quark production in proton–proton (proton–antiproton) collisions via gluon–gluon interactions and (*d*) diagram formally violating factorization, which is restored to a logarithmic accuracy.

$$\varphi(x, q^2) = 4\sqrt{2}\pi^3 \frac{\partial[xG(x, q^2)]}{\partial q^2}. \quad (8)$$

This definition of $\varphi(x, q^2)$ makes it possible to consider correctly effects induced by gluon virtualities.

Strictly speaking, the doubly logarithmic Sudakov form factor must be included in the quantity differentiated in (8) [20]. It was shown in [20] that the LLA expression for the probability of finding a parton with a given longitudinal-momentum fraction x and a given transverse momentum k_t has the form

$$f_a(x, k_t^2) = \frac{\partial}{\partial k_t^2}[xa(x, k_t^2)T_a(k_t^2, \mu^2)], \quad (9)$$

where $a = g, q$; T is the doubly logarithmic Sudakov form factor; and

$$\varphi_a(x, q^2) = 4\sqrt{2}\pi^3 f_a(x, q^2). \quad (10)$$

The first factor in (9) is obvious. It corresponds to the real contribution of radiation to the DGLAP evolution. When the normalization point is changed from μ^2 to $\mu^2 + \delta\mu^2$, a new parton is produced with a k_t^2 value between μ^2 and $\mu^2 + \delta\mu^2$. In the limit $\ln(1/x) \longrightarrow \infty$ (when $T_a \longrightarrow 1$), we then have

$$f_a^{\text{BFKL}}(x, k_t^2) = \frac{\partial}{\partial k_t^2}[xa(x, k_t^2)]. \quad (11)$$

The factor

$$T = \exp\left(-C\int_{k_t^2}^{\mu^2}\frac{\alpha_s(q^2)}{2\pi}\ln\left(\frac{\mu^2}{q^2}\right)\frac{dq^2}{q^2}\right) \qquad (12)$$

[$C = C_F = (N_c^2 - 1)/2N_c$ for quarks and C = $C = C_A = N_c$ for gluons] takes into account the contributions of virtual loops in the DGLAP scheme, which are necessary both for a normalization of the parton wave functions and for fulfillment of sum rules (that is, for conservation of the momentum, flavors, and so on). Here, the quantity T determines the probability that extra partons (gluons) with transverse momenta $q_t' \subset [k_t, \mu]$ are not emitted.

We note that the doubly logarithmic contributions from real and virtual soft gluons are canceled in the DGLAP equation written for the integrated parton distributions (that is, all $k_t \leq \mu$ are included). The emission of soft gluons with a momentum faction $(1 - z) \longrightarrow 0$ does not change the x distributions of parent partons. Owing to this, the contributions of virtual and real radiations generated by a $1/(1 - z)$ singularity of the function $P(z)$ indeed cancel each other.

A totally different pattern is observed if the parton distribution is not integrated. In this case, the emission of soft gluons (those for which $q_t' > k_t$) changes the transverse momentum of the parent (t-channel) parton, and this is taken into account by including the factor T in expression (9). As a result, the nonintegrated distribution $f_a(x, k_t^2)$ remains positive even at comparatively large values of x in the region where the integrated parton density $a(x, \mu^2)$ decreases with μ^2 owing to the virtual contribution to the DGLAP evolution equation.

Unfortunately, the factor T is known only to a doubly logarithmic accuracy. When $k_t > \mu$, there are no doubly logarithmic contributions; therefore, we set $T = 1$ in this region.

In terms of Feynman diagrams in the axial (physical) gauge, the factor T arises from self-energy contributions. In the Feynman gauge, these contributions do not feature a doubly logarithmic enhancement. In this case, doubly logarithmic contributions arise owing to diagrams in which a gluon embraces the hard block (as this occurs, for example, in Fig. 1*b*). Any diagram where a soft gluon is emitted from one of the external lines of the hard block (for example, the gluon q_2 in Fig. 2) and where this gluon is absorbed by the other external line of this block involves the same dilogarithm, but it differs from other ones by a color factor. The sum of the color factors for all three diagrams (a soft gluon can be absorbed by a heavy quark, an antiquark, or a gluon q_1) is equal to the color factor of the self-energy diagram. It follows that the distribution in (9) is obtained in the Feynman gauge as well.

Thus, the true probability of finding a parton carrying the longitudinal-momentum fraction x and the transverse momentum $k_T^2 = -k^2$ is given by (9) (see [20]). With the aim of performing a more consistent analysis, we postpone the use of the more precise expression (9) to the end of Section 4 and begin by considering expression (8) without taking into account the doubly logarithmic contribution T.[5)]

In the following, we will make use of Sudakov's expansions for the quark momenta p_1 and p_2 in terms of colliding-hadron momenta p_A and p_B ($p_A^2 = p_B^2 \simeq 0$) and the transverse momenta $p_{1,2T}$:

$$p_{1,2} = x_{1,2}p_B + y_{1,2}p_A + p_{1,2T}. \qquad (13)$$

The differential cross section for heavy-quark production in hadron collisions has the form[6)]

$$\frac{d\sigma_{pp}}{dy_1^* dy_2^* d^2p_{1T} d^2p_{2T}} = \frac{1}{(2\pi)^8}\frac{1}{(s)^2}\int d^2q_{1T}d^2q_{2T}\delta(q_{1T} + q_{2T} - p_{1T} - p_{2T})\frac{\alpha_s(q_1^2)}{q_1^2}\frac{\alpha_s(q_2^2)}{q_2^2}\varphi(q_1^2, y)\varphi(q_2^2, x)|M_{QQ}|^2, \qquad (14)$$

where $s = 2p_Ap_B$; $q_{1,2T}$ are the gluon transverse momenta; $y_{1,2}^*$ are the quark rapidities in the hadron–hadron c.m. frame;

$$x_1 = \frac{m_{1T}}{\sqrt{s}}e^{-y_1^*}, \quad x_2 = \frac{m_{2T}}{\sqrt{s}}e^{-y_2^*}, \quad x = x_1 + x_2,$$
$$y_1 = \frac{m_{1T}}{\sqrt{s}}e^{y_1^*}, \quad y_2 = \frac{m_{2T}}{\sqrt{s}}e^{y_2^*}, \quad y = y_1 + y_2, \qquad (15)$$
$$m_{1,2T}^2 = m_Q^2 + p_{1,2T}^2;$$

and $|M_{QQ}|^2$ is the square of the matrix element for the production of a heavy-quark pair in a gluon–gluon collision.

In LLA kinematics, we have

$$q_1 \simeq yp_A + q_{1T}, \quad q_2 \simeq xp_B + q_{2T}, \qquad (16)$$

whence it follows that

$$q_1^2 \simeq -q_{1T}^2, \quad q_2^2 \simeq -q_{2T}^2. \qquad (17)$$

(More precisely, $q_1^2 = -q_{1T}^2/(1 - y)$ and $q_2^2 = -q_{2T}^2/(1 - x)$, but we consider the case where $x, y \ll 1$.)

The matrix element M_{QQ} is calculated in the Born approximation of QCD without resort to the conventional simplifications of the parton model. In the axial

[5)] A different method for taking into account the q_T distribution of gluons was proposed in [26] on the basis of the Fourier transform of structure functions.

[6)] The argument α_s is taken to be equal to the gluon virtuality, and this is very close to what occurs in the Brodsky–Lepage–Mackenzie scheme [27] (see also [19]).

gauge ($p_B^\mu A_\mu = 0$), the gluon propagator has the form $D_{\mu\nu}(q) = d_{\mu\nu}(q)/q^2$, where

$$d_{\mu\nu}(q) = \delta_{\mu\nu} - (q^\mu p_B^\nu + q^\nu p_B^\mu)/(p_B q). \quad (18)$$

For t-channel gluons, the main contribution to the cross section for heavy-quark production comes from the so-called nonsense polarizations. It is convenient to single out these polarizations by decomposing the unit tensor in the numerator of the gluon propagator into the longitudinal and the transverse component as

$$\delta_{\mu\nu} = 2(p_B^\mu p_A^\nu + p_A^\mu p_B^\nu)/s + \delta_{\mu\nu}^T.$$

Since the sum of the diagrams in Figs. 2*a*–2*c* is gauge-invariant, we have $q_{1\mu} M_\mu^{A,B} = 0$, where $M_\mu^{A,B}$ stands for the amplitude that describes the interaction between the gluon q_1 and the hadron with the momentum p_A or p_B and which is represented by the upper (A) or the lower (B) parts of the diagrams in Figs. 2*a*–2*c*. By virtue of this, there remains only the unit tensor in the numerator of the t-channel propagator; considering that $p_A^\mu M_\mu^A$, $p_B^\mu M_\mu^B$, and the transverse structures are suppressed by powers s, we obtain

$$\delta_{\mu\nu} \approx 2 p_B^\mu p_A^\nu / s. \quad (19)$$

By using expression (16) for the momentum q_1, we arrive at

$$p_A^\mu M_\mu^B \simeq -\frac{q_{1T}^\mu}{y} M_\mu^B,$$

which leads to the expression

$$d_{\mu\nu}(q) \approx -2\frac{p_B^\mu q_T^\nu}{ys} \quad (20)$$

or, alternatively, to

$$d_{\mu\nu}(q) \approx 2\frac{q_T^\mu q_T^\nu}{xys}, \quad (21)$$

if the same operation is implemented for the vector p_B.[7)] It is possible to use either expression for $d_{\mu\nu}$, but, in the case of expression (20), all possibilities of gluon emission are taken into account only upon redefining the gluon vertex as (see [28])

$$\Gamma_{\text{eff}}^\nu = \frac{2}{xys}[(xys - q_{1T}^2)q_{1T}^\nu - q_{1T}^2 q_{2T}^\nu + 2x(q_{1T}q_{2T})p_B^\nu]. \quad (22)$$

As a result, colliding gluons can be considered as those that are aligned in such a way that their polarization vectors are directed along the transverse momenta. It follows that there must arise nontrivial azimuthal correlations between the transverse momenta of the product heavy quarks.

Formally, gauge invariance can be lost in dealing with off-mass-shell gluons. By way of example, we indicate that, in the covariant Feynman gauge, there are diagrams that are analogous to those that feature bremsstrahlung from the initial or from the final quark line (as is shown in Fig. 2*d*) and which can contribute to the rapidity region of the central plateau. But in fact, this does not occur. Within the accuracy of the theory of semihard processes, the three-gluon vertex in (22) effectively includes all leading logarithmic contributions of the type in Fig. 2*d* if all contributions of the form $\alpha_s^k (\ln q^2)^n (\ln(1/x))^m$, with $n + m \geq k$, are retained in the function $\varphi(x, q^2)$ [18, 25]. For example, the upper part of the diagram in Fig. 2*d* corresponds, in terms of the BFKL equation, to the Reggeization of the t-channel gluon. Thus, we conclude that, apart from the small nonlogarithmic correction of order α, the eventual expression is gauge-invariant.[8)]

Although the situation described above seems absolutely dissimilar to that in the parton model, there is a limit [28] where the formulas obtained in the k_T-factorization approach coincide with the corresponding formulas of the parton model. This occurs if the quark transverse momenta $p_{1,2T}$ are much higher than the initial-gluon transverse momenta $q_{1,2T}$.

4. RESULTS OF NUMERICAL CALCULATIONS

Expression (14) makes it possible to calculate both single-particle and pair distributions of product heavy quarks. In order to illustrate the distinctions between the present approach and the approach that relies on the standard parton model, we will consider above all the results obtained by calculating the production of charm quarks ($m_c = 1.4$ GeV [29, 30]) with high p_T at $\sqrt{s} = 1$, 10, and 10^3 TeV and the same value

$$x_T = \frac{2p_T}{\sqrt{s}} = 0.02. \quad (23)$$

At the above three energy values, this corresponds to $p_T = 10$, 100, and 10^4 GeV.

We will use the normalization points $\mu_F = m_T = \sqrt{m_c^2 + p_T^2}$ and $\mu_R = m_c$—that is, a fixed coupling constant at $N_f = 3$ and $\Lambda = 248$ MeV.

[7)] In connection with this transformation, we can say that the matrix elements in the k_T-factorization approach are gauge-invariant. As to the polarization vectors of the initial gluons q_1 and q_2, they are fixed as $-q_{1T}^\mu/y$ and $-q_{2T}^\nu/x$, respectively, instead of being arbitrary—for details, the reader is referred to [16].

[8)] Taking the gluon polarization vector in the form $-q_{1T}^\mu/y$, we completely eliminate leading logarithmic contributions arising from the diagram in Fig. 2*d*.

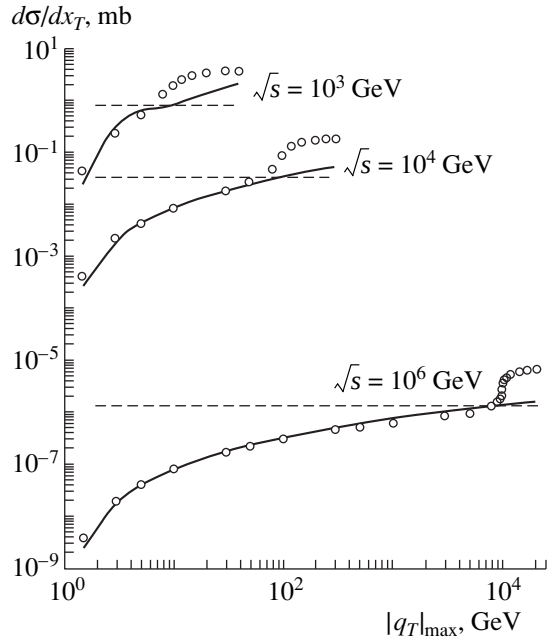

Fig. 3. Differential cross section $d\sigma/dx_T$ for charm production in hadron collisions at $x_T = 0.02$ versus the upper limit of the integral in Eq. (14): (points) results obtained within the k_T-factorization approach, (dashed lines) results produced by the standard parton model, (solid curves) values of the expression on the right-hand side of Eq. (26).

In the case of k_T factorization, there arises the problem of taking into account the infrared region, since the functions $\varphi(x, q_2^2)$ and $\varphi(y, q_1^2)$ are unknown at small values of $q_{1,2}^2$. Moreover, it can be shown for all realistic gluon structure functions that $\varphi(x, q^2)$ is positive at small x and negative at large x. The boundary between these regions, where $\varphi(x, q^2) = 0$, depends on q^2; therefore, their relative contributions are determined by the characteristic hardness of the process—for example, by the quark transverse momentum p_T.

In order to avoid, at the first stage, additional problems associated with the infrared region, we present the results of our numerical calculations within the k_T-factorization approach and within the leading-order parton model, using the strongly simplified gluon distribution

$$xG(x, q^2) = (1-x)^5 \ln(q^2/Q_0^2) \qquad (24)$$

for $q^2 > Q_0^2$ and setting $xG(x, q^2) = 0$ for $q^2 < Q_0^2$ at $Q_0^2 = 1$ GeV^2.

The calculation of the charm-production cross section on the basis of expressions (1) and (8), on one hand, and expression (14), on the other hand, shows that, at $x_T = 0.02$, the $d\sigma/dx_T$ value as obtained in the k_T-factorization approach is four to five times as large as that within the leading-order parton model. This distinction should not be taken to be overly great: as was discussed above, a significant part of the NLO and NNLO corrections to the leading-order parton model is contained in the leading order of the k_T-factorization approach, and the sum of leading-order and next-to-leading order contributions in the parton model is two to three times as great as the leading-order contribution alone [31].

In order to single out the most important region of the variables $q_{1,2T}$ in expression (14) and the kinematical region that is predominantly responsible for deviations from the parton model, the results of the calculation performed on the basis of the k_T-factorization approach with the constraint $|\,|q_{1,2T}| \le q_{\max}$ are displayed in Fig. 3 versus $q_{T\max}$. In this calculation, the fixed coupling constant $\alpha_s(m_c^2)$ was used in (14) instead of $\alpha_s(q_{1,2}^2)$. The dashes in Fig. 3 represent the predictions of the standard leading-order parton model with the normalization points $\mu_F = \sqrt{m_c^2 + p_T^2}$ and $\mu_R = m_c$. It can be seen that, for $q_{\max} \ge p_T$, the predictions of the k_T-factorization approach are in excess of the results produced by the leading-order parton model.

Let us test the statement that, in the case where transverse momenta of the product quarks, $p_{1,2T}$, considerably exceed the momenta of initial gluons, $q_{1,2T}$, the predictions of the k_T-factorization approach coincide with the corresponding predictions of the leading-order parton model [28].[9)] If the $q_{1,2T}$ dependence is disregarded in the matrix element everywhere, with the exception of the vertices, this matrix element will indeed coincide with that in the leading order of the parton model. On the other hand, we can find from (8) that [33]

$$xG(x, q^2) = xG(x, Q_0^2) + \frac{1}{4\sqrt{2}\pi^3}\int_{Q_0^2}^{q^2} \varphi(x, q_1^2)\,dq_1^2, \qquad (25)$$

if expression (14) is taken under the conditions $|q_{1,2T}| \le q_{\max}$, and the eventual result will be proportional to $xG(x, q_{\max}^2) \cdot yG(y, q_{\max}^2)$. At the same time, the result in the parton model is proportional to $xG(x, \mu_F^2) \cdot yG(y, \mu_F^2)$ with $\mu_F = \sqrt{m_c^2 + p_T^2}$. A comparison must be drawn at identical values of the structure functions; therefore, it can be expected that, upon multiplication by an appropriate factor, the result in the parton model will be

[9)] We note that, in contrast to the statement in [32], the Jacobian of the transition from the variables x_1 and x_2 to the rapidities y_1 and y_2 is included in the matrix element; accordingly, our expression in the limit $q_{1,2T} \ll p_{1,2T}$ exactly reproduces the result obtained in the leading-order parton model.

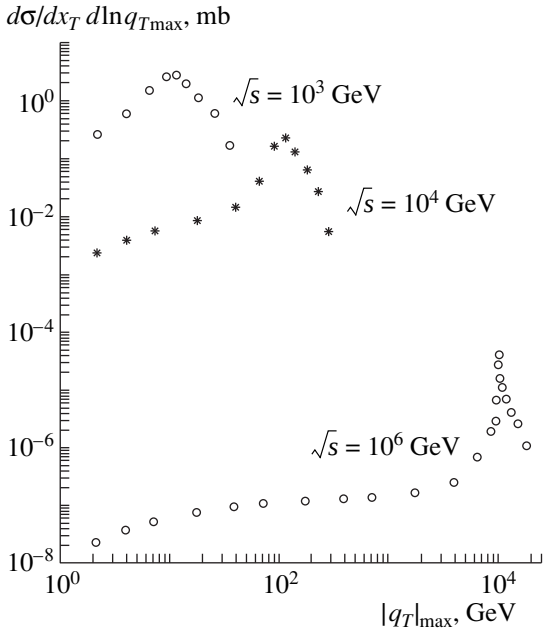

Fig. 4. Differential cross section $d\sigma/dx_T d\ln q_{T\max}$ for charm production in hadron collisions at $x_T = 0.02$ versus the upper limit of the integral in Eq. (14) according to the calculation in the k_T-factorization approach.

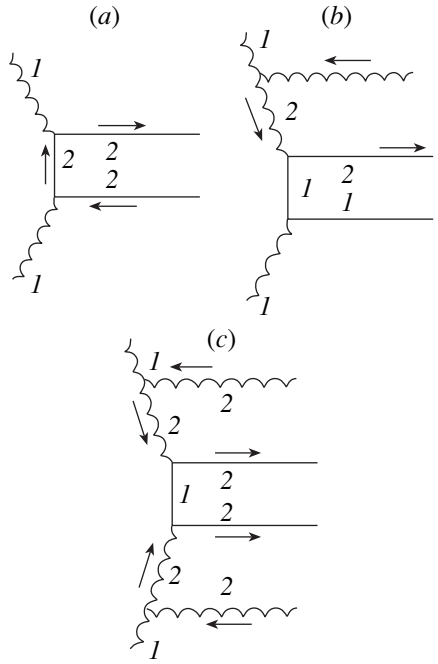

Fig. 5. Diagrams making significant contributions to single-particle distributions of heavy quarks having high transverse momenta (parametrically high transverse momenta flow along lines *2*, the directions of these momenta being indicated by arrows; relatively low transverse momenta flow along lines *1*): (*a*) situation typical of the leading-order parton model; (*b*) case characteristic of the NLO contribution in the parton model (the high transverse momentum p_T of the quark is compensated by the hard-gluon momentum, and the fermion propagator is close to the mass shell); and (*c*) numerically modest contribution that arises when the high transverse momenta of the two heavy quarks are compensated by the momenta of two hard gluons, in which case the fermion propagator is close to the mass shell.

coincident with the results of our calculations with the gluon distributions in (24) for $p_T \gg m_c$ and $|q_{1,2T}| \le q_{\max}$:

$$\left.\frac{d\sigma}{dx_T}\right|_{q_{iT} \ll p_{iT}} = \left.\frac{d\sigma}{dx_T}\right|_{\mathrm{PM}} \left(\frac{\ln(q_{\max}^2/Q_0^2)}{\ln(p_T^2/Q_0^2)}\right)^2. \qquad (26)$$

Even if $q_{\max}$ is only slightly less (at the highest energies) than p_T, the expression on the right-hand side of Eq. (26) take values, shown by solid curves in Fig. 3, that are in good agreement with the results obtained within the k_T-factorization approach and represented by open symbols. The same cross sections $d\sigma/dx_T$ as in Fig. 3 that were deduced within the k_T-factorization approach and which were differentiated with respect to $\ln q_{T\max}$ are displayed in Fig. 4. At higher energies, we can clearly see a logarithmic growth with $q_{\max}$ as long as $q_{\max} \sim p_T$. In this region, there is a narrow maximum saturating 70 to 80% of the cross section $d\sigma/dx_T$ integrated over the entire $q_{1,2T}$ region.

The physical origin of this maximum is quite obvious. In the *t*- and *u*-channel diagrams in Figs. 2*a* and 2*b*, there are two kinematical regions that contribute significantly to $d\sigma/dx_T$ at high energies and transverse momenta of a product heavy quark. One of these, corresponds to the kinematics of the standard parton model, where the transverse momenta of both initial gluons, $q_{1,2T}$, are sufficiently small in relation to $p_{1,2T}$ (see Fig. 5*a*). The other large contribution comes from the region where, for example, $q_{1T} \sim p_{1T}$, while q_{2T} and p_{2T} are comparatively small (see Fig. 5*b*). In this case, the quark propagator $1/((\hat{p}_1 - \hat{q}_1) - m_Q) = 1/((\hat{q}_2 - \hat{p}_2) - m_Q)$ is close to the mass shell, whereby there arise narrow peaks seen in Fig. 4. That the cross sections for such processes are generally small is explained by a large virtuality in the gluon propagator in Fig. 5*b*, and this is the reason why they prove to be on the same order of magnitude as the cross sections for the processes illustrated in Fig. 5*a* (in fact, the cross sections for the processes in Fig. 5*b* are somewhat larger because, in the case of the diagrams in Fig. 5*a*, the fermion propagator suppresses the contribution from the region where the difference of the rapidities of the product heavy quarks is large).

Since the diagram in Fig. 5*b* involves the exchange of a *t*-channel vector gluon, it represents one of the most important contributions in the NLO parton model at high energies [1]. For this and for combinatorial reasons and because of the interference between different terms, the integrated contribution of the peak to the cross section $d\sigma/dx_T$ is considerably greater than the contribution of the leading-order parton model. The

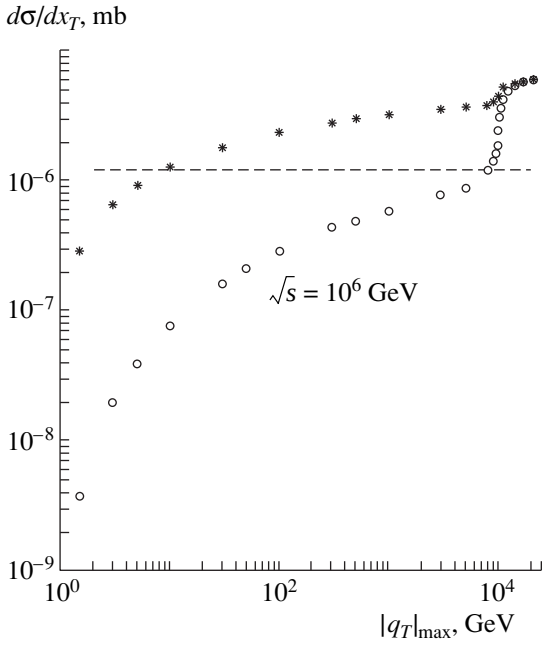

Fig. 6. As in Fig. 3 for values represented by the open circles and the dashed line. The asterisks correspond to the $d\sigma/dx_T$ values calculated for the case where only the integration with respect to q_{2T} is bounded from above by $q_{\max}$.

ratios of the total cross sections calculated for the production of heavy-quark pairs within the above two approaches, R_{tot}, and the ratios $R(x_T)$ of the quantities $d\sigma/dx_T$ calculated analogously at $x_T = 0.02$ and integrated with respect to rapidities are quoted in the table.

We can see that the relative contributions of the peaks being discussed first increase with energy because of the growth of the phase space, but they reach saturation at $\sqrt{s} \sim 10$ TeV. Further, the relative contribution of the leading-order parton model grows logarithmically with p_T and comes to be dominant at extremely high energies and transverse momenta.

The data presented in Fig. 6 confirm the aforesaid. Here, we again display the same results in the leading-order parton model as in Fig. 3 and the results of the calculations performed within the k_T-factorization approach under the condition $|q_{1,2T}| \le q_{\max}$. The predictions of the k_T-factorization approach that were obtained for all values of q_{1T} under the condition $|q_{2T}| \le q_{\max}$ are shown by asterisks versus $q_{T\max}$. The last result appears to be in excess of the results in the leading-order parton model even at not overly high values of q_{2T}, since the contributions of the above peaks have already been taken into account, at least partly, in performing integration with respect to q_{1T}.

Ratio of the differential cross sections computed for $c\bar{c}$ production in the k_T-factorization approach and in the leading-order parton model

$\sqrt{s}$, TeV	0.3	1	10	100	1000
R_{tot}	4.0	4.0	4.0	3.9	3.9
R ($x_T = 0.02$)	3.4	4.5	5.5	5.4	5.2

The contributions of the diagrams that involve a few propagators with a large virtuality are relatively small. For example, a calculation of the cross section $d\sigma/dx_T$ at $\sqrt{s} = 10$ TeV and $x_T = 0.02$ under the conditions $|q_{1,2T}| \ge p_T/2$ (see Fig. 5*c*) yields only 2% of the total $d\sigma/dx_T$ value at $x_T = 0.02$.

In our calculations, the important values of $q_{1,2T}$ increase with increasing transverse momentum p_T of the recorded charmed quark and become $q_{1,2T} \sim p_T$ at sufficiently high primary energies. In terms of the k_T^{kick} method, this means that $\langle k_T^2 \rangle$ must also grow.

The calculated distributions $d\sigma/dp_T$ are displayed in Fig. 7. The dashed curves (the lowest ones at each energy value) were computed within the leading-order parton model. The solid curves were plotted on the basis of the results deduced by using the k_T-factorization approach with the gluon distribution $\varphi(x, q^2)$ (8). The dash-dotted curves represent results that also emerged from the application of the k_T-factorization approach, but which take into account the doubly logarithmic form factor T (12) at various values of μ^2 and which were obtained with aid of expressions (9) and (10) (see the relevant discussion at the end of Section 3). We emphasize once again that the factor T allows for the total contribution of the diagrams that, in the Feynman gauge, involve gluon lines embracing the hard-interaction block, as is shown in Fig. 1*b*. In the axial gauge, the relevant doubly logarithmic contribution comes from diagrams associated with the parton (gluon) self-energy—that is, with the term proportional to $\delta(1 - z)$ in the DGLAP evolution equation. The factor T reproduces the majority of virtual NLO corrections to the standard leading-order parton model; as can be seen from Fig. 7, this factor reduces the calculated cross sections for heavy-quark production. It suppresses the contributions from small parton virtualities ($q_{1,2}^2 \ll m_T^2 = m_Q^2 + p_T^2$) in expression (14), concurrently increasing [owing to the derivative $\partial T/\partial k_t^2$ in expression (9) for f_a] the contribution from the region where $q_{1,2T}^2$ is commensurate with m_T^2 (in fact, a few times smaller than that).

It should be recalled that, within the k_T-factorization approach, there have arisen no problems so far that are associated with the choice of the normalization points since the integral in (14) has been calculated over all values of the parton virtualities $q_{1,2}^2$ and since the

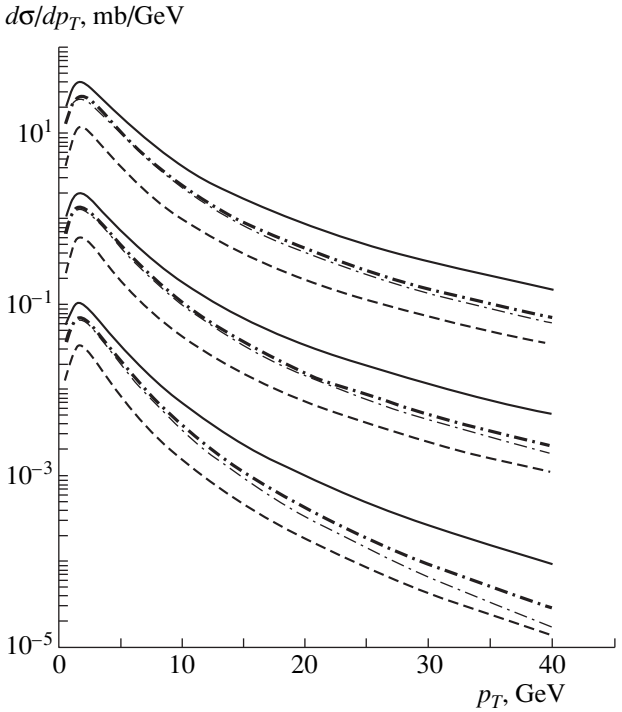

Fig. 7. Transverse-momentum distributions of c quarks produced at various primary energies. The different sets of curves correspond (from top to bottom) to $\sqrt{s}$ = 1000, 10, and 1 TeV (the results for the first and the second energy value are multiplied by 100 and 10, respectively). The dashed curves represent the results obtained in the leading order of the parton model. All other curves were calculated within the k_T-factorization approach: (solid curves) results of the calculations employing the gluon distributions in the form (8), (thin dash-dotted curves) results of the calculations employing expressions (9) and (10) and taking into account the doubly logarithmic form factor T (12) at μ^2 set to $\hat{s}/4$ in (12), and (thick dash-dotted curves) results of the calculations employing expressions (9) and (10) and taking into account the doubly logarithmic form factor T (12) at μ^2 set to m_T^2 in (12).

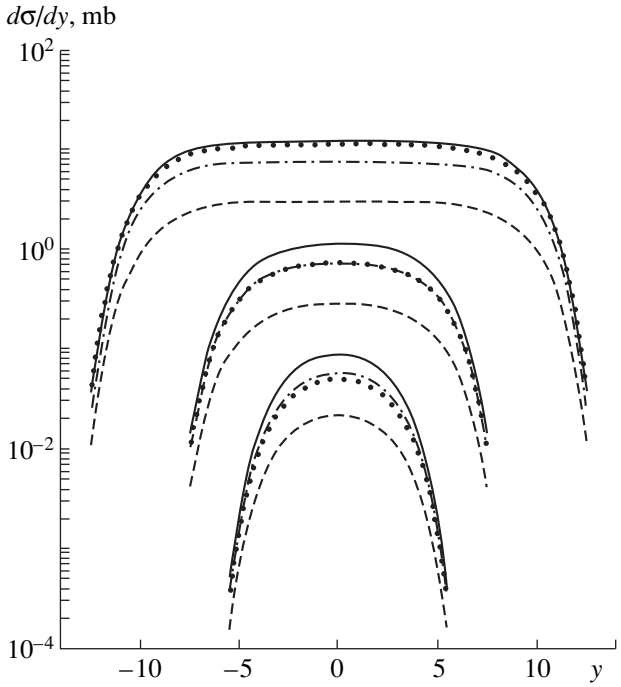

Fig. 8. Rapidity distributions of c quarks produced at various primary energies. The different sets of curves correspond (from top to bottom) to $\sqrt{s}$ = 1000, 10, and 1 TeV (the results for the first and the second energy value are multiplied by 100 and 10, respectively). The dashed curves and points represent the results obtained in, respectively, the leading and the next-to-leading order of the parton model. All other curves were calculated within the k_T-factorization approach: (solid curves) results of the calculations employing the gluon distributions in the form (8) and (dash-dotted curves) results of the calculations employing expressions (9) and (10) and taking into account the doubly logarithmic form factor T (12) at μ^2 set to m_T^2 in (12).

dependence of the matrix element $M(q_{1T}, q_{2T}, p_{1T}, p_{2T})$ on $q_{1,2T}$ ensured convergence, automatically fixing the normalization point μ_F.

Upon the inclusion of the factor T, the problem of choosing the normalization point arises anew. In Eq. (12), which was derived in the leading order, the normalization point μ^2 was not defined. Reasonable values of μ^2 are expected somewhere between m_T^2 and $\hat{s} = M_{Q\bar{Q}}^2 = xys - (\mathbf{q}_{1T} + \mathbf{q}_{2T})^2$. As can be seen from Fig. 7, the distinctions between the relevant numerical results are very small.

Figure 8 displays the rapidity distributions of product c quarks. The dashed curves again represent the results that arise in the leading-order parton model. The dotted curves correspond to the results of the calculations performed within the parton model with allowance for NLO corrections at $\mu_F^2 = \mu_R^2 = \mu^2 = 8m_c^2$ in (1) and (2). It should be noted that, at primary energies s so high that significant values of hard-interaction energy $\hat{s} = x_1x_2s$ are sufficiently high—that is, $\rho \ll 1$ in (3)—the NLO corrections grow considerably and greatly depend on the choice of μ^2. Let us dwell on this point at some length. As was shown in [1], the leading-order contribution—that is, the quantity $f_{gg}^{(0)}$ in Eq. (2)—tends to zero when $\rho \longrightarrow 0$, whereas the contributions $f_{gg}^{(1)}$ and $\bar{f}_{gg}^{(1)}$ take nonzero values: for $\rho \longrightarrow 0$, we have $f_{gg}^{(1)} \longrightarrow 0.1$ and $\bar{f}_{gg}^{(1)} \longrightarrow -0.04$. Thus, the NLO contribution, which is proportional to $\alpha_s^3(f_{gg}^{(1)}(\rho) + \bar{f}_{gg}^{(1)}(\rho))\ln(\mu^2/m_c^2)$, becomes dominant at small values of ρ and changes sign at $\mu^2 \sim 12m_c^2$. For $\mu^2 > 12m_c^2$, the

cross section σ_{LO+NLO} can prove to be negative. In Fig. 8, we have chosen $\mu^2 = 8m_c^2$, which corresponds to reasonable values of the energy of two heavy quarks, $\hat{s} \geq 4(m_Q^2 + p_T^2) \approx 8m_Q^2$, and leads to K values close to those used in describing experimental data. In this case, the NLO correction is positive ($K \approx 2$ to 3) and grows slowly with increasing energy.

The solid curve in Fig. 8 represents the predictions of the k_T-factorization approach employing the distribution function $\varphi(x, q^2)$ (8), while the dash-dotted curve corresponds to the calculation that was performed within the same conceptual framework, but which takes into account the doubly logarithmic form factor T (12) with $T(m_T^2)$ and invokes expressions (9) and (10). It can be seen that the inclusion of the form factor T reduces the cross sections obtained in the k_T-factorization approach by a factor of about 1.5 and, in the energy-range $\sqrt{s} \sim 10^3$–10^4 GeV, yields cross-section values that are very close to those computed within the parton model including leading- and next-to-leading order corrections (dotted curves). With increasing energy, the distinctions between these results increase somewhat.

5. CONCLUSION

A comparison of the predictions obtained within the standard leading-order parton model and within the k_T-factorization approach has been drawn for heavy-quark production in hadronic processes. In order to reveal, in this comparison, conceptual distinctions between the two approaches in a pure form not masked by the details of parton distributions, we have deliberately chosen the simplest parametrization (24) for the gluon structure function.

It has been shown that, within the k_T-factorization approach, the contribution from the region where there is a strong q_T ordering ($q_{1,2T} \ll m_T = \sqrt{m_Q^2 + p_T^2}$) coincides with the predictions of the leading-order parton model. In addition to this contribution, however, there are numerically large contributions in the k_T-factorization approach that are associated with the region $q_{1,2T} \geq m_T$. Kinematically, these contributions correspond to events in which the large transverse momentum of the heavy quark Q is compensated by the momentum of the nearest gluon rather than by the momentum of the antiquark $\bar{Q}$.

In terms of the parton model with a fixed number of flavors (that is, under the assumption that no heavy quarks are involved in the evolution processes), such configurations arise in the NLO (or even in the NNLO if q_{1T} and q_{2T} are both not less than m_T). Indeed, it was indicated in [1] that nearly 80% of the total NLO cross section is saturated by events in which the transverse momentum of a heavy quark is compensated by the nearest gluon jet. Thus, the large values of the NLO contributions, especially those at high p_T, are due to the small virtualities of the t- or u-channel quarks in the q_T region around p_T, in which case the singularities of the quark propagators $1/((\hat{p} - \hat{q}) - m_Q)$ begin to manifest themselves in the hard QCD matrix element $M(q_{1T}, q_{2T}, p_{1T}, p_{2T})$.

The inclusion of the doubly logarithmic Sudakov form factor T in the definition of the unintegrated parton density (9) amounts to taking into account a considerable part of NLO virtual loops, which appear to be corrections to the results in the leading-order parton model. Hence, the leading-order results in the k_T-factorization approach contain a major part of the contributions that play the role of NLO or even NNLO corrections in the standard parton model. This gives sufficient ground to believe that higher α_s corrections in the k_T-factorization approach will be modest.

That a nonzero transverse momentum of the $Q\bar{Q}$ system ($p_{1T} + p_{2T} = q_{1T} + q_{2T}$) arises quite naturally within k_T factorization is another appealing feature of this approach. Typical values of this transverse momentum depend on the form of the parton structure function. They become higher with increasing primary energy (that is, decreasing typical values of x and y for initial partons), as well as with increasing transverse momenta of the product heavy quarks. Owing to this, one can in principle describe nontrivial azimuthal correlations in the product pairs without phenomenologically introducing high transverse momenta for the partons.

A more detailed treatment of heavy-quark production in hadron collisions, including the description of correlations between the product heavy quarks, within the k_T-factorization approach employing realistic structure functions will be given in a separate publication.

ACKNOWLEDGMENTS

The main part of the calculations presented here were performed at the International Centre for Theoretical Physics (ICTP, Trieste). One of us (Yu.M. Shabelski) is indebted to Prof. S. Randjbar-Daemi for extending him this possibility and to the ICTP personnel for creating favorable conditions for the work. Special thanks are due to E.M. Levin, who participated in the early stage of this research. We are also grateful to Yu.L. Dokshitzer, G.P. Korchemskiĭ, and M.L. Mangano for stimulating discussions.

This work was supported by NATO (grant no. OUTR.LG 971390) and by the Russian Foundation for Basic Research (project no. 98-02-17629).

REFERENCES

1. P. Nason, S. Dawson, and R. K. Ellis, Nucl. Phys. B **303**, 607 (1988).

2. G. Altarelli *et al.*, Nucl. Phys. B **308**, 724 (1988).
3. P. Nason, S. Dawson, and R. K. Ellis, Nucl. Phys. B **327**, 49 (1989).
4. W. Beenakker, H. Kuijf, W. L. van Neerven, and J. Smith, Phys. Rev. D **40**, 54 (1989).
5. W. Beenakker, W. L. van Neerven, R. Meng, *et al.*, Nucl. Phys. B **351**, 507 (1991).
6. M. L. Mangano, P. Nason, and G. Ridolfi, Nucl. Phys. B **373**, 295 (1992).
7. S. Frixione, M. L. Mangano, P. Nason, and G. Ridolfi, Preprint CERN-TH/97-16 (Geneva, 1997); hep-ph/9702287.
8. BEATRICE Collab. (M. Adamovich *et al.*), Phys. Lett. B **348**, 256 (1995).
9. BEATRICE Collab. (Y. Alexandrov *et al.*), Phys. Lett. B **433**, 217 (1998).
10. Yu. M. Shabelski, Talk given at HERA Monte Carlo Workshop, April 27–30, 1998, DESY, Hamburg; hep-ph/9904492.
11. S. Catani, M. Ciafaloni, and F. Hautmann, Phys. Lett. B **242**, 97 (1990); Nucl. Phys. B **366**, 135 (1991).
12. J. C. Collins and R. C. Ellis, Nucl. Phys. B **360**, 3 (1991).
13. G. Marchesini and B. R. Webber, Nucl. Phys. B **386**, 215 (1992).
14. S. Catani and F. Hautmann, Phys. Lett. B **315**, 475 (1993); Nucl. Phys. B **427**, 475 (1994).
15. S. Camici and M. Ciafaloni, Nucl. Phys. B **467**, 25 (1996); Phys. Lett. B **396**, 406 (1997).
16. L. V. Gribov, E. M. Levin, and M. G. Ryskin, Phys. Rep. **100**, 1 (1983).
17. E. M. Levin and M. G. Ryskin, Phys. Rep. **189**, 267 (1990).
18. E. M. Levin, M. G. Ryskin, Yu. M. Shabelski, and A. G. Shuvaev, Yad. Fiz. **53**, 1059 (1991) [Sov. J. Nucl. Phys. **53**, 657 (1991)].
19. E. M. Levin, M. G. Ryskin, Yu. M. Shabelski, and A. G. Shuvaev, Yad. Fiz. **54**, 1420 (1991) [Sov. J. Nucl. Phys. **54**, 867 (1991)].
20. Yu. L. Dokshitzer, I. M. Dyakonov, and S. I. Troyan, Phys. Rep. **58**, 270 (1980).
21. Ya. I. Azimov, O. P. Strogova, and Yu. M. Shabel'skii, Yad. Fiz. **57**, 715 (1994) [Phys. At. Nucl. **57**, 674 (1994)].
22. J. C. Collins, D. E. Soper, and G. Sterman, Nucl. Phys. B **308**, 833 (1988).
23. M. L. Mangano, P. Nason, and G. Ridolfi, Nucl. Phys. B **405**, 507 (1993).
24. J. Blümlein, Preprint DESY 95-121 (Hamburg, 1995).
25. E. A. Kuraev, L. N. Lipatov, and V. S. Fadin, Zh. Éksp. Teor. Fiz. **72**, 377 (1977) [Sov. Phys. JETP **45**, 199 (1977)].
26. G. P. Korchemsky and G. Sterman, Nucl. Phys. B **437**, 415 (1995).
27. S. J. Brodsky, G. P. Lepage, and P. B. Mackenzie, Phys. Rev. D **28**, 228 (1983).
28. M. G. Ryskin, Yu. M. Shabelski, and A. G. Shuvaev, Z. Phys. C **69**, 269 (1996).
29. S. Narison, Phys. Lett. B **341**, 73 (1994).
30. P. Ball, M. Beneke, and V. M. Braun, Phys. Rev. D **52**, 3929 (1995).
31. Liu Wenjie, O. P. Strogova, L. Cifarelli, and Yu. M. Shabel'skii, Yad. Fiz. **57**, 900 (1994) [Phys. At. Nucl. **57**, 844 (1994)].
32. S. P. Baranov and M. Smizanska, Phys. Rev. D **62**, 014012 (2000).
33. J. Kwiechinski, Z. Phys. C **29**, 561 (1985).

Translated by A. Isaakyan

Physics of Atomic Nuclei, Vol. 64, No. 1, 2001, pp. 132–139. Translated from Yadernaya Fizika, Vol. 64, No. 1, 2001, pp. 135–142.

ELEMENTARY PARTICLES AND FIELDS
Theory

Free Energy in the (2 + 1)-Dimensional *SU*(2) QCD Model against the Background of a Gauge-Field Condensate

V. Ch. Zhukovsky and V. V. Khudyakov

Moscow State University, Vorob'evy gory, Moscow, 119899 Russia

Received January 22, 1999; in final form, November 12, 1999

Abstract—The thermodynamic potential (free energy) for quarks and gluons in (2 + 1)-dimensional spacetime is calculated in the one-loop approximation at finite temperatures against the background of a constant uniform color magnetic field H and a constant uniform A_0 condensate. The problem of interpreting the tachyon mode in the gluon energy spectrum is discussed. The question of whether the free energy may develop a minimum at nonzero values of H and A_0 is analyzed. © *2001 MAIK "Nauka/Interperiodica".*

1. INTRODUCTION

Investigation of low-dimensional quantum-field theories [1–3] is of interest because such models are tightly related to their (3 + 1)-dimensional analogs [4–6] and because they provide a clue to some phenomena of real nature. For example, the dimensional-reduction method developed in [7] makes it possible to study quark–gluon plasma in (3 + 1)-dimensional QCD above the critical temperature of the confinement–deconfinement phase transition. The single-particle model of two-dimensional electrons interacting with an external electromagnetic field is used to explain the quantum Hall effect [8, 9].

In recent years, a large number of studies have been devoted to an analysis of the effective potential against the background of a condensate and at high temperatures, either in the one-loop approximation [10–15] or with allowance for multiloop contributions [16–18]. In this problem, calculations in higher orders of a loop expansion may lead to results dependent on the gauge-fixing method [19]. The assumption that there is an A_0 condensate in QCD (see, for example, [10]) has important physical implications, such as a spontaneous breakdown of global gauge symmetry and elimination of the imaginary part in the effective potential and of the infrared divergence.

This article is organized as follows. In Section 2, we present basic formulas that are necessary for describing quantum-field systems at finite temperatures and establish the relation between the effective potential and the energy spectrum of single-particle field excitations. In Section 3, we calculate the free-energy density for the gluon fields within (2 + 1)-dimensional QCD. The presence of a tachyon mode in the gluon energy spectrum results in a nonanalytic dependence of the thermodynamic potential on the condensate fields. A method is proposed here for eliminating this nonanalyticity. It is shown that the free energy has a nontrivial minimum and that, below the critical temperature, there exist a confining and a deconfining phase. In Section 4, we calculated the free-energy density for the quark fields and demonstrate that, in contrast to what is observed for gluons, it attains a minimum in the absence of condensate fields.

2. ENERGY SPECTRUM OF EXCITATIONS AND FREE ENERGY

Let us consider the QCD(2 + 1) model involving a gluon gauge field A_μ^a in the adjoint representation of the $SU(2)$ color group and represent the potential A_μ^a as the sum $A_\mu^a = \bar{A}_\mu^a + a_\mu^a$, where $\bar{A}_\mu^a$ is the background potential and a_μ^a describes quantum fluctuations of gluons. In Euclidean spacetime, the Lagrangian of the gauge field in the Lorentz gauge can be written as

$$\mathcal{L}_g = \frac{1}{4}(F_{\mu\nu}^a)^2 + \frac{1}{2}(\bar{D}_\mu^{ab} a_\mu^b)^2 + \bar{\chi}^a(\bar{D}^2)^{ab}\chi^b, \qquad (1)$$

where $\bar{D}_\mu^{ab} = \delta^{ab}\partial_\mu - gf^{abc}\bar{A}_\mu^c$ is the covariant derivative, χ and $\bar{\chi}$ are ghost fields, and $(\bar{D}^2)^{ab} = \bar{D}_\mu^{ac}\bar{D}_\mu^{cb}$. In going over to Euclidean space, we keep the index 0 for the time components of vectors; thus, we have $x_0 = it$, and $\mu, \nu = 0, 1, 2$. In the three-dimensional representation, one can choose, by way of example, the following representation for the Clifford algebra:

$$\gamma^0 = \sigma^3, \quad \gamma^1 = i\sigma^1, \quad \gamma^2 = i\sigma^2, \qquad (2)$$

where σ^1, σ^2, and σ^3 are Pauli matrices. The quark Lagrangian then takes the form

$$\mathcal{L}_q = \sum_{j=1}^{N_f} \bar{\psi}_j\left[\gamma_\mu\left(\partial_\mu - ig\frac{\lambda_a}{2}A_\mu^a\right) + m_j\right]\psi_j, \qquad (3)$$

where N_f is the number of flavors and the matrices λ_a are the color-group generators. In order to calculate the generating functional

$$Z[\bar{A}, j, \eta, \bar{\eta}] = \int da_\mu^a d\bar{\chi} d\chi d\bar{\psi} d\psi \times \exp\left[-\int d^3x(\mathcal{L} + j_\mu^a a_\mu^a + \bar{\psi}\eta + \bar{\eta}\psi)\right], \quad (4)$$

which involves the QCD Lagrangian $\mathcal{L} = \mathcal{L}_g + \mathcal{L}_q$, in the one-loop approximation, it is sufficient to retain only those terms in $\mathcal{L}_g$ where the order of the gluon fluctuations a_μ^a is not higher than two. These are

$$\mathcal{L}_g = \mathcal{L}_g^{(0)} + \mathcal{L}_g^{(2)}, \quad \mathcal{L}_g^{(0)} = \frac{1}{4}(\bar{F}_{\mu\nu}^a)^2,$$
$$\mathcal{L}_g^{(2)} = -\frac{1}{2}a_\mu^a[(\bar{D}^2)^{ab}\delta_{\mu\nu} + 2g\bar{F}_{\mu\nu}^c f^{abc}]a_\nu^b, \quad (5)$$

where $\bar{F}_{\mu\nu}^a = \partial_\mu \bar{A}_\nu^a - \partial_\nu \bar{A}_\mu^a + g f^{abc}\bar{A}_\mu^b \bar{A}_\nu^c$. In this case, the functional integrals in (4) have a Gaussian form and can easily be calculated. The result is

$$Z[\bar{A}] = \exp\left\{-\frac{1}{4}\int d^3x(\bar{F}_{\mu\nu}^a)^2\right\} \times [\det(-\bar{D}^2\delta_{\mu\nu} - 2g\bar{F}_{\mu\nu}f)]^{-1/2}\det(-\bar{D}^2) \times \prod_{j=1}^{N_f}\det\left[\gamma_\mu\left(\partial_\mu - ig\frac{\lambda_a}{2}\bar{A}_\mu^a\right) + m_j\right]. \quad (6)$$

Representing Z in the form $Z = \exp(W_E)$, we obtain the effective Euclidean action

$$W_E = -\frac{1}{2}\int\frac{dq_0}{2\pi}\sum_r \ln[q_0^2 + (\varepsilon_r^g)^2] + \sum_{j=1}^{N_f}\int\frac{dp_0}{2\pi}\sum_k \ln[p_0^2 + (\varepsilon_{jk}^q)^2], \quad (7)$$

where we have considered that the contribution of the longitudinal components of the gauge field is canceled by the ghost contribution. The summation of the energy spectra of gluons, ε_r^g, and quarks, ε_{jk}^q, over the quantum numbers r and k must involve only physical degrees of freedom. Formally, we consider our field system within a three-dimensional cube of volume L^3, imposing periodic boundary conditions. In this case, the effective potential is given by

$$V = -W_E/L^3. \quad (8)$$

In the one-loop approximation, we can represent V as $V = V^{(0)} + v$, where $V^{(0)} = (\bar{F}_{\mu\nu}^a)^2/4$ is the energy density for the classical background field and $v = v^g + v^q$ is the one-loop contribution of gluon and quark fluctuations. In order to go over to infinite Euclidean spacetime, it is necessary to consider the limit $L \longrightarrow \infty$. Since the explicit expression (16) for the effective potential (see below) is independent of L, we will omit details associated with this limiting transition.

Further, we introduce the temperature $T \equiv 1/\beta$, requiring that boson (fermion) fields be periodic (antiperiodic) in x_0 with a period of β. According to the well-known procedure, this is achieved by going from q_0 and p_0 to Matsubara frequencies via the substitution $q_0 \longrightarrow 2\pi l/\beta - i\kappa\mu_1$ for bosons and the substitution $p_0 \longrightarrow 2\pi(l + 1/2)/\beta - i\kappa\mu_2$ for fermions, where μ_1 and μ_2 are the chemical potentials of gluons and quarks, respectively; $\kappa = \pm 1$ specifies the sign of the charges for particles and antiparticles; and $l \in \mathbb{Z}$ ($\mathbb{Z}$ is the set of integers). The one-loop effective potential defined in (8) then becomes proportional to the free-energy density,

$$V = \frac{-T\ln Z}{L^2} = \frac{\Omega}{L^2}. \quad (9)$$

Upon the above substitution, the one-loop contribution of gluon and quark fluctuations assumes the form

$$v = v^g + v^q = \frac{1}{2\beta L^2}\sum_{l=-\infty}^{+\infty}\sum_{r,\kappa=\pm 1}\ln\left[\left(\frac{2\pi l}{\beta} - i\kappa\mu_1\right)^2 + (\varepsilon_r^g)^2\right] - \frac{1}{\beta L^2}\sum_{j=1}^{N_f}\sum_{l=-\infty}^{+\infty}\sum_{k,\kappa=\pm 1}\ln\left[\left(\frac{2\pi(l+1/2)}{\beta} - i\kappa\mu_2\right)^2 + (\varepsilon_{jk}^q)^2\right]. \quad (10)$$

We define an external field as a superposition of a field H and a potential A_0, which are both uniform and constant and are directed along the third color axis:

$$\bar{A}_\mu^a = \delta_{\mu 2}\delta_{a3}Hx_1 + \delta_{\mu 0}\delta_{a3}A_0 = \delta_{a3}\bar{A}_\mu. \quad (11)$$

In order to allow for the A_0 condensate, it is sufficient to make the substitutions $i\mu_1 \longrightarrow gA_0$ and $i\mu_2 \longrightarrow gA_0/2$.

In three-dimensional spacetime, fermions are described by two-component spinors [see Eq. (2)]; therefore, they do not exhibit a spin degree of freedom. Moreover, the gauge fixing specified by $a_0^b = 0$ and $D^i a_i^b = 0$ leads to a linear relation between the positive- and the negative-frequency solutions to the Lagrange equations,

$$[(\bar{D}^2)^{ab}\delta_{\mu\nu} + 2g\bar{F}_{\mu\nu}^c f^{abc}]a_\nu^b = 0, \quad (12)$$

which follow from the Lagrangian density (5). In order to demonstrate this explicitly, we can represent an arbitrary solution to Eq. (12) as an expansion in eigenvectors,

$$a^\pm = a_1 \pm ia_2 = \sum_n N_n^\pm f_n(x), \quad (13)$$

where N_n are constant coefficients and $f_n(x)$ are eigenvectors of Eq. (12). It is possible to show (see [20]) that the gauge-fixing condition $D^-a^- + D^+a^+ = 0$ leads to the following constraints on the coefficients: $N_n^- = 2(n+2)N_{n+2}^+$, $n = 0, 1, 2, \ldots$; $N_1^+ = 0$. There are no constraints on the coefficient N_0^+ of the tachyon mode. By setting the chemical potentials μ_1 and μ_2 to zero, we then find that the energy spectra of gluons and quarks in a chromomagnetic fields are given by

$$\varepsilon_g^2 = 2gH\left(n - \frac{1}{2}\right) - i\epsilon, \quad n = 0, 2, 3, 4, \ldots; \tag{14}$$

$$\varepsilon_q^2 = gHn + m^2 - i\epsilon, \quad n = 0, 1, 2, 3, \ldots; \tag{15}$$

$$\epsilon > 0.$$

An infinitely small negative imaginary term $-i\epsilon$ specifies the procedure for circumventing poles and enables us to define correctly the limiting transition $T \longrightarrow 0$ for the tachyon mode [see Eq. (22) below].

3. GLUON CONTRIBUTION TO THE FREE-ENERGY DENSITY

In order to obtain an explicit expression for the effective potential, it is necessary to substitute (14) and (15) into (10) and to take into account the degeneracy multiplicity of the energy levels in a homogeneous magnetic field (Landau levels). In the case of three-dimensional spacetime, this degeneracy multiplicity is equal to $gHL^2/(2\pi)$. The contribution v^g of the charged-gluon loop to the thermodynamic potential v is then given by

$$v^g = \frac{gH}{2\pi\beta}\sum_{l=-\infty}^{+\infty}\left\{\ln\left[\left(\frac{2\pi l}{\beta} + gA_0\right)^2 - gH - i\epsilon\right]\right. \\ \left. + \sum_{n=2}^{\infty}\ln\left[\left(\frac{2\pi l}{\beta} + gA_0\right)^2 + 2gH\left(n - \frac{1}{2}\right) - i\epsilon\right]\right\}, \tag{16}$$

where the contribution of the tachyon mode (for which the energy squared is negative) is included in the first term. Since summation over l is performed over an infinite interval, expression (16) has a period of $2\pi/\beta$ in gA_0. This fact is tightly related to gauge invariance. At $T = 0$, we can make the gauge transformation

$$A_0' = UA_0U^+ + \frac{i}{g}U\partial_0U^+, \quad A_i' = UA_iU^+, \tag{17}$$

where

$$U = \exp\left(-igx_0A_0^a\frac{\lambda^a}{2}\right).$$

We then have $A_0' = 0$; hence, A_0 is not a physical parameter. At $T \neq 0$, the boundary conditions $A_\mu(x_0, \mathbf{x}) = A_\mu(x_0 + \beta, \mathbf{x})$ lead to the additional commutation condition $[U, \lambda^a] = 0$ for any λ^a. By definition, this means that U must belong to the gauge-group center. In the case of the $SU(2)$ group, only gauge transformations that respect $\mathbb{Z}_2$ symmetry are therefore admissible,

$$A_0 \longrightarrow A_0' = A_0 + \frac{2\pi n}{\beta g}, \quad n \in \mathbb{Z}, \tag{18}$$

and the region of gauge-nonequvivalent values of the potential A_0 reduces to values for which $gA_0 \in [0, 2\pi T]$.

It can be seen from (16) that v^g takes real values if the argument of the first logarithm is positive, which is equivalent to

$$\sqrt{gH} < gA_0 < 2\pi T - \sqrt{gH}; \tag{19}$$

otherwise, the vacuum becomes unstable. Calculations reveal that, in the (3 + 1)-dimensional case, the one-loop effective potential has a finite nontrivial minimum, which, however, appears to be unstable [10, 11]. According to (16), allowance for higher loops (ring diagrams) in the high-temperature limit also leads to the appearance of an unstable minimum at fields such that $(gH)^{1/2} \sim g^{4/3}T$. For small α_s, this exceeds the estimates obtained for the field in the one-loop approximation. Returning to the general expression (16), we can see that, under the condition $gA_0 = \sqrt{gH}$, the free energy v^g tends to negative infinity. There does not arise such a singularity in the (3 + 1)-dimensional case, because integration with respect to the third momentum component, which is absent in the (2 + 1)-dimensional case, has a smoothing effect.

In the case under consideration, the divergence is removed by taking into account radiative corrections—namely, owing to the presence of the imaginary part in the gluon polarization operator. We are interested in the radiative energy shift only for the tachyon mode, since it is this mode that controls the singular behavior of the effective potential. Without performing detailed calculations, we will obtain a qualitative estimate by representing the gluon self-energy in the form $\Pi(\varepsilon, T) = \alpha_s\varepsilon(\Pi_1 + i\Pi_2)$, where Π_1 and Π_2 are functions of field and temperature (as a matter of fact, their explicit form has virtually no effect on the ensuing analysis of the model and on the qualitative results of this analysis), the quantity Π_2 being responsible for gluon decay. The self-energy contribution becomes important only in the vicinity of the singularity of the effective potential. We will now consider the dispersion equation $\varepsilon^2 = \varepsilon_g^2 + \langle\Pi(\varepsilon, T)\rangle$, making use of the assumption (which seems quite reasonable and which is in fact supported by numerical calculations) that, within the parameter region in question, the behavior of the free energy near the singular point is not very sensitive to the values of $\Pi_1 \sim \Pi_2 \sim 1$.

For $\alpha_s < (gH)^{1/2}$, we can estimate the energy squared of the tachyon mode with allowance for the radiative correction and the equality $\varepsilon_g^2 = -gH$. The result is

$$\varepsilon_{\text{tach}}^2 \simeq -gH - iC\alpha_s\sqrt{gH}, \tag{20}$$

where C is a coefficient of the order of unity. It is seen from (20) that the presence of the imaginary part $\varepsilon_{\text{tach}}^2$ ensures a nonvanishing argument (having just a nonzero imaginary part) of the first logarithm in (16) at $gH \neq 0$. Applying the well-known identity [21]

$$\prod_l \left[1 + \left(\frac{x}{2\pi l - a}\right)^2\right] = \frac{\cosh x - \cos a}{1 - \cos a} \tag{21}$$

to relation (16) and omitting the immaterial additive constant, we arrive, by analogy with [11], at

$$\begin{aligned} v^{\text{tach}} &= \frac{gH}{2\pi}\left\{\omega_0 + \frac{1}{\beta}\ln[1 + e^{-2\beta\omega_0} - 2e^{-\beta\omega_0}\cos(\beta g A_0)]\right\} \qquad (22)\\ &= \frac{gH}{2\pi\beta}\ln\left\{2\cos\left[\beta\left(\sqrt{gH} + \frac{i}{2}C\alpha_s\right)\right] - 2\cos(\beta g A_0)\right\}, \end{aligned}$$

$$\begin{aligned} v^g &= v^{\text{tach}} \\ &+ \frac{gH}{2\pi}\sum_{n=2}^{\infty}\left\{\omega_n + \frac{1}{\beta}\ln[1 + e^{-2\beta\omega_n} - 2e^{-\beta\omega_n}\cos(\beta g A_0)]\right\}, \end{aligned} \tag{23}$$

where

$$\omega_0 = -i\sqrt{gH} + \frac{1}{2}C\alpha_s, \quad \omega_n^2 = 2gH\left(n - \frac{1}{2}\right). \tag{24}$$

In order to analyze the effective potential in the region of small values of gH, it is advisable to make use of the expression for v^g derived by the Fock–Schwinger proper-time method. We begin by applying the standard integral representation

$$\ln A = -\int_0^\infty \frac{ds}{s}\exp(-sA), \tag{25}$$

which is valid if an infinite additive constant is discarded, to the second term in (16). This yields

$$\begin{aligned} v^g &= v^{\text{tach}} - \frac{gH}{2\pi\beta}\sum_{n=2}^{\infty}\sum_{l=-\infty}^{+\infty}\int_0^\infty \frac{ds}{s} \\ &\times \exp\left\{-s\left[\left(\frac{2\pi l}{\beta} + gA_0\right)^2 + 2gH\left(n - \frac{1}{2}\right)\right]\right\}. \end{aligned} \tag{26}$$

Further, we single out the temperature-dependent part v_T^g of the effective potential, representing this potential as $v^g = v_{T=0}^g + v_T^g$, where the zero-temperature part $v_{T=0}^g$ is independent of A_0 [it will be considered below; see (35)]. For this, we transform summation over Matsubara frequencies in (26) with the aid of the identity (see [10] or [21])

$$\begin{aligned} &\sum_{l=-\infty}^{+\infty}\exp\left[-s\left(\frac{2\pi l}{\beta} + gA_0\right)^2\right] \\ &= \frac{\beta}{2\sqrt{\pi s}}\sum_{l=-\infty}^{+\infty}\exp\left(-\frac{\beta^2 l^2}{4s}\right)\cos(\beta g A_0 l). \end{aligned} \tag{27}$$

Upon summing the expansion in (26) over n, we arrive at

$$\begin{aligned} v_T^g &= v_T^{\text{tach}} - \frac{gH}{2\pi^{3/2}}\int_0^\infty \frac{ds}{s^{3/2}}\left[\frac{1}{2\sinh(sgH)} - e^{-sgH}\right] \\ &\times \sum_{l=1}^{\infty}\exp\left(-\frac{\beta^2 l^2}{4s}\right)\cos(\beta g A_0 l). \end{aligned} \tag{28}$$

Numerical estimates confirm that expression (28) complies with the temperature-dependent part of (23). At the same time, expression (28) is advantageous in that its limit for $gH \longrightarrow 0$ is obvious,

$$v_{T,H=0}^g = -\frac{1}{\pi\beta^3}\sum_{l=1}^{\infty}\frac{\cos(\beta g A_0 l)}{l^3}. \tag{29}$$

In the high-temperature limit ($T \gg gA_0$), we obtain the estimate

$$v_{T,H=0}^g \approx -\frac{1}{\pi\beta^3}\left\{\zeta(3) + \frac{(\beta g A_0)^2}{2}\left[\ln(\beta g A_0) - \frac{3}{2}\right]\right\}, \tag{30}$$

which demonstrates a nonanalytic background-field dependence of the effective potential.

Substituting $A_0 = 0$ into Eq. (29), we obtain the doubled effective potential for neutral gluons (since v^g involves the contribution from gluons of two opposite color charges),

$$2v^{g_0} = -\zeta(3)T^3/\pi. \tag{31}$$

As might have been expected, we have derived an analog of the Planck law for equilibrium blackbody radiation in the (2 + 1)-dimensional case. In order to obtain the total free-energy density, it is necessary to add v^{g_0} to (23). However, v^{g_0} depends only on temperature, but it is independent of the condensate fields; therefore, this free-energy component is of no interest to us.

In order to perform a numerical analysis of the above results, it is convenient to go over to the dimen-

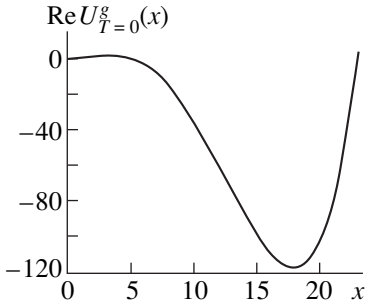

Fig. 1. Zero-temperature part Re $U^g_{T=0}(x)$ at $T/g^2 = 0.01$.

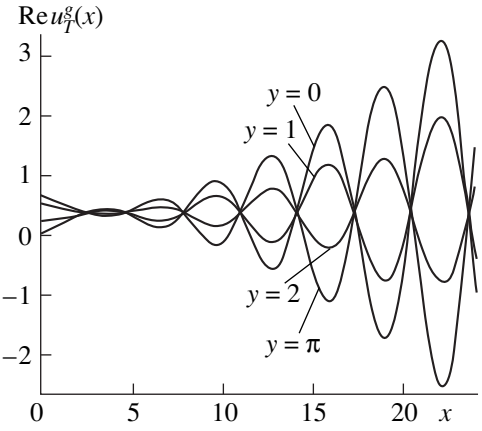

Fig. 2. Temperature-dependent part Re $u^g_T(x)$ at $T/g^2 = 0.01$.

sionless variables

$$x = \beta\sqrt{gH}, \quad y = \beta g A_0. \tag{32}$$

At $T = 0$, this change of variables is obviously impossible. For the sake of uniformity, we will nevertheless employ x and y at zero temperature as well, implying a finite number for β in (32) at $T = 0$. To v, we also add a constant defined in such a way as to ensure, in the absence of condensate fields, the vanishing of the quantity

$$u(x, y, T) = \frac{v(H, A_0, T)}{T^3}; \tag{33}$$

that is, $u(0, 0) = 0$.

The problem at hand now amounts to minimizing the real part of the function

$$U(x, y, T) = U^{(0)}(x, T) + u(x, y, T),$$
$$U^{(0)}(x, T) = \frac{x^4}{2}\frac{T}{g^2}, \tag{34}$$

where the factor T/g^2 specifies the temperature scale with respect to the coupling constant g. We denote by u^g and u^q, respectively, the gluon and the quark contribution to the dimensionless effective potential u and introduce the notation $U^g = U^{(0)} + u^g$. We isolate the temperature-dependent and the zero-temperature part of the potential u, u_T and $u_{T=0}$, respectively, so that $u = u_{T=0} + u_T$ and $U^g_{T=0} = U^{(0)} + u^g_{T=0}$.

Going over to the limit $\beta \longrightarrow \infty$ in (23) and setting $C = 1$, we easily obtain the zero-temperature contribution in the form

$$v^g_{T=0} = \frac{gH}{2\pi}\sum_{n=0,2}^{\infty}\omega_n$$
$$= -\frac{(gH)^{3/2}}{2\pi}\left[1 - \frac{\sqrt{2}-1}{4\pi}\zeta\left(\frac{3}{2}\right)\right] - i\frac{(gH)^{3/2}}{2\pi} + \frac{gH}{4\pi}\alpha_s, \tag{35}$$

which coincides, apart from the contribution to the effective potential from the tachyon mode of the gluons, with the result from [20]. The global minimum $U^g_{T=0}$ is achieved at $\sqrt{gH} \approx 0.185g^2$ (see Fig. 1). There also exists a local minimum of $U^g_{T=0}$ at $gH = 0$ (in contrast to what was obtained in [20])—this minimum is controlled by the tachyon-mode contribution, which is linear in gH and which is dominant when $gH \longrightarrow 0$. If $C \gg 1$ in Eq. (20), this contribution will shift the global minimum to the point $gH = 0$.

Trottier [20] states that the condensate of the chromomagnetic field H evaporates above the critical temperature (at $T > T_{cr}$). At the same time, he assumes that the tachyon mode of gluons is unphysical and does not take it into consideration. At zero temperature, however, the term v^{tach} contributes both to the imaginary and to the real part of the free-energy density; therefore, there are no reasons to ignore this mode. Moreover, it is just due to allowing for v^{tach} that the minimum v^g can appear at $A_0 \neq 0$ [11].

An analysis of the real part of $U^g(x, y = \text{const})$ as a function of x reveals the existence of a nontrivial minimum at $x = x_{min}$ for temperatures below some critical value, $T < T_{cr} \sim 0.15g^2$, in which case the temperature-dependent part u^g_T is small in relation to the zero-temperature part $u^g_{T=0}$. Owing to the choice of scale according to (33), the temperature-dependent part depends only slightly on T, while the zero-temperature temperature acquires an explicit dependence on T. Thus, the oscillating contribution u^g_T (Fig. 2) modulates the zero-temperature potential $U^g_{T=0}$ featuring a nontrivial minimum (Fig. 1). With decreasing temperature, x_{min} increases, taking values close to $n\pi$, $n \in \mathbb{N}$. Concurrently, there successively occur second-order transitions between the phases where the function $U^g(x_{min}, y)$ attains a minimum either at π or at zero. When $T \longrightarrow 0$, there are indefinitely many such phases.

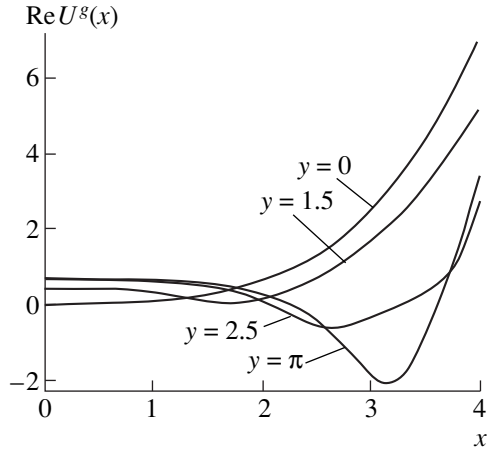

Fig. 3. Gluon potential $\mathrm{Re}\,U^g(x)$ at $T/g^2 = 0.1$.

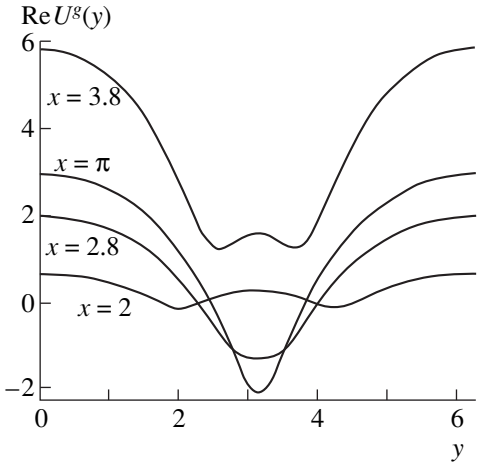

Fig. 4. Gluon potential $\mathrm{Re}\,U^g(y)$ at $T/g^2 = 0.1$.

By way of example, we indicate that, at $T/g^2 = 0.1$, the global minimum of the thermodynamic potential is achieved at $x = 3.14$ and $y = \pi$ (Figs. 3, 4). That U^g has a nonzero imaginary part implies, however, that this condensate configuration is unstable. When temperature increases in the region $T > T_{\mathrm{cr}}$, the condensate values $y_{\min}$ and $x_{\min}$ decrease from π to zero, with the approximate equality $x_{\min} \simeq y_{\min}$ still remaining valid.

It is well known that, if the trace case of the Polaykov loop [22, 23] vanishes in the fundamental representation, $\mathrm{tr}_F(\mathcal{P}) = 0$, the system is in the confining phase. The Polyakov loop is defined as

$$\mathcal{P} = \mathcal{T}\exp\left[i\int_0^\beta dt A_0^a \frac{\lambda^a}{2}\right]. \tag{36}$$

In the case under consideration, which is specified by Eq. (11), the potential A_0 is directed along the third axis in color space. Therefore, $\mathrm{tr}_F(\mathcal{P}) = 2\cos(\beta g A_0/2)$. The condition $\mathrm{tr}_F(\mathcal{P}) = 0$ is obviously satisfied at $\beta g A_0 = \pi$. Thus, the alternating minima of the effective potential for $T < T_{\mathrm{cr}}$ correspond to the confining and deconfining phases.

4. QUARK CONTRIBUTION TO THE FREE-ENERGY DENSITY

Here, we consider the quark contribution to the free-energy density in a way similar to that used in Section 3 for gluons. The degeneracy multiplicity of quark energy levels in an external chromomagnetic field is proportional to the quark color charge, which is $\pm 1/2$; the corresponding degeneracy multiplicity is controlled by the quantity $gHL^2/(4\pi)$, which is half of that for the gluons. Substituting (15) into (10), we obtain the effective potential for the quarks and antiquarks in the form

$$N_f^{-1}\nu^q = -\frac{gH}{4\pi\beta}\sum_{l=-\infty}^{+\infty}\sum_{n=0,\lambda=\pm1}^{\infty}\ln\left\{\left[\frac{\pi(2l+1)}{\beta} + \frac{\lambda}{2}gA_0\right]^2 + gHn + m^2\right\}, \tag{37}$$

where $\lambda = \pm 1$ relates to the quark color charge. This spectrum differs from the gluon spectrum by the absence of the tachyon mode, which is peculiar to non-Abelian gauge fields in a chromomagnetic field. Therefore, ν^q appears to be a well-defined function of the condensate fields over the entire domain $0 < gH < \infty$, $0 < gA_0 < \infty$. Specifically, we have

$$N_f^{-1}\nu^q = -\frac{gH}{2\pi}\sum_{n=0}^{\infty}\left\{\omega_n + \frac{1}{\beta}\ln\left[1 + e^{-2\beta\omega_n} + 2e^{-\beta\omega_n}\cos\left(\frac{\beta g A_0}{2}\right)\right]\right\}, \tag{38}$$

where

$$\omega_n^2 = gHn + m^2. \tag{39}$$

It is well known that, within nonzero-temperature theory, the quark field satisfies the antiperiodicity condition $\psi(x_0, \mathbf{x}) = -\psi(x_0 + \beta, \mathbf{x})$. This is the reason why, in (38), the period in gA_0 is $4\pi T$, which is twice as large as that in (23). This fact suggests the breakdown of the residual gauge symmetry corresponding to $\mathbb{Z}_2$ group [$\mathbb{Z}_N$ in the case of the $SU(N)$ gauge group]. We restrict our consideration to the chiral limit for quark fields, $m = 0$. In this case, the zero-temperature contribution of the quarks is given by

$$N_f^{-1}\nu^q_{T=0} = -\frac{gH}{2\pi}\sum_{n=1}^{\infty}\sqrt{gHn} = \frac{(gH)^{3/2}}{8\pi^2}\zeta\left(\frac{3}{2}\right), \tag{40}$$

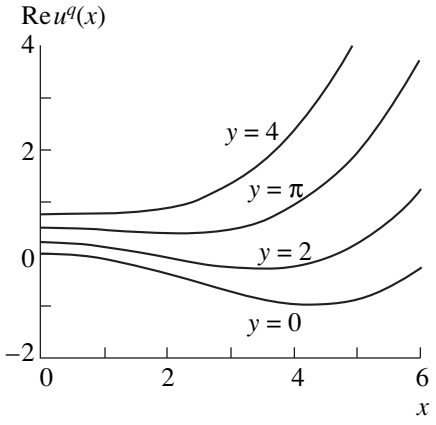

Fig. 5. Quark contribution Re$u^q(x)$.

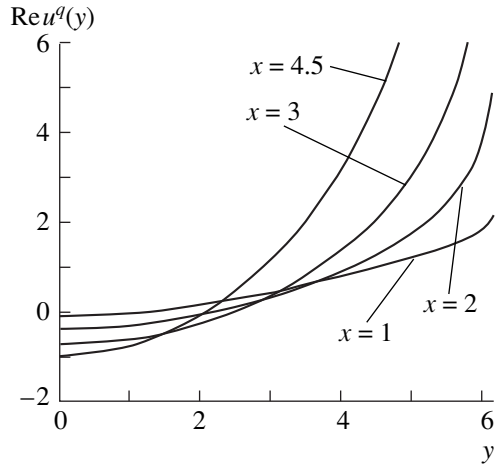

Fig. 6. Quark contribution Re$u^q(y)$.

which coincides with the result from [20]. In contrast to the gluon potential $v^g_{T=0}$, $v^q_{T=0}$ is always positive, which prevents the emergence of a nontrivial minimum. By applying the proper-time method, we rewrite the temperature-dependent part of (38), v^q_T, in the form of the integral representation

$$N_f^{-1} v^q_T = \frac{gH}{2\pi^{3/2}} \int_0^\infty \frac{ds}{s^{3/2}} \times \sum_{l=1}^{\infty} \exp\left(-\frac{\beta^2 l^2}{4s}\right) \frac{\cos(\beta g A_0 l/2 + \pi l)}{1 - e^{-sgH}}. \quad (41)$$

In the limit $gH \longrightarrow 0$, this yields

$$N_f^{-1} v^q_{T,H=0} = \frac{2T^3}{\pi} \sum_{l=1}^{\infty} (-1)^l \frac{\cos(\beta g A_0 l/2)}{l^3}. \quad (42)$$

By virtue of the definition in (33), the dimensionless effective potential $u^q(x, y)$ does not depend on temperature explicitly. Figures 5 and 6 present the families of the plots for u^q at fixed field values y = const and x = const, respectively. It can be seen that, for all constant values of x, the function $u^q(x, y)$ achieves a minimum at $y_{\min} = 0$. At the same time, there exists a nontrivial minimum at $x_{\min} \neq 0$ for $y_{\min}$ = const < 3.5. The global minimum of the quark effective potential is achieved at the point $x = 4.30$, $y = 0$. The quark contribution to the free-energy density exceeds the gluon contribution at $y > 4$, in which case the quark zero mode, increasing indefinitely for $y \longrightarrow 2\pi$, becomes dominant. Therefore, the conclusions concerning the presence of a field condensate and the occurrence of confinement–deconfinement phase transitions for $0 \leq y \leq \pi$ remain in force for the total free energy.

5. CONCLUSION

In the one-loop approximation, the quark and gluon contributions to the thermodynamic potential (free energy) in (2 + 1)-dimensional spacetime at finite temperatures have been calculated against the background of a constant uniform chromomagnetic field H and a constant uniform A_0 condensate. An analysis of the tachyon mode in the energy spectrum of gluons has enabled us to conclude, in contrast to the results from [20], that this mode cannot be neglected. The inclusion of the one-loop radiative correction to the energy spectrum of gluons has made it possible to correct the zero-mode-induced nonanalytic behavior of the effective potential. The free-energy minimum has been investigated, and the possibility of its formation at nonzero values of the strength H and the potential A_0 has been demonstrated. An analysis of the temperature dependence of the results has revealed that, below some critical temperature, the region of the model parameters splits into a set of alternating subregions corresponding to a confining or a deconfining phase. This pattern is associated with the oscillating contribution of the tachyon mode to the free-energy density. Unfortunately, the imaginary part of the effective potential does not vanish at the points $x_{\min} \simeq \pi n$, $n \in \mathbb{N}$, where the function $V(x, y)$ achieves a minimum. Thus, the nontrivial minimum induced in the effective potential by the condensates of the fields H and A_0 is unstable. Such an instability is due to the choice of the model of a uniform vacuum field. It is reasonable to assume that, in the realistic case of a nonuniform vacuum field at large distances (that is, in the infrared region, which is responsible for the formation of confinement), this instability would be suppressed (see also the relevant arguments in [11]). In this connection, the states found here can be considered to be quasistable. In order to justify the adopted assumptions more rigorously, it is necessary to analyze the nonuniform-field model and to take into account higher loop contributions along the lines adopted in [16]. Unfortunately, we have not been

able to do this at present because of obvious technical difficulties.

REFERENCES

1. S. Deser, R. Jackiw, and S. Templeton, Ann. Phys. (N.Y.) **140**, 372 (1982).
2. S. M. Carroll, G. B. Field, and R. Jackiw, Phys. Rev. D **41**, 1231 (1990).
3. V. Ch. Zhukovsky and D. Ebert, in *Proceedings of the 31st International Symposium Ahrenshoop on the Theory of Elementary Particles, Buckow, 1997*, p. 189; D. Ebert and V. Ch. Zhukovsky, Preprint No. HU-EP-97/87, 1997; hep-th/9712016.
4. D. Ebert and V. Ch. Zhukovsky, Mod. Phys. Lett. A **12**, 2567 (1997); hep-ph/9701323.
5. A. S. Vshivtsev, B. V. Magnitskiĭ, V. Ch. Zhukovskiĭ, and K. G. Klimenko, Fiz. Élem. Chastits At. Yadra **29**, 1259 (1998) [Phys. Part. Nucl. **29**, 523 (1998)].
6. V. P. Gusynin, V. A. Miransky, and I. A. Shovkovy, Phys. Lett. B **349**, 477 (1995).
7. K. Kajantie, M. Laine, K. Rummukaine, and M. Shaposhnikov, Nucl. Phys. B **503**, 357 (1997); hep-ph/9704416.
8. A. Niemi and G. Semenoff, Phys. Rev. Lett. **51**, 2077 (1983).
9. I. M. Ternov, V. Ch. Zhukovskiĭ, and A. V. Borisov, *Quantum Mechanics and Macroscopic Effects* (Mosk. Gos. Univ., Moscow, 1993).
10. D. Ebert, V. Ch. Zhukovsky, and A. S. Vshivtsev, Int. J. Mod. Phys. A **13**, 1723 (1998).
11. P. N. Meisinger and M. C. Ogilvie, Phys. Lett. B **407**, 297 (1997).
12. H. Reinhardt, Mod. Phys. Lett. A **11**, 2451 (1996); hep-th/9602047; Nucl. Phys. B **503**, 505 (1997); hep-th/9702049.
13. N. Weiss, Phys. Rev. D **24**, 475 (1981).
14. A. O. Starinets, A. S. Vshivtsev, and V. Ch. Zhukovsky, Phys. Lett. B **322**, 403 (1994).
15. V. V. Skalozub, Int. J. Mod. Phys. A **11**, 5643 (1996).
16. V. Skalozub and M. Bordag, hep-ph/9905302.
17. V. M. Belyaev, Phys. Lett. B **241**, 91 (1990).
18. V. M. Belayev and V. L. Eletsky, Z. Phys. C **45**, 355 (1990).
19. V. V. Skalozub, Mod. Phys. Lett. A **7**, 2895 (1992); O. A. Borisenko, J. Bohacik, and V. V. Skalozub, Fortschr. Phys. **43**, 301 (1995).
20. H. D. Trottier, Phys. Rev. D **44**, 464 (1991).
21. A. P. Prudnikov, Yu. A. Brychkov, and O. I. Marichev, *Integrals and Series* (Nauka, Moscow, 1981; Gordon and Breach, New York, 1986).
22. A. M. Polyakov, Phys. Lett. B **72B**, 477 (1978).
23. L. Susskind, Phys. Rev. D **20**, 2610 (1979).

Translated by O. Chernavskaya

Physics of Atomic Nuclei, Vol. 64, No. 1, 2001, pp. 140–142. Translated from Yadernaya Fizika, Vol. 64, No. 1, 2001, pp. 143–146.

ELEMENTARY PARTICLES AND FIELDS
Theory

Decay of a Large-Amplitude Bubble of a Disoriented Chiral Condensate

T. I. Belova*, V. A. Gani[1), **], and A. E. Kudryavtsev***

Institute of Theoretical and Experimental Physics, Bol'shaya Cheremushkinskaya ul. 25, Moscow, 117259 Russia

Received March 15, 2000

Abstract—The time evolution of a large-amplitude bubble of a disoriented chiral condensate (DCC) is studied. It is found that the evolution of such objects may have a relatively long predecay stage. A simple explanation of such a delay is proposed for the case of the DCC bubble decay. This delay is associated with the existence of approximate multisoliton solutions to the relevant radial sine-Gordon equation in (3+1) dimensions at a large bubble radius. © *2001 MAIK "Nauka/Interperiodica".*

In our previous study [1], we discussed the time evolution of bubbles of a disoriented chiral condensate (DCC) in a simplified chiral two-component sigma model ($\sigma^2 + \pi^2 = f_\pi^2$), where it is convenient to introduce the field variable ϕ defined by the relations $\pi = f_\pi \sin\phi$ and $\sigma = f_\pi \cos\phi$. The equation of motion in terms of ϕ—this equation was studied in [1]—has the form

$$\phi_{tt} - \phi_{rr} - \frac{2}{r}\phi_r + \frac{m^2}{n}\sin(n\phi) = 0, \qquad (1)$$

where $\phi \in [0, 2\pi]$, m is the mass of the field ϕ, and n is an integer. If $m = 0$, we have the case of unbroken chiral symmetry. If $m \neq 0$, chiral symmetry is broken. In the case of $n = 1$, the theory has the only vacuum state at $\phi = 0$. In terms of the field variable ϕ, the field configuration corresponding to a DCC bubble is the following: ϕ is a nonzero constant (vacuum is disoriented) everywhere within a spherically symmetric domain and is zero (true vacuum—that is, $\langle\sigma\rangle = 1$, $\langle\pi\rangle = 1$, and $\phi = 0$) everywhere outside this domain. In the model with $n = 1$, the decay of such a DCC bubble eventually leads to the formation of a breather [1, 2], which is located at the center of the original bubble. The formation of long-lived breatherlike states is a feature peculiar to a wide class of nonlinear systems, including that described by Eq. (1). It is worth noting that, owing to the nonlinearity of the problem, the mean lifetime of a large-amplitude DCC bubble significantly exceeds the lifetime of a linearized DCC system in the presence of external sources (see, for example, [3]).

The case of $n \geq 2$ corresponds to the theory featuring n degenerate vacua at $\phi = 0, 2\pi/n, 4\pi/n, \ldots, 2(n-1)\pi/n$. It was shown in [1] that, in this case, the evolution of a DCC bubble crucially depends on its initial amplitude. The case of a small amplitude for $n \geq 2$ also leads to the formation of a breatherlike state. However, an initially formed large-amplitude bubble evolves in somewhat different way. Its evolution involves a rather long predecay stage characterized by relatively low radiation. This first stage of the evolution consists in the splitting of the shell of the initial bubble into a few concentric subshells of different radii and smaller amplitudes. At the next step, these subshells interact, with the result that eventually the bulk of the initial-bubble energy is converted into radiation of small-amplitude waves that is accompanied by the formation of a long-lived breather localized at the center. This, rather complicated, pattern of the evolution of a DCC bubble may be dubbed a delayed decay of such an object. Here, we continue our investigation of the decay of DCC bubbles for the special initial conditions

$$\phi(r, 0) = \frac{2\pi}{1 + (r/r_0)^K}, \quad \phi_t(r, 0) \equiv 0, \qquad (2)$$

where K is a large positive number set to 20 in our calculations. As was discussed in [1], the evolution of a bubble crucially depends on the dimensionless parameter $\xi = mr_0$. For the case of small $\xi < \xi_{cr}$ in the model with $n = 2$, we observe a prompt decay of DCC bubbles that is followed by the formation of a breatherlike solution. But for $\xi > \xi_{cr}$, we have the splitting of the initial 2π shell into a pair of 1π shells. A clear illustration of the transition from prompt to delayed decay is provided by the data in Fig. 1, which displays the energy flux through the sphere of radius $R > r_0$ in units of the total energy at two typical instants of time as a function of the parameter ξ. From this figure, we can see the following: at $\xi < \xi_{cr}$, the bulk of the energy release is emitted from the region of the bubble within a relatively

[1)] Moscow State Engineering Physics Institute (Technical University), Kashirskoe sh. 31, Moscow, 115409 Russia, and Institute of Theoretical and Experimental Physics, Bol'shaya Cheremushkinskaya ul. 25, Moscow, 117259 Russia.

* e-mail: belova@vxitep.itep.ru

** e-mail: gani@heron.itep.ru

*** e-mail: kudryavtsev@heron.itep.ru

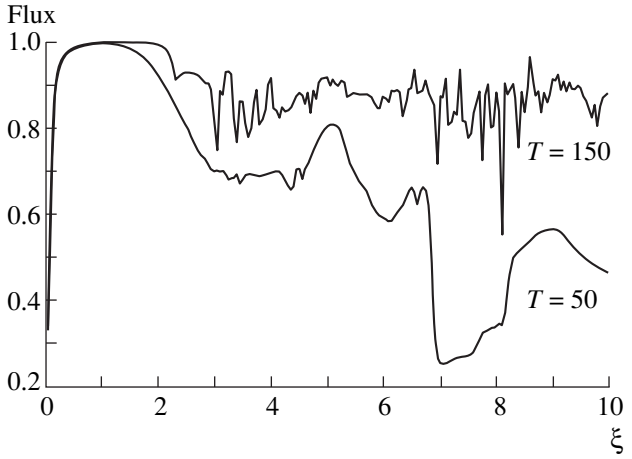

Fig. 1. Energy flux (in units of the total energy) that has passed through a sphere of radius $R = 20$ by the instant T as a function of the dimensionless parameter ξ.

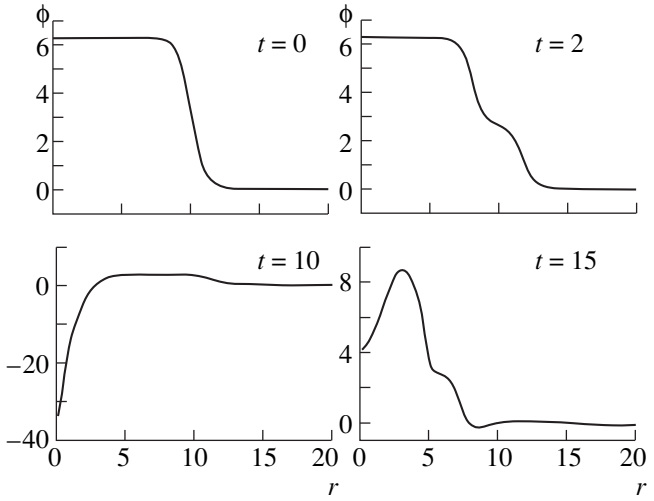

Fig. 2. Field configurations at a few instants t_i during the evolution of the initial configuration (2) in the model with $n = 2$.

short time interval T of less than 50 (in dimensionless units), while, at $\xi > \xi_{cr}$, only some part of it escapes through the sphere of the same radius within the same period of time. It is this phenomenon that we call the delayed decay of a DCC bubble. In Fig. 2, we present the field configurations ($n = 2$, $\xi = 10$) at some instants t_i. We can see that the further evolution of the 1π shells produced upon the splitting of the 2π shell leads to their secondary interaction. This interaction is of a repulsive character and occurs when the radii of the shells coincide. After a few collisions of the 1π shells, a localized breatherlike solution is formed at the center of the initial DCC bubble.

Qualitatively, the observed splitting of the 2π shell of the initial bubble (2) into a pair of concentric 1π-shells can be explained as follows. Suppose that, at a sufficiently large bubble radius r_0, the term $(2/r)\phi_r$ on the left-hand side of Eq. (1) becomes immaterial and can be discarded. Equation (1) then reduces to the one-dimensional sine-Gordon equation defined on the semiaxis $r \in [0, \infty)$. Therefore, solutions to this equation at large positive r must have the same form as solutions to the integrable sine-Gordon equation. Multisoliton solutions to the latter equation are known in an analytical form. In particular, the two-soliton solution for $n = 2$ is given by [4]

$$\phi(x, t) = 2\arctan\left(\frac{v\sinh(mx/\sqrt{1-v^2})}{\cosh(mt/\sqrt{1-v^2})}\right), \qquad (3)$$

where v is the soliton velocity at infinity. At an arbitrary instant t, this solution appears to be a superposition of two solitons, with the quantity

$$\phi(+\infty, t) - \phi(-\infty, t) \equiv 2\pi,$$

which is referred to as a topological charge, being an integral of the motion. At $t = 0$, the solution in (3) reduces to a step of height 2π and characteristic size $x_{char} \sim \sqrt{1-v^2}/mv$. In the relativistic limit $(1 - v) \ll 1$, the size x_{char} is small, $x_{char} \ll m^{-1}$. Owing to the similarity of the profiles of the initial condition (2) for $K \gg 1$ and the solution in (3) at $t = 0$ in the relativistic case, it can be expected that the two configurations will evolve similarly, at least at small positive t. By considering the solution in (3) at $t > 0$, we find that the 2π kink splits into a pair of 1π kinks moving in opposite directions. The same occurs in solving Eq. (1) with the initial condition (2). Therefore, we conclude that a three-dimensional 2π shell of large initial radius behaves in the same way as the double-soliton solution (3), at least at small positive t.

The split 1π shells further evolve differently. The inner 1π bubble behaves as an ordinary large-amplitude DCC bubble in the case of $n = 1$. The evolution of such initial configurations was considered in the pioneering study of Bogolyubskiĭ and Makhan'kov [5] (see also [6]). It shrinks and expands again, emitting part of its energy. The outer 1π shell expands, then stops, and begins to shrink. The maximal expansion radius of this 1π shell can be estimated on the basis of simple energy considerations. Some field configurations arising in the process of interaction of the inner and outer 1π shells are presented in Fig. 2. The splitting of the shell of the initial bubble is also clearly seen in Fig. 3, which displays the radial energy density $\varepsilon(r)$ related to the total energy by the equation $E = \int_0^\infty \varepsilon(r)dr$.

In a numerical simulation, we also observed a similar splitting of the 2π shell (2) of the initial DCC bubble in the model with $n = 3$. In this case, the initial 2π shell first splits into two subshells of amplitudes $2\pi/3$ and $4\pi/3$; later on, the $4\pi/3$ shell splits into a pair of $2\pi/3$

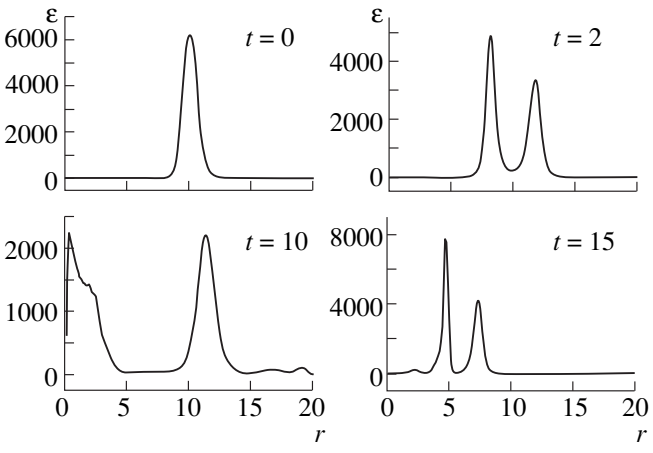

Fig. 3. Radial energy densities corresponding to the field configurations in Fig. 2.

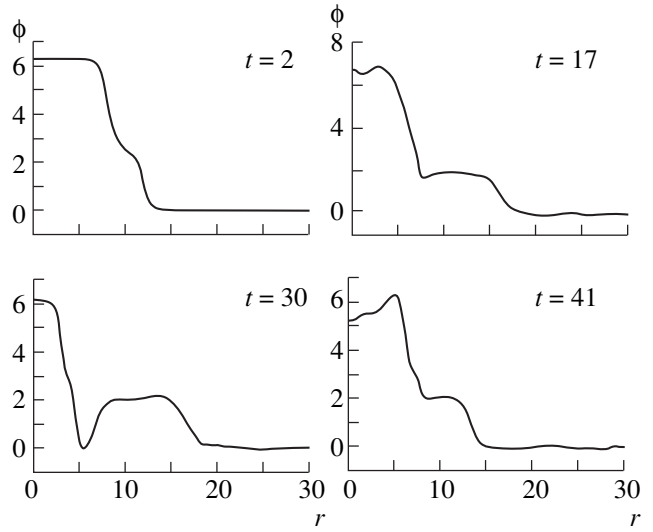

Fig. 4. Field configurations at a few instants t_i during the evolution of the initial configuration (2) in the model with $n = 3$.

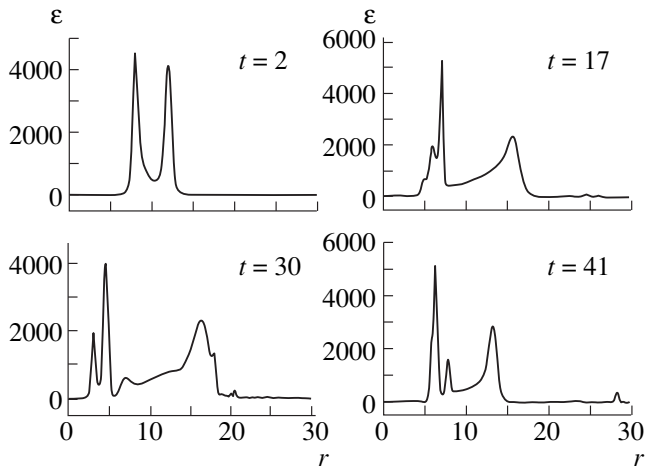

Fig. 5. Radial energy densities corresponding to the field configurations in Fig. 4.

shells. During the subsequent evolution, all three $2\pi/3$ shells interact. The corresponding field configurations and radial energy densities at a few typical instants are shown in Figs. 4 and 5.

We note that, in fact, the discarded term $(2/r)\phi_r$ in Eq. (1) has a pronounced effect on the time evolution of the solutions—in particular, it is responsible for instability of the bubbles to collapse. It is convenient to study the evolution of such configurations by the method of effective Lagrangians. The collapse of a spherically symmetric bubble in $\lambda\phi^4$ theory was first analyzed by this method in the thin-wall approximation [7] (see also [8]). In the future, we are going to study the form of the effective Lagrangian and the corresponding equations of motion for multishell configurations considered in the present article.

In conclusion, we emphasize that the observed splitting of the large-size and large-amplitude shell of an original DCC bubble leads to a significant increase in its lifetime. For this reason, the emission of waves from the DCC region appears to be quite a long process, and it is the nonlinearity of DCC bubble decay that is basically responsible for the prolongation of the bubble lifetime.

ACKNOWLEDGMENTS

This work was supported in part by the Russian Foundation for Basic Research (project nos. 98-02-17316 and 96-15-96578). The work of V.A. Gani was also supported by INTAS (grant no. 96-0457) within the research program of the International Center for Fundamental Physics in Moscow.

REFERENCES

1. V. A. Gani, A. E. Kudryavtsev, and T. I. Belova, Yad. Fiz. **62**, 956 (1999) [Phys. At. Nucl. **62**, 895 (1999)].
2. J. Hormuzdiar and S. Hsu, Phys. Rev. C **59**, 889 (1999).
3. G. Amelino-Camelia, J. D. Bjorken, and S. E. Larsson, Phys. Rev. D **56**, 6942 (1997).
4. R. Rajaraman, *Solitons and Instantons: An Introduction to Solitons and Instantons in Quantum Field Theory* (North-Holland, Amsterdam, 1982; Mir, Moscow, 1985).
5. I. Bogolyubskiĭ and V. Makhan'kov, Pis'ma Zh. Éksp. Teor. Fiz. **25**, 120 (1977) [JETP Lett. **25**, 107 (1977)].
6. T. I. Belova and A. E. Kudryavtsev, Usp. Fiz. Nauk **167**, 377 (1997) [Phys. Usp. **40**, 359 (1997)].
7. Ya. B. Zel'dovich, I. Yu. Kobzarev, and L. B. Okun', Zh. Éksp. Teor. Fiz. **67**, 3 (1974) [Sov. Phys. JETP **40**, 1 (1975)].
8. M. B. Voloshin, I. Yu. Kobzarev, and L. B. Okun', Yad. Fiz. **20**, 1229 (1974) [Sov. J. Nucl. Phys. **20**, 644 (1975)].

Translated by S. Slabospitsky

Physics of Atomic Nuclei, Vol. 64, No. 1, 2001, pp. 143–150. Translated from Yadernaya Fizika, Vol. 64, No. 1, 2001, pp. 147–155.

ELEMENTARY PARTICLES AND FIELDS
Theory

Formation of Dense Groups of Particles in Intermediate-Energy Nucleus–Nucleus Collisions

G. L. Gogiberidze[1], L. K. Gelovani[1], and E. K. Sarkisyan[2]

Joint Institute for Nuclear Research, Dubna, Moscow oblast, 141980 Russia

Received August 13, 1999

Abstract—The formation of dense groups (fluctuations) of particles produced in the central CCu and MgMg collisions at the projectile momenta of, respectively, 4.5 and 4.3 GeV/*c* per nucleon is analyzed. The distributions of the maximum densities and of the centers of charged-particle fluctuations in pseudorapidity space are studied in searches for dynamical multiparticle correlations. The distributions of the centers show two peaks above the statistical background with a structure similar to that which is expected in the model of coherent gluon emission and which was observed in hadronic interactions. The charge independence of the distributions in question and an azimuthal isotropy of events involving pseudorapidity fluctuations are observed. The distributions of events with respect to the maximum density of fluctuations are governed primarily by the statistical contribution, although the behavior of the distributions in CCu collisions is in qualitative agreement with the prediction of the one-dimensional intermittency model. It is found that the resulting distributions are of a non-Poisson character both in CCu and in MgMg collisions. The results of this study indicate that, in describing local dynamical fluctuations in multiparticle production processes, the coherent and the stochastic approach supplement each other. The procedure employed in the analysis described here makes it possible to draw a direct comparison of the present results with the results of similar investigations of different reactions. © *2001 MAIK "Nauka/Interperiodica".*

1. INTRODUCTION

Recent numerous investigations of the formation of dense groups of particles in the distributions of hadrons produced in multiparticle processes [1, 2] led to the conclusion that irregularities observed in these distributions reflect process dynamics rather than the inadequacy of event statistics. The formation of such dynamical fluctuations was found to be of a regular character; that is, dense groups of particles appear at fixed values of the polar angle (pseudorapidity), thus producing ring-shaped events.

Ring-shaped structures can be revealed owing to the presence of maxima on the pseudorapidity scale in searches for dense groups of particles in an event. Such events were first observed in cosmic-ray experiments and later in accelerator experiments [2]. It is worth noting that the azimuthal-angle and transverse-momentum distributions in such events are usually rather uniform.

Further investigations of irregularities in the distributions of product particles were performed primarily within the stochastic approach relying on the intermittency model borrowed from fluid dynamics (for an overview, see [1, 2]). This approach made it possible to reveal a dynamical character of the fluctuations in question, which suggests the intermittency (fractal) structure of events in all types of interactions [2, 3]. Nevertheless, the observed stochastic nature of the fluctuations has not yet been explained, although numerous dynamical models have been proposed.

At the same time, the ring-shaped structure is well known in electrodynamics (Cherenkov radiation). Conditions necessary for the emergence of such radiation may be realized in the strong interactions of hadrons and nuclei as well [4, 5]. This approach was implemented in the model that assumes coherent gluon emission from a finite length [5] and which predicts an interference peak in the polar-angle distributions for collisions of a quark with an antiquark or a gluon. On the other hand, collisions between quarks of the same color are expected to result in the appearance of dips in the distribution (destructive interference). Experimental results from [6–8], which were obtained on the basis of this model, lend support to this quark-parton description.

In this article, we present an analysis of ring-shaped events in intermediate-energy nucleus–nucleus collisions. Our study employs both the stochastic and the coherent approach. In the first case, we rely on the one-dimensional intermittency model [9], which considers maximum particle fluctuations. The coherent component in the hadron-production process is investigated within the coherent-gluon-emission model, which considers the properties of the distributions of fluctuation centers.

It is worth noting that previous searches for dynamical effects in studying maximum fluctuations yielded

[1] Institute of Physics, Georgian Academy of Sciences, ul. Tamarashvili 6, GE-380077 Tbilisi, Republic of Georgia.
[2] School of Physics and Astronomy, Tel Aviv University, Tel Aviv 69978, Israel.

different results [10, 11]. Specifically, no such effects were revealed in [10], where investigations were conducted for reactions similar to those considered here. At the same time, Ghosh *et al.* [11] found indications of multiparticle dynamical correlations in collisions of hadrons with emulsion nuclei at 200–400 GeV. The distinctions between these conclusions may be associated with the method used to single out maximum fluctuations, which reduces the searches for dense clusters to exploring the distribution sections with the maximum probability density (maximum in the distribution). In order to circumvent these difficulties, we use here, both for the stochastic and for the coherent contribution, a cumulative variable that has a uniform distribution [12].

2. EXPERIMENTAL DATA

The experimental data subjected to analysis were obtained by processing the photographs of events from the 2-m streamer chamber of the SKM-200 facility [13] involving internal copper (^{64}Cu) and magnesium (^{24}Mg) targets. The chamber was placed in a magnetic field of strength 0.8 T and irradiated at the JINR synchrophasotron with relativistic beams of ^{12}C nuclei with a momentum of 4.5 GeV/*c* per nucleon and ^{24}Mg nuclei with a momentum of 4.3 GeV/*c* per nucleon. The streamer chamber was driven by a central-collision trigger that actuated the chamber when, in the forward cone with an apex angle of the 2.4°, there were no charged particles with momenta above 3 GeV/*c*. A more detailed description of the facility can be found in [13, 14]. Systematic errors associated with the operation of the trigger, the detection of low-energy pions and protons, electron admixtures, secondary interactions in the target, and other sources of systematic effects are described in detail elsewhere [15]. Each of these systematic effects is modest, their total contribution to the uncertainty being within 3%.

The film data were viewed and processed at the Lebedev Institute of Physics (Moscow, Russian Academy of Sciences) on the UPS 50/80 scanning tables by using the method developed in [16]. The average relative error of momentum measurements, $\langle \varepsilon_p/p \rangle$, amounted to 12%; for the polar emission angle ϑ, the error ε_ϑ was about 2°, which does not exceed the error in the pseudorapidity measurement ($\varepsilon_\eta = 0.1$), the pseudorapidity being defined as $\eta = -\ln\tan(\vartheta/2)$. Among 663 events of CCu collisions, we selected charged particles in the pseudorapidity interval $\Delta\eta = 0.2$–2.8 (in the laboratory frame), but we excluded, from our consideration, positively charged particles with transverse momenta in excess of 1 GeV/*c*, because no negatively charged particles with such transverse momenta were observed. We assumed equal numbers of positively and negatively charged particles, thereby minimizing the effect of the proton contribution. The mean multiplicity in CCu collisions was 22.8 ± 0.3. In 14218 MgMg events, we considered only negatively charged particles (pions with a 1%, admixture of kaons), their mean multiplicity in the interval $\Delta\eta = 0.4$–2.4 being 6.20 ± 0.02.

3. PROCEDURE FOR ISOLATING DENSE GROUPS OF PARTICLES

In the present study, fluctuations and their centers were singled out by means of the following procedure. In each event, ordered pseudorapidities were subjected to binning over the entire pseudorapidity interval $\Delta\eta$ under consideration, with the bin size $\delta\eta$ being fixed. We isolated dense groups featuring δn particles in a given bin. The centers of fluctuations for all events were calculated by the formula

$$\eta_0 = (1/\delta n)\sum_{j=1}^{\delta n}\eta_j.$$

As was mentioned earlier, the conclusion on the contribution of dynamical fluctuations strongly depends on the shape of the pseudorapidity spectrum, its nonuniformity complicating isolation of the η region where interaction dynamics reveals itself most clearly. In order to get rid of the effect of the spectrum shape and to be able to compare the results of different experiments, the pseudorapidity distributions were recast into distributions with respect to a cumulative variable $\tilde{\eta}$ according to the method proposed in [12],

$$\tilde{\eta}(\eta) = \int_{\eta_{\min}}^{\eta}\rho(\eta')d\eta' \Big/ \int_{\eta_{\min}}^{\eta_{\max}}\rho(\eta')d\eta', \qquad (1)$$

with the transformed probability density $\rho(\tilde{\eta})$ that is constant in the interval [0, 1]. This transformation was used earlier in studying intermittency in high-energy particle collisions [1, 2] and in [17–19]. The application of the cumulative variable [18, 19] made it possible to separate two essentially different types of fluctuations, which are leveled out upon averaging over various pseudorapidity bins, and to trace hints as to the occurrence of a possible nonequilibrium phase transition in the hadronization process. It should be noted that the pseudorapidity is the most appropriate variable for studying correlations governed by the intermittency structure in high-energy interactions [20].

4. RESULTS AND DISCUSSION

4.1. Distributions of the Fluctuation Centers

Figure 1 displays the distributions of the centers of dense particle groups in CCu interactions for various bins $\delta\tilde{\eta}$ and various numbers of particles, δn, in a bin. We chose the bin widths $\delta\tilde{\eta}$ to be commensurate with those in [10, 21].

A structure with many peaks is seen for $\delta\tilde{\eta} = 0.04$ ($\delta\eta \approx 0.1$) and $\delta\tilde{\eta} = 0.08$ ($\delta\eta \approx 0.2$) in Figs. 1*a* and 1*b*,

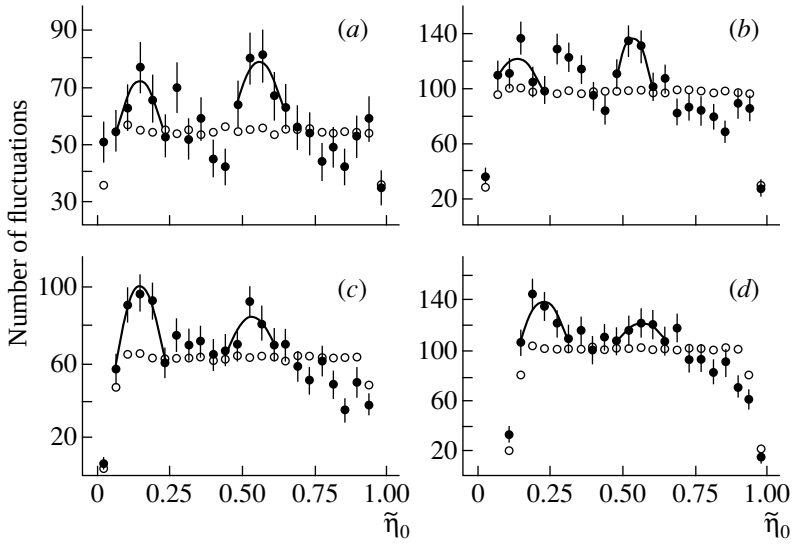

Fig. 1. Experimental (closed circles) and generated (open circles) distributions of fluctuation centers in CCu interactions at (*a*) $\delta\tilde{\eta} = 0.04$ and $\delta n = 4$, (*b*) $\delta\tilde{\eta} = 0.08$ and $\delta n = 5$, (*c*) $\delta\tilde{\eta} = 0.12$ and $\delta n = 7$, and (*d*) $\delta\tilde{\eta} = 0.2$ and $\delta n = 9$. The solid curves represent Gaussian approximations.

respectively. With increasing width $\delta\tilde{\eta}$, there is a tendency toward the formation of a structure featuring two peaks whose centers $\tilde{\eta}_0$ do not change with δn. For the mean positions of the maxima for groups involving different numbers of particles, a Gaussian approximation of these two peaks yields values in the vicinity of the points $\tilde{\eta}_0 = 0.17$ and 0.57. The rescaling to the original variable η results in $\eta_0 = 0.60 \pm 0.05 \pm 0.12$ and $1.30 \pm 0.03 \pm 0.10$ (hereafter, the first and the second error are statistical and systematic, respectively) for the peak positions. The spacing between the peaks is

$$d_0 = 0.68 \pm 0.06 \pm 0.16. \quad (2)$$

A similar investigation was performed for MgMg interactions, where tracks were measured only for negatively charged particles. The $\tilde{\eta}_0$ distributions are displayed in Fig. 2, where the notation used is identical to that in Fig. 1. As in the case of CCu interactions, we observe a structure having two peaks at the points $\tilde{\eta}_0 \approx 0.19$ and 0.63, which corresponds to $\eta_0 = 0.89 \pm 0.03 \pm 0.08$ and $1.63 \pm 0.05 \pm 0.10$, with the spacing between the peaks being

$$d_0 = 0.75 \pm 0.06 \pm 0.13. \quad (3)$$

That the structures of $\tilde{\eta}_0$ distributions for negatively charged particles and for all charged particles are similar suggests the charge independence of the destructive-interference effect. At the same time, the close values of the spacings between the peaks in (2) and (3) are indirect evidence for a central character of the selected CCu events in collisions and, hence, for the correctness of the selection criteria described in Section 2.

In order to reveal the possible contribution of hadron jets to the observed effect, we performed an additional analysis for MgMg interactions, taking into account the isotropy criterion for the azimuthal distribution of particles. For an *n*-particle event, the azimuthal asymmetry was defined as [22]

$$\beta = \frac{\sum_{i>j}^{n} \cos 2(\phi_i - \phi_j)}{\sqrt{n(n-1)}}, \quad (4)$$

where ϕ_i is the azimuthal angle of the emission of the *i*th particle.

Events characterized by the jet structure were removed by imposing the constraint $\beta < 0$, which reduced event statistics nearly by a factor of 2. The resulting distributions of the fluctuation centers (for the same $\delta\tilde{\eta}$ and δn as in Fig. 2, which show data subjected to no criterion of azimuthal isotropy) are displayed in Fig. 3.

The structure of the distributions in Fig. 3 is similar to that in Fig. 2: we again observe two pronounced peaks. For the positions of the peaks and the spacing between them, a Gaussian approximation of the spectra yields $\eta_0 \approx 0.88$ and 1.63; $d_0 = 0.75 \pm 0.06 \pm 0.15$.

Thus, the removal of narrow-jet events did not affect the structure of the distribution of the fluctuation centers. The agreement between the peak positions and spacing in the distributions constructed with and without the β criterion confirms the azimuthal symmetry of ring-shaped events.

The two-peaked spectrum that we obtained for central nucleus–nucleus collisions is similar to that found in [6, 7] for proton–proton interactions. This suggests

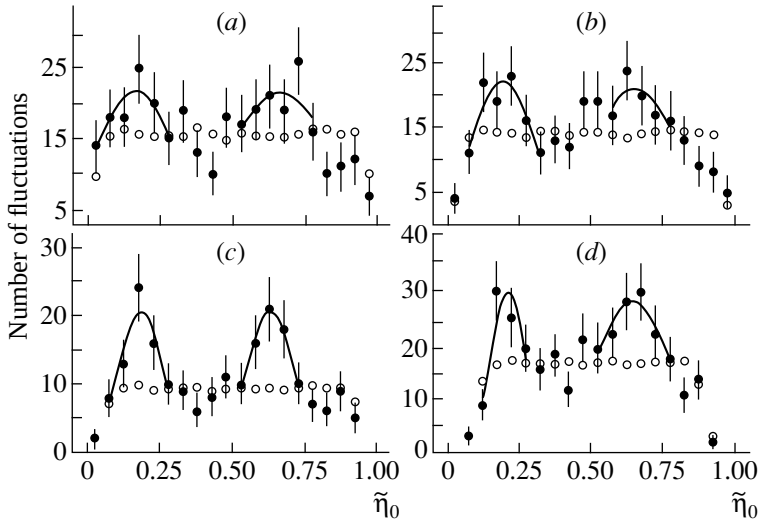

Fig. 2. Experimental (closed circles) and generated (open circles) distributions of fluctuation centers in MgMg interactions at (*a*) $\delta\tilde{\eta} = 0.05$ and $\delta n = 4$, (*b*) $\delta\tilde{\eta} = 0.1$ and $\delta n = 5$, (*c*) $\delta\tilde{\eta} = 0.15$ and $\delta n = 6$, and (*d*) $\delta\tilde{\eta} = 0.25$ and $\delta n = 7$. The solid curves represent Gaussian approximations.

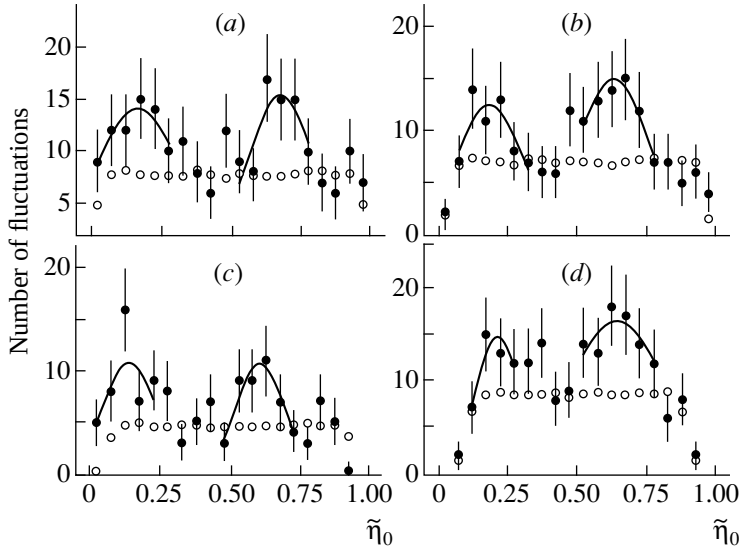

Fig. 3. As in Fig. 2, but for events characterized by azimuthal isotropy [see main body of the text and expression (4)].

that nucleus–nucleus collisions represent a superposition of nucleon–nucleon interactions. The spacing between the peaks in our analysis exceeds that in hadronic collisions ($d_0 = 0.57 \pm 0.03 \pm 0.12$ and 0.50 ± 0.15 in proton–proton interactions at 205–360 [6] and 400 GeV/*c* [7], respectively). This observation complies with theoretical expectations that take into account the intranuclear interactions of nucleons [23].

In order to reveal the contribution of dynamical correlations in the distribution of the fluctuation centers, we constructed analogous distributions for the simulated single-particle spectra $\rho(\tilde{\eta})$. Let us describe our simulation procedure. We generated a random number of tracks in accordance with the multiplicity distribution in experimental events. After that, the particles involved were distributed according to the actual spectrum $\rho(\tilde{\eta})$. The total number of events simulated in this way was 66300 for CCu collisions and 1421800 for MgMg collisions, exceeding experimental statistics by a factor of 100. The statistical properties of this event sample fully correspond to the properties of the ensemble that could be constructed by mixing tracks from different events with the same $\rho(\tilde{\eta})$ and comply with the hypothesis of independent-particle emission, where there is no information about two- or multiparticle correlations.

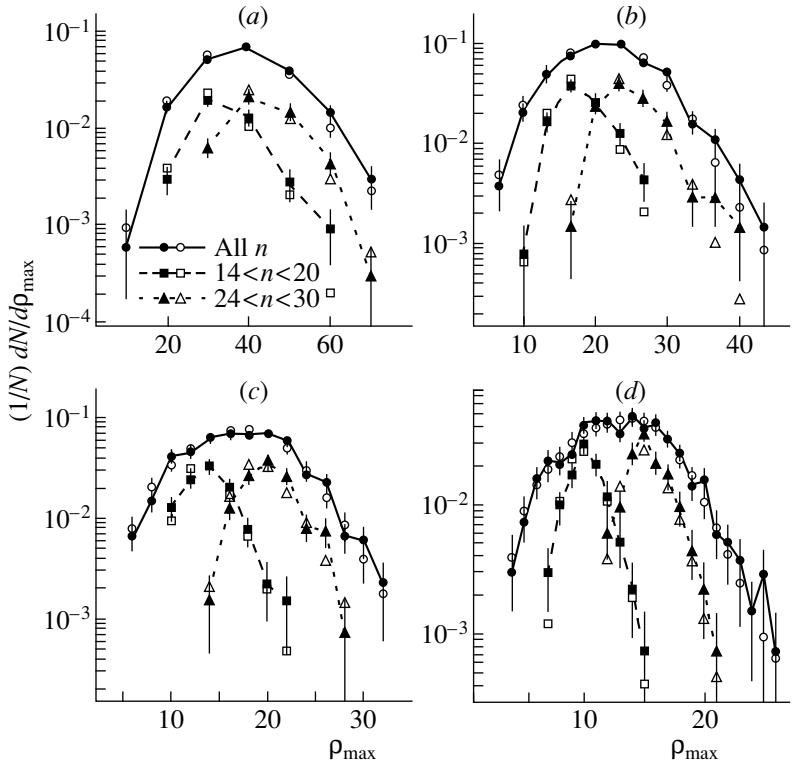

Fig. 4. Experimental (closed symbols) and generated (open symbols) distributions of maximum-density fluctuations ρ_{max} in CCu interactions for three n and various values of $\delta\tilde{\eta}$: (*a*) $\delta\tilde{\eta} = 0.04$, $\chi^2/\mathrm{NDF} \simeq 1.3$ (all n, $\langle\rho_{max}\rangle \simeq 39.4$, rms $\simeq 11.2$), $\chi^2/\mathrm{NDF} \simeq 0.5$ ($14 < n < 20$, 38.6, 8.1), and $\chi^2/\mathrm{NDF} \simeq 0.7$ ($24 < n < 30$, 49.2, 9.0); (*b*) $\delta\tilde{\eta} = 0.12$, $\chi^2/\mathrm{NDF} \simeq 1.2$ (all n, 22.0, 6.6), $\chi^2/\mathrm{NDF} \simeq 1.3$ ($14 < n < 20$, 12.8, 3.6), and $\chi^2/\mathrm{NDF} \simeq 2.0$ ($24 < n < 30$, 25.2, 4.4); (*c*) $\delta\tilde{\eta} = 0.2$, $\chi^2/\mathrm{NDF} \simeq 1.1$ (all n, 17.4, 5.2), $\chi^2/\mathrm{NDF} \simeq 1.0$ ($14 < n < 20$, 14.0, 2.6), and $\chi^2/\mathrm{NDF} \simeq 1.7$ ($24 < n < 30$, 20.2, 2.8); and (*d*) $\delta\tilde{\eta} = 0.4$, $\chi^2/\mathrm{NDF} \simeq 0.9$ (all n, 13.2, 4.2), $\chi^2/\mathrm{NDF} \simeq 0.7$ ($14 < n < 20$, 10.3, 1.6), and $\chi^2/\mathrm{NDF} \simeq 0.9$ ($24 < n < 30$, 18.2, 1.8).

Open circles in Figs. 1–3 represent the $\tilde{\eta}_0$ distributions for simulated events. The figures show that the experimental distributions differ significantly from the distributions obtained under the assumption of noncorrelated particle emission: there are no peaks in the latter case.

Comparing the experimental and the simulated distributions of the fluctuation centers for various widths $\delta\tilde{\eta}$ and various multiplicity values δn, we arrive at the conclusion that multiparticle correlations are of a dynamical origin. In analyzing the dynamics of the intermittency structure being considered, it would be natural to invoke the model of coherent gluon emission [5] as one of the most appropriate mechanisms of the formation of the observed ring-shaped events featuring azimuthal symmetry.

In order to assess the reliability of the above conclusion, we scanned various intervals $\Delta\eta$ and various polar angles ϑ within the experimental error $\langle\varepsilon_\vartheta\rangle$. That the observed properties of the $\tilde{\eta}_0$ distributions did not exhibit significant changes throughout this scanning confirms our conclusion.

The aforementioned charge independence of the coherent mechanism of dynamical-fluctuation formation may lend additional support to the conjecture that Bose–Einstein correlations are of a coherent origin [24].

4.2. Maximum Density Fluctuations

For CCu collisions, Fig. 4 shows the normalized distributions $(1/N)dN/d\rho_{max}$ with respect to maximum density fluctuations ρ_{max} at various values of $\delta\tilde{\eta}$ in. Here, N is the number of events, while the maximum fluctuations are defined as $\rho_{max} = \delta n_{max}/\delta\tilde{\eta}$, where δn_{max} is the maximum number of particles in a fluctuation for a specific bin $\delta\tilde{\eta}$ in an individual event.

A feature peculiar to the distributions being considered is that they decrease exponentially for $\rho_{max} > \langle\rho_{max}\rangle$. The distributions averaged over all multiplicities n behave similarly to the distributions studied by our group in [10, 21] and to the distributions obtained in [11, 25, 26] for different reactions. This behavior differs from the Poisson behavior, which is expected to be realized in processes where the correlations between product hadrons are weak and which is predicted in

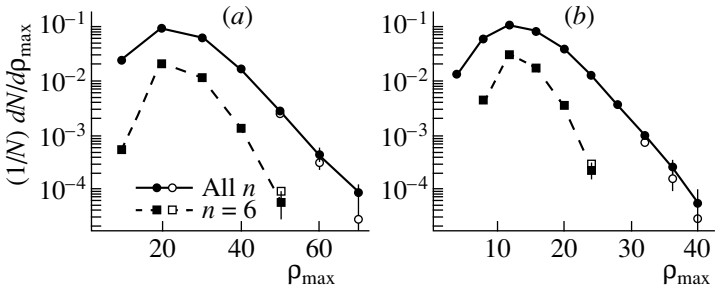

Fig. 5. Experimental (closed symbols) and generated (open symbols) distributions of maximum-fluctuation densities ρ_{max} in MgMg interactions for all n and $n = 6$ for two values of $\delta\tilde{\eta}$: (*a*) $\delta\tilde{\eta} = 0.1$, $\chi^2/\mathrm{NDF} \simeq 2.1$ (all n, $\langle\rho_{max}\rangle \simeq 24.2$, rms $\simeq 19.1$) and $\chi^2/\mathrm{NDF} \simeq 0.4$ ($n = 6$, 23.9, 15.4) and (*b*) $\delta\tilde{\eta} = 0.25$, $\chi^2/\mathrm{NDF} \simeq 2.7$ (all n, 13.8, 10.6) and $\chi^2/\mathrm{NDF} \simeq 0.4$ ($n = 6$, 13.4, 5.7).

the models of the multiperipheral or the Regge type that involve a bounded number of Reggeons. The exponential character of the ρ_{max} spectrum is evidence to suggest that primary multiparticle correlations do not reduce to two-particle correlations [3]. A nonzero difference of the variance and $\langle\rho_{max}\rangle$ confirms a non-Poisson character of distribution, revealing a significant contribution of correlations to the observed local fluctuations.

A comparison with the results presented in [10, 21], where fluctuations were considered in η space, shows that the transformation to the cumulative variable $\tilde{\eta}$ according to (1) does not affect significantly the bell-like shape of the distributions at small $\delta\tilde{\eta}$ (see Fig. 4*a*); with increasing $\delta\tilde{\eta}$, however, the use of $\tilde{\eta}$ instead of η results in the emergence of large tails in the ρ_{max} spectra for $\rho_{max} > \langle\rho_{max}\rangle$ (Figs. 4*b*, 4*c*).

That the exponential maximum-density distribution becomes flatter at large values of ρ_{max} complies with the shape expected in the one-dimensional intermittency model [9], which, in the multiparticle production process, admits a turbulent and a laminar regime generating two maxima in the ρ_{max} distributions. However, the model considers distributions with respect to maximum density fluctuations at a fixed multiplicity n, in which case the distributions are independent of energy and reaction type. As a result, it is possible to enlarge statistics by comparing results from different experiments. Previously, distributions at fixed values of n were studied in hadron–hadron interactions, where $\delta\eta = 0.1$ binning revealed large tails in the ρ_{max} distributions [25].

In order to ensure that the multiplicity was fixed, but that a statistically significant result was obtained, we considered, in CCu interactions, maximum fluctuations averaged over fixed narrow multiplicity intervals. Figure 4 presents the resulting ρ_{max} distributions for two such regions: $14 < n < 20$ (squares) and $24 < n < 30$ (triangles). Here, the deviation of the distributions from the exponential form at large ρ_{max} becomes more pronounced than in the case of averaging over all n. Even at $\delta\tilde{\eta} = 0.04$ ($\delta\eta \approx 0.1$), the distribution develops tails for $\rho_{max} > \langle\rho_{max}\rangle$. Such tails are clearly seen at $\delta\tilde{\eta} = 0.12$ and 0.2, but only for events characterized by large multiplicities, $24 < n < 30$.

In just the same way as the shape of the spectrum for all multiplicities, the distributions for fixed intervals of n indicate that the multiparticle production process is of a non-Poisson character: that the variances of the distributions differ from the mean values $\langle\rho_{max}\rangle$ proves the presence of multiparticle correlations.

In order to reveal correlations associated with the dynamics of the process, we compared the experimental distributions with the distributions that were obtained for the generated sample of 66300 events that was described in the preceding section and which features no dynamical correlations. The resulting distributions (for four values of $\delta\tilde{\eta}$) are shown in Fig. 4 (open symbols) for all multiplicities and for two intervals considered above.

The χ^2/NDF values indicate good agreement between the experimental and the generated spectra, irrespective of the width $\delta\tilde{\eta}$ and multiplicity values, so that it is impossible to draw a definitive conclusion as to whether intermittency dynamics is present in the formation of fluctuations. Most likely, the dynamical correlations in the maximum-density distributions are suppressed by statistical noises to such an extent that they cannot be observed. Nevertheless, it is worth noting that the generated ρ_{max} distributions at $\delta\tilde{\eta} = 0.12$ and 0.2 for $24 < n < 30$ (Figs. 4*b* and 4*c*) differ significantly at large ρ_{max} from the experimental spectra: the latter become flatter, while the former do not show such changes.

A similar analysis was performed for negatively charged particles in MgMg collisions. For all multiplicities and for the fixed multiplicity value of $n = 6$, Fig. 5 displays the resulting ρ_{max} distributions at $\delta\tilde{\eta} = 0.1$ and 0.25.

In contrast to what was observed for CCu collisions, the distributions in Fig. 5 have no tails for $\rho_{max} > \langle\rho_{max}\rangle$; that is, they continue exponentially decreasing as the

maximum density fluctuations grow. At the same time, a comparison of the mean values $\langle \rho_{max} \rangle$ and the standard deviations proves a non-Poisson character of the quoted distributions. However, the χ^2/NDF values for the comparison of the experimental data with the results of our statistical simulation (in the case being considered, we have also used the generated sample of 1421800 events from the preceding section) suggest that the dynamical component in the formation of fluctuations is strongly suppressed by statistical fluctuations and cannot be isolated by the method of maximum densities.

An analysis of the effect of the errors $\langle \varepsilon_\vartheta \rangle$ in the measured polar angle ϑ of product particles showed stability of the distributions that we obtained and, hence, the reliability of our conclusions for both types of nuclear collisions considered here.

In summary, we emphasize that the non-Poisson behavior of the ρ_{max} spectra (especially at small values of $\delta\tilde{\eta}$) and the difference between the experimental and the generated distributions at large values of the maximum density in CCu interactions seem to be associated with a nonstatistical character of the fluctuations in question. It is precisely the result that our group deduced in [17, 18, 27] by the method of normalized scale factorial moments. In [28], it was proposed to seek strong fluctuations associated with this.

5. CONCLUSION

Results have been presented that were obtained by studying the formation of dense particle groups (fluctuations) in multiparticle processes induced by intermediate-energy nucleus–nucleus collisions. These fluctuations have been explored in the pseudorapidity distributions of all charged particles from the central CCu collisions and of negatively charged particles from MgMg collisions at projectile momenta of, respectively, 4.5 and 4.3 GeV/*c* per nucleon.

In order to reveal dynamical collective effects, we have considered the distributions of the centers of dense particle groups and the spectra of maximum density fluctuations. We have compared them with the predictions of the coherent-emission model in the first case and with the predictions of the stochastic model in the second case; a comparison with the simulated results for completely noncorrelated particle production has also been drawn. Taking into account the effect of the shape of the distribution of product particles in searches for fluctuations, we have recast original pseudorapidity distributions into flat distributions.

In the distributions of fluctuation centers in CCu collisions, we have found two peaks occurring near the same pseudorapidity values for fluctuations of different sizes. A similar structure has been observed for the distributions of the centers of fluctuations of negatively charged particles from MgMg interactions, the spacing between the peaks in that case being commensurate with the similar spacing for all charged particles in CCu interactions.

The search for possible azimuthal asymmetries in ring-shaped events that has been performed for MgMg collisions has shown the isotropy of the azimuthal angular distribution of particles: the positions of the peaks in the distribution of fluctuation centers and the spacing between these peaks have been found to take the same values for the event sample from which the jet structure has been removed and the event sample involving this structure.

A comparison with similar distributions based on a statistical simulation suggests the dynamical origin of the observed two-peak structure of these distributions. This structure is in accord with the model of coherent gluon emission from a finite length and is similar to the structure recently discovered in proton–proton collisions at a few hundred GeV. That the spacings between the peaks for all charged particles and for negatively charged particles have close values can be treated as evidence of a significant contribution of the coherent component to the formation of Bose–Einstein correlations.

The distributions of maximum-density fluctuations have been studied for all values of the multiplicity *n* and for fixed intervals of *n* in CCu collisions and for fixed *n* in MgMg collisions. The observed non-Poisson character of the distributions suggests that multiparticle correlations contribute to the formation of dense particle groups. The observed flattening of the distribution at large maximum densities in CCu interactions is in agreement with the predictions of the one-dimensional intermittency model. We have not observed this effect for negatively charged particles in MgMg collisions.

A comparison with the results predicted by the model of independent particle production has shown that, within this approach, the stochastic dynamics of correlation formation is masked by strong statistical fluctuations; nevertheless, there are noticeable differences in the behavior of the generated and experimental distributions. It should be recalled that the stochastic nature of fluctuations and correlations has been observed in all types of interactions in studying the intermittency structure.

It is of interest to compare the results that we have obtained here with the results of a similar analysis of fluctuations in reactions characterized by higher mean multiplicities of product particles, the more so as this comparison would depend neither on the shape of the spectrum nor on the reaction type and energy owing to the use of the cumulative variable and fixed multiplicities.

Our analysis of the formation of local dynamical fluctuations in nucleus–nucleus interactions has revealed that the coherent and the stochastic approach to multiparticle production processes supplement each other.

ACKNOWLEDGMENTS

We are grateful to the GIBS (SKM-200) collaboration for kindly placing film data at our disposal and to G.G. Taran for assistance in data processing. We are also indebted to I.M. Dremin for stimulating discussions.

The work of L.K. Gelovani was supported by the Russian Foundation for Basic Research (project no. 96-02-19359a).

REFERENCES

1. P. Bożek, M. Ploszajczak, and R. Botet, Phys. Rep. **252**, 1 (1995).
2. E. A. de Wolf, I. M. Dremin, and W. Kittel, Phys. Rep. **270**, 101 (1996).
3. I. M. Dremin, Usp. Fiz. Nauk **160** (8), 105 (1990) [Sov. Phys. Usp. **33**, 647 (1990)].
4. D. B. Ion and W. Stocker, Phys. Rev. C **52**, 3332 (1995) and references therein.
5. I. M. Dremin, Pis'ma Zh. Éksp. Teor. Fiz. **30**, 152 (1979) [JETP Lett. **30**, 140 (1979)]; Fiz. Élem. Chastits At. Yadra **18**, 79 (1987) [Sov. J. Part. Nucl. **18**, 31 (1987)].
6. I. M. Dremin *et al.*, Yad. Fiz. **52**, 840 (1990) [Sov. J. Nucl. Phys. **52**, 536 (1990)]; EHS/NA22 Collab. (N. M. Agababyan *et al.*), Phys. Lett. B **389**, 397 (1996).
7. Shoushun Wang *et al.*, Phys. Lett. B **427**, 385 (1998).
8. G. L. Gogiberidze, L. K. Gelovani, and E. K. Sarkisyan, Phys. Lett. B **430**, 368 (1998).
9. J. Dias de Deus, Phys. Lett. B **194**, 297 (1987).
10. É. K. Sarkisyan, I. V. Paziashvili, and G. G. Taran, Yad. Fiz. **53**, 1336 (1991) [Sov. J. Nucl. Phys. **53**, 824 (1991)].
11. D. Ghosh, S. Sen, and J. Roy, Phys. Rev. D **47**, 1235 (1993).
12. A. A. Bialas and M. Gazdzicki, Phys. Lett. B **252**, 483 (1990); W. Ochs, Z. Phys. C **50**, 339 (1991).
13. A. Kh. Abdurakhimov *et al.*, Prib. Tekh. Éksp., No. 5, 53 (1978).
14. M. Kh. Anikina *et al.*, Yad. Fiz. **27**, 724 (1978) [Sov. J. Nucl. Phys. **27**, 387 (1978)].
15. SKM-200 Collab. (M. Kh. Anikina *et al.*), Report No. E1-84-785 (Joint Institute for Nuclear Research, Dubna, 1984); M. Kh. Anikina *et al.*, Phys. Rev. C **33**, 895 (1986).
16. G. G. Taran *et al.*, Preprint No. 20, FIAN (Lebedev Institute of Physics, USSR Academy of Sciences, Moscow, 1987).
17. E. K. Sarkisyan *et al.*, Phys. Lett. B **347**, 439 (1995).
18. L. K. Gelovani *et al.*, in *Proceedings of the European Conference on Advances in Nuclear Physics and Related Areas, Thessaloniki, 1997*; hep-ph/9803240.
19. L. K. Gelovani *et al.*, in *Proceedings of the 8th International Workshop on Multiparticle Production: "Correlations and Fluctuations'98: From QCD to Particle Interferometry," Mátraháza, 1998*, Ed. by T. Csörgö *et al.* (World Sci., Singapore, 1999), p. 498.
20. I. V. Andreev *et al.*, Int. J. Mod. Phys. A **10**, 3951 (1995).
21. E. K. Sarkisyan and G. G. Taran, Phys. Lett. B **279**, 177 (1992); É. K. Sarkisyan and G. G. Taran, Yad. Fiz. **55**, 417 (1992) [Sov. J. Nucl. Phys. **55**, 230 (1992)].
22. A. Kh. Babaev *et al.*, Yad. Fiz. **50**, 1324 (1989) [Sov. J. Nucl. Phys. **50**, 824 (1989)]; I. M. Dremin and V. I. Manko, Nuovo Cimento A **111**, 439 (1998).
23. I. M. Dremin, private communication.
24. R. M. Weiner, Phys. Rep. **327**, 249 (2000).
25. EHS/NA22 Collab. (I. V. Ajinenko *et al.*), Phys. Lett. B **222**, 306 (1989).
26. G. Singh, K. Sengupta, and P. L. Jain, Phys. Rev. Lett. **61**, 1073 (1988); P. L. Jain and G. Singh, Phys. Rev. C **54**, 1892 (1996); A. Abduzhamilov *et al.*, Preprint No. 160, FIAN (Lebedev Institute of Physics, USSR Academy of Sciences, Moscow, 1989).
27. L. K. Gelovani, É. K. Sarkisyan, and G. G. Taran, Yad. Fiz. **55**, 2481 (1992) [Sov. J. Nucl. Phys. **55**, 1380 (1992)]; E. K. Sarkisyan *et al.*, Phys. Lett. B **318**, 568 (1993).
28. T. Takagi and D. Kiang, Phys. Rev. D **56**, 5862 (1997).

Translated by M. Kobrinsky

Physics of Atomic Nuclei, Vol. 64, No. 1, 2001, pp. 151–152. Translated from Yadernaya Fizika, Vol. 64, No. 1, 2001, pp. 156–157.

LETTERS TO THE EDITOR

Effect of Taking into Account the Radiative Decay Mode in Measurements of the Antineutrino–Spin Correlation in Neutron Decay

Yu. A. Mostovoĭ[1)], I. A. Kuznetsov[2)], A. P. Serebrov[2)], and B. G. Yerozolimsky[3)]

Received April 26, 2000

Although photons accompanying neutron decay have not been observed so far, there is no doubt about the existence of this decay mode. Thus, the problems to be addressed here are those of assessing the probability of the process and of establishing the relevant photon spectrum. Among theoretical studies devoted to this decay mode, the calculations reported in [1] stand out because they yielded large radiative corrections (8% for the total decay probability). For this reason, the accuracy of the measurements described in [2] was questioned in [1].

The procedure for calculating the coefficient B describing the antineutrino–spin correlation is based on the analysis of the kinematics in the system formed by the decay electron and the recoil proton, because a direct measurement of the antineutrino momentum is not possible at present. If, however, an undetected photon is emitted in the decay process, the above procedure becomes ambiguous, which adversely affects the accuracy achievable in the calculations. In order to estimate relevant uncertainties, it is necessary to compute the correction that stems from taking into account the probability of photon emission under the detection conditions realized experimentally.

Here, we estimate the uncertainties in question for the corrections presented in [3, 4]. For various values of the emitted-electron energy E and of the cosine of the angle between the emitted-antineutrino momentum and the direction of the guiding magnetic field, $\cos(s\nu)$, these corrections were computed by comparing the formula used in [2] and the formula corrected for photon emission without imposing specific experimental conditions. For five intervals of the electron energy over the Fermi distribution and ten values of the cosine, the resulting corrections were tabulated in [3].

An analysis of the table from [3] reveals a feature at $|\cos(s\nu)| = 0$. However, the effect of this feature decreases with increasing $|\cos(s\nu)|$: the correction is less than 0.4% at $|\cos(s\nu)| \approx 0.2$, falling down to 0.02% at $|\cos(s\nu)| \approx 0.8$. On the basis of these values alone, it might be expected that the total correction is small because the maximum correction values correspond to the domain where the efficiency with which the decays were recorded experimentally is low [2], whereas the minimum correction values occur in the domain of the highest efficiency. Nevertheless, the conclusion that the experimental accuracy [2] is not well justified was drawn in [3, 4] without regard to experimental conditions.

In order to estimate the effect of the radiative mode of neutron decay, we have analyzed the overlap of the corrections obtained in [3] and the array of experimental data from [2]. Recall that the sign of the calculated corrections is sensitive to the direction of the guiding magnetic field because the electron momentum singles out a specific direction. In view of this, we have considered that this field was periodically changed in the experiment being discussed.

Our calculations involved the following steps:

(i) The experimental data from [2] were distributed among five energy intervals E_i (i = 1–5) corresponding to the intervals chosen in [3].

(ii) In each interval, the data were distributed among 14 bins corresponding to the mean values $\langle\cos(s\nu)\rangle_j$ (j = 1–14), and the correction was evaluated for each bin by using the values of E_i and $\langle\cos(s\nu)\rangle_j$ presented in the tables from [3].

(iii) These 14 corrections were summed with allowance for their statistical weights w_j defined as $w_j = \frac{1}{\sigma_j^2}/\left(\sum_j \frac{1}{\sigma_j^2}\right)$, where σ_j is the uncertainty in the experimental asymmetry $P \cdot B$ within the corresponding bin.

(iv)) The corrections obtained in each of the five energy intervals were averaged with the weights determined on the basis of the number of events in these intervals.

These calculations have revealed that, upon the inclusion of the radiative neutron-decay mode predicted in [1], the coefficient $B = 0.9821 \pm 0.0040$ measured in [2] for the antineutrino–spin correlation may be shifted only slightly, by not more than 0.2 of the

[1)] Russian Research Centre Kurchatov Institute, pl. Kurchatova 1, Moscow, 123182 Russia.
[2)] Petersburg Nuclear Physics Institute, Russian Academy of Sciences, Gatchina,188350 Russia.
[3)] Harvard University, 42 Oxford St., Cambridge, MA 02138 USA.

1063-7788/01/6401-0151$21.00

standard error of the measurements. This estimate is associated with a specific computation of the probability of the radiative decay mode, which, in turn, calls for verification. But even if we put aside the question of whether the computations of the probability in [1] are valid, there is every reason to claim that the accuracy of the experimental data was indicated correctly in [2] merely because the resulting correction proved to be negligible at the largest values of the expected effect.

ACKNOWLEDGMENTS

This work was supported in part by the Russian Foundation for Basic Research (project no. 00-02-17383).

REFERENCES

1. G. G. Bunatian, Yad. Fiz. **62**, 697 (1999) [Phys. At. Nucl. **62**, 648 (1999)].
2. A. P. Serebrov *et al.*, Zh. Éksp. Teor. Fiz. **113**, 1963 (1998) [JETP **86**, 1074 (1998)].
3. G. G. Bunatjan, Preprint No. E4-9962, OIYaI (Joint Institute for Nuclear Research, Dubna, 1999).
4. G. G. Bunatyan, Pis'ma Zh. Éksp. Teor. Fiz. **69**, 681 (1999) [JETP Lett. **69**, 728 (1999)].

Translated by R. Rogalyov

Physics of Atomic Nuclei, Vol. 64, No. 1, 2001, pp. 17–26. Translated from Yadernaya Fizika, Vol. 64, No. 1, 2001, pp. 19–28.

NUCLEI
Theory

Dynamical Polarization of Radioactive Nuclei

Yu. F. Kiselev and V. L. Lyuboshitz

Joint Institute for Nuclear Research, Dubna, Moscow oblast, 141980 Russia

Received October 15, 1999; in final form, March 24, 2000

Abstract—In order to polarize radioactive nuclei implanted in a highly polarized protonic target, it is proposed to use methods for the dynamical orientation of nuclei. The angular distribution of photons that originate from the cascade beta–gamma decay of the $^{22}Na(3^+)$ state in a strong magnetic field is calculated. It is shown that, if the populations of Zeeman magnetic sublevels obey the Boltzmann distribution, the angular distribution of emitted photons is independent of the sign of spin temperature; at the same time, the tensor polarization of quadrupole nuclei occurring in the intrinsic field of a crystal causes a strong dependence of the anisotropy on the sign of spin temperature. A rich potential of a dynamical orientation for studying the magnetic structure of rare nuclei and the dynamics of their spin–spin interactions in dielectric host materials is demonstrated. Physical and technological advantages and disadvantages of the method in the on-line regime of the implantation of heavy nuclei are discussed. © *2001 MAIK "Nauka/Interperiodica".*

1. INTRODUCTION

Measurement of the anisotropy of angular distributions of beta–gamma radiations is the most sensitive method for studying the magnetic moments of nuclei and their hyperfine interactions [1]. As a rule, the nuclei being studied are implanted in ferromagnetic substances, where they are polarized owing to a significant intrinsic magnetic induction of about 50 T and owing to cooling down to ultralow temperatures (10–30 mK). Because of a high rate of spin–lattice relaxation, a Boltzmann (equilibrium) distribution characterized by the lattice temperature is established in the system of nuclear spins, but a tight spin–lattice coupling prevents the use of the entire toolkit of known methods for studying spin systems—for example, the spin temperature cannot be inverted under such conditions.

In amorphous dielectric materials (such as butanol and propanediol [2, 3]), which have long since been used as frozen polarized protonic targets, and in single crystals—for example, in LiF featuring F centers—methods of dynamical nuclear polarization are applied, which ensure nearly a 100% polarization of nuclear spins of either sign [4–6]. In contrast to ferromagnetic host materials, dielectric materials are transparent to electromagnetic fields, at least up to frequencies of 10^{11} Hz, and have negligibly small intrinsic local magnetic fields (about 10^{-3} T); at the same time, a high degree of proton polarization in them can be obtained under easily accessible experimental conditions (temperature in the range 0.2–0.5 K and conventional magnetic fields of about 2.5 T). A feature that distinguishes dielectric host materials from ferromagnetic ones is that the times of spin–lattice relaxation are enormous in the former—1000 h or even greater—whence it follows that the magnetic moments virtually decouple from the lattice. Owing to this, it becomes possible to achieve a high degree of the vector and tensor polarizations of admixed nuclei, to prepare non-Boltzmann populations of spin states [7, 8], and even to focus spins in a pure quantum state [9].

In the present study, we analyze the application of dynamical nuclear polarization to polarizing radioactive nuclei implanted in a polarized target. We show that, by using dynamical nuclear polarization, it is possible to achieve a high anisotropy of gamma radiation; for the case of a tensor polarization of quadrupole nuclei occurring in a nonuniform magnetic field, we additionally find the dependence of the angular distribution of photons on spin temperature.

We dedicate this article to the blessed memory of our friend and teacher M.I. Podgoretskiĭ, who initiated investigations along this lines [10].

2. POLARIZATION OF QUADRUPOLE NUCLEI

We begin by recalling the idea content of three methods of dynamical nuclear polarization [4–8], which show promise for the investigation of quadrupole nuclei. These methods were tested by applying them to substances featuring high spin concentrations, but, as far as we know, they were not explored in the case of rare radioactive nuclei.

The most popular method is that of dynamical cooling [5, 6]. In order to implement this method, a paramagnetic impurity (Kramers centers [4]), with a concentration N_s of about 10^{20} cm^{-3}, is introduced in a target material by means of dissolution, diffusion, or irradiation. In a magnetic field H_0, the unpaired electrons ($S = 1/2$) of the molecules of the impurities are polarized to the degree

$$P_s = 100\% \times \tanh\left(\frac{h\gamma_s H_0}{2kT_0}\right), \qquad (1)$$

1063-7788/01/6401-0017$21.00

where T_0 is temperature, h is the Planck constant, γ_s is the gyromagnetic ratio for electrons, and k is the Boltzmann constant. At H_0 = 2.5 T and T_0 = 0.3 K, the degree of polarization is P_s = 99.997%. From Eq. (1), it follows that, under the same conditions, the proton spins (the corresponding quantities are labeled with the subscript p) are polarized only to the degree of P_p = 0.85% since $\gamma_s/\gamma_p \cong 656$.

The method consists in transferring a high polarization of electron spins to admixed nuclei. For this, the host material is irradiated with a microwave field whose frequency ν is close to the center of the line of the electron resonance that corresponds to the Larmor frequency $\nu_{s0} = \gamma_s H_0$ equal to about 7×10^{10} Hz in a field of 2.5 T. It was shown by Provotorov [11] that, in the presence of a saturating field, the behavior of a spin system is governed by two spin temperatures rather than by one. Of these, one—Zeeman temperature—characterizes the distribution of spins over magnetic sublevels, while the other—the temperature of the spin–spin reservoir—is associated with the energy of spin–spin interactions. A nonresonance irradiation of electron spins leads to a significant reduction of the latter temperature, since the difference energy quantum $h|\nu - \nu_{s0}|$ falls within the frequency spectrum of the spin–spin reservoir, which has a comparatively low heat capacity and a broad frequency spectrum of width about 300 MHz. It can easily be seen that, in a field of 2.5 T, this spectrum covers the characteristic Larmor frequencies of nuclear spins; therefore, the temperature of the electron spin–spin reservoir and the spin temperature of nuclei eventually tend to equalize. From this, it follows, among other things, that, in the case of polarized radioactive nuclei, the anisotropy of the angular distribution of beta–gamma radiation originating from them furnishes information about the temperature of the reservoir of spin–spin interactions. A positive frequency separation $(\nu - \nu_{s0})$ favors negative spin temperatures of nuclei because the energy quantum $h(\nu - \nu_{s0})$ is transferred to nuclear spins in this case. If the frequency separation $(\nu - \nu_{s0})$ is negative, nuclear spins supply the missing energy quantum $h(\nu_{s0} - \nu)$ to the electron spin–spin reservoir [6]. An increase in the degree of nuclear polarization is accompanied by a decrease in the corresponding nuclear spin temperature T_J in relation to the lattice temperature T_0 by a factor of about $T_0/T_J \approx \pm\omega_{s0}/(2\sqrt{M_2})$ [6], where M_2 is the second moment of the ESR absorption line and $\omega_{s0} = 2\pi\nu_{s0}$. In the case of an optimum concentration of paramagnetic centers, the maximum enhancement of the degree of polarization is achieved at frequencies corresponding to the slopes of the relevant ESR line, in which case the absolute value of the ratio $|T_0/T_J|$ can be as great as a few hundred units. As a matter of fact, this method makes it possible to achieve a nearly complete polarizations of protons (±98%) and a ±55% polarization of deuterons. A feature peculiar to dynamical orientation is that, over a time interval of 1 h, the Boltzmann distribution corresponding to a minimal temperature of about ±1 mK is established for all nuclear spins in a host material, including the spins of quadrupole nuclei (it should be recalled that, in this case, the lattice temperature lies in the range 0.1–0.3 K).

A similar effect of a thermal contact with admixed atoms arises if polarized proton spins are used instead of electron spins [7, 8]. The difference is that it is not the electron spins, but the polarized protons that are exposed in this case to alternating-field radiation in a strong magnetic field at a frequency close the Larmor frequency $\nu_{J0} = \gamma_p H_0$ (about 106 MHz at a field strength of 2.5 T). The width of the spectrum of local nuclear fields is about a few tens of kHz (this is about three orders of magnitude narrower than in the case of electron spins); therefore, such a spectrum cannot stimulate Zeeman transitions of admixed nuclei and affect their vector polarization, but it can change the energy of spin–spin interactions of other nuclear spins [12]. In the case of rare quadrupole nuclei dissolved in a polarized target—and we are interested precisely in this case—the role of their dipole–dipole interaction can be disregarded, in which case the quadrupole interaction of spins with an electric field in a host material appears to be a resonating system [8, 9]. As a result, the difference energy $h\nu_Q \approx h(\nu - \nu_{J0})$ will increase or decrease, depending on the sign of the frequency separation and on the sign of proton polarization, the mean energy $\langle \hat{H}_Q \rangle$ of the interaction of quadrupole nuclei with a crystal field. The Hamiltonian describing the interaction of a nucleus with a nonuniform intrinsic crystal field has the form [13]

$$\hat{H}_Q = \frac{1}{6}\sum_{i=1}^{3}\sum_{j=1}^{3} e\hat{Q}_{ij}\frac{\partial^2\varphi}{\partial x_i \partial x_j}, \qquad (2)$$

where e is the proton charge, φ is the potential of the electric field in the crystal being considered, and

$$Q_{ij} = \frac{3Q}{2J(2J-1)}\left(\hat{J}_i\hat{J}_j + \hat{J}_j\hat{J}_i - \frac{2}{3}J(J+1)\delta_{ij}\right) \qquad (3)$$

is the tensor operator of the quadrupole moment [14, 15]. In Eq. (3), we have used the following notation: Q is the nuclear quadrupole moment measured in cm^2, J is the nuclear spin, and $\hat{J}_i$ and $\hat{J}_j$ are the operators of the spin projections onto three mutually orthogonal axes. In the presence of a constant magnetic field H_0, the total Hamiltonian of the interaction between the nucleus and an external electromagnetic field is given by

$$\hat{H} = -\mu\frac{e}{2m_p c}\hat{\mathbf{J}}\cdot\mathbf{H}_0 + \hat{H}_Q, \qquad (4)$$

where μ is the magnetic moment in units of the nuclear magneton and m_p is the proton mass.

If the quadrupole interaction is much weaker than the Zeeman magnetic interaction, the eigenstates of the Hamiltonian $\hat{H}$ are virtually coincident with states corresponding to specific values of the nuclear-spin projection m onto the magnetic-field direction. The contribution of the quadrupole interaction to the energy E_m of magnetic sublevels can be calculated on the basis of perturbation theory. In the first order of perturbation theory, we have

$$E_m = -\mu\frac{e}{2m_p c}mH_0 + \langle m|\hat{H}_Q|m\rangle. \quad (5)$$

If the intrinsic crystal field is axisymmetric with respect to the principal z axis of the tensor Q_{ij}, the diagonal elements of the quadrupole-interaction operator can be represented in the form [13]

$$\langle m|\hat{H}_Q|m\rangle = X(\phi)\langle 3m^2 - J(J+1)\rangle, \quad (6)$$

where ϕ is the angle between the constant-magnetic-field direction and the principal z axis of the tensor Q_{ij} and

$$X(\phi) = h\nu_Q(3\cos^2\phi - 1). \quad (7)$$

Here, ν_Q is the characteristic frequency of quadrupole interactions, which is given by

$$\nu_Q = \frac{e^2qQ}{8hJ(2J-1)}, \quad (8)$$

where $eq = \partial^2\varphi/\partial z^2 = -2\partial^2\varphi/\partial x^2 = -2\partial^2\varphi/\partial y^2$. It is convenient to recast the mean energy of the quadrupole interaction of a nucleus with the intrinsic crystal field [see Eq. (5)] into the form [8]

$$\langle \hat{H}_Q\rangle = X(\phi)A, \quad (9)$$

where

$$A = \sum_{m=-J}^{J}\rho_{mm}(3m^2 - J(J+1)), \quad (10)$$

ρ_{mm} being magnetic-sublevel populations normalized to unity, has the meaning of nuclear alignment (tensor polarization). From Eq. (9), it can easily be seen that the change undergone by the mean energy of the quadrupole-interaction reservoir when it comes into contact with the spin–spin reservoir will lead to a change in the alignment of admixed nuclei. It should be emphasized that the above relations are valid both for nuclei with integral spins and for nuclei with half-integer spins and that the quadrupole interaction (6) vanishes at $J = 0$ and at $J = 1/2$.

In the case being considered, we generally need two spin temperatures T_Z and T_Q—of these, the first characterizes the mean energy of the Zeeman interaction of spins with a magnetic field, while the second is associated with the energy of quadrupole interactions of spins that are in thermal equilibrium with the reservoir of proton spin–spin interactions—in order to describe the populations of stationary nuclear states that are pure in the spin projection onto the magnetic-field direction. The situation admitting the most straightforward type of analysis is that of zero vector polarization of quadrupole nuclei, in which case the mean energy of Zeeman splitting is equal to zero, the temperature T_Z of admixed nuclei going to infinity [8]. In practice, the procedure that results in the vanishing of the mean Zeeman energy amounts to an irradiation with a saturating radio-frequency field corresponding to the absorption line of admixed nuclei. Under such initial conditions, the populations of stationary nuclear states characterized by fixed values of the spin projection m onto the magnetic-field direction are determined exclusively by the quadrupole interaction featuring only one spin temperature. Specifically, we have

$$\rho_{mm} = \frac{\exp[-\beta\langle m|\hat{H}_Q|m\rangle]}{\sum_{m=-J}^{J}\exp[-\beta\langle m|\hat{H}_Q|m\rangle]} = \frac{\exp[-\beta X(\phi)(3m^2 - J(J+1))]}{\sum_{m=-J}^{J}\exp[-\beta X(\phi)(3m^2 - J(J+1))]}, \quad (11)$$

where $\beta = 1/(kT_Q)$ is the inverse spin temperature of the quadrupole-interaction reservoir. The sign of T_Q is determined by the sign of the product $P_p\cdot(\nu - \nu_{J0})$. The populations ρ_{mm} appear to be elements of the nuclear spin density matrix, which is diagonal in the case being considered. Taking into account Eq. (11), we can recast expression (10) for the alignment of nuclei into the form

$$A = \frac{3\sum_{m=-J}^{J} m^2\exp[-\beta X(\phi)(3m^2 - J(J+1))]}{\sum_{m=-J}^{J}\exp[-\beta X(\phi)(3m^2 - J(J+1))]} - J(J+1). \quad (12)$$

For the particular case of $J = 1$, this expression was derived in [8] and was confirmed there in experiments with deuterons. For $\nu_Q > 0$, it can be shown that, at integral values of J, $A \longrightarrow -J(J+1)$ in the limit of very low positive temperatures T_Q at angle values lying in the range $0 \le \phi < \arccos(3^{-1/2})$—that is, all nuclei are in the state where the spin projection is $m = 0$; at $\arccos(3^{-1/2}) < \phi \le \pi/2$, the populations are equally distributed among the $m = J$ and the $m = -J$ state, while the alignment behaves as $A \longrightarrow J(2J-1)$. A totally different situation is observed at very low negative temperatures. If the spins have half-integer values and if $\nu_Q > 0$, all spins populate the $m = 1/2$ and the $m = -1/2$ state

with equal probabilities for angle values in the range $0 \le \phi < \arccos(3^{-1/2})$, the alignment A then tending to the limit $3/4 - J(J+1)$.

The method discussed above was proposed in [7, 8]; it can prove to be of use at modest quadrupole moments of about 3×10^{-27} cm^2, in which case $h\nu_Q \approx h(\nu - \nu_{J0})$. Experimentally, it takes a few tens of seconds to implement polarization by this method, the spin temperature reaching ± 10 μK.

Because of typically low magnetic moments of quadrupole nuclei, the degrees of polarization that are achievable for admixed nuclei within the conventional dynamical-orientation method will hardly exceed ±20%; therefore, a considerable enhancement of polarization on the basis of the cross-relaxation method featuring polarized protons [16] appears to be a considerable advancement toward a practical utilization of dynamical methods. Basically, the idea consists in the following: suppose that, in addition to $J \ge 1$ nuclei, a host material contains some highly abundant nuclei—for example, polarized protons ($J = 1/2$)—which, in view of a large gyromagnetic ratio, are characterized by a large heat capacity of the spin system. Since the proton spin is 1/2, the interaction specified by Eq. (9) vanish for them. On the contrary, the interaction of quadrupole nuclei ($J > 1/2$) with the lattice survives in zero magnetic field as well; by reducing H_0, we can therefore render the Larmor frequency of the proton spins equal to the quadrupole splitting of the spins of admixed atoms. Just at this point, there occurs a cross-relaxation transfer of a high proton polarization to the quadrupole nuclei.

Relevant experiments were performed with ammonia (NH_3) [16]. In the field of 0.056 T, the quadrupole splitting of stable nitrogen nuclei, $6\nu_Q = 2.4$ MHz, is equal to the Larmor frequency of protons; under such conditions, ^{14}N nuclei are polarized to a nearly 50% degree as the result of the cross-relaxation process [16], which ensures a high polarization rate estimated at [17]

$$W = (\gamma_N/\gamma_H)^2\left(T_2\cosh\left(\xi\frac{\Delta_0}{\Delta_H}\right)\right)^{-1}, \qquad (13)$$

where $\gamma_N/\gamma_H \approx 7 \times 10^{-2}$ is the ratio of the relevant nuclear gyromagnetic constants, $T_2 \approx 10^{-5}$ s is the time of the transverse relaxation of proton spins, Δ_0 is the frequency separation between the spins, Δ_H is the proton line width, and ξ is a free parameter on the order of unity. Setting $\Delta_0 \approx \Delta_H$, we obtain the rough estimate $W^{-1} \approx 2$ ms—that is, an extremely short polarization time; it would be profitable to use this in the on-line regime of implantation of nuclei in the target. The distribution of spins among magnetic sublevels that is obtained by this method is not a Boltzmann distribution, but it can be frozen for a long time. This is because the magnetic sublevels of quadrupole nuclei are not equidistant, so that equilibration with respect to internal degrees of freedom is associated with long times of spin-lattice relaxation. Theoretically, spins can be focused into a pure quantum state in such systems [9].

The method considered above can also be used in the case of radioactive nuclei that are implanted in a polarized target and which enter into the composition of diamagnetic atoms or Kramers paramagnetic centers [4]. However, the very idea that underlies the dynamical orientation method as applied to rare nuclei and which relies on the dynamics of collective spin–spin interactions must be tested experimentally. It is convenient to implement such tests by using comparatively long-lived radioactive nuclei like the ^{22}Na isotope. For this nuclear species, the angular distribution of the relevant radiations is analyzed in detail below.

3. CALCULATION OF THE ANGULAR DISTRIBUTION OF GAMMA RADIATION

Here, we will derive the required formulas for the anisotropy in the angular distribution of photons originating from the decay of polarized nuclei. The existence of this anisotropy is an immediate corollary of the fact that the diagonal density-matrix elements ρ_{mm} associated with the action of any mechanism of dynamical polarization differ significantly from the value $(2J+1)^{-1}$, which corresponds to unpolarized nuclei. The resulting formulas can be used for any distribution of spins among magnetic sublevels—in particular, they make it possible to calculate, in the case of tensor polarization that arises owing to quadrupole splitting, the angular distribution of photons versus the sign of spin temperature [see Eqs. (11), (12)].

If the excited nucleus being considered has a spin J and if the spin of the final nucleus is $J' = 0$, the angular distribution of photons that is taken with respect to the magnetic-field direction and which is normalized to unity has the form

$$W(\theta) = \frac{2J+1}{8\pi}\sum_{m=-J}^{J}\rho_{mm}^{(J)}[(d_{m,1}^{(J)}(\theta))^2 + (d_{m,-1}^{(J)}(\theta))^2], \qquad (14)$$

where $d_{m,1}^{(J)}(\theta)$ and $d_{m,-1}^{(J)}(\theta)$ are Wigner functions (elements of the matrix of finite rotations) and $\rho_{mm}^{(J)}$ are the populations of spin states (these populations coincide with diagonal density-matrix elements). Equation (14) immediately follows from the formalism of helicity amplitudes, which is convenient for describing two-body decays [18, 19] (see Appendix). For $J' \ne 0$, a similar formula for purely electric or purely magnetic gamma transitions of specific multipole order L has the form

$$W(\theta) = \frac{2J+1}{8\pi}\sum_{m=-J}^{J}\sum_{\mu=-L}^{L}(C_{J'm-\mu\,L\mu}^{Jm})^2 \times \rho_{mm}^{(J)}[(d_{\mu 1}^{(L)}(\theta))^2 + (d_{\mu -1}^{(L)}(\theta))^2], \qquad (15)$$

where C is a Clebsch–Gordan coefficient. In $J \longrightarrow J' + \gamma$ decays, the multipole order L of the radiation can generally take all integral values in the interval $|J - J'| \le L \le J + J'$; in the particular case of $J' = 0$, we have $L = J$, and expression (15) reduces to (14). Frequently, gamma decay is dominated by an electric transition of the lowest multipole order $L_{\min} = |J - J'|$, in which case we can use expression (15) as an approximation. The spins J and J' can then be either both integral or both half-integer.

In the case where a dynamical polarization is implemented with the aid of polarized protons (see Section 2), the population probabilities are described by Eq. (11). If Zeeman levels in a magnetic field H_0 obey a Boltzmann distribution, one has [20]

$$\begin{aligned} \rho_{mm} &= e^{mx} / \sum_{m=-j}^{j} e^{mx/J} \\ &= e^{mx/J} \sinh\left(\frac{x}{2J}\right) / \sinh\left(x\left(1 + \frac{1}{2J}\right)\right), \end{aligned} \tag{16}$$

where

$$x = \mu \frac{e}{2m_p c} \frac{H_0}{kT}. \tag{17}$$

Here, μ is the magnetic moment in units of the nuclear magneton, m_p is the proton mass, c is the speed of light in a vacuum, and T is spin temperature.

Let us now consider the angular anisotropy of photon emission in cascade beta–gamma transitions of nuclei having a nonzero magnetic moment (nonzero spin J) [10]. Suppose that intermediate daughter nuclei that have a nonzero spin J' and which in turn undergo a fast gamma decay are formed as the result of beta decay. We will see below that, if a total orbital angular momentum L is transferred to the emitted electron and the emitted antineutrino and if their linear momenta are not detected (that is, the relevant averaging is performed), the polarization of the daughter nucleus immediately following the beta-decay process is unambiguously related to the polarization of the initial long-lived nucleus and, through it, to the initial spin temperature. The lifetime of intermediate nuclei must be so short that their spin state does not have time to change sizably. More specifically, this means that the lifetime of an intermediate nucleus must be much smaller than the inverse frequency of hyperfine splitting of atomic levels ($\tau \ll 10^{-8}$–10^{-9} s). Under these conditions, the angular distribution of photons with respect to the direction of the magnetic field H_0 contains information about the unified spin temperature of initial radioactive nuclei and nonradioactive nuclei under study that surround them. Let us consider the generic decay process

$$a^{(J)} \longrightarrow b^{(J')} + X^{(L)}$$

under the condition that the set of particles X whose momenta are not fixed carries away a total orbital angular momentum L. Since, in the case being considered, there are no specific directions other than those that are associated with the polarizations of particle a, the polarization parameters of particle b formed as the result of the above decay process are determined exclusively by the vectorial composition of angular momenta. In other words, we can replace the set of particles X by a fictitious particle whose spin is L, assuming that the orbital angular momentum of the $(b + X)$ system is equal to zero. The elements of the spin density matrix for particle b are then related to the elements of the spin density matrix for particle a by the simple equation

$$\rho^{(J')}_{m\tilde{m}} = \sum_{\mu=-L}^{L} C^{J\ m+\mu}_{J'm\ L\mu} C^{J\ \tilde{m}+\mu}_{J'\tilde{m}\ L\mu} \rho^{(J)}_{m+\mu\ \tilde{m}+\mu}, \tag{18}$$

where C stands for Clebsch–Gordan coefficients. It can easily be seen that, if the spin density matrix for the primary particle a is diagonal, the density matrix for the final particle b is also diagonal and that

$$\rho^{(J')}_{mm} = \sum_{\mu=-L}^{L} (C^{J\ m+\mu}_{J'm\ L\mu})^2 \rho^{(J)}_{m+\mu\ m+\mu}. \tag{19}$$

From Eq. (11) and from the relation

$$\sum_{\mu} (C^{J\ m+\mu}_{J'm\ L\mu})^2 = \frac{2J+1}{2J'+1}, \tag{20}$$

which is known from the theory of the composition of angular momenta, it follows that, if the decaying particle is unpolarized [$\rho^{(J)}_{m+\mu\ m+\mu} = (2J+1)^{-1}$ for $|m+\mu| \le J$], then the product particle b is also unpolarized: $\rho^{(J')}_{m\tilde{m}} = (2J'+1)^{-1}\delta_{m\tilde{m}}$. Equation (18) is well known in the theory of the gamma decay of oriented nuclei—for a final nucleus produced via transitions of specific multipole order L, this equation determines polarization features averaged over all directions of photon emission [19, 21]. By X, we mean a photon in this case. In accordance with the aforesaid, Eqs. (18) and (19) describe the beta decay of nuclei as well (and also K capture), provided that the orbital angular momentum L is transferred to the product leptons and that the direction of their emission is not recorded. In particular, the angular momentum of the electron–antineutrino (positron–neutrino) system is equal to unity in the case of an allowed Gamow–Teller transition [22]. If $|J - J'| = 1$, the allowed Gamow–Teller transition is dominant (the remaining transitions are strongly suppressed); in this case, the polarization of the nucleus produced via beta decay is accurately described by Eqs. (18) and (19) at $L = 1$.

Let us consider the case where, in the beta decay of polarized admixed nuclei with a spin J, the spin of the intermediate short-lived nucleus takes the value of $J' = J - 1$ or $J' = J + 1$. Further, we assume that, as the result of gamma decay, the intermediate nucleus goes over to

a spinless state. Taking into account Eqs. (14) and (19), we then find that the angular distribution of photons that is taken with respect to the magnetic-field direction (quantization axis) and which is normalized to unity can be reduced to the form [10]

$$W(\theta) = \frac{2J'+1}{8\pi}\Bigg\{\sum_{m=1}^{J'}(\rho_{mm}^{(J')} + \rho_{-m-m}^{(J')}) \times [(d_{m,1}^{(J')}(\theta))^2 + (d_{m,-1}^{(J')}(\theta))^2] + 2\rho_{00}^{(J')}(d_{01}^{(J')}(\theta))^2\Bigg\}, \quad (21)$$

where $\rho_{mm}^{(J')} = \sum_{\mu=0,\pm1}(C_{J'm\,1\mu}^{J\,m+\mu})^2\rho_{m+\mu\,m+\mu'}^{(J)}$. At $J = 3$ and $J' = 2$, we have

$$W(\theta) = \frac{5}{8\pi}\Bigg\{\frac{1}{2}(\rho_{22}^{(2)} + \rho_{-2-2}^{(2)})(1+\cos^2\theta)\sin^2\theta + \frac{1}{2}(\rho_{11}^{(2)} + \rho_{-1-1}^{(2)})(4\cos^4\theta - 3\cos^2\theta + 1) + 3\rho_{00}^{(2)}\cos^2\theta\sin^2\theta\Bigg\}, \quad (22)$$

where

$$\rho_{22}^{(2)} = \rho_{33}^{(3)} + \frac{1}{3}\rho_{22}^{(3)} + \frac{1}{15}\rho_{11}^{(3)},$$

$$\rho_{11}^{(2)} = \frac{2}{3}\rho_{22}^{(3)} + \frac{8}{15}\rho_{11}^{(3)} + \frac{1}{5}\rho_{00}^{(3)},$$

$$\rho_{00}^{(2)} = \frac{2}{5}\rho_{11}^{(3)} + \frac{3}{5}\rho_{00}^{(3)} + \frac{2}{5}\rho_{-1-1}^{(3)}, \quad (23)$$

$$\rho_{-1-1}^{(2)} = \frac{2}{3}\rho_{-2-2}^{(3)} + \frac{8}{15}\rho_{-1-1}^{(3)} + \frac{1}{5}\rho_{00}^{(3)},$$

$$\rho_{-2-2}^{(2)} = \rho_{-3-3}^{(3)} + \frac{1}{3}\rho_{-2-2}^{(3)} + \frac{1}{15}\rho_{-1-1}^{(3)}.$$

If $J = 2$ and $J' = 1$, the angular distribution in question is given by

$$W(\theta) = \frac{3}{8\pi}\Bigg\{\frac{1}{2}(\rho_{11}^{(1)} + \rho_{-1-1}^{(1)})(1+\cos^2\theta) + \rho_{00}^{(1)}\sin^2\theta\Bigg\}, \quad (24)$$

where

$$\rho_{11}^{(1)} = \rho_{22}^{(2)} + \frac{1}{2}\rho_{11}^{(2)} + \frac{1}{6}\rho_{00}^{(3)},$$

$$\rho_{00}^{(1)} = \frac{1}{2}\rho_{11}^{(2)} + \frac{2}{3}\rho_{00}^{(2)} + \frac{1}{2}\rho_{-1-1}^{(2)}, \quad (25)$$

$$\rho_{-1-1}^{(1)} = \rho_{-2-2}^{(2)} + \frac{1}{2}\rho_{-1-1}^{(2)} + \frac{1}{6}\rho_{00}^{(2)}.$$

At $J = 1$ and $J' = 2$, the angular distribution of photons has the form (22) with

$$\rho_{22}^{(2)} = \frac{3}{5}\rho_{11}^{(1)},$$

$$\rho_{11}^{(2)} = \frac{3}{10}\rho_{11}^{(1)} + \frac{3}{10}\rho_{00}^{(1)},$$

$$\rho_{00}^{(2)} = \frac{1}{10}\rho_{11}^{(1)} + \frac{1}{10}\rho_{-1-1}^{(1)} + \frac{2}{5}\rho_{00}^{(1)}, \quad (26)$$

$$\rho_{-1-1}^{(2)} = \frac{3}{10}\rho_{-1-1}^{(1)} + \frac{3}{10}\rho_{00}^{(1)},$$

$$\rho_{-2-2}^{(2)} = \frac{3}{5}\rho_{-1-1}^{(1)}.$$

From expressions (16) and (21)–(26), it follows that, in the case of the Boltzmann distribution of Zeeman levels in a magnetic field, reversal of the sign of spin temperature does not affect the form of the angular distribution of gamma radiation because these expressions are symmetric under the substitution $\rho_{mm} \rightleftharpoons \rho_{-m-m}$. On the other hand, reversal of the sign of temperature inevitably changes the angular distribution in the case where there is a quadrupole splitting of the levels. To illustrate the validity of this statement, we note that, at sufficiently low spin temperatures, the elements of the spin density matrix are transformed as $\rho_{JJ} + \rho_{-J-J} \rightleftharpoons \rho_{00}$ under the above reversal of the sign [see comments to Eq. (12)].

4. CALCULATION FOR THE CASCADE TRANSITION $^{22}Na(3^+) \xrightarrow{\beta} {}^{22}Ne(2^+) \xrightarrow{\gamma} {}^{22}Ne(0^+)$

By way of example, Podgoretskiĭ proposed studying the angular correlations of gamma radiation in the process $^{22}Na(3^+) \xrightarrow{\beta} {}^{22}Ne(2^+) \xrightarrow{\gamma} {}^{22}Ne(0^+)$ [10]. We have analyzed the behavior of the angular distribution, considering the various methods of dynamical nuclear polarization that were discussed in Section 2 (see above). Recall that the experiments being discussed must be conducted at an invariable H_0, the only difference in the implementation of these experiments being the following: in the case of dynamical orientation, the electron spins of paramagnetic centers are irradiated with a nonresonance microwave field, while, in the alternative case, it is polarized protons that are subjected to the effect of a nonresonance radio-frequency field. It follows that the diagonal elements must be calculated by formulas (16) and (11), respectively.

The radioactive nucleus ^{22}Na (see Fig. 1) has a half-life of 2.6 yr, its spin–parity and the magnetic moment (in units of the nuclear magneton) being 3^+ and $\mu = +1.75$ [23], respectively. Presently, we do not know

experimental data that would suggest a nonzero quadrupole moment of the ^{22}Na nucleus (see [23, 24]). In order to demonstrate the potential of the new procedure for measuring quadrupole moments, we will nevertheless assume that this nuclear species has a small quadrupole moment, whose magnitude is to be determined. An intermediate nucleus ^{22}Na with spin $J' = 2$ is formed as the result of a Gamow–Teller β^+ transition characterized by an endpoint positron energy of 550 keV (or K capture). The half-life of this intermediate nucleus is 3.7×10^{-12} s; that is, its lifetime is much smaller than the characteristic period for the hyperfine splitting of atomic levels. The ^{22}Ne(2^+) state emits 1270-keV photons, going over to the stable spinless isotope ^{22}Ne [23].

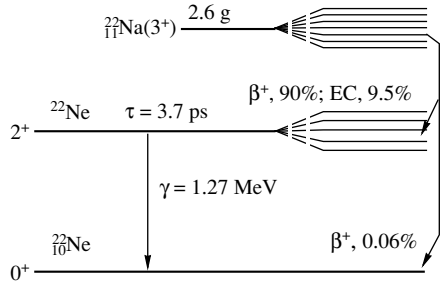

Fig. 1. Diagram of beta–gamma transitions for ^{22}Na(3^+) nuclear state.

In the case being considered, the angular distribution of 1270-keV photons with respect to the magnetic-field direction can be calculated by formulas (22) and (23), irrespective of the channel through which the transition ^{22}Na(3^+) $\longrightarrow$ ^{22}Ne(2^+) $\longrightarrow$ ^{22}Ne(0^+) occurs, β^+ decay into a positron and neutrino or K capture. In general, the ratio of the intensities of the gamma radiations emitted at zero and a right angle is given by

$$\frac{W(x,0)}{W(x,\pi/2)} = \frac{2}{3}\frac{10(\rho_{22}^{(3)}+\rho_{-2-2}^{(3)})+8(\rho_{11}^{(3)}+\rho_{-1-1}^{(3)})+3\rho_{00}}{5(\rho_{33}^{(3)}+\rho_{-3-3}^{(3)})+5(\rho_{22}^{(3)}+\rho_{-2-2}^{(3)})+3(\rho_{11}^{(3)}+\rho_{-1-1}^{(3)})+\rho_{00}}. \quad (27)$$

With the aid of Eqs. (16) and (17), it can be shown that, in the case of the Boltzmann distribution of Zeeman levels in a magnetic field, expression (27) assumes the form

$$\frac{W(x,0)}{W(x,\pi/2)} = \frac{2}{3}\frac{10\cosh(2x/3)+8\cosh(x/3)+3}{5\cosh(x)+5\cosh(2x/3)+3\cosh(x/3)+1}. \quad (28)$$

In experiments, it is convenient to calibrate detectors of nuclear radiation by using unpolarized nuclei, in which case the radiation is isotropic—that is, $W(x = 0) = W_0 = 1/(4\pi)$. Figure 2 shows the angular distributions of the gamma radiation from polarized nuclei ^{22}Na. These distributions, normalized to W_0, were calculated by formulas (22) and (23) with the distribution (16) of spins among magnetic sublevels at $J = 3$ and

$$x = 0.64\frac{H_0}{T}, \quad (29)$$

where H_0 and T are measured in T and mK, respectively. If $x \ll 1$ (weak magnetic field, high spin temperature), it can easily be shown that all the quantities $\rho_{mm}^{(3)}$ are approximately equal to one another, so that the angular distribution of photons is isotropic. At $x \gg 1$, in which case $\rho_{22}^{(2)} = \rho_{33}^{(3)} = 1$, there is a sharp anisotropy: expression (22) yields

$$W(\theta) = \frac{5}{16\pi}(1-\cos^4\theta). \quad (30)$$

If the quadrupole moment of ^{22}Na is equal to zero exactly, the Zeeman magnetic sublevels are equidistant; for a polycrystalline or an amorphous host material, the angular distribution has the shape shown in Fig. 2. In the process of dynamical orientation, spin temperature is reduced, whereby the vector polarization, which is determined by the Brillouin function

$$P_J = \frac{1}{J}\sum_{m=-J}^{J} m\rho_{mm} = B(x, J=3), \quad (31)$$

is increased. The angular distribution at $x = \pm 0.25$ in Fig. 2 corresponds to spin temperatures of about ± 6.6 mK, which are easily accessible in experiments; the distributions at $x = \pm 1.5$ are associated with the lowest temperatures of ± 1.1 mK. As was mentioned above, the shape of the distribution undergoes no changes upon reversal of the sign of temperature.

Another case of the angular distribution of gamma radiation, that of zero vector polarization and a high tensor polarization of radioactive nuclei, is illustrated in Fig. 3. It is assumed here that the microwave field that generated a dynamical orientation of nuclei owing to electron spins is switched off and that spin-3 radioactive nuclei having a nonzero quadrupole moment and occurring within a crystalline host material are polarized as the result of the radio-frequency saturation of polarized proton spins surrounding these radioactive nuclei (see Section 2). A calculation reveals that, at zero angle between the principal axis of the single crystal and the magnetic-field direction, the angular distribution of gamma radiation from the cascade beta–gamma decay of ^{22}Na is affected by a weak quadrupole interaction of the nucleus with a nonuniform electric field of the crystal. Solid and dashed curves represent the results for, respectively, positive and negative spin temperatures. The populations of spin states were deter-

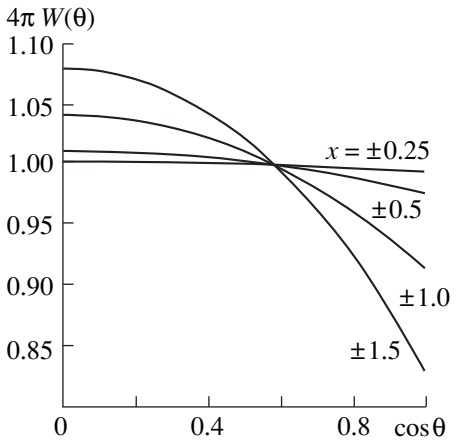

Fig. 2. Ratio of the angular distribution of gamma radiation in the cascade beta–gamma decay of the $^{22}Na(3^+)$ nuclear state to the isotropic distribution $W_0 = (4\pi)^{-1}$. The parameter x is given by Eq. (29).

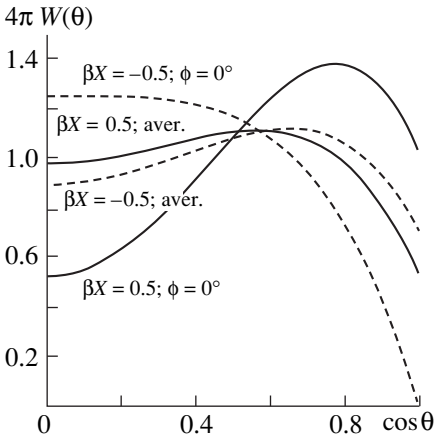

Fig. 3. Angular distributions of gamma radiation in the cascade beta–gamma decay of the $^{22}Na(3^+)$ nuclear state in a single crystal ($\phi = 0$) and in an amorphous host material (aver.) for specific spin temperatures of the same magnitude but of opposite signs. The label "aver." on the distributions for the latter case denotes that they are averaged over the angle ϕ. The graphs were calculated for a high tensor and zero vector polarization. It is assumed that $^{22}Na(3^+)$ nuclei in a dielectric host material have a small quadrupole moment.

mined by formula (11). It can be seen that, in the presence of quadrupole interaction, the shape of the angular distribution changes qualitatively upon reversal of the sign of temperature. In amorphous and polycrystalline samples, the density-matrix elements $\rho^{(3)}_{mm}(\cos\phi)$ in Eq. (23) must be averaged over the isotropic distribution of axes, the integration measure being $d(\cos\phi)$. As a result, the anisotropy is smoothed out to a considerable extent (see Fig. 3), but the dependence of the angular distribution of photons on the sign of spin temperature still survives.

In order to polarize nuclei having a large quadrupole moment, it is convenient to use the cross-relaxation method featuring polarized protons. For this, the field H_0 must be adiabatically reduced to a value at which the Zeeman splitting of proton spins in the residual field coincides with the frequency of the quadrupole transition [16] in the nuclei being considered. In the reduced field, the fast cross-relaxation process occurs between the proton spins and the spins of rare quadrupole nuclei [see Eq. (13)]. There is every reason to hope that the on-line polarization of quadrupole nuclei implanted in a polarized protonic target can be accomplished by using this method. As was mentioned above, this concurrently opens the possibility for preparing pure quantum states characterized by specific values of spin projections onto the magnetic-field direction [9]. For the same decay scheme $3^+ \xrightarrow[\beta]{} 2^+ \xrightarrow[\gamma]{} 0^+$ as for ^{22}Na, we have calculated the angular distribution of gamma radiation from nuclei occurring in pure quantum states. The results of this calculation are displayed in Fig. 4.

Dielectric host materials are advantageous in that the lattice temperature at which it is still possible to polarize quadrupole nuclei is higher in them (about 0.1 K) than in ferromagnetic host materials (about 0.01 K). This is because the cooling rate in a cooler employing a dissolution of ^3He in ^4He decreases quadratically with decreasing temperature, so that the rate of cooling of the material used is approximately 100 times higher at 0.1 K than at 0.01 K. By way of example, we indicate that, if a beam of intensity 10^5 radioactive nuclei per second that have an energy of 10 MeV/nucleon and a mass number of 60 is fully absorbed in a polarized target, the dissipated power is about 0.1 mW. At a temperature of about 0.1 K, this heat influx can readily be removed by a dissolution cooler of conventional power, but, at 0.01 K, the required cooling rate is inaccessible in practice. That it is necessary to reduce the field H_0 is a disadvantage of the method of cross-relaxation polarization because the time of nuclear spin–lattice relaxation decreases in this case down to a few tens of hours. Nonetheless, these times remain sufficiently long for on-line investigations in the realms of short-lived nuclei to be accomplished.

The above analysis implies that the method of dynamical orientation will be applicable in the case of rare nuclei as well. The question of whether this is so requires an experimental verification. Some other questions—for example, that of determining the rate at which rare nuclei are polarized by the dynamical-orientation method if they are implanted in a target that contains preliminarily polarized protons—also remain unclear. These and many other questions cannot be solved within classical NMR methods; here, it is necessary to perform direct experimental tests with radioactive nuclei.

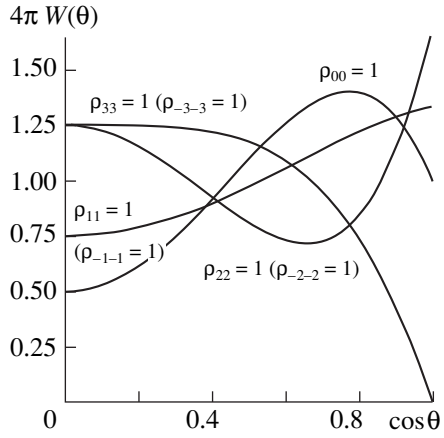

Fig. 4. Angular distributions of gamma radiation in the $3^+ \xrightarrow[\beta]{} 2^+ \xrightarrow[\gamma]{} 0^+$ cascade beta–gamma decay of a nucleus for the case where all spins are focused in the m_J state.

5. CONCLUSION

In applying methods of dynamical nuclear polarization to studying magnetic and quadrupole moments of implanted nuclei, an advantage offered by dielectric host materials in relation to ferromagnetic ones is that the former make it possible to do this at higher lattice temperatures (about 0.1 to 0.2 K), to eliminate the effect of the lattice on the spin system, and to weaken the effect of local intrinsic magnetic fields. Fundamentally, the dynamical polarization of radioactive nuclei will open the way to study special features of the statistics of rare nuclei and their spin–spin interactions and enable one to employ reversal of spin temperature to explore the quadrupole moments of such nuclei; we also hope that this method can be harnessed to implement on-line polarization of nuclei implanted in a polarized target. The above analysis reveals the physics and technological potential of the methods of dynamical nuclear polarization, as well as the possible limitations on the applications of these methods.

ACKNOWLEDGMENTS

We are grateful to F.S. Dzheparov for enlightening discussions on the methods of dynamical nuclear polarization.

APPENDIX

Let us consider an arbitrary two-body decay $C \longrightarrow a + b$. In the rest frame of the decaying particle C, the angular distribution of decay products has the form (see [18, p. 314])

$$W(\theta, \varphi) = \frac{2J+1}{4\pi}\sum_{\lambda_a\lambda_b}\sum_{mm'}|a(\lambda_a, \lambda_b)|^2 d^{(J)}_{\Lambda m}(\theta) \times d^{(J)}_{\Lambda m'}(\theta)e^{i(m-m')\varphi}\rho_{mm'}, \quad (A.1)$$

where θ and φ are, respectively, the polar and the azimuthal angle; J is the spin of particle C; λ_a and λ_b are the helicities (spin projections onto the momentum direction) of the final particles a and b, respectively; $\Lambda = \lambda_a - \lambda_b$; $a(\lambda_a, \lambda_b)$ are the helicity amplitudes normalized by the condition

$$\sum_{\lambda_a\lambda_b}|a(\lambda_a, \lambda_b)|^2 = 1; \quad (A.2)$$

m and m' are the projections of the spin of particle C onto the quantization axis; and $\rho_{mm'}$ are elements of the spin density matrix for particle C. The angular distribution in (A.1) satisfies the normalization condition

$$\int_0^{2\pi}\int_0^{\pi} W(\theta, \varphi)\sin\theta d\varphi d\theta = 1. \quad (A.3)$$

We further apply expression (A.1) to the decay of an excited spin-J particle into a photon and a final spinless nucleus. In this case, there is 2^J-pole radiation [of electric type if the relative parity of the parent and the daughter nucleus is $\eta = (-1)^J$ and of magnetic type if $\eta = (-1)^{J+1}$]. If particle a is a photon, its helicity can take only the values of $\lambda_a = +1$ and -1 because of zero photon mass. For particle b, we take here a final spinless nucleus ($\lambda_b = 0$). Taking into account parity conservation and Eq. (A.2), we obtain

$$|a(+1, 0)|^2 = |a(-1, 0)|^2 = \frac{1}{2}. \quad (A.4)$$

Assuming that, in equilibrium, the spin density matrix is diagonal in the representation of states characterized by specific values of the spin projection onto the magnetic-field direction and considering that d functions possess the property

$$\left|d^{(J)}_{\Lambda m}(\theta)\right|^2 = \left|d^{(J)}_{m\Lambda}(\theta)\right|^2,$$

we arrive at expression (14), which involves no additional gamma-decay parameters. If J' is nonzero, the angular distribution of photons depends on the ratio of helicity amplitudes. In the case of a diagonal spin density matrix, the angular distribution of photons that is constructed with allowance for parity conservation can be represented as

$$W(\theta) = \frac{2J+1}{4\pi}\sum_{\lambda_b=-J'}^{J'}|a(1, \lambda_b)|^2 \times [(d^{(J)}_{m,1-\lambda_b}(\theta))^2 + (d^{(J)}_{m,-(1-\lambda_b)}(\theta))^2], \quad (A.5)$$

where

$$|a(+1, \lambda_b)|^2 = |a(-1, -\lambda_b)|^2,$$
$$\sum_{\lambda_b}|a(+1, \lambda_b)|^2 = \sum_{\lambda_b}|a(-1, -\lambda_b)|^2 = \frac{1}{2}. \quad (A.6)$$

REFERENCES

1. *Alpha-, Beta-, and Gamma-Ray Spectroscopy*, Ed. by K. Siegbahn (North-Holland, Amsterdam, 1968; Atomizdat, Moscow, 1969).
2. D. G. Crabb and W. Meyer, Annu. Rev. Nucl. Part. Sci. **47**, 67 (1997).
3. N. S. Borisov *et al.*, Preprints Nos. 13-10253, 13-10257, OIYaI (Joint Institute for Nuclear Research, Dubna, 1976); Prib. Tekh. Éksp., No. 2, 32 (1978).
4. A. Abragam and M. Goldman, *Nuclear Magnetism: Order and Disorder* (Clarendon, Oxford, 1982; Mir, Moscow, 1984), Vol. 2, Chap. 6.
5. M. A. Kozhushner, Zh. Éksp. Teor. Fiz. **56**, 246 (1969) [Sov. Phys. JETP **29**, 136 (1969)].
6. V. A. Atsarkin, *Dynamical Polarization of Atomic Nuclei in Solid Dielectrics* (Nauka, Moscow, 1980).
7. W. De Boer *et al.*, Phys. Lett. A **46**, 143 (1973).
8. W. De Boer, Yellow Report 74-11, CERN (Geneva, 1974).
9. F. S. Dzheparov and Yu. F. Kiselev, Pis'ma Zh. Éksp. Teor. Fiz. **68**, 539 (1998) [JETP Lett. **68**, 563 (1998)].
10. Yu. F. Kiselev, V. L. Lyuboshits, M. I. Podgoretskiĭ, and A. N. Chernikov, Kratk. Soobshch. Ob'edin. Inst. Yad. Issled., Dubna, No. 3-[29] (1988); Soobshch. Ob'edin. Inst. Yad. Issled., Dubna, No. E14-89-195 (1989).
11. B. N. Provotorov, Zh. Éksp. Teor. Fiz. **41**, 1582 (1961) [Sov. Phys. JETP **14**, 1126 (1961)]; Zh. Éksp. Teor. Fiz. **42**, 882 (1962) [Sov. Phys. JETP **15**, 611 (1962)].
12. M. E. Zhabotinskiĭ, A. E. Mefed, and M. I. Rodak, Pis'ma Zh. Éksp. Teor. Fiz. **11**, 482 (1970) [JETP Lett. **11**, 328 (1970)].
13. C. P. Slichter, *Principles of Magnetic Resonance* (Springer-Verlag, Berlin, 1980; Mir, Moscow, 1981), Chap. 9.
14. L. D. Landau and E. M. Lifshitz, *The Classical Theory of Fields* (Pergamon, Oxford, 1975; Nauka, Moscow, 1988).
15. L. D. Landau and E. M. Lifshitz, *Quantum Mechanics: Non-Relativistic Theory* (Nauka, Moscow, 1989, 4th ed.; Pergamon, Oxford, 1977, 3rd ed.).
16. B. Adeva *et al.*, Preprint CERN-PPE/97-66, CERN (Geneva, 1997); D. Adams *et al.*, Nucl. Instrum. Methods Phys. Res. A **437**, 23 (1999).
17. F. S. Dzheparov, Zh. Éksp. Teor. Fiz. **99**, 982 (1991) [Sov. Phys. JETP **72**, 546 (1991)]; Yu. G. Abov, A. D. Gul'ko, F. S. Dzheparov, *et al.*, Fiz. Élem. Chastits At. Yadra **26**, 1654 (1995) [Phys. Part. Nucl. **26**, 692 (1995)].
18. A. M. Baldin, V. I. Goldanskiĭ, and I. L. Rozental', *Kinematics of Nuclear Reactions* (Oxford Univ. Press, London, 1961; Atomizdat, Moscow, 1968, 2nd ed.), Chap. II.
19. V. B. Berestetskiĭ, E. M. Lifshitz, and L. P. Pitaevskiĭ, *Quantum Electrodynamics* (Nauka, Moscow, 1980; Pergamon, Oxford, 1982).
20. J. S. Smart, *Effective Field Theories of Magnetism* (Saunders, London, 1966; Mir, Moscow, 1986).
21. A. I. Akhiezer and V. B. Berestetskii, *Quantum Electrodynamics* (Wiley, New York, 1965; Nauka, Moscow, 1969).
22. A. S. Davydov, *Theory of Atomic Nucleus* (GIFML, Moscow, 1958), Chap. 6.
23. *Table of Isotopes*, Ed. by M. C. Lederer and V. S. Shirley (Wiley, New York, 1978).
24. *Physical Quantities: A Handbook*, Ed. by A. P. Babichev *et al*. (Énergoatomizdat, Moscow, 1991).

Translated by A. Isaakyan

Physics of Atomic Nuclei, Vol. 64, No. 1, 2001, pp. 27–37. Translated from Yadernaya Fizika, Vol. 64, No. 1, 2001, pp. 29–39.

NUCLEI
Theory

Effective Adiabatic Approximation in the Problem of Three Bodies Coupled via Short-Range Potentials

S. I. Vinitsky, S. Y. Larsen[1)], D. V. Pavlov, and D. V. Proskurin*

Joint Institute for Nuclear Research, Dubna, Moscow oblast, 141980 Russia

Received December 23, 1999; in final form, May 12, 2000

Abstract—The effective adiabatic approximation is constructed for the problem of three bodies on a straight line that are coupled via short-range attractive delta-function potentials. It is shown that, in this system, there arise a nonlocal momentum-dependent long-range effective potential and a polarization potential. A lower bound on the binding energy of the system is obtained to a relative precision of about 10^{-6}. It is shown that, to within 0.03%, this approximation yields a correct asymptotic behavior of solutions and a correct behavior of the phase shift for elastic scattering at relative momenta below the three-body-breakup threshold. A local convergence of the adiabatic expansion in a finite interval of the radial variable is demonstrated. © *2001 MAIK "Nauka/Interperiodica".*

Dedicated to the blessed memory of Professor Vladimir Vasil'evich Babikov

1. INTRODUCTION

Nonlocal potentials and momentum-dependent potentials, referred to in the literature as velocity-dependent potentials, have been widely used to construct a phenomenological description of nucleon–nucleon interaction [1]. Similar potentials arise in the adiabatic representation of the three-body problem [2] as the result of implementing projection onto open channels via a canonical transformation [3]. This construction of the effective adiabatic approximation is similar to projecting solutions to the Dirac equations onto large components by means of the well-known canonical Foldy–Wouthuysen transformation [4]. It is of topical interest to investigate the convergence of the adiabatic method and to construct an effective approximation of solutions that is consistent with correct boundary conditions [5]. For investigations of the proposed type, it is convenient to use the problem of three particles on a straight line that are coupled by pair delta-function potentials [6] since this problem has an analytic solution [7]. The first steps along these lines were made in [8]. It was shown there that the standard adiabatic approximation yields an upper bound on the exact value of energy and a lower bound on the phase shift for elastic scattering. However, the exact phase-shift value and the phase shift in the adiabatic approximation were found to diverge significantly as the relative momentum increases up to the three-body-breakup threshold. This is because the full set of adiabatic equations is truncated to one equation of the conventional adiabatic approximation. A direct analysis of the convergence of the adiabatic expansion for an infinite set of coupled equations is a rather cumbersome problem, so that the application of an alternative approach within the effective adiabatic approximation seems preferable.

For a system of three identical particles on a straight line that interact via attractive pair delta-function potentials, we construct here an effective adiabatic approximation involving a momentum-dependent potential. Within the effective adiabatic approximation, asymptotic expressions for solutions to an infinite set of equations in the adiabatic representation are derived by isolating an asymptotic energy-dependent centrifugal potential that is calculated on the basis of sum rules for a complete set of asymptotic adiabatic basis functions. The convergence of the adiabatic expansion is checked numerically by considering saturation of the sum rules. It is shown that the inclusion of nonadiabatic channel coupling restores exact values of elastic-scattering phase shifts in asymptotic solutions. By means of direct calculations in the effective adiabatic approximation, we find a new lower bound on the exact value of energy and reproduce a correct behavior of the phase shift as the relative momentum increases up to the three-body-breakup threshold.

2. FORMULATION OF THE PROBLEM

For three identical particles on a straight line, we introduce local Jacobi coordinates $\{\xi, \eta\} \in \mathbf{R}^2$ in the c.m. frame as

$$\eta = \left(\frac{1}{2}\right)^{1/2}(x_1 - x_2),$$
$$\xi = \left(\frac{2}{3}\right)^{1/2}\left[\left(\frac{x_1 + x_2}{2}\right) - x_3\right], \quad (1)$$

[1)] Temple University, Barton Hall, 1900 N. 13th St., Philadelphia, PA 19122-6082, USA.
* e-mail: proskur@thsun1.jinr.ru

where $\{x_1, x_2, x_3\} \in \mathbf{R}^1$ are the Cartesian coordinates of the particles. Let us now go over to hyperspherical coordinates ρ and θ, which, in our case, appear to be the conventional polar coordinates

$$\eta = \rho\cos\theta, \quad \xi = \rho\sin\theta, \quad -\pi \le \theta \le \pi. \tag{2}$$

In terms of the hyperspherical coordinates, the Schrödinger equation for the wave function takes the form

$$-\frac{\hbar^2}{2m}\left[\frac{1}{\rho}\frac{\partial}{\partial\rho}\rho\frac{\partial}{\partial\rho} + \frac{1}{\rho^2}\frac{\partial^2}{\partial\theta^2}\right]\Psi(\rho,\theta) + V(\rho,\theta)\Psi(\rho,\theta) = E\Psi(\rho,\theta), \tag{3}$$

where E is the c.m. energy and $m = (m_1m_2 + m_1m_3 + m_2m_3)/(m_1 + m_2 + m_3)$ is the effective mass [9], which coincides, for identical particles ($m_1 = m_2 = m_3 = m$), with the mass m of each particle. Let us define the potential $V(\rho, \theta)$ as the sum of pair potentials

$$V(\rho,\theta) = V(\sqrt{2}\rho|\cos\theta|) + V(\sqrt{2}\rho|\cos(\theta - 2\pi/3)|) + V(\sqrt{2}\rho|\cos(\theta + 2\pi/3)|). \tag{4}$$

In order to be able to draw a comparison with an exactly solvable problem [7], we investigate the reduced two-body Hamiltonian

$$h^{(0)} = -\frac{\partial^2}{\partial\eta^2} + \frac{2m}{\hbar^2}V(\sqrt{2}\eta),$$

which involves a pair potential proportional to a delta function, $V(\sqrt{2}\,\eta) = g\delta(|\eta|)/\sqrt{2}$, with the coupling constant $g = c\kappa(\hbar^2/m)$ being taken at $\kappa = \sqrt{2}\,\pi/6$. In the case of attraction ($c = -1$), the Schrödinger equation in the local representation of the pair channel ($\eta/\rho \gg 1$) then has the form (in the system of units where $\hbar = m = 1$)

$$\left(-\frac{\partial^2}{\partial\eta^2} - 2\bar{\kappa}\delta(|\eta|) - \epsilon_j^{(0)}\right)\phi_j(\eta) = 0, \tag{5}$$

where $\bar{\kappa} = \kappa/\sqrt{2} = \pi/6$ is the effective coupling constant in the pair potential and $\epsilon_j^{(0)} = 2mE_j/\hbar^2$ is the doubled energy of the two-particle system. A complete set of solutions belonging to the discrete and the continuous spectrum of the two-body Hamiltonian has the form

$$\epsilon_0^{(0)} = -\bar{\kappa}^2, \quad \phi_0(\eta) = \sqrt{\bar{\kappa}}\exp(-\bar{\kappa}|\eta|),$$

$$\langle 0|0\rangle = \int_{-\infty}^{+\infty}\phi_0^*(\eta)\phi_0(\eta)d\eta = 1,$$

$$\epsilon_p^{(0)} = p^2, \quad \phi_p(\eta) = \frac{1}{\sqrt{2\pi}}\left(\exp(ip\eta) + \frac{it_p}{|p|}\exp(i|p||\eta|)\right), \tag{6}$$

$$t_p = \frac{\bar{\kappa}|p|}{|p| - i\bar{\kappa}},$$

$$\langle 0|p\rangle = \int_{-\infty}^{+\infty}\phi_0^*(\eta)\phi_p(\eta)d\eta = 0,$$

$$\langle p|p'\rangle = \int_{-\infty}^{+\infty}\phi_p^*(\eta)\phi_{p'}(\eta)d\eta = \delta(p - p').$$

Having isolated the factor $\rho^{-1/2}$ in solutions to Eq. (3) with the aid of the standard substitution $\Psi = \rho^{-1/2}\tilde{\Psi}$, we obtain

$$\left[-\frac{\partial^2}{\partial\rho^2} + \bar{h}_\rho - \frac{2mE}{\hbar^2}\right]\tilde{\Psi}(\rho,\theta) = 0, \tag{7}$$

where $\bar{h}_\rho$ is a parametric Hamiltonian at each fixed value of $\rho \in \mathbf{R}_+^1$. Specifically, we have

$$\bar{h}_\rho = h_\rho - \frac{1}{4\rho^2}, \quad h_\rho = h_\rho^{(0)} + \frac{2m}{\hbar^2}V(\rho,\theta), \quad h_\rho^{(0)} = -\frac{1}{\rho^2}\frac{\partial^2}{\partial\theta^2}, \tag{8}$$

where the potential energy (4) for the case of attraction ($c = -1$) characterized by the effective coupling constant $\bar{\kappa} = \pi/6$ is given by

$$\frac{2m}{\hbar^2}V(\rho,\theta) = 2\frac{c\bar{\kappa}}{\rho}\sum_n\delta(\theta - \theta_n), \quad \theta_n = n\pi/3 + \pi/6, \quad n = 0, 1, \ldots, 5.$$

A complete orthogonal set of the adiabatic functions $B_j(\rho, \theta) \in F_\rho \sim L_2(C)$ is determined by solutions to the eigenvalue problem on the circle C ($-\pi \le \theta \le \pi$); that is,

$$\bar{h}_\rho B_j(\rho,\theta) = \Lambda_j(\rho)B_j(\rho,\theta), \quad \Lambda_j(\rho) = \epsilon_j(\rho) - \frac{1}{4\rho^2},$$

$$\langle B_i(\rho)|B_j(\rho)\rangle_C = \int_{-\pi}^{\pi}B_i^*(\rho,\theta)V(\rho,\theta)B_j(\rho,\theta)d\theta = \delta_{ij}. \tag{9}$$

The set of the eigenfunctions that are fully symmetric with respect to permutations of identical particles,

which includes the ground state, has the form [6]

$$B_0(\rho,\theta) = \sqrt{\frac{y_0^2 - x^2}{\pi(y_0^2 - x^2) + |x|}}\cosh[6y_0(\theta - n\pi/3)],$$
$$B_j(\rho,\theta) = \sqrt{\frac{y_j^2 + x^2}{\pi(y_j^2 + x^2) - |x|}}\cos[6y_j(\theta - n\pi/3)] \quad (10)$$

for the following six sectors of the circle C:

$$n\pi/3 - \pi/6 \le \theta \le n\pi/3 + \pi/6, \quad n = 0, 1, \ldots, 5.$$

The eigenvalues $\epsilon_0(\rho)$ and $\epsilon_j(\rho)$ can be expressed in terms of the reduced eigenvalues y_0 and y_j as

$$\epsilon_0(\rho) = -\left(\frac{6y_0}{\rho}\right)^2, \quad \epsilon_j(\rho) = \left(\frac{6y_j}{\rho}\right)^2.$$

The eigenvalues y_0 and y_j are determined from the transcendental equations

$$y_0\tanh(\pi y_0) = -x, \quad y_j\tan(\pi y_j) = x,$$
$$j - 1/2 < y_j < j, \quad j = 1, 2, 3, \ldots, \quad (11)$$

where

$$x = c\frac{\bar{\kappa}}{6}\rho = c\frac{\pi}{36}\rho.$$

We note that the matrix elements $V_{KK'}(\rho)$ of the potential energy (4) that are taken between the solutions $B_K^{(0)}(\theta) \in F_0 \sim L_2(C)$ to the problem of a free rotation on the circle C with the Hamiltonian $h_\rho^{(0)}$ and which do not vanish at $K - K' \equiv 0 (\mathrm{mod}\ 6)$ are given by

$$(2m/\hbar^2)\langle K|V(\rho)|K'\rangle_C = (c/\rho)\exp(-iK\pi/2)\exp(iK'\pi/2).$$

In the vicinity of the triple collision point $\rho = 0$, these matrix elements are negligibly small in relation to the matrix elements of the rotation operator that have the form

$$\langle K|h_\rho^{(0)}|K'\rangle_C = \rho^{-2}K(K+1)\delta_{KK'}.$$

Therefore, the set $K \equiv j (\mathrm{mod}\, 6)$—that is, $K = 6j$, $j = 0, 1, 2, \ldots$—classifies the eigenfunctions of the parametric Hamiltonian $\bar{h}_\rho$

$$\Lambda_j(\rho) \longrightarrow \Lambda_K^{(0)}(\rho) = \frac{K^2 - 1/4}{\rho^2},$$
$$B_j(\rho,\theta) \longrightarrow B_K^{(0)}(\theta) = \frac{1}{\sqrt{2\pi}}\exp(iK\theta). \quad (12)$$

For large values of ρ, it can be shown that, in one of the sectors of the circle C, local asymptotic solutions to the parametric problem (9) correspond to the solution in (6) for the $\phi_j(\eta)$ pair channel. In particular, the eigenfunctions of the Hamiltonian h_ρ correspond to the solutions for the pair channel at $j = 0$, that is,

$$\epsilon_0(\rho) \longrightarrow \epsilon_0^{(0)}, \quad B_0(\rho,\theta) \longrightarrow \sqrt{\rho}\phi_0(\eta). \quad (13)$$

If, however, $j \neq 0$, then it follows from the rule of alternation of solutions to the transcendental Eq. (11) that we can determine the countable covering $K/\rho \sim p$ and use the correspondence

$$\epsilon_j(\rho) \longrightarrow \epsilon_p^{(0)}, \quad B_j(\rho,\theta) \longrightarrow \sqrt{\rho}\phi_p(\eta), \quad (14)$$

which completes a formal classification of the set of adiabatic basis functions. An additional symmetrization of asymptotic sets is performed by means of a simple transformation of the exponential functions into cosines; however, it is more straightforward to calculate matrix elements in the exponential representation. By using the above correspondence of the bases at small and large ρ values, we can introduce a global adiabatic representation formed by the K-harmonic representation and a local Jacobi representation for the radial wave function Ψ in terms of the coordinates (ρ, θ) and (ρ, η), respectively; that is,

$$\Psi = \rho^{-1/2}\sum_j B_j(\rho,\theta)\chi_j(\rho)$$
$$\longrightarrow \left\{\begin{array}{l} \rho^{-1/2}\displaystyle\sum_{K=-\infty}^{\infty} B_K^{(0)}(\theta)\chi_K^{(0)}(\rho) \\ \phi_0(\eta)\chi_0(\rho) + \displaystyle\int_{-\infty}^{\infty} dp\,\phi_p(\eta)\chi_p(\rho) \end{array}\right\}. \quad (15)$$

Averaging Eq. (7) over the basis $B_K^{(0)}(\theta)$, we arrive at a set of coupled equations ($\hbar = m = 1$) in the K-harmonic representation [9]:

$$\left(-\frac{d^2}{d\rho^2} + \Lambda_K^{(0)}(\rho) - 2E\right)\chi_K^{(0)}(\rho)$$
$$+ \sum_{K'} V_{KK'}(\rho)\chi_{K'}^{(0)}(\rho) = 0. \quad (16)$$

Upon averaging Eq. (7) over the basis $B_i(\rho, \theta) = \sum_K B_K^{(0)}(\theta)U_{Ki}(\rho)$, where $U_{Ki}(\rho) = \langle B_K^{(0)}|B_i(\rho)\rangle_C$ is a unitary operator ($U(\rho)$: $F_0 \mapsto F_\rho$) that implements the transportation of the basis F_ρ from the point $\rho = 0$ to the point ρ, $U(\rho)$: $F_0 \mapsto F_\rho$, we obtain the set of coupled adiabatic equations

$$\left(-\frac{d^2}{d\rho^2} + \Lambda_i(\rho) - 2E\right)\chi_i(\rho)$$
$$+ \sum_j\left(-A_{ij}(\rho)\frac{d}{d\rho} - \frac{d}{d\rho}A_{ij}(\rho) + H_{ij}(\rho)\right)\chi_j(\rho) = 0, \quad (17)$$

where

$$A_{ij}(\rho) = \left\langle B_i(\rho)\left|\frac{\partial}{\partial\rho}B_j(\rho)\right\rangle_C,\right.$$
$$H_{ij}(\rho) = \left\langle \frac{\partial}{\partial\rho}B_i(\rho)\left|\frac{\partial}{\partial\rho}B_j(\rho)\right\rangle_C.\right. \quad (18)$$

It should be noted that the $A = \{A\}_{ij}$ is an anti-Hermitian matrix and that $H = \{H\}_{ij}$ is a Hermitian matrix:

$$A_{ij}(\rho) = \sum_K U^{-1}_{iK}(\rho)\frac{\partial}{\partial\rho}U_{Kj}(\rho),$$
$$H_{ij} = -(A^2)_{ij} = -\sum_{j'} A_{ij'}A_{j'j}. \quad (19)$$

The set of adiabatic Eqs. (17) can be represented in the gauge-invariant form [2]

$$\left(-\left(1\otimes\frac{d}{d\rho}+A(\rho)\right)^2+\Lambda(\rho)-2E\otimes 1\right)\chi(\rho) = 0.$$

In order to calculate the matrix elements $A_{ij}(\rho)$, we make use of the standard relation

$$A_{ij}(\rho) = -\frac{1}{\rho}\frac{\langle i|2V(\rho)|j\rangle}{\epsilon_i(\rho)-\epsilon_j(\rho)},$$

where the matrix elements of the potential energy (4) are calculated by using the functions in (10). In order to determine $B_0(\rho,\theta)$ and $B_j(\rho,\theta)$ explicitly, it is convenient to represent the transcendental Eqs. (11) in the form

$$\cosh(\pi y_0) = \frac{|y_0|}{\sqrt{y_0^2-x^2}},\quad \cos(\pi y_j) = \frac{(-1)^j y_j}{\sqrt{y_j^2+x^2}}.$$

Eventually, we derive analytic expressions for $A_{jj'}$ in terms of the solutions y_0 and y_j to the transcendental equations [10]

$$A_{jj'}(\rho) = \begin{cases} -\dfrac{c\pi}{18}\dfrac{(-1)^j y_j|y_0|}{(y_0^2+y_j^2)\sqrt{\pi(y_j^2+x^2)-|x|}\sqrt{\pi(y_0^2-x^2)+|x|}}, \\ j' = 0, \quad (19a) \\ \dfrac{c\pi}{18}\dfrac{(-1)^{j-j'}y_j y_{j'}}{(y_{j'}^2-y_j^2)\sqrt{\pi(y_j^2+x^2)-|x|}\sqrt{\pi(y_{j'}^2+x^2)-|x|}}, \\ j\neq 0,\quad j'\neq 0. \end{cases}$$

At large values of ρ, the asymptotic behavior of the matrix elements $A_{ij}(\rho)$ in the local representation are given by

$$A_{ij}(\rho) = A_{ij}^{(0)}\rho^{-1}+O(\rho^{-3}),$$
$$A_{ij}^{(0)} = \int_{-\infty}^{+\infty} d\eta\,\phi_i^*(\eta)\hat{A}^{(0)}\phi_j(\eta), \quad (20)$$
$$\hat{A}^{(0)} = \frac{1}{2}+\eta\frac{\partial}{\partial\eta}.$$

For the matrix elements between the functions of the discrete and the continuous spectrum for the pair channel, we arrive at the standard representation

$$A_{ij}^{(0)} = \frac{1}{4}\langle\phi_i[\eta^2, h^{(0)}]\phi_j\rangle$$
$$= -\frac{1}{4}(\epsilon_i^{(0)}-\epsilon_j^{(0)})\langle\phi_i|\eta^2|\phi_j\rangle. \quad (21)$$

The corresponding expressions for the matrix elements $\langle 0|\eta^2|j\rangle$ can be written in the form

$$\langle 0|\eta^2|0\rangle = \frac{1}{2\bar{\kappa}^2},\quad \langle 0|\eta^2|p\rangle = \sqrt{\frac{\bar{\kappa}}{2\pi}}\frac{8\bar{\kappa}p}{(\bar{\kappa}^2+p^2)^{5/2}}. \quad (22)$$

By going over from summation over j in (15) to integration and substituting the expressions for the matrix elements (21) and (22), we obtain the sum rule

$$4\sum_{j\neq i}\frac{A_{0j}^{(0)}A_{j0}^{(0)}}{\epsilon_0^{(0)}-\epsilon_j^{(0)}} = -\langle 0|\eta^2\hat{A}^{(0)}|0\rangle = \langle 0|\eta^2|0\rangle = \frac{1}{2\bar{\kappa}^2}. \quad (23)$$

By substituting the relevant expressions (20)–(22) into the definition of the diagonal matrix element $H_{00}(\rho)$ in terms of $A_{0j}^{(0)}(\rho)$, using expression (19), and replacing summation over j by integration with respect to p, we find from a direct calculation that $H_{00}(\rho) = 1/(4\rho^2) + O(\rho^{-4})$. This expression ensures a correct asymptotic behavior of the adiabatic potential $\Lambda(\rho) + H_{00}(\rho) = \epsilon_0^{(0)} + O(\rho^{-4})$ and can be used to verify the validity of the sum rule (19) by performing summation of the matrix elements $A_{jj'}$ calculated in terms of roots of the transcendental Eqs. (11) over j. As a result, Eqs. (17) in the local representation of the pair channel $|0\rangle$ can be written in the form

$$\left(-\frac{d^2}{d\rho^2}+\epsilon_i^{(0)}-\epsilon_0^{(0)}-q^2\right)\chi_{i0}(\rho,q)$$
$$-\frac{2}{\rho}\sum_i A_{ij}^{(0)}\frac{d}{d\rho}\chi_{j0}(\rho,q) = 0, \quad (24)$$

where $q^2 = \epsilon = 2E - \epsilon_0^{(0)}$ is the doubled relative energy reckoned from the two-body threshold $\epsilon_0^{(0)} = \bar{\kappa}^2$.

3. EFFECTIVE ADIABATIC APPROXIMATION

Let us define the effective adiabatic approximation as the result of projecting the set of adiabatic Eqs. (17) onto the two-body channel:

$$\left(\frac{d}{d\rho}\mu^{-1}(\rho)\frac{d}{d\rho}-U_{\rm eff}(\rho)+q^2\right)\chi_{\rm eff}(\rho) = 0. \quad (25)$$

The solution $\chi_{\text{eff}}(\rho) \equiv \chi_i^{\text{new}}$ is related to the solution $\chi_j(\rho)$ of the set of Eqs. (17) by the canonical transformation

$$\chi_i^{\text{new}} = T_{ij}\chi_j = \sum_{jj'}\langle i|e^{iS^{(2)}}|j'\rangle\langle j'|e^{iS^{(1)}}|j\rangle\chi_j, \qquad (26)$$

where

$$iS_{ij}^{(1)} = \Delta_{ij}^{-1}\left(H_{ij} - A'_{ij} - 2A_{ij}\frac{d}{d\rho}\right),$$
$$iS_{ij}^{(2)} = -2\Delta_{ij}^{-2}A_{ij}V'_{jj}. \qquad (27)$$

The effective potential $U_{\text{eff}}(\rho)$ and the effective mass $\mu(\rho)$ are given by

$$U_{\text{eff}}(\rho) = U_{\text{ad}}(\rho) + \delta U(\rho),$$
$$U_{\text{ad}}(\rho) = -\frac{1}{4\rho^2} + \epsilon_0(\rho) - \epsilon_0^{(0)} + H_{00}(\rho), \qquad (28)$$

$$\mu^{-1}(\rho) = 1 + W(\rho), \qquad (29)$$

$$W(\rho) = -4\sum_{j\neq 0}A_{0j}(\rho)A_{j0}(\rho)\Delta_{0j}^{-1}(\rho), \qquad (30)$$

$$\delta U(\rho) = \sum_{j\neq 0}(\Delta_{0j}^{-1}V_{0j}^{(1)} + \Delta_{0j}^{-2}V_{0j}^{(2)} + \Delta_{0j}^{-3}V_{0j}^{(3)}), \qquad (31)$$

where $U_{\text{ad}}(\rho)$ is the adiabatic potential and $\delta U(\rho)$ is the effective nonadiabatic correction. Here, we have used the relations

$$V_{0j}^{(1)} = H_{0j}^2 - (A'_{0j})^2 - 2A_{0j}H'_{0j} - 2A_{0j}A''_{0j},$$
$$V_{0j}^{(2)} = -H_{0j}A_{0j}(\Sigma'_{0j} - \Delta'_{0j})$$
$$+ A_{0j}A'_{0j}(\Sigma'_{0j} + 3\Delta'_{0j}) + A_{0j}^2(\Sigma''_{0j} + \Delta''_{0j}),$$
$$V_{0j}^{(3)} = A_{0j}^2(\Sigma'_{0j} + \Delta'_{0j})(\Sigma'_{0j} - 2\Delta'_{0j}),$$
$$V_{00} = V_{00}(\rho) = \Lambda_0(\rho) + H_{00}(\rho),$$
$$V_{jj} = V_{jj}(\rho) = \Lambda_j(\rho) + H_{jj}(\rho), \qquad (32)$$
$$H_{00} = H_{00}(\rho) = -\sum_i A_{0i}A_{i0},$$
$$H_{0j} = H_{0j}(\rho) = -\sum_i A_{0i}A_{ij},$$
$$\Delta_{0j} = \Delta_{0j}(\rho) = V_{00} - V_{jj},$$
$$\Sigma_{0j} = \Sigma_{0j}(\rho) = V_{00} + V_{jj},$$

where primes denote differentiation with respect to ρ. All quantities that appear in Eqs. (28)–(32), with the exception of $\epsilon_0^{(0)}$, are functions of ρ and are calculated in terms of the roots of the transcendental Eqs. (11) by using the analytic expressions (19) and (19a) for $A_{0j}(\rho)$ and $H_{0j}(\rho)$. The correction $W(\rho)$ to the effective mass $\mu(\rho)$ is displayed in Fig. 1*a*, while saturation of the relevant sum in (30) calculated at various values of the harmonic number j is illustrated in Fig. 1*b*. The graph of the nonadiabatic correction $\delta U(\rho)$ to the effective potential is shown in Fig. 2*a*. The adiabatic potential $U_{\text{ad}}(\rho) = U_{\text{eff}}(\rho) - \delta U(\rho)$ and the effective potential $U_{\text{eff}}(\rho)$ reckoned from the doubled energy of the two-body threshold, $\epsilon_0 = 2E_0 = -\pi^2/36$, are compared in Fig. 2*b*. We note that the exponential behavior of the adiabatic potential U_{ad} over the range $\rho \in (25, 40)$ (see the inset in Fig. 2*b*) is compensated in the effective potential U_{eff} by the nonadiabatic correction δU shown in Fig. 2*a*. In Fig. 3*a*, we can see how, with increasing number j of the adiabatic state, the relevant sum (19) converges to the correct asymptotic expression of the exponentially decreasing adiabatic potential $U_{\text{ad}}(\rho) = -(\pi^2/9)\exp\{-\rho\pi^2/18\}\{1 - \rho\pi^4/1944 + \pi^2/36 + 1/2\rho\}$ [8]. Figure 3*b* illustrates the analogous convergence of the sum in (31) multiplied by ρ^4 to the effective polarization potential U_{eff} tending to the constant $-18/\pi^2$. By using expressions (20)–(23) in order to describe the asymptotic behavior of $A_{ij}(\rho)$, we find that the asymptotic expression for the effective mass is

$$\mu^{-1}(\rho) \sim 1 + \frac{W_{00}^{(0)}}{\rho^2},$$
$$W_{00}^{(0)} = -\langle 0|\eta^2|0\rangle = -\frac{1}{2\bar{\kappa}^2} \quad \text{for} \quad \rho \longrightarrow +\infty. \qquad (33)$$

From Fig. 1*a*, it can be seen that, for $\rho \longrightarrow +\infty$, the asymptotic behavior of the function $W(\rho)$ determined by Eq. (30) is given by $\rho^2 W(\rho_{\max}) \longrightarrow -18/\pi^2$. Figure 1*b* shows that the maximal value of j necessary for ensuring a preset accuracy of the approximation of the sum rule in Eq. (23) grows with ρ. Taking into account the consistency conditions at large values of ρ,

$$-A_{00}^2(\rho) - \frac{1}{4}\rho^{-2} = O(\rho^{-4}), \qquad (34)$$

we can recast Eqs. (17) into the form

$$\left[\frac{d^2}{d\rho^2} + q^2\left(1 - \frac{W_{00}^{(0)}}{\rho^2}\right)\right]\chi_{\text{eff}}(\rho) = 0. \qquad (35)$$

For $q\langle 0|\eta^2|0\rangle/(2\rho) \ll 1$, the solutions to Eq. (25) that are associated with the continuous spectrum can be represented in the form

$$\chi_{\text{eff}}(\rho) \sim \sin\left[q\rho\left(1 - \frac{\langle 0|\eta^2|0\rangle}{2\rho^2}\right) + \delta\right] \sim \sin(q\rho + \delta)$$
$$- q\frac{\langle 0|\eta^2|0\rangle}{2\rho}\cos(q\rho + \delta). \qquad (36)$$

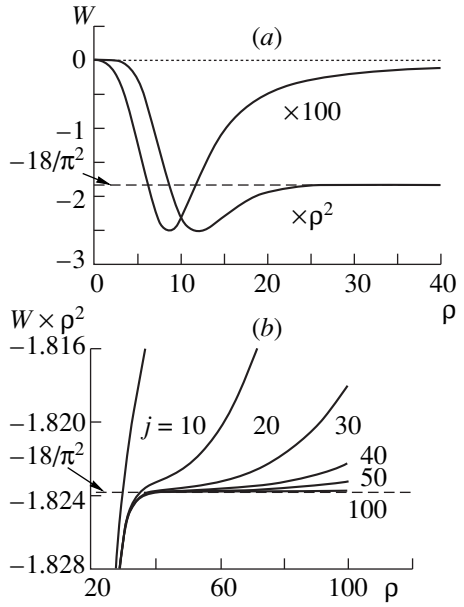

Fig. 1. (*a*) Correction $W(\rho)$ (30) to the effective mass $\mu(\rho)$ and (*b*) saturation of the sum in (30) calculated at various values of the harmonic number j.

The solutions $\chi_j(\rho)$ to the set of Eqs. (17) and the solutions $\chi_{\text{eff}}(\rho)$ to the effective Eq. (25) are related by the inverse transformation (26). At large values of ρ, there exists correspondence between solutions to Eqs. (17) and Eq. (25),

$$\begin{aligned}\chi_j(\rho) &= T_{j0}^{-1}\chi_0^{\text{new}}(\rho)\\ &\sim \exp\left[-\frac{\langle j|\eta^2|0\rangle(1-\delta_{j0})}{2\rho}\frac{d}{d\rho}\right]\chi_0^{\text{new}}(\rho),\end{aligned} \tag{37}$$

which is specified by the operator $-\frac{2}{\rho}A_{ij}^{(0)}\frac{d}{d\rho}$ of the kinematical coupling $\chi_j(\rho)$ of the open ($|i\rangle = 0$) and closed ($|j\rangle \neq 0$) channels in the local representation (24) of each pair channel of the system of three identical particles. It should be noted that, in the Jacobi parametrization (1), there is no kinematical coupling of the channels since, in the corresponding pair of the Jacobi coordinates, the variables for the open channel and the closed channels are asymptotically separated; that is, $\Psi = \phi_0(\eta)\chi_0(\xi)$ for $\eta/\xi \ll 1$. Upon substituting the asymptotic expression (36) into relation (37), we find that solutions to the asymptotic set of Eqs. (24) can be represented as

$$\begin{aligned}\chi_0(\rho) &\sim \chi_0^{\text{new}}(\rho),\\ \chi_j(\rho) &= T_{j0}^{-1}\chi_0^{\text{new}}(\rho)\\ &\sim -\frac{\langle j|\eta^2|0\rangle(1-\delta_{j0})}{2\rho}q\cos(q\rho+\delta).\end{aligned} \tag{38}$$

The asymptotic expression for the wave function Ψ below the three-body-breakup threshold in the pair channel $|0\rangle$ has the form

$$\Psi_0 = \rho^{-1/2}\sum_j |B_j\rangle\langle B_j|T^{-1}|B_0\rangle\chi_0^{\text{new}}(\rho). \tag{39}$$

Taking into account the completeness condition

$$\sum_j |B_j\rangle\langle B_j| = 1, \tag{40}$$

we then arrive at

$$\Psi_0 \sim \rho^{-1/2}B_0\left[\sin(q\rho+\delta) - q\frac{\eta^2}{2\rho}\cos(q\rho+\delta)\right]. \tag{41}$$

For $q\eta^2/(2\rho) \ll 1$, the $O(\rho^{-1})$ asymptotic expression for this wave function is

$$\begin{aligned}\Psi_0(\rho,\theta) &\sim \rho^{-1/2}B_0(\rho,\theta)\sin\left[q\left(\rho-\frac{\eta^2}{2\rho}\right)+\delta\right]\\ &\longrightarrow \phi_0(\eta)\sin(q\xi+\delta).\end{aligned} \tag{42}$$

By eliminating the nonadiabatic correction $W_{00}^{(0)}/\rho^2$ from Eq. (35) and considering the adiabatic behavior

$$\chi_{\text{ad}} \sim \sin(q\rho+\delta_{\text{ad}}) \tag{43}$$

of the solutions, we can obtain a relation between the exact phase shift δ and the adiabatic phase shift δ_{ad} in the form

$$\delta = \delta_{\text{ad}} + \frac{\langle 0|\eta^2|0\rangle q}{2\rho}. \tag{44}$$

It is obvious that the role of the nonadiabatic coupling between the channels becomes more pronounced with increasing q. In general, the difference between $\xi \sim \rho(1-\eta^2/(2\rho^2))$ and $\rho = \sqrt{\xi^2+\eta^2}$, which leads to the kinematical relation (37), can be neglected only in the adiabatic limit $q \longrightarrow 0$ and also for the bound states,

$$\langle\chi_{\text{eff}}(\rho)|\chi_{\text{eff}}(\rho)\rangle = \int_0^{+\infty}\chi_{\text{eff}}(\rho)\chi_{\text{eff}}(\rho)d\rho = 1. \tag{45}$$

In order to obtain correct results, however, care should be taken in some special cases [11]—for example, if the scattering cross section has threshold singularities or if there are zero-energy states of the three-body system ($q^2 = \epsilon = 0$). In particular, such a state exists in the system of three identical particles on a straight line that are coupled by attractive pair delta-function potentials of the same strength (this is precisely the case considered in the present study). The transformation in (26) changes the form of the solution since the original value of ξ is conserved only in the general solution Ψ given by Eqs. (39)–(42). For this reason, it is necessary to determine the value of the average-position operator

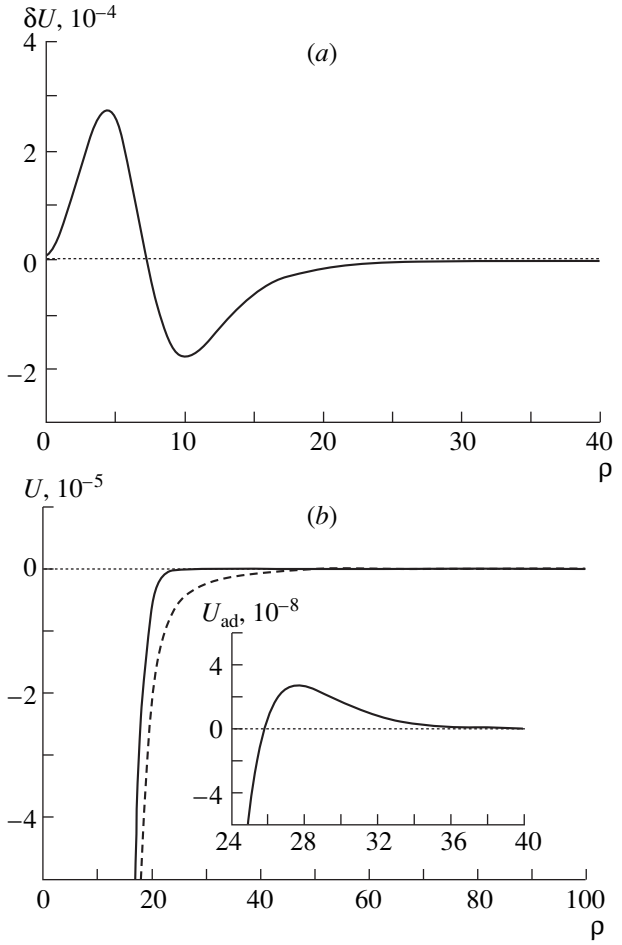

Fig. 2. (*a*) Nonadiabatic correction $\delta U(\rho)$ (31) to the effective potential and (*b*) adiabatic potential $U_{ad}(\rho)$ (solid curve) and effective potential $U_{eff}(\rho)$ (dashed curve).

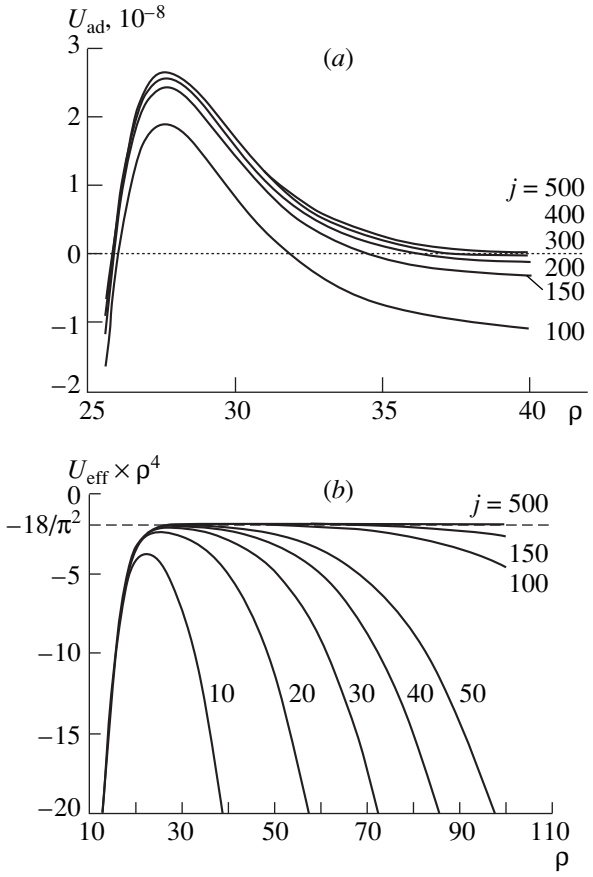

Fig. 3. (*a*) Convergence of the sum in (19) to the asymptotic expression for the adiabatic potential $U_{ad}(\rho)$ and (*b*) convergence of the sum in (31) multiplied by ρ^4 to the asymptotic expression for the effective polarization potential $U_{eff}(\rho)$ tending to the constant $-18/\pi^2$ at various values of the adiabatic-state number *j*.

$\hat{\rho}_m^{new}$ in the new representation $\chi_0^{new} = T\chi$ of the pair channel:

$$\rho_m^{new} = \langle\chi_0^{new}|\hat{\rho}_m^{new}|\chi_0^{new}\rangle = \langle\chi|T^{-1}\hat{\rho}_m^{new}T|\chi\rangle = \langle\chi|\hat{\rho}_m|\chi\rangle = \rho_m. \quad (46)$$

Here, the average-position operator $\hat{\rho}_m^{new} = \rho$ corresponds asymptotically to the Jacobi coordinate ξ in the original representation—that is, in the effective representation of delocalization, the variable ξ is contained in the new radial function $\chi_0^{new} = T\chi$. In the adiabatic representation of χ, the average-position operator $\hat{\rho}_m$ is indeed determined by the relation

$$\hat{\rho}_m = T^{-1}\hat{\rho}_m^{new}T = T^{-1}\rho T = \rho + \delta\hat{\rho}, \quad (47)$$

where $\delta\hat{\rho}$ is the delocalization of ξ; at large ρ, $\rho \gg 1$, it appears to be on the order of $\langle 0|\eta^2|0\rangle/2\rho \ll 1$, that is,

$$\hat{\rho}_m = T^{-1}\rho T \sim \langle\xi\rangle. \quad (48)$$

This construction makes it possible to visualize the delocalization in $\hat{\rho}_m$ near ρ with the amplitude $\delta\hat{\rho}$ proportional to the root-mean-square size of the target in the ground state. This construction is similar to the definition of the average-position operator [4]. Thus, we have constructed the effective approximation (25)–(32) for the set of adiabatic Eqs. (17) and found an analytic representation for the asymptotic behavior of the relevant solutions. It was shown above that, in the adiabatic approximation, it is necessary to take into account the asymptotic coupling of channels in the scattering problem, since the slow variable ρ exactly goes over to the corresponding Jacobi coordinate ξ only upon expanding the three-particle wave functions in a complete set of adiabatic functions. The above transition from the original Eq. (17) to the effective Eq. (25) can be compared with the elegant method that makes it possible to eliminate small components of solutions to the Dirac equation via the Foldy–Wouthuysen transformation and which reveals delocalization (Zitterbewegung) of the average-electron-position operator at dimensions

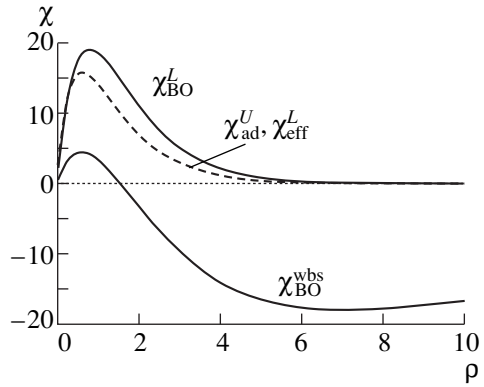

Fig. 4. Radial wave functions for the ground state $\chi^L_{BO}(\rho)$ and the loosely bound state $\chi^{wbs}_{BO}(\rho)$ in the Born–Oppenheimer approximation (solid curves) and radial wave functions in the adiabatic $\chi^U_{ad}(\rho)$ and the effective adiabatic $\chi^L_{eff}(\rho)$ approximation [dashed curve].

on the order of the Compton wavelength for an electron [4], whereby the correct probabilistic interpretation for all observables like the coordinate and the momentum can be obtained.

It should also be noted that, by means of the standard substitution $\chi_{eff}(\rho) = \mu^{1/2}(\rho)\tilde{\chi}_{eff}(\rho)$, Eq. (25) with a momentum-dependent potential can be reduced to the equation

$$\left(\frac{d^2}{d\rho^2} - V_{eff}(q^2, \rho) + q^2\right)\tilde{\chi}_{eff}(\rho) = 0, \qquad (49)$$

which involves the q^2-dependent potential

$$V_{eff}(q^2, \rho) = (U_{eff}(\rho) + q^2 W(\rho))\mu(\rho) + \Delta U_{eff}(\rho),$$
$$\Delta U_{eff}(\rho) = \frac{1}{2}W''(\rho)\mu(\rho) - \frac{1}{4}(W'(\rho)\mu(\rho))^2. \qquad (50)$$

In some cases, this potential is more convenient for analyzing the characteristics of solutions. This representation makes it possible to compare the effective adiabatic Eq. (25) and the standard equation involving an energy-dependent potential [1],

$$\left(\frac{d}{d\rho}(1 + W(\rho))\frac{d}{d\rho} - U_{ad}(\rho) + \frac{1}{2}\frac{d^2}{d\rho^2}W(\rho) + q^2\right)\chi_{eff}(\rho) = 0. \qquad (51)$$

Here, the term $-(1/2)W''$ corresponds to the nonadiabatic effective correction $\delta U_{eff}(\rho)$. This means that it is legitimate to compare the effective potential in (50) with the standard definition of the energy-dependent potential,

$$V^{st}_{eff}(q^2, \rho) = \frac{U_{ad}(\rho) + q^2 W(\rho)}{1 + W(\rho)} - \frac{1}{4}\left[\frac{d}{d\rho}\ln(1 + W(\rho))\right]^2.$$

Here, the second term corresponds to $\Delta U_{eff}(\rho)$ from Eq. (50). Analytic solutions to similar equations with a potential in the form of a modified well were considered in [12]. As will be demonstrated in the sections that follow, the approach considered above can be used to develop adequate methods for solving the three-body scattering problem.

4. DISCRETE SPECTRUM OF THE THREE-BODY PROBLEM

Let us consider the eigenvalue problem for an equation of the type in (25) with the boundary conditions $\chi(0) = 0$ and $\chi(+\infty) = 0$ and assume the normalization condition $\langle\chi|\chi\rangle = 1$. In order to solve the problem for the discrete spectrum, we made use of the fourth-order finite-difference scheme and of a multiparameter continuous analog of the Newton method, implementing preliminarily a reduction of a singular boundary-value problem to a regular one [13, 14]—that is, a transition from an infinite interval to the finite interval $\zeta \in [0, 1]$.

For the first two versions of solving the problem, we set $W(\rho) = 0$; that is, $\mu(\rho) = 1$ and $\delta U(\rho) = 0$. In the first version, we choose the Born–Oppenheimer approximation $U_{BO}(\rho) = U_{ad}(\rho) - \delta U(\rho)$ for the $U_{eff}(\rho)$. The solutions for the ground state $\chi^L_{BO}(\rho)$ and for a loosely bound state $\chi^{wbs}_{BO}(\rho)$ of the eigenvalue problem (25) with the Born–Oppenheimer potential are presented in Fig. 4. The Born–Oppenheimer approximation gives a lower bound on the ground-state energy E^L_{BO} and ensures the presence of a loosely bound state occurring at energy E^{wbs}_{BO} and corresponding to the state at zero energy $q^2 = \epsilon = 0$ reckoned from the pair-threshold energy $E = E_{pth}$. In the second version of solving the problem, we choose the standard adiabatic approximation $U_{ad}(\rho)$ for the $U_{eff}(\rho)$. In this case, the loosely bound state obtained in the Born–Oppenheimer approximation disappears; that is, the standard adiabatic approximation with the potential $U_{ad}(\rho)$ provides an upper bound on the energy E^U_{ad}. The corresponding radial wave function $\chi^U_{ad}(\rho)$ that was found in the adiabatic approximation is plotted in Fig. 4.

In the third version, we solved the problem with the effective potential $U_{eff}(\rho)$ for Eq. (25) and the boundary conditions $\chi_{eff}(0) = 0$ and $\chi_{eff}(+\infty) = 0$, imposing the normalization condition (45). The corrections $W(\rho)$ and

$\delta U(\rho)$ were calculated by formulas (30) and (31), respectively, their graphs being displayed in Fig. 1*a* and Fig. 2*a*. Solving this eigenvalue problem for the effective approximation leads to the new lower bound of $E^L_{\text{eff}} = -1.096626(\hbar^2/2m)$ on the exact energy value $E_{\text{exct}} = -\pi^2/9(\hbar^2/2m)$ with a deviation equal to 2.6×10^{-6}. The radial wave function $\chi^L_{\text{eff}}(\rho)$ calculated in the effective adiabatic approximation is shown in Fig. 4. It should be noted that, on the chosen scale, the distinction between the functions $\chi^U_{\text{ad}}(\rho)$ and $\chi^L_{\text{eff}}(\rho)$ is negligibly small. The results of the numerical calculations for the above three versions of deducing bounds on the energy are presented in Fig. 5*a*—these are the lower bounds $E^{\text{wbs}}_{\text{BO}}$ and E^L_{BO} that the numerical calculation within the Born–Oppenheimer approximation yields for the exact energies of the loosely bound and the ground state, respectively, and the upper adiabatic bound E^U_{ad} and the lower effective bound E^L_{eff} on the exact energy value E_{exct}. For the sake of completeness, the doubled energy of the three-particle threshold E_{tth} and the doubled energy of the two-particle threshold E_{pth} are also shown in Fig. 5*a*.

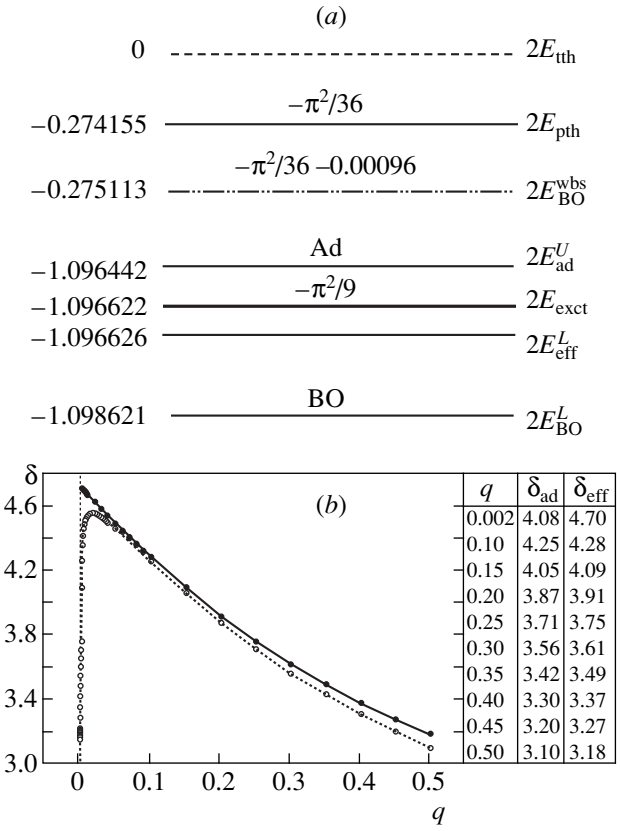

q	δ_{ad}	δ_{eff}
0.002	4.08	4.70
0.10	4.25	4.28
0.15	4.05	4.09
0.20	3.87	3.91
0.25	3.71	3.75
0.30	3.56	3.61
0.35	3.42	3.49
0.40	3.30	3.37
0.45	3.20	3.27
0.50	3.10	3.18

Fig. 5. (*a*) Diagram of the energy levels in the system involving three identical particles interacting via attractive pair delta-function potentials. Shown in this panel are the doubled values of the energies corresponding to the three-body-breakup threshold (E_{tth}) and the two-body-breakup threshold (E_{pth}); to the results obtained numerically in the Born–Oppenheimer approximation for the lower bounds $E^{\text{wbs}}_{\text{BO}}$ and E^L_{BO} on the exact values of the energies of, respectively, the loosely bound and the ground state; and to the upper adiabatic bound E^U_{ad} and the lower effective bound E^L_{eff} on the exact value of energy E_{exct}. (*b*) Elastic-scattering phase shift δ as a function of the relative momentum q of the incident particle and the pair below the three-body-breakup threshold: (solid curve) exact analytic solution δ_{exct}; (dotted curve with open circles) results in the adiabatic approximation; and (closed circles) results in the effective adiabatic approximation, δ_{eff}.

5. CONTINUOUS SPECTRUM

In the continuous spectrum below the three-body-breakup threshold, $E_0 < E < 0$, we used the equation for the phase function [1] in the adiabatic-approximation version with the potential U_{ad} and in the effective-adiabatic-approximation version with the potentials $\mu(\rho)$ and $U_{\text{eff}}(\rho)$; that is, we reduced the corresponding boundary-value problems for the continuous spectrum on the semiaxis $\rho \in [0, \infty)$ to the Cauchy problems for the equations describing phase functions. The latter problems were solved by the fourth-order Runge–Kutta method. Let us recall that the phase shift $\delta(q)$ as a function of the relative momentum q ($q^2 = 2(E - E_0)$, $0 < q^2 < (\pi/6)^2$) is obtained as the asymptotic expression for the phase function $\delta(q, \rho)$—that is, $\delta(q) = \lim_{\rho \to +\infty} \delta(q, \rho)$. The phase shift $\delta_{\text{eff}}(q)$ corresponding to the effective adiabatic approximation is then determined by the asymptotic behavior of the solution to the Cauchy problem for the phase function $\delta_{\text{eff}}(q, \rho) = \delta(q, \rho)$,

$$\frac{d\delta(q,\rho)}{d\rho} = -\frac{1}{1+W(\rho)}\frac{U_{\text{eff}}(\rho) + q^2 W(\rho)}{q}\sin^2(q\rho + \delta(q,\rho)) + \frac{1}{1+W(\rho)}\frac{dW}{d\rho}\sin(q\rho + \delta(q,\rho))\cos(q\rho + \delta(q,\rho)), \quad (52)$$

$$\delta(q, 0) = 0,$$

where the equation for this function, with a potential dependent on the momentum q, follows from Eq. (25) with the potential given by (28)–(31).

Similarly, the phase shift $\delta_{\text{ad}}(q)$ corresponding to the adiabatic approximation is determined from Eq. (52) by deriving the asymptotic expression for the solution to the Cauchy problem specified by the relevant equation for the phase function $\delta_{\text{ad}}(q, \rho) = \delta(q, \rho)$ at $W(\rho) = 0$ and $\delta U(\rho) = 0$. The graphs of $\delta_{\text{exct}}(q)$, $\delta_{\text{ad}}(q)$, and $\delta_{\text{eff}}(q)$ are displayed in Fig. 5*b*. We note that the results of the calculations for the adiabatic phase shift $\delta_{\text{ad}}(q)$

coincide with the results from [8]. In that study, the phase shift for the exact value $\delta_{exct}(q)$ was determined under assumption that, at large values of ρ, the wave function in the pair channel has the form

$$\Psi \sim \rho^{-1/2} B_0(\rho, \theta)\chi(\rho), \quad \chi(\rho) \sim \sin(q\rho + \delta_{exct}), \quad (53)$$

where

$$\delta_{exct} = \frac{3\pi}{2} - \arctan\frac{8\sqrt{3}q/\pi}{1 - 36q^2/\pi^2}. \quad (54)$$

From a comparison with the exact value of the phase shift, $\delta_{exct}(q)$, it follows that, in the range $4 \times 10^{-6} < q^2 < (\pi/6)^2$, the effective adiabatic approximation yields a correct behavior of the function $\delta_{eff}(q)$ to an absolute precision of 2×10^{-3}. It can be seen from Fig. 5*b* and from the table there that, at small q, the phase shift calculated in the adiabatic approximation tends to π, but that the phase shift calculated in the effective adiabatic approximation tends to $3\pi/2$, in accord with the exact phase-shift value, the latter corresponding to a state in the three-body system at zero energy ($\epsilon = q^2 = 0$) reckoned from the pair-threshold energy $E = E_{pth}$. This comparison confirms the convergence of the effective adiabatic approximation and gives a lower bound on the bound-state energy to within 2×10^{-6}. As can be seen from Eq. (52), the phase-shift values calculated in the adiabatic and the effective adiabatic approximation are indeed related by Eq. (44).

6. CONCLUSION

We have presented an explicit scheme that makes it possible to calculate, within the effective adiabatic approximation for the three-body problem, the energy levels of a discrete spectrum to a relative precision of 10^{-6} and the elastic-scattering phase shift as a function of the relative momentum of the third particle with respect to the center of mass of the pair below the three-particle-breakup threshold to a relative precision of 3×10^{-4}. In order to highlight the efficiency of the method, we have chosen an exactly solvable problem, whereby it is possible to demonstrate the convergence of our approximate results to exact ones and, hence, to prove that the proposed approach does indeed give correct results and can be used to solve actual problems. As an example of such a problem, we indicate the well-known calculation of the loosely bound state of a mesomolecular ion of the deuteron and the triton in [11]. The problem considered here—that of three identical particles on a straight line that interact via attractive pair delta-function potentials—exhibits special features peculiar to more interesting three-body systems involving loosely bound states. In the system of particles under investigation, a three-particle state at zero energy reckoned from the pair-threshold energy corresponds to the above loosely bound state because, in this system, there are no transitions from the pair channel into the channel featuring breakup into three particles. Below the three-body-breakup threshold, the elastic-scattering phase shift calculated in the effective adiabatic approximation as a function of the relative momentum of the third particle with respect to the center of mass of the pair agrees, to a preset accuracy, with the known values calculated by the analytic formula (54). In the vicinity of the pair threshold, both the above phase shift in the effective adiabatic approximation and the known analytic solution tend to $3\pi/2$; this corresponds to the presence of a bound state and a zero-energy state in the three-particle system.

The present formulation of the problem and the set of figures illustrating intermediate and final results make it possible to understand the basic features of the realization of the proposed approach and show that, in order to calculate, to a preset precision, the characteristics of actual three-particle systems over a finite interval of the slow variable, it is necessary to investigate in detail the asymptotic behavior of effective potentials.

The proposed approach is based on reducing the set of adiabatic equations to one effective adiabatic equation for the open pair channel with the aid of the operator canonical transformation and on constructing the corresponding effective potential (momentum-dependent potential) and the corresponding effective mass. For the problem considered here, this reduction has been implemented, in quite a transparent way, by using the analytic representation of the parametric spectral problem on a circle. As a result, we have illustrated the convergence of the adiabatic-expansion method within the effective adiabatic approximation and shown that the relevant sum rules are saturated and form the correct asymptotic behavior of the effective and the momentum-dependent potential. It has been established that, below the threshold for three-body breakup, the kinematical coupling of closed channels transforms into an asymptotic centrifugal energy-dependent potential proportional to the root-mean-square dimension of the open-channel pair subsystem. As to the asymptotic behavior of the effective potential, it is determined by polarization interaction. This circumstance ensures a correct behavior of the phase shift over the entire energy region below the three-body-breakup threshold, with the exception of a narrow energy interval (of width less than 4×10^{-6}) above the two-body threshold (investigation of this interval is beyond the accuracy of the effective-adiabatic-approximation method).

Our analysis has demonstrated that the standard adiabatic approximation gives no way to obtain a correct threshold behavior. It has been shown that reducing the original problem that involves short-range pair potentials to an effective problem for the open pair channel can be represented as a problem featuring a nonlocal momentum-dependent potential. As consequence, there arise long-range potentials, and it is required to explore and construct relevant asymptotic expressions. In this sense, the approach based on the effective adiabatic approximation can be compared with the well-

known method for constructing the effective nonadiabatic potential for exotic three-particle systems featuring Coulomb interaction [15, 16]. From our analysis of the convergence of the adiabatic expansion, it follows that the expansion of the three-body wave function in the truncated set of the eigenfunctions of the operator of rotations on a circle—this is an important part of the expansion in the K harmonics—cannot ensure a correct behavior of the asymptotic expressions or the spectrum of three-body problem in the pair channel. It can be expected that a further development of the effective adiabatic approximation proposed here will lead to the formulation of an adequate method for treating the problem of three-body scattering.

ACKNOWLEDGMENTS

We are grateful to A. Amaya-Tapia for collaboration and to F.M. Pen'kov, V.V. Pupyshev, and I.V. Puzynin for stimulating discussions and enlightening comments.

This work was supported in part by a joint grant (no. 95-0512) from the Russian Foundation for Basic Research (RFBR) and the International Association for the Promotion of Cooperation with Scientists from the Independent States of the Former Soviet Union and by the RFBR (project nos. 96-02-17715, 00-02-16337, 00-02-81023, and 00-01-00617).

REFERENCES

1. V. V. Babikov, *Method of Phase Functions in Quantum Mechanics* (Nauka, Moscow, 1976).
2. S. I. Vinitskiĭ, B. L. Markovski, and A. A. Suz'ko, Yad. Fiz. **55**, 669 (1992) [Sov. J. Nucl. Phys. **55**, 371 (1992)].
3. A. G. Abraskevich, I. V. Puzynin, Yu. S. Smirnov, and S. I. Vinitsky, Hyperfine Interact. **101/102**, 381 (1996).
4. L. L. Foldy and S. A. Wouthuysen, Phys. Rev. **78**, 29 (1950); A. A. Izmest'ev, Yad. Fiz. **43**, 1004 (1986) [Sov. J. Nucl. Phys. **43**, 641 (1986)].
5. M. B. Kadomtsev, S. I. Vinitsky, and F. R. Vukajlovich, Phys. Rev. A **36**, 4652 (1987).
6. W. Gibson, S. Y. Larsen, and J. J. Popiel, Phys. Rev. A **35**, 4919 (1987).
7. J. B. McGuire, J. Math. Phys. **5**, 622 (1964); L. R. Dodd, J. Math. Phys. **11**, 207 (1970).
8. A. Amaya-Tapia, S. Y. Larsen, and J. J. Popiel, Few-Body Syst. **23**, 87 (1997).
9. R. D. Amado and H. T. Coelho, Am. J. Phys. **46**, 1057 (1978).
10. J. J. Popiel and S. Y. Larsen, Few-Body Syst. **15**, 129 (1993).
11. I. V. Puzynin, T. P. Puzynina, Yu. S. Smirnov, and S. I. Vinitsky, Yad. Fiz. **56** (7), 82 (1993) [Phys. At. Nucl. **56**, 902 (1993)].
12. M. Razavy, G. Field, and J. S. Levinger, Phys. Rev. **125**, 269 (1962).
13. S. I. Vinitskiĭ, I. V. Puzynin, and Yu. S. Smirnov, Yad. Fiz. **52**, 1176 (1990) [Sov. J. Nucl. Phys. **52**, 746 (1990)].
14. D. V. Pavlov, I. V. Puzynin, and S. I. Vinitsky, Preprint No. E4-99-141, OIYaI (Joint Institute for Nuclear Research, Dubna, 1999).
15. D. A. Kirzhnits and F. M. Pen'kov, Zh. Éksp. Teor. Fiz. **85**, 80 (1983) [Sov. Phys. JETP **58**, 46 (1983)].
16. D. A. Kirzhnits, in *Problems in Theoretical Physics and Astrophysics*, Ed. by L. V. Keldysh and V. Ya. Faĭnberg (Nauka, Moscow, 1989), p. 225.

Translated by A. Isaakyan

Physics of Atomic Nuclei, Vol. 64, No. 1, 2001, pp. 38–48. Translated from Yadernaya Fizika, Vol. 64, No. 1, 2001, pp. 40–50.

NUCLEI
Theory

Self-Consistent and Optical Potentials for Nucleons at Positive and Negative Energies

S. G. Kadmensky and M. M. Lesnykh

Voronezh State University, Universitetskaya pl. 1, Voronezh, 394693 Russia

Received August 13, 1999

Abstract—The properties of the Hartree–Fock potential that coincides with the self-consistent potential and with the real part of the optical potential for nucleons in the case of a global regime of averaging are investigated by consistently taking into account the velocity-dependent components of nucleon–nucleon forces and nonlocality effects. For the first time, the properties of the effective energy-dependent Hartree–Fock potential are analyzed at negative nucleon energies. It is shown that the form of this potential undergoes a significant change upon reversal of the sign of nucleon energy. The conditions of applicability of the semiclassical approximation are found. © *2001 MAIK "Nauka/Interperiodica".*

1. INTRODUCTION

Within generalized Fermi liquid theory [1] and the theory of open Fermi systems [2], it can be shown that the true self-consistent field for nucleons in nuclei and the real part of the optical potential for nucleons in the case of a global regime of averaging do not include nuclear-polarizability effects and that they coincide with generalized Hartree–Fock nonlocal potential determined by realistic nucleon–nucleon (*NN*) forces. The nonlocal Hartree–Fock potential can be expressed in terms of a local Hartree–Fock potential that is dependent on the nucleon-momentum operator. In turn, the local Hartree–Fock potential can be reduced to a local energy-dependent potential that is usually used to analyze experimental data. The local energy-dependent potential in nuclear matter was calculated in [3] as a function of nucleon energy, and it was shown there, for some sets of the parameters of realistic *NN* forces, that the calculated values of this potential are consistent with the depths of phenomenological optical potentials for nucleons at the center of comparatively heavy nuclei. The features of the self-consistent field and of the real part of the optical potential for nucleons in finite nuclei were comprehensively investigated in [4, 5] by using the second-order approximation for the momentum dependence of the local Hartree–Fock potential for nucleons. Here, we aim at studying the radial and the energy characteristics of the self-consistent and the optical potential for nucleons in nuclei at positive and negative nucleon energies. In doing this, we take consistently into account both the velocity-dependent components of *NN* interactions and the nucleon-momentum dependence of the local Hartree–Fock potential.

2. GENERAL PROPERTIES OF THE HARTREE–FOCK POTENTIAL FOR SPHERICAL NUCLEI

In the Hartree–Fock approximation, the Schrödinger equation for the wave function $\varphi_E(\mathbf{r}_1)$ describing a nucleon of energy E has the form

$$\left\{\frac{\hbar^2\mathbf{k}_1^2}{2m} + \hat{V}(\mathbf{r}_1) - E\right\}\varphi_E(\mathbf{r}_1) = 0, \quad (1)$$

where $\mathbf{r}_1$ is the set of nucleon coordinates, including spatial, spin, and isospin variables; $\mathbf{k}_1 = -i\dfrac{\partial}{\partial\mathbf{r}_1}$ is the nucleon-momentum operator; and $\hat{V}(\mathbf{r}_1)$ is the nonlocal Hartree–Fock potential

$$\hat{V}(\mathbf{r}_1) = V_{\mathrm{H}}(\mathbf{r}_1) + \hat{V}_{\mathrm{F}}(\mathbf{r}_1). \quad (2)$$

Here, the Hartree potential $V_{\mathrm{H}}(\mathbf{r}_1)$ is given by [1]

$$V_{\mathrm{H}}(\mathbf{r}_1) = \int\hat{V}^{\mathrm{H}}(\mathbf{r}_1, \mathbf{r}_2)\rho(\mathbf{r}_2)d\mathbf{r}_2, \quad (3)$$

where $\hat{V}^{\mathrm{H}}(\mathbf{r}_1, \mathbf{r}_2)$ is the Hartree part of the potential representing the pair nuclear interaction of nucleons and $\rho(\mathbf{r}_1) = \rho_n(\mathbf{r}_1) + \rho_p(\mathbf{r}_1)$ is the total nucleon density in the nucleus, $\rho_n(\mathbf{r}_1)$ and $\rho_p(\mathbf{r}_1)$ being, respectively, the neutron and the proton density. The nonlocal Fock potential $\hat{V}_{\mathrm{F}}(\mathbf{r}_1)$ has the form [1]

$$\hat{V}_{\mathrm{F}}(\mathbf{r}_1)\varphi(\mathbf{r}_1) = -\frac{1}{4}\int\hat{V}^{\mathrm{F}}(\mathbf{r}_1, \mathbf{r}_2)\rho(\mathbf{r}_1, \mathbf{r}_2)\varphi(\mathbf{r}_2)d\mathbf{r}_2, \quad (4)$$

where $\hat{V}^{\mathrm{F}}(\mathbf{r}_1, \mathbf{r}_2)$ is the Fock part of the potential representing the pair nuclear interaction of nucleons and $\rho(\mathbf{r}_1, \mathbf{r}_2) = \rho_n(\mathbf{r}_1, \mathbf{r}_2) + \rho_p(\mathbf{r}_1, \mathbf{r}_2)$ is the total density matrix for intranuclear nucleons.

In the potential (2), we have omitted the terms that are generated by the Coulomb interaction of protons and which were considered in [6] and terms depending on the projection of the nucleon isospin, which are associated with the difference of the numbers of protons and neutrons in the nucleus under investigation. In general, the *NN* potential includes a central (*c*) and a tensor (*t*) interaction, as well as nucleon-velocity-dependent interactions like the first-order spin–orbit interaction (*ls*), the second-order interaction in *l* (*l*2), and the second-order spin–orbit interaction (*ls*2).

Let us consider the properties of the self-consistent and the optical potential for nucleons without taking into account the tensor interaction, whose contribution to the potential (2) is strictly equal to zero in spherical nuclei, and the contribution of the first-order spin–orbit interaction, which was considered in detail elsewhere [4].

The Fock potential $\hat{V}_{\rm F}(\mathbf{r}_1)$ (4) is real-valued because the pair-potential $\hat{V}^{\rm F}(\mathbf{r}_1, \mathbf{r}_2)$ and the density matrix $\rho(\mathbf{r}_1, \mathbf{r}_2)$ are real valued, and it is self-conjugate. The last property follows from the fact that the matrix element $\int \varphi^*_{E'}(\mathbf{r}_1)\hat{V}^{\rm F}(\mathbf{r}_1, \mathbf{r}_2)\rho(\mathbf{r}_1, \mathbf{r}_2)\varphi_E(\mathbf{r}_2)d\mathbf{r}_1 d\mathbf{r}_2$ can be reduced to the Hermitian conjugate form $\int \varphi_E(\mathbf{r}_1)\hat{V}^{\rm F}(\mathbf{r}_1, \mathbf{r}_2)\rho(\mathbf{r}_1, \mathbf{r}_2)\varphi^*_{E'}(\mathbf{r}_2)d\mathbf{r}_1 d\mathbf{r}_2$ by making the substitution $\mathbf{r}_1 \longleftrightarrow \mathbf{r}_2$ and by using the self-conjugacy and symmetry properties of the *NN* potential, $\hat{V}^{\rm F}(\mathbf{r}_1, \mathbf{r}_2) = \hat{V}^{\rm F}(\mathbf{r}_2, \mathbf{r}_1)$, and of the density matrix,

$$\rho(\mathbf{r}_1, \mathbf{r}_2) = \rho(\mathbf{r}_2, \mathbf{r}_1). \quad (5)$$

That the potential $\hat{V}_{\rm F}(\mathbf{r}_1)$ is real-valued and self-conjugate leads to invariance of this potential under time reversal, in which case the modulus of the nucleon momentum changes sign, and, as a consequence, to fulfillment of the detailed-balance principle [7].

Upon taking into account the *l*2 and the *ls*2 *NN* interaction, the Hartree potential (3) becomes dependent on the nucleon-wave-vector operator $\mathbf{k}_1$ and can be represented in the form

$$V_{\rm H}(\mathbf{r}_1) = V^c_{\rm H}(\mathbf{r}_1) + V^{(0)}_{\rm H}(\mathbf{r}_1) + (\mathbf{k}_1 J(r_1))\cdot\mathbf{k}_1 + V^{(2)}_{\rm H}(\mathbf{r}_1)\mathbf{k}_1^2, \quad (6)$$

where

$$J(r_1) = \int_{r_1}^{\infty} V^{(1)}_{\rm H}(\mathbf{r}_1)dr_1. \quad (7)$$

As to the quantities $V^c_{\rm H}(\mathbf{r}_1)$ and $V^{(i)}_{\rm H}(\mathbf{r}_1)$ $(i = 0, 1, 2)$, the explicit expressions for them are given in the Appendix.

By using the operator of finite translations along the nucleon spatial coordinate $\mathbf{r}_1$ [8], we can go over from the nonlocal potential $\hat{V}_{\rm F}(\mathbf{r}_1)$ to the local momentum-dependent potential

$$V_{\rm F}(\mathbf{r}_1, \mathbf{k}_1) = -\frac{1}{4}\int \hat{V}^{\rm F}(\mathbf{r})\rho(\mathbf{r}_1, \mathbf{r}_1 + \mathbf{r})e^{i\mathbf{r}\cdot\mathbf{k}_1}d\mathbf{r}, \quad (8)$$

where $\mathbf{r} = \mathbf{r}_2 - \mathbf{r}_1$. It is important to note that, in addition to the explicit dependence on $\mathbf{k}_1$ through the translation operator, the Fock potential $V_{\rm F}(\mathbf{r}_1, \mathbf{k}_1)$ features an additional $\mathbf{k}_1$ dependence that is associated with the nucleon-velocity-dependent components of the *NN* interaction. Analytic formulas for calculating the terms in the Fock potential that correspond to the *l*2 and *ls*2 *NN* interactions are presented in the Appendix. As will be shown below, the total contribution of these terms to the optical potential grows monotonically with increasing energy, but its modulus at the center of the nucleus does not exceed 1.2 MeV in the energy range $-60 \le E \le 100$ MeV. To the above precision, only the central nuclear interaction of nucleons can be taken into account in the Fock potential $V_{\rm F}(\mathbf{r}_1, \mathbf{k}_1)$.

For a spherical nucleus, we make use of the transformations

$$e^{i\mathbf{r}\cdot\mathbf{k}_1} = 4\pi\sum_{lm} i^l j_l(rk_1)Y^*_{lm}(\mathbf{r})Y_{lm}(\mathbf{k}_1), \quad (9)$$

$$\rho(\mathbf{r}_1, \mathbf{r}_1 + \mathbf{r}) = \sum_{lm}\rho_l(r_1, r)Y_{lm}(\mathbf{r})Y^*_{lm}(\mathbf{r}_1), \quad (10)$$

where

$$\rho_l(r_1, r) = 2\pi\int_{-1}^{1}\rho(\mathbf{r}_1, \mathbf{r}_1 + \mathbf{r})P_l(\xi)d\xi. \quad (11)$$

The potential $V_{\rm F}(\mathbf{r}_1, \mathbf{k}_1)$ (8) can then be represented in the form

$$V_{\rm F}(\mathbf{r}_1, \mathbf{k}_1) = \sum_l V_l(r_1, k_1)P_l(\xi_1), \quad (12)$$

where ξ_1 is the cosine of the angle between the vectors $\mathbf{r}_1$ and $\mathbf{k}_1$ and

$$V_l(r_1, k_1) = -\frac{(2l+1)}{4}i^l\int V^{\rm F}_c(r)\rho(\mathbf{r}_1, \mathbf{r}_1 + \mathbf{r})j_l(rk_1)P_l(\xi)d\mathbf{r}. \quad (13)$$

Here, $V^{\rm F}_c(r)$ is the Fock part of the central nuclear *NN* interaction.

From (12), it can be seen that the Fock potential for a spherical nucleus generally depends not only on the modulus of the vector $\mathbf{k}_1$ but also on its projection onto the direction of $\mathbf{r}_1$ [7]. In contrast to the nonlocal representation in (4), the representations in (8) and in (12) do not exhibit explicitly invariance of the Fock potential under time reversal. In order to verify this invariance,

we represent the Fock potential $V_F(\mathbf{r}_1, \mathbf{k}_1)$ (8) in the more symmetric form

$$V_F(\mathbf{r}_1, \mathbf{k}_1) = -\frac{1}{4}\int V_c^F(r) e^{i\mathbf{r}\cdot\mathbf{k}_1'/2} \rho\left(\mathbf{r}_1 - \frac{\mathbf{r}}{2}, \mathbf{r}_1 + \frac{\mathbf{r}}{2}\right) e^{i\mathbf{r}\cdot\mathbf{k}_1} d\mathbf{r}, \quad (14)$$

where the operator $\mathbf{k}_1'$ coincides with the operator $\mathbf{k}_1$, but the former acts only on the coordinate $\mathbf{r}_1$ of the symmetrized density matrix $\rho(\mathbf{r}_1 - \mathbf{r}/2, \mathbf{r}_1 + \mathbf{r}/2)$.

Upon the removal of the factor $V_c^F(r)e^{i\mathbf{r}\cdot\mathbf{k}_1'/2}$ from the integral in Eq. (14), it becomes coincident with the Wigner matrix [9], which is extensively used in the semiclassical approximation.

By using representation (9) for exponentials in Eq. (14) and an expansion of the type (10) for $\rho(\mathbf{r}_1 - \mathbf{r}/2, \mathbf{r}_1 + \mathbf{r}/2)$, we arrive at

$$V_F(\mathbf{r}_1, \mathbf{k}_1) = -\frac{1}{4}(4\pi)^2 \sum_{ll_1l_2mm_1m_2} i^{l+l_2} Y_{lm}(\mathbf{k}_1') Y_{l_1m_1}(\mathbf{r}_1) Y^*_{l_2m_2}(\mathbf{k}_1) \times \int V_c^F(r) j_l(rk_1'/2) \tilde{\rho}_{l_1}(r_1, r) j_{l_2}(rk_1) Y^*_{lm}(\mathbf{r}) Y^*_{l_1m_1}(\mathbf{r}) \times Y_{l_2m_2}(\mathbf{r}) d\mathbf{r}, \quad (15)$$

where $\tilde{\rho}_{l_1}(r_1, r)$ is given by Eq. (11) with the substitution of $\rho(\mathbf{r}_1 - \mathbf{r}/2, \mathbf{r}_1 + \mathbf{r}/2)$ for $\rho(\mathbf{r}_1, \mathbf{r}_1 + \mathbf{r})$. By virtue of relation (5), the function $\rho(\mathbf{r}_1 - \mathbf{r}/2, \mathbf{r}_1 + \mathbf{r}/2)$ does not change under the inversion of the coordinate r; therefore, the quantity l_1 in Eq. (15) takes only even values, and the relevant integral with respect to $d\mathbf{r}$ is nonzero if the parities of the momenta l and l_2 coincide. Because of this, expression (15) is invariant under the time reversal, which results in $\mathbf{k}_1 \longrightarrow -\mathbf{k}_1$ and $\mathbf{k}_1' \longrightarrow -\mathbf{k}_1'$.

It will be shown below that, for a spherical nucleus, the symmetrized density matrix $\rho(\mathbf{r}_1 - \mathbf{r}/2, \mathbf{r}_1 + \mathbf{r}/2)$ is virtually independent of the angle between the vectors $\mathbf{r}_1$ and $\mathbf{r}$ and coincides with the quantity $[\frac{1}{4\pi}\tilde{\rho}_0(r_1, r)]$. It follows that the vector operator $\mathbf{k}_1'$, which acts on the coordinate $\mathbf{r}_1$ in the density matrix $\rho(\mathbf{r}_1 - \mathbf{r}/2, \mathbf{r}_1 + \mathbf{r}/2)$, is directed along the radius vector $\mathbf{r}_1$ and that this operator can be represented as $\mathbf{k}_1' = -i\frac{\mathbf{r}_1}{r_1}\frac{\partial}{\partial r_1}$. In this case, formula (15) is simplified significantly to become

$$V_F(\mathbf{r}_1, \mathbf{k}_1) = -\frac{1}{4}\sum_l (-1)^l \frac{(2l+1)}{4\pi} \times \int V_c^F(r) j_l\left(\frac{rk_1'}{2}\right) \tilde{\rho}_0(r_1, r) j_l(rk_1) d\mathbf{r} P_l(\xi_1). \quad (16)$$

3. EFFECTIVE ENERGY-DEPENDENT POTENTIAL FOR NUCLEONS

As will be shown below, the series in l in Eq. (12) converges rather fast, so that it is possible to discard all terms from $l = 2$ because of their smallness. The Fock potential (12) then takes the form

$$V_F(\mathbf{r}_1, \mathbf{k}_1) = V_0(r_1, k_1) + V_1(\mathbf{r}_1, \mathbf{k}_1)\frac{\mathbf{r}_1\cdot\mathbf{k}_1}{r_1k_1}, \quad (17)$$

where

$$V_0(r_1, k_1) = -\frac{1}{4}\int V_c^F(r)\rho(\mathbf{r}_1, \mathbf{r}_1 + \mathbf{r}) j_0(rk_1) d\mathbf{r}, \quad (18)$$

$$V_1(\mathbf{r}_1, \mathbf{k}_1)\frac{\mathbf{r}_1\cdot\mathbf{k}_1}{r_1k_1} = -\frac{3i}{4}\int V_c^F(r)\rho(\mathbf{r}_1, \mathbf{r}_1 + \mathbf{r}) j_1(rk_1) P_1(\xi) d\mathbf{r}\frac{\mathbf{r}_1\cdot\mathbf{k}_1}{r_1k_1} = (\mathbf{k}_1 I(r_1, k_1))\cdot\mathbf{k}_1, \quad (19)$$

with

$$I(r_1, k_1) = -i\int_{r_1}^{\infty} V_1(r_1, k_1)\frac{1}{k_1} dr_1. \quad (20)$$

With the aid of Eqs. (6) and (17), the Schrödinger equation (1) can be written in the form

$$\left(\mathbf{k}_1\frac{\hbar^2}{2m^*(r_1, k_1)}\mathbf{k}_1 + V_H^c(r_1) + V_H^{(0)}(r_1) + V_0(r_1, k_1) - (I(r_1, k_1) + J(r_1) + V_H^{(2)}(r_1))\mathbf{k}_1^2 - E\right)\varphi_E(\mathbf{r}_1) = 0, \quad (21)$$

where the effective nucleon mass $m^*(r_1, k_1)$ is defined as

$$\frac{1}{m^*(r_1, k_1)} = \frac{1}{m} + \frac{2(I(r_1, k_1) + J(r_1))}{\hbar^2}. \quad (22)$$

For all terms in (21) that are dependent on the modulus of the nucleon-momentum operator k_1, their expansions in power series in k_1 involve only even powers of k_1. Further, the operator k_1^2 can be replaced by $\bar{k}_1^2$ in using Eq. (28), which is derived below. At the same time, the operators k_1^n, where $n = 4, 6, \ldots$, can be replaced by the numbers $(\bar{k}_1^2)^{n/2}$ if we employ the results presented in Section 4 below. At nucleon energies $E \geq 10$ MeV, the semiclassical approximation is valid, in which case $k_1^n = (\bar{k}_1^2)^{n/2}$; at lower energies, k_1^n differs from $(\bar{k}_1^2)^{n/2}$ only in the surface region of the nucleus, where the modulus of the nucleon–nucleus potential decreases noticeably with increasing r_1 and where k_1^n becomes much less than k_1^2 for $n = 4, 6, \ldots$.

We will seek a solution to Eq. (21) in the form [5]

$$\varphi_E(\mathbf{r}_1) = f(r_1, \bar{k}_1)\tilde{\varphi}_E(\mathbf{r}_1), \quad (23)$$

where the form factor $f(r_1, \bar{k}_1)$ will be chosen in such a way as to ensure the vanishing of gradient terms of the form $\mathbf{k}_1\tilde{\varphi}_E(\mathbf{r}_1)$ in this equation. Our calculations—the results are presented in Section 4 below—reveal that, for all r_1 and for $\bar{k}_1 \leq 2.5$ fm^{-1} (these values corresponding to the entire energy region $E \leq 100$ MeV), $\hbar^2\bar{k}_1^2/(2m^*(r_1, \bar{k}_1))$ exceeds the potential $[V_0(r_1, \bar{k}_1) - (I(r_1, \bar{k}_1) + J(r_1) + V_H^{(2)}(r_1))\bar{k}_1^2 - V_0(r_1, 0)]$ [see Eq. (21)] in absolute value by a factor greater than 4. Taking all the above into account, we find that, to a precision of 25%, the function $f(r_1, \bar{k}_1)$ satisfies the equation

$$\left(\mathbf{k}_1\frac{1}{2m^*(r_1, \bar{k}_1)}\right)f(r_1, \bar{k}_1) + \frac{1}{m^*(r_1, \bar{k}_1)}\mathbf{k}_1 f(r_1, \bar{k}_1) = 0.$$

The solution that satisfies this equation and the boundary condition $f(r_1, \bar{k}_1) \xrightarrow[r_1\to\infty]{} 1$ has the form

$$f(r_1, \bar{k}_1) = \left[\frac{m^*(r_1, \bar{k}_1)}{m}\right]^{1/2}. \quad (24)$$

For the function $\tilde{\varphi}_E(\mathbf{r}_1)$, we then have the equation

$$\left(\frac{\hbar^2\mathbf{k}_1^2}{2m} + V(r_1, \bar{k}_1) - E\right)\tilde{\varphi}_E(\mathbf{r}_1) = 0, \quad (25)$$

where

$$V(r_1, \bar{k}_1) = \frac{m^*(r_1, \bar{k}_1)}{m}[V_H^c(r_1) + V_H^{(0)}(r_1) + V_0(r_1, \bar{k}_1) - (I(r_1, \bar{k}_1) + J(r_1) + V_H^{(2)}(r_1))\bar{k}_1^2 + V_{\text{grad}}(r_1, \bar{k}_1)] + (1 - m^*(r_1, \bar{k}_1)/m)E, \quad (26)$$

$$V_{\text{grad}}(r_1, \bar{k}_1) = -\frac{\hbar^2}{2m^*(r_1, \bar{k}_1)}\left(\frac{1}{2}\frac{\nabla^2 m^*(r_1, \bar{k}_1)}{m^*(r_1, \bar{k}_1)} - \frac{3}{4}\left(\frac{\nabla m^*(r_1, \bar{k}_1)}{m^*(r_1, \bar{k}_1)}\right)^2\right). \quad (27)$$

By using Eq. (22) and the relation

$$k_1 \longrightarrow \bar{k}_1(r_1, E) = \sqrt{\frac{2m}{\hbar^2}[E - V(r_1, \bar{k}_1(r_1, E))]}, \quad (28)$$

which follows from (25), we now find that the effective local energy-dependent potential $V(r_1, E)$, which appears in Eq. (25) instead of the potential (26), satisfies the nonlinear equation

$$V(r_1, E) = V_H^c(r_1) + V_H^{(0)}(r_1) + V_0(r_1, \bar{k}_1(r_1, E)) + V_{\text{grad}}(r_1, \bar{k}_1(r_1, E)) + V_H^{(2)}(r_1)\bar{k}_1^2(r_1, E). \quad (29)$$

The potential $V(r_1, E)$ in (29) differs from similar potentials that are widely used in calculating optical potentials for nucleons [10] in that the former involves a gradient term and in that it employs realistic *NN* forces instead of effective ones. As was shown in [1], solving the elastic-scattering problem on the basis of the wave function $\tilde{\varphi}_E(\mathbf{r}_1)$ determined by the Schrödinger equation (25) with the effective energy-dependent potential $V(r_1, E)$ is equivalent to analogously solving the Schrödinger equation (1) with a nonlocal Hartree–Fock potential. The energy dependence of the potential $V(r_1, E)$ results in that, for discrete states at rather close negative-energy values, the orthonormalization condition for the functions $\tilde{\varphi}_E(\mathbf{r}_1)$ obeying Eq. (25) takes the form

$$\int\tilde{\varphi}_E^*(\mathbf{r}_1)\frac{m_1^*(r_1, E)}{m}\tilde{\varphi}_{E'}(\mathbf{r}_1)d\mathbf{r}_1 = \delta_{EE'}, \quad (30)$$

where the quantity $m_1^*(r_1, E)$ is determined by the relation

$$\frac{m_1^*(r_1, E)}{m} = 1 - \frac{dV(r_1, E)}{dE}. \quad (31)$$

The calculations presented in the next section show that, in the entire energy range $-60 \leq E \leq 100$ MeV, the quantity $m_1^*(r_1, E)$ (31) is close to the effective mass $m^*(r_1, E) \equiv m^*(r_1, \bar{k}_1(r_1, E))$ (22); it follows that, with allowance for Eq. (24), the condition in (30) reduces to the standard orthonormalization condition for the functions $\varphi_E(\mathbf{r}_1)$:

$$\int\varphi_E^*(\mathbf{r}_1)\varphi_{E'}(\mathbf{r}_1)d\mathbf{r}_1 = \delta_{EE'}. \quad (32)$$

Therefore, the energy-dependent potential $V(r_1, E)$ simulates both the self-consistent and the optical potential for nucleons.

It is convenient to represent this potential in the form

$$V(r_1, E) = V(0, E)f_E^0(r_1), \quad (33)$$

where $f_E^0(r_1)$ is a function that is equal to unity at $r_1 = 0$ and which has a form close to that of the Fermi distribution

$$f(r) = \left(1 + \exp\frac{r - R_A}{a}\right)^{-1}. \quad (34)$$

Moreover, the potential $V(r_1, E)$ can be written in the form that is usually used to represent phenomenological optical potentials for nucleons; that is,

$$V(r_1, E) = V(0, 0)f_0^0(r_1) + \alpha(0, E)f_E^1(r_1)E, \quad (35)$$

where

$$\alpha(0, E) = \frac{V(0, E) - V(0, 0)}{E},$$
$$f_E^1(r_1) = \frac{V(r_1, E) - V(r_1, 0)}{V(0, E) - V(0, 0)}. \quad (36)$$

It is interesting to compare the above formulas for the effective potential $V(r_1, E)$ with similar formulas derived in the semiclassical approximation, which is valid in the case of particles having high momenta and moving in slowly varying potential fields such that (see [8])

$$\left|\frac{\partial V(r_1, E)}{\partial r_1}\right| \ll \frac{\hbar^2 \bar{k}_1^3(r_1, E)}{m}. \quad (37)$$

In this approximation, we can retain only the zero- and first-order terms in $r_1 k_1'/2$ in Eq. (16) and discard derivatives of the function $m^*(r_1, E)$ with respect to r_1 (gradient potential). As a result, we obtain

$$V(r_1, E) = V_H^c(r_1) + V_H^{(0)}(r_1) + V_0(r_1, \bar{k}_1(r_1, E)) + V_H^{(2)}(r_1)\bar{k}_1^2(r_1, E), \quad (38)$$

where

$$V_0(r_1, k_1) = -\frac{1}{4}\frac{1}{4\pi}\int V_c^F(r)\tilde{\rho}_0(r_1, r) j_0(rk_1) d\mathbf{r}. \quad (39)$$

Under the same conditions, the effective mass $m^*(r_1, E)$ (22) becomes nearly coincident with the quantity $m_1^*(r_1, E)$ determined by Eq. (31) with the potential $V(r_1, E)$ (38).

It is also interesting to compare the potential (29) with that which is obtained by using the second-order approximation in $\bar{k}_1$ in the momentum dependence of the Fock potential [3–5]. For this, we expand the spherical Bessel functions j_0 and j_1 in Eqs. (18) and (19) in series in $\bar{k}_1$ and retain terms of order not higher than two. The effective mass (22) then becomes independent of energy, $m^*(r_1, E) = m^*(r_1)$, and the potential $V(r_1, E)$ appears to be a linear function of energy,

$$V(r_1, E) = \frac{m^*(r_1)}{m}[V_H^c(r_1) + V_H^{(0)}(r_1) + V_0(r_1) + V_{\text{grad}}(r_1)] + \beta(r_1)E, \quad (40)$$

where

$$V_0(r_1) = -\frac{1}{4}\int V_c^F(r)\rho(\mathbf{r}_1, \mathbf{r}_1 + \mathbf{r}) d\mathbf{r},$$
$$\beta(r_1) = 1 - \frac{m^*(r_1)}{m}, \quad (41)$$

and $V_{\text{grad}}(r_1)$ is determined by Eq. (27) with the effective mass

$$\frac{m^*(r_1)}{m} = \left(1 + \frac{m}{12\hbar^2}\int V_c^F(r)\rho(\mathbf{r}_1, \mathbf{r}_1 + \mathbf{r}) r^2 d\mathbf{r} + \frac{2m}{\hbar^2}V_H^{(2)}(r_1)\right)^{-1}. \quad (42)$$

4. PROPERTIES OF THE SELF-CONSISTENT AND THE OPTICAL POTENTIAL FOR NUCLEONS

Let us investigate the characteristics of the self-consistent and the optical potential for nucleons by considering the example of the ^{208}Pb nucleus. The proton and the neutron density are chosen here in the standard Fermi form [11], that is,

$$\rho_{n,p}(r_1) = \rho_{n,p}^0\left(1 + \exp\frac{r_1 - R_A}{a_0}\right)^{-1}, \quad (43)$$

where $\rho_n^0 + \rho_p^0 = \rho^0 = 0.17$ fm^{-3}, $R_A = 1.1A^{1/3}$ fm, and $a_0 = 0.54$ fm. The single-nucleon density matrix is represented in the semiclassical form

$$\rho_{n,p}(\mathbf{r}_1, \mathbf{r}_1 + \mathbf{r}) = 2\int_0^{k_F^{n,p}(R)} e^{i\mathbf{k}\cdot\mathbf{r}}\frac{d\mathbf{k}}{(2\pi)^3} = \frac{1}{\pi^2 r^2}(\sin k_F^{n,p}(R) r - k_F^{n,p}(R) r \cos k_F^{n,p}(R) r), \quad (44)$$

where $R = \left|\mathbf{r}_1 + \frac{\mathbf{r}}{2}\right|$ and $k_F^{n,p}(R) = (3\pi^2\rho_{n,p}(R))^{1/3}$ is the semiclassical Fermi momentum with $\rho_n(R) = \frac{A - Z}{A}\rho(R)$ and $\rho_p(R) = \frac{Z}{A}\rho(R)$.

For the quantity $\omega_{n,p}(r_1)$ defined in the Appendix as the density of the square of the nucleon momentum, we use the semiclassical approximation

$$\omega_{n,p}(r_1) = \frac{[k_F^{n,p}(r_1)]^5}{5\pi^2} = \frac{3}{5}[k_F^{n,p}(r_1)]^2\rho_{n,p}(r_1). \quad (45)$$

For the potentials (29), (38), and (40), the effective diffuseness a, which appears in expressions of the type in (34), will be calculated according to the scheme

$$f(R_1) = f(0)(1 + \exp 1)^{-1}, \quad a = R_1 - R_A. \quad (46)$$

For the parameters of vacuum NN forces, we take the set from [12], which was successfully used in investigating the properties of optical potentials for nucleons in nuclear matter. The ensuing analysis is performed for the nucleon-energy range $-60 \le E \le 100$ MeV.

The sum of the Hartree potentials $V_{\mathrm{H}}^{c}(r_1)$ and $V_{\mathrm{H}}^{(0)}(r_1)$ is independent of the nucleon momentum and is of an attractive character, its value at the center of the nucleus, –40.5 MeV, being maximal in magnitude. The quantities $J(r_1)$ and $V_{\mathrm{H}}^{(2)}(r_1)$ are close (over the entire region of r_1, their difference does not exceed 0.07 MeV fm^2), their maximum absolute values of 2.26 MeV fm^2 being attained at the center of the nucleus.

Let us explore the convergence of the expansion (12) of the Fock potential $V_{\mathrm{F}}(\mathbf{r}_1, \mathbf{k}_1)$ in orbital angular momenta l. From Fig. 1, which displays the functions $i^{-l}V_l(r_1, \bar{k}_1) \equiv \bar{V}_l(r_1, \bar{k}_1)$ for $l = 0, 1, 2$, it can be seen that, with increasing l, these functions decrease very fast in absolute value. By way of example, we indicate that, over the entire significant region of the parameters r_1 and $\bar{k}_1$, the absolute value of the function $\bar{V}_2(r_1, \bar{k}_1)$ does not exceed 0.87 MeV, this value being achieved in the surface region of the nucleus at $\bar{k}_1 \cong 1.8$ fm^{-1} ($E \cong 40$ MeV). To a precision higher than 0.9 MeV, only the $l = 0$ and $l = 1$ terms can therefore be retained in expansion (12), but this corresponds to Eq. (17). In the energy interval under investigation, the Fock components of the potential that are associated with the $l2$ and $ls2$ interactions do not exceed 1.2 MeV in absolute value (0.74 MeV for $E \le 40$ MeV) over the entire region $0 \le r_1 < \infty$; they induce virtually no changes in the shape of the potential and can be discarded to the above accuracy.

Let us compare the properties of the local energy-dependent potential (29) with the properties of the potentials (38) and (40), which were derived in the semiclassical approximation and in the second-order approximation in momentum, respectively. From the data in Table 1, it can be seen that, in all cases, the depths of the potentials $V(0, E)$ increase with energy. The depths of the potentials (38) and (29) virtually coincide over the entire energy range under investigation. The depth of the potential (40) is close to that of the potential (29) at $E = -60$ MeV and grows faster with energy than the depth of the potential (29) (the difference of the potential depths is 7 MeV at $E = 0$ MeV). At energies close to $E = 100$ MeV, the value $V(0, E)$ for the potential (40) changes sign, becoming repulsive.

The depth of the potential (29) coincides with the corresponding values of the local energy-dependent potential in nuclear matter [3]. The effect of the velocity-dependent forces on the depth of the potential (29) leads to the emergence of an additional repulsion (+5.68 MeV at the center of the nucleus at $E = 0$), which increases with energy.

As can be seen from Fig. 2, the shape of the potentials (29) and (38) can be described by the Fermi distribution (34) for positive nucleon energies; at negative energies, sizable deviations from (34) are observed in the large-r_1 region. This is because, at negative energies, the nucleon momentum becomes imaginary for r_1 values lying to the right of the classical turning point, so that the Bessel functions of an imaginary argument that are involved transform into a combination of Hankel functions containing divergent exponentials of the form $e^{r|\bar{k}_1|}$. As r_1 increases, the potential $V(r_1, E)$ therefore decreases much more slowly than in the case of

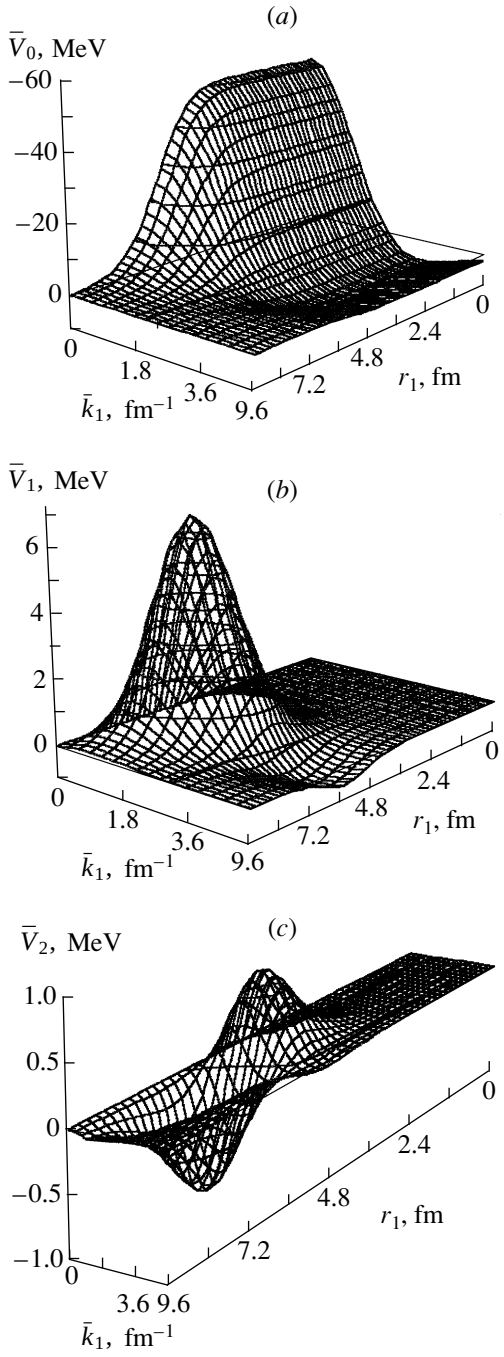

Fig. 1. Potentials $\bar{V}_l(r_1, \bar{k}_1)$ as functions of r_1 and $\bar{k}_1$ for $l =$ (*a*) 0, (*b*) 1, and (*c*) 2.

Table 1. Parameters of the radial and energy dependences of the potentials (29), (38), and (40)

E, MeV	$V(r_1, E)$ (29)			$V(r_1, E)$ (38)			$V(r_1, E)$ (40)		
	r_0, fm	a, fm	$V(0, E)$, MeV	r_0, fm	a, fm	$V(0, E)$, MeV	r_0, fm	a, fm	$V(0, E)$, MeV
–60	1.23	0.90	–75.86	1.24	1.31	–75.91	1.22	0.72	–75.08
–40	1.21	0.79	–66.72	1.21	0.89	–66.77	1.22	0.73	–64.65
0	1.17	0.79	–50.74	1.17	0.85	–50.75	1.20	0.74	–43.71
40	1.14	0.91	–37.92	1.14	1.03	–37.93	1.15	0.79	–22.76
70	1.11	1.11	–30.31	1.10	1.32	–30.32	0.78	0.65	–7.08
100	1.06	1.57	–24.19	1.02	1.92	–24.21	1.38	0.53	8.62

Table 2. Parameters of the function f_E^1 and α for the potentials (29), (38), and (40)

E, MeV	$V(r_1, E)$ (29)			$V(r_1, E)$ (38)			$V(r_1, E)$ (40)		
	$f_E^1(r_1)$		$\alpha(0, E)$	$f_E^1(r_1)$		$\alpha(0, E)$	$f_E^1(r_1)$		$\alpha(0, E)$
	r_0, fm	a, fm		r_0, fm	a, fm		r_0, fm	a, fm	
–60	1.36	2.68	0.42	1.56	1.03	0.42			
–40	1.30	0.93	0.40	1.32	1.31	0.40			
0	1.28	0.69	0.36	1.26	0.64	0.38	1.25	0.70	0.522
40	1.24	0.55	0.32	1.23	0.59	0.32			
70	1.22	0.54	0.29	1.22	0.58	0.29			
100	1.20	0.56	0.27	1.20	0.60	0.27			

real-valued nucleon momenta. At the same time, the potential (40) is of the Fermi form for $E \le 40$ MeV and differs from it markedly at higher positive energies.

From the data in Table 1, it can be seen that, even if the potentials (29), (38), and (40) are of the Fermi form, the parameters of these distributions are strongly dependent on the nucleon energy. Here, the values of the parameter r_0 ($r_0 = R_A A^{-1/3}$) of the potentials (29) and (38) decrease with increasing energy, but they remain close to each other at all energy values and close to the radius r_0 of the potential (40) for $E \le 40$ MeV. At the same time, the diffuseness values for the potentials (29), (38), and (40) increase on average with increasing energy. We note that the quoted parameters of the distribution in (34) for the potential (40) are consistent with the corresponding parameters from [2–5] at $E = 0$ [$V(0, E) = -43.5$ MeV, $r_0 = 1.20$ fm, and $a = 0.72$ fm]. The values of the coefficient $\alpha(0, E)$ in (36), which characterizes the energy dependence of the depths of the potentials $V(0, E)$, are presented in Table 2; it can be seen that they coincide for the potentials (29) and (38) and decrease with increasing energy from $\alpha = 0.42$ at $E = -60$ MeV to 0.27 at $E = 100$ MeV. These results are consistent with the phenomenological values of $\alpha(0, E) = 0.4$ and $\alpha(0, E) = 0.3$ for, respectively, negative and positive nucleon energies [11]. The energy-independent value of $\alpha(0, E) = 0.522$ for the potentials (40) is close to the value of 0.525 obtained by authors of [4] and is overly large in relation to the phenomenological values.

Phenomenological optical potentials are usually represented in the form (35) if we take the functions $f_E^0(r_1)$ and $f_E^1(r_1)$ to be coincident. A comparison of the data in Tables 1 and 2 and in Figs. 2 and 3 shows that the functions $f_E^0(r_1)$ and $f_E^1(r_1)$ generally have different features. For all the potentials (29), (38), and (40), the parameter r_0 of the function $f_E^1(r_1)$ is noticeably greater than the corresponding parameter of the function $f_E^0(r_1)$, while the diffuseness parameter a is smaller for $f_E^1(r_1)$ than for $f_E^0(r_1)$.

As can be seen from Fig. 4, the ratio of the effective mass (22) to the free-nucleon mass increases with energy, changing from 0.53 at $E = -60$ MeV to 0.82 at $E = 100$ MeV at the center of the nucleus and tending to unity for $r_1 \longrightarrow \infty$ at all energy values. Owing to the presence of the $l2$ and $ls2$ terms in the NN potential, the effective mass tends to $0.9m$ rather than to m in the high-energy limit, where the integrals of the quickly oscillating functions in (22) vanish. A comparison of the effective mass m^* (22) and the effective mass m_1^* (31) shows that they coincide at $r_1 = 0$ and that, over the entire region of r_1, their difference does not exceed, in

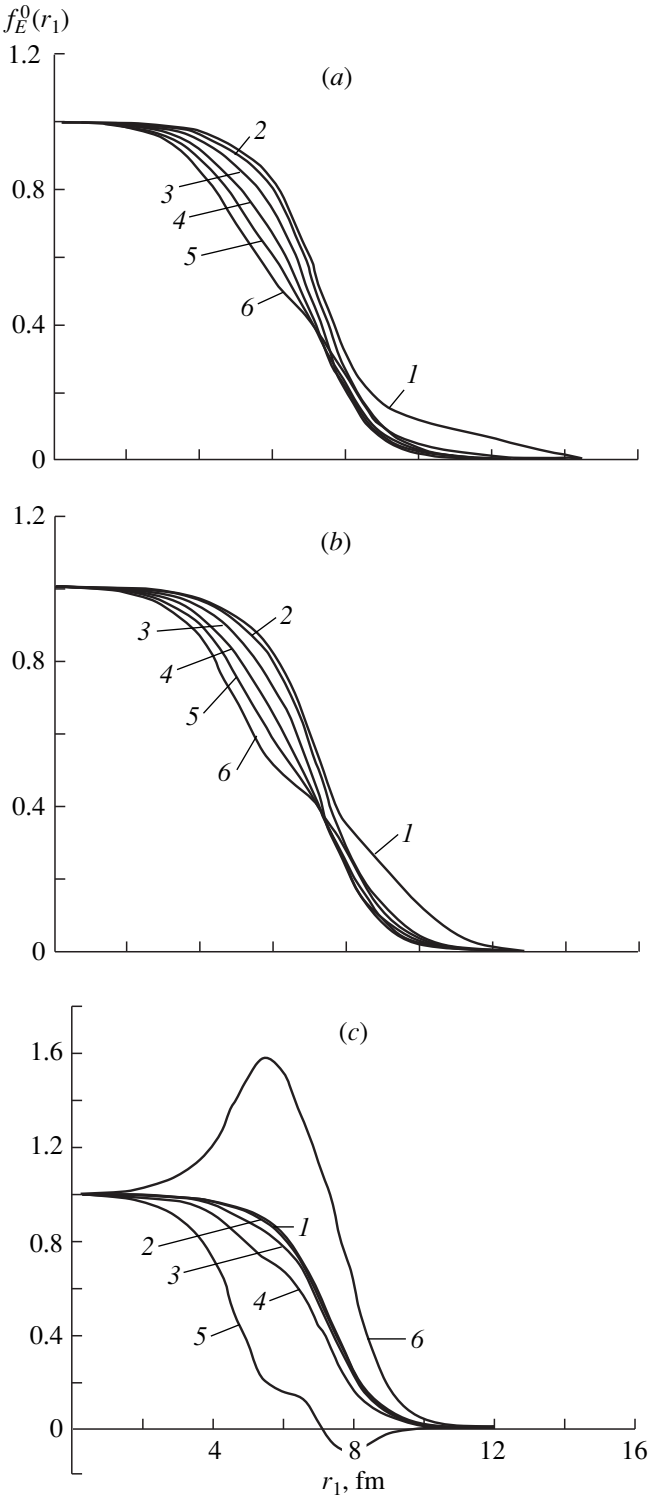

Fig. 2. Radial dependences of the functions $f_E^0(r_1)$ for the potentials (*a*) (29), (*b*) (38), and (*c*) (40) at –60, –40, 0, 40, 70, and 100 MeV (curves *1*, *2*, *3*, *4*, *5*, and *6*, respectively).

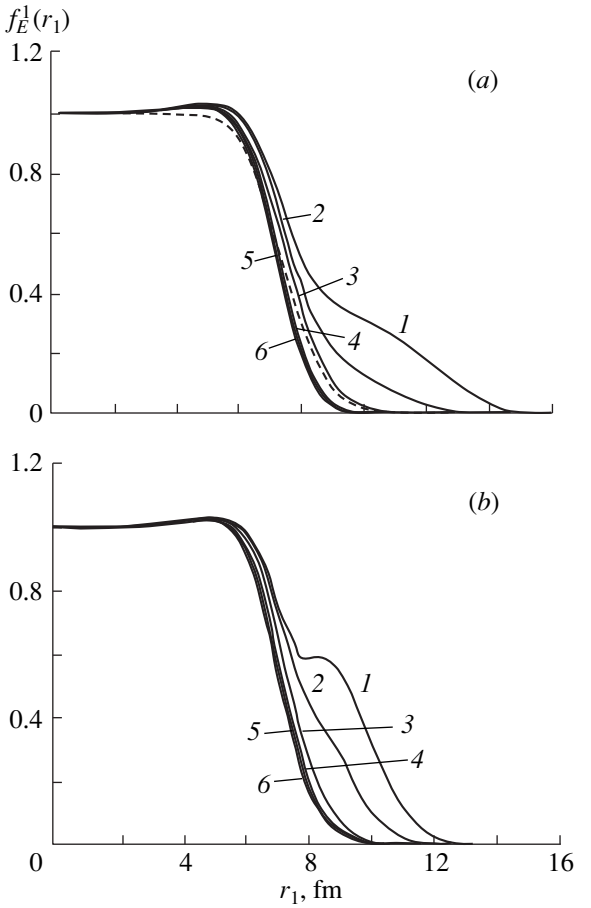

Fig. 3. Radial dependences of the functions $f_E^1(r_1)$ for the potentials (*a*) (29) and (*b*) (38) at –60, –40, 0, 40, 70, and 100 MeV (solid curves *1*, *2*, *3*, *4*, *5*, and *6*, respectively) and for the potential (40) (dashed curve).

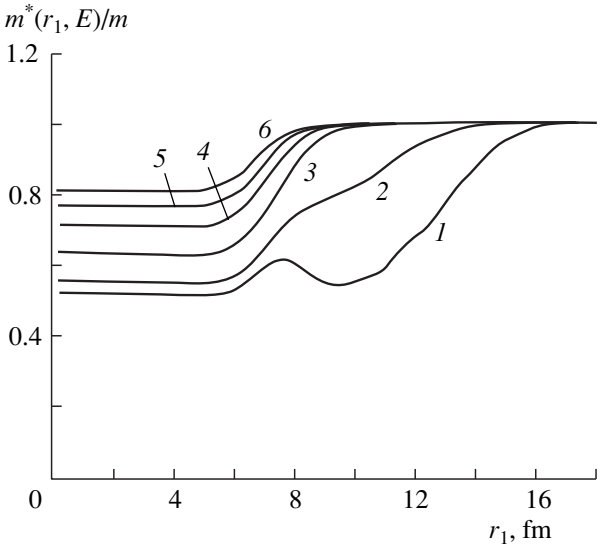

Fig. 4. Radial dependences of the ratio of the effective mass (22) to the free-nucleon mass at –60, –40, 0, 40, 70, and 100 MeV (curves *1*, *2*, *3*, *4*, *5*, and *6*, respectively).

Table 3. Parameters of the radial dependence of the potentials (29) and (40) with and without allowance for the gradient potential (27)

E, MeV	$V(r_1, E)$ (29)		$V(r_1, E)$ (29) without $V_{\text{grad}}(r_1, E)$		$V(r_1, E)$ (40)		$V(r_1, E)$ (40) without $V_{\text{grad}}(r_1)$	
	r_0, fm	a, fm	r_0, fm	a, fm	r_0, fm	a, fm	r_0, fm	a, fm
–60	1.23	0.90	1.24	0.97	1.22	0.72	1.23	0.79
–40	1.21	0.79	1.21	0.89	1.22	0.73	1.22	0.81
0	1.17	0.79	1.18	0.91	1.20	0.74	1.21	0.89
40	1.14	0.91	1.14	1.05	1.15	0.79	1.12	1.30
70	1.11	1.11	1.11	1.30	0.78	0.65	0.76	0.49
100	1.06	1.57	1.03	1.85	1.38	0.53	1.32	0.45

absolute value, $0.08m$ at $E = -60$ MeV and $0.02m$ for $E > 0$, decreasing as the energy grows.

As can be seen from Fig. 5, the gradient potential (27) has an alternating superficial character and increases with decreasing energy. At negative energies, it differs only slightly from the gradient potential appearing in (40); this is explained by the applicability of the second-order approximation in $\bar{k}_1$ near the turning points, where the absolute values of the nucleon momentum are small. The inclusion of the gradient potential reduces the effective diffuseness of the optical potentials (29) and (40) (see Table 3), but this leads to virtually no changes in the potential depths or in the parameter r_0.

The analysis of the potentials (29) and (38) reveals that the semiclassical approximation (37) is valid over the entire region $0 \le r_1 \le \infty$ for $E \ge 10$ MeV. In the energy region $0 \le E \le 10$ MeV, the difference of the potentials (29) and (38) does not exceed, in absolute value, 1.2 MeV at any value of r_1. The potential (40) noticeably differs from the potential (29), but they tend to approach each other with decreasing nucleon energy.

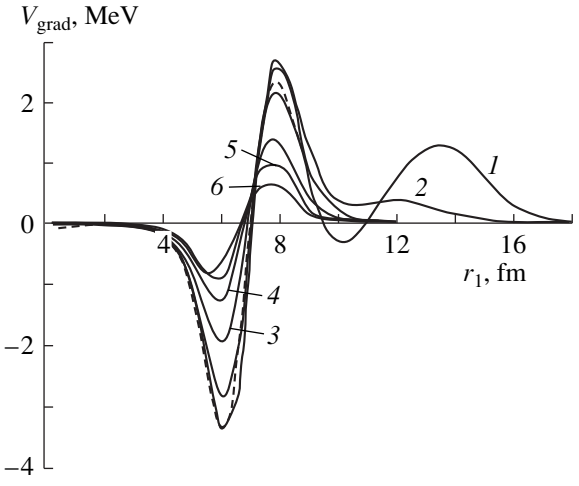

Fig. 5. Radial dependences of the gradient term $V_{\text{grad}}(r_1, E)$ for the potential (29) at –60, –40, 0, 40, 70, and 100 MeV (curves *1*, *2*, *3*, *4*, *5*, and *6*, respectively) and for the potential (40) (dashed curve).

5. CONCLUSION

The parameters of the effective energy-dependent potential that is equivalent to the nonlocal Hartree–Fock potential both for positive and for negative nucleon energies have been determined for the first time without resort to the assumption that the Fock potential is proportional to the momentum squared. It has appeared that the shape of the effective energy-dependent potential that describes simultaneously the self-consistent field and the real part of the optical potential for nucleons undergoes significant changes upon reversal of the sign of nucleon energy. We have demonstrated the validity of the semiclassical approximation at nucleon energies in excess of 10 MeV. It has been shown that, at nucleon energies below this value, it is important to take into account the gradient term that was not included in the conventional computational schemes.

APPENDIX

1. Components of the Local Hartree–Fock Potential in Spherical Nuclei with Allowance for Velocity-Dependent NN Interactions

The components of the Hartree potential can be represented as

$$V_{\text{H}}^{c}(\mathbf{r}_1) = \int V_{c}^{\text{H}}(r)\rho(r_2)d\mathbf{r}, \tag{A.1}$$

$$\begin{aligned} V_{\text{H}}^{(0)}(\mathbf{r}_1) &= \frac{1}{2}\int V_{l2,\,ls2}^{\text{H}}(r) r \frac{d\rho(r_2)}{dr_2}\left(\frac{r_1\xi + r}{r_2}\right)d\mathbf{r} \\ &- \frac{1}{8}\int V_{l2,\,ls2}^{\text{H}}(r) r^2 \left\{ \frac{d^2\rho(r_2)}{dr_2^2}\left(\frac{r_1}{r_2}\right)^2 (1-\xi^2) \right. \\ &\left. + \frac{1}{r_2}\frac{d\rho(r_2)}{dr_2}\left(1 + \left(\frac{r_1\xi + r}{r_2}\right)^2\right)\right\} d\mathbf{r} \\ &+ \frac{1}{6}\int V_{l2,\,ls2}^{\text{H}}(r) r^2 \omega(r_2) d\mathbf{r}, \end{aligned} \tag{A.2}$$

$$V_{\text{H}}^{(1)}(\mathbf{r}_1) = -\frac{1}{2}\int V_{l2,\,ls2}^{\text{H}}(r)\rho(r_2) r\xi d\mathbf{r}, \tag{A.3}$$

$$V_{\rm H}^{(2)}(\mathbf{r}_1) = \frac{1}{4}\int V_{l2,\,ls2}^{\rm H}(r)\rho(r_2)r^2(1-\xi^2)d\mathbf{r}, \quad \text{(A.4)}$$

$$V_{l2,\,ls2}^{\rm H}(r) = V_{l2}^{\rm H}(r) + V_{ls2}^{\rm H}(r), \quad \text{(A.5)}$$

where $V_c^{\rm H}(r)$, $V_{l2}^{\rm H}(r)$, and $V_{ls2}^{\rm H}(r)$ are the Hartree parts of, respectively, the central, the $l2$, and the $ls2$ interaction of nucleons; ξ is the cosine of the angle between the vectors $\mathbf{r}$ and $\mathbf{r}_1$; and $\omega(r_2) = \omega_n(r_2) + \omega_p(r_2)$ is the total density of the square of the nucleon momentum with

$$\bar{\omega}_{n,\,p}(r_2) = \nabla_{2'}\cdot\nabla_2\rho_{n,\,p}(\mathbf{r}_2, \mathbf{r}_2')\big|_{\mathbf{r}_2' = \mathbf{r}_2}. \quad \text{(A.6)}$$

The components of the Fock potential are given by

$$\begin{aligned} V_{\rm F}^{l2,\,ls2}(\mathbf{r}_1, \mathbf{k}_1) &= -\frac{1}{16}\int V_{l2,\,ls2}^{\rm F}(r)\rho(\mathbf{r}_1, \mathbf{r}_1+\mathbf{r})\{[\mathbf{r}\times\mathbf{k}_1]^2 \\ &\quad + 4i\mathbf{r}\cdot\mathbf{k}_1\}e^{i\mathbf{r}\cdot\mathbf{k}_1}d\mathbf{r} \\ &\quad + \frac{1}{16}\int V_{l2,\,ls2}^{\rm F}(r) f(\mathbf{r}_1, \mathbf{r}_1+\mathbf{r})e^{i\mathbf{r}\cdot\mathbf{k}_1}d\mathbf{r} \\ &\quad + \frac{1}{8}\int V_{l2,\,ls2}^{\rm F}(r)\left(\frac{\partial\rho(\mathbf{r}_1, \mathbf{r}_1+\mathbf{r})}{\partial\xi} - r\frac{\partial\rho(\mathbf{r}_1, \mathbf{r}_1+\mathbf{r})}{\partial r_1}\right) \\ &\quad \times\left(\frac{y\mathbf{i}-x\mathbf{j}}{r}\right)\cdot[\mathbf{r}\times i\mathbf{k}_1]e^{i\mathbf{r}\cdot\mathbf{k}_1}d\mathbf{r}, \end{aligned} \quad \text{(A.7)}$$

$$V_{l2,\,ls2}^{\rm F}(r) = V_{l2}^{\rm F}(r) + V_{ls2}^{\rm F}(r), \quad \text{(A.8)}$$

where $V_{l2}^{\rm F}(r)$ and $V_{ls2}^{\rm F}(r)$ are the Fock parts of, respectively, the $l2$ and the $ls2$ interactions of nucleons; $\mathbf{i}$ and $\mathbf{j}$ are unit vectors in the x and y directions, respectively; and the function $f(\mathbf{r}_1, \mathbf{r}_1+\mathbf{r})$ has the form

$$\begin{aligned} f(\mathbf{r}_1, \mathbf{r}_1+\mathbf{r}) &= (1-\xi^2)\left(r^2\frac{\partial^2\rho(\mathbf{r}_1, \mathbf{r}_1+\mathbf{r})}{\partial r_1^2}\right. \\ &\quad \left. - 2r\frac{\partial^2\rho(\mathbf{r}_1, \mathbf{r}_1+\mathbf{r})}{\partial r_1\partial\xi} + \frac{\partial^2\rho(\mathbf{r}_1, \mathbf{r}_1+\mathbf{r})}{\partial\xi^2}\right) \\ &\quad + \left\{(1+\xi^2)\frac{r^2}{r_1} + 4r\xi\right\}\frac{\partial\rho(\mathbf{r}_1, \mathbf{r}_1+\mathbf{r})}{\partial r_1} \\ &\quad - 2\xi\frac{\partial\rho(\mathbf{r}_1, \mathbf{r}_1+\mathbf{r})}{\partial\xi} - 2r\frac{\partial\rho(\mathbf{r}_1, \mathbf{r}_1+\mathbf{r})}{\partial r}. \end{aligned} \quad \text{(A.9)}$$

By recasting the potential $V_{\rm F}^{l2,\,ls2}(\mathbf{r}_1, \mathbf{k}_1)$ into the form (12), we arrive at

$$\begin{aligned} &V_{\rm F}^{l2,\,ls2}(\mathbf{r}_1, \mathbf{k}_1) \\ &= \sum_l\left[V_l^{l2,\,ls2}(r_1, k_1) + \tilde{V}_l^{l2,\,ls2}(r_1, k_1)\frac{\mathbf{r}_1\cdot\mathbf{k}_1}{r_1k_1}\right]P_l(\xi_1), \end{aligned} \quad \text{(A.10)}$$

where

$$\begin{aligned} V_l^{l2,\,ls2}(r_1, k_1) &= i^l(2l+1) \\ &\quad \times\left\{-\frac{1}{16}\int V_{l2,\,ls2}^{\rm F}(r)\rho_l(r_1, r)j_l(rk_1)r^4drk_1^2\right. \\ &\quad - \frac{1}{16}\int V_{l2,\,ls2}^{\rm F}(r)\rho_l(r_1, r)\left[\frac{l(l-1)}{(rk_1)^2}j_l(rk_1)\right. \\ &\quad \left.\left. - \frac{(2l+1)}{rk_1}j_{l+1}(rk_1) + j_{l+2}(rk_1)\right]r^4drk_1^2\right. \\ &\quad - \frac{1}{4}\int V_{l2,\,ls2}^{\rm F}(r)\rho_l(r_1, r)\left[\frac{l}{rk_1}j_l(rk_1) - j_{l+1}(rk_1)\right]r^3drk_1 \\ &\quad + \frac{1}{16}\int V_{l2,\,ls2}^{\rm F}(r)f_l(r_1, r)j_l(rk_1)r^2dr \\ &\quad \left. - \frac{1}{8}\int V_{l2,\,ls2}^{\rm F}(r)f_l'(r_1, r)\left[\frac{l}{rk_1}j_l(rk_1) - j_{l+1}(rk_1)\right]r^3drk_1\right\}; \end{aligned} \quad \text{(A.11)}$$

$$\begin{aligned} &\tilde{V}_l^{l2,\,ls2}(r_1, k_1) \\ &= i^{l+1}(2l+1)\frac{1}{8}\int V_{l2,\,ls2}^{\rm F}(r)\tilde{f}_l(r_1, r)j_l(rk_1)r^3drk_1. \end{aligned} \quad \text{(A.12)}$$

In Eqs. (A.11) and (A.12), we have used the notation

$$\rho_l(r_1, r) = 2\pi\int\rho(\mathbf{r}_1, \mathbf{r}_1+\mathbf{r})P_l(\xi)d\xi, \quad \text{(A.13)}$$

$$f_l(r_1, r) = 2\pi\int f(\mathbf{r}_1, \mathbf{r}_1+\mathbf{r})P_l(\xi)d\xi, \quad \text{(A.14)}$$

$$\begin{aligned} f_l'(r_1, r) &= 2\pi\int\left[\frac{\partial\rho(\mathbf{r}_1, \mathbf{r}_1+\mathbf{r})}{\partial\xi}\right. \\ &\quad \left. - r\frac{\partial\rho(\mathbf{r}_1, \mathbf{r}_1+\mathbf{r})}{\partial r_1}\right]\xi P_l(\xi)d\xi, \end{aligned} \quad \text{(A.15)}$$

$$\begin{aligned} \tilde{f}_l(r_1, r) &= 2\pi\int\left[\frac{\partial\rho(\mathbf{r}_1, \mathbf{r}_1+\mathbf{r})}{\partial\xi}\right. \\ &\quad \left. - r\frac{\partial\rho(\mathbf{r}_1, \mathbf{r}_1+\mathbf{r})}{\partial r_1}\right]P_l(\xi)d\xi. \end{aligned} \quad \text{(A.16)}$$

2. Local Energy-Dependent Potential in Spherical Nuclei with Allowance for Velocity-Dependent NN Interactions

By taking into account the Fock parts of the $l2$ and $ls2$ interactions and discarding the $l \geq 2$ terms in Eqs. (12) and (A.10), we reduce the potential $V_F(\mathbf{r}_1, \mathbf{k}_1)$ to the form

$$V_F(\mathbf{r}_1, \mathbf{k}_1) = V_0(r_1, k_1) + V_0^{l2,ls2}(r_1, k_1) + [V_1(r_1, k_1) + \tilde{V}_0^{l2,ls2}(r_1, k_1) + V_1^{l2,ls2}(r_1, k_1)]\frac{\mathbf{r}_1 \cdot \mathbf{k}_1}{r_1 k_1}. \quad \text{(A.17)}$$

Instead of the Schrödinger equation (21), we then obtain

$$\left(\mathbf{k}_1 \frac{\hbar^2}{2m^*(r_1, k_1)}\mathbf{k}_1 + V_H^c(r_1) + V_H^{(0)}(r_1) + V_0(r_1, k_1) + V_0^{l2,ls2}(r_1, k_1) - (\tilde{I}(r_1, k_1) + J(r_1) + V_H^{(2)}(r_1))\mathbf{k}_1^2 - E\right)\varphi_E(\mathbf{r}_1) = 0, \quad \text{(A.18)}$$

where the effective mass $m^*(r_1, k_1)$ is determined by Eq. (22), in which

$$\tilde{I}(r_1, k_1) = -i\int_{r_1}^{\infty}(V_1(r_1, k_1) + V_1^{l2,ls2}(r_1, k_1) + \tilde{V}_0^{l2,ls2}(r_1, k_1))\frac{1}{k_1}dr_1 \quad \text{(A.19)}$$

is substituted for $I(r_1, k_1)$.

Representing the wave function $\varphi_E(\mathbf{r}_1)$ in the form (23) and defining the form factor $f(r_1, k_1)$ by expression (24), we find that the function $\tilde{\varphi}_E(\mathbf{r}_1)$ satisfies an equation of the type (25) with the potential

$$V(r_1, \bar{k}_1) = \frac{m^*(r_1, \bar{k}_1)}{m}(V_H^c(r_1) + V_H^{(0)}(r_1) + V_0(r_1, \bar{k}_1) + V_0^{l2,ls2}(r_1, \bar{k}_1) - (J(r_1) + \tilde{I}(r_1, \bar{k}_1) + V_H^{(2)}(r_1))\bar{k}_1^2 + V_{\text{grad}}(r_1, \bar{k}_1) + \left(1 - \frac{m^*(r_1, \bar{k}_1)}{m}\right)E, \quad \text{(A.20)}$$

where $V_{\text{grad}}(r_1, \bar{k}_1)$ is given by Eq. (27). With allowance for the velocity-dependent NN interactions, the effective local energy-dependent potential then assumes the form

$$V(r_1, E) = V_H^c(r_1) + V_H^{(0)}(r_1) + V_0(r_1, \bar{k}_1(r_1, E)) + V_0^{l2,ls2}(r_1, \bar{k}_1(r_1, E)) + V_H^{(2)}(r_1)\bar{k}_1^2(r_1, E) + V_{\text{grad}}(r_1, \bar{k}_1(r_1, E)). \quad \text{(A.21)}$$

REFERENCES

1. S. G. Kadmensky, Fiz. Élem. Chastits At. Yadra **28**, 391 (1997) [Phys. Part. Nucl. **28**, 159 (1997)].
2. S. G. Kadmenskiĭ, Izv. Akad. Nauk, Ser. Fiz. **63**, 60 (1999).
3. S. G. Kadmenskiĭ, P. A. Luk'yanovich, and V. V. Lyuboshits, Yad. Fiz. **56** (9), 86 (1993) [Phys. At. Nucl. **56**, 1201 (1993)].
4. S. G. Kadmensky, V. V. Lyuboshitz, and A. A. Shaikina, Yad. Fiz. **58**, 982, 1222, 1606 (1995) [Phys. At. Nucl. **58**, 910, 1143, 1514 (1995)].
5. S. G. Kadmensky and V. V. Lyuboshitz, Yad. Fiz. **59**, 239 (1996) [Phys. At. Nucl. **59**, 220 (1996)].
6. S. G. Kadmensky and S. A. Dedov, Yad. Fiz. **60**, 1765 (1997) [Phys. At. Nucl. **60**, 1610 (1997)].
7. N. F. Mott and H. S. W. Massey, *The Theory of Atomic Collisions* (Clarendon, Oxford, 1965; Mir, Moscow, 1969).
8. L. D. Landau and E. M. Lifshitz, *Quantum Mechanics: Non-Relativistic Theory* (Nauka, Moscow, 1974; Pergamon, Oxford, 1977).
9. R. P. Feynman, *Statistical Mechanics: A Set of Lectures* (Benjamin, Reading, Mass., 1972; Mir, Moscow, 1975).
10. F. G. Perey and D. S. Saxon, Phys. Lett. **10**, 107 (1964).
11. A. Bohr and B. R. Mottelson, *Nuclear Structure*, Vol. 1: *Single-Particle Motion* (Benjamin, New York, 1969; Mir, Moscow, 1971).
12. D. Gogny *et al.*, Phys. Lett. B **32B**, 591 (1970).

Translated by A. Isaakyan

Physics of Atomic Nuclei, Vol. 64, No. 1, 2001, pp. 49–56. Translated from Yadernaya Fizika, Vol. 64, No. 1, 2001, pp. 51–59.

NUCLEI
Theory

Radiative Strength Functions for Nuclei in Which the Number of Protons Is Close to the Magic Number of $Z = 28$

I. D. Fedorets

Kharkov State University, Sumskaya ul. 35, Kharkov, 310022 Ukraine

Received July 23, 1999; in final form, January 19, 2000

Abstract—The distribution of the radiative strength in nuclei where the number of nucleons of one type is nearly magic ($Z = 28 \pm 1$) and where there are a few valence nucleons of the other type is investigated. It is shown that the statistical approach that is based on Fermi liquid theory and which takes into account temperature and the shell structure of nuclei leads to good agreement with experimental data on radiative strength functions below the neutron binding energy in such nuclei. Only for the ^{59}Co and ^{65}Cu nuclei, which have the largest number of valence neutrons among the cobalt and copper isotopes being investigated, is the energy dependence of the radiative strength compatible with a Lorentz distribution as well. © *2001 MAIK "Nauka/Interperiodica".*

1. INTRODUCTION

Experimental and theoretical investigations of the energy dependence of radiative strength functions for nuclei in which the number of protons is close to the magic number of $Z = 28$ revealed that, for the majority of these nuclei, experimental data on radiative strength functions comply, neither in magnitude nor in shape, with a low-energy extrapolation of the Lorentz distribution that successfully describes giant electric-dipole resonances. The radiative strength functions obtained in [1, 2] for $E1$ transitions in the $^{61–63}$Cu nuclei exhibit a much sharper energy dependence than that which follows from an extrapolation of the Lorentz distribution to low gamma-ray energies. For the ^{59}Co nucleus, such an extrapolation yields a radiative-strength-function value eight times as great as the experimental result of Nilson *et al.* [1]. Since the attempts undertaken in [1] to improve the agreement by varying the parameters used to determine the pursued radiative strength function, its behavior was considered to be anomalous. At the same time, the data on the radiative strength function that were obtained by the same group for the ^{65}Cu nucleus [3] are closely approximated by a Lorentz distribution in the region of low photon energies as well. In [4, 5], it was assumed that a Lorentzian form is also appropriate for describing the experimental radiative strength function for the ^{61}Cu and ^{63}Cu nuclei in the same range of photon energies as in [1–3]. Possible deviations of the radiative strength functions from the behavior specified by a low-energy extrapolation of this form would suggest that the strength function depends on the properties of the final nucleus. This would contradict the well-known hypothesis of Axel and Brink, who conjectured that primary $E1$ transitions observed in radiative nucleon capture must be induced by the same processes as the giant dipole resonance (GDR), which is approximated by a Lorentz distribution, and that giant resonances built on the ground state and on an excited state must be characterized by identical parameter values.

In this study, we aim at determining the absolute values of radiative strength functions and at comprehensively investigating their energy dependence below the neutron binding energy for $E1$ transitions in the $^{57, 59}$Co nuclei, where only one proton is needed to fill completely the $1f_{7/2}$ shell, and in the $^{61–63, 65}$Cu nuclei, where there is one extra proton above the filled $1f_{7/2}$ shell and where the number of valence neutrons increases. It is assumed that the structure of these nuclei can be described by the shell model and that the paucity of information about the properties of these nuclei will not complicate data analysis.

Since much attention is given here to the question of why the conventional treatment of radiative strength functions fails in the case of ^{61}Cu and ^{63}Cu nuclei [1, 2, 4], while providing a fairly good description of experimental data for the ^{65}Cu nucleus [3, 5], it is reasonable to consider energies in the same range as in [1–5]. Preliminary results on primary gamma transitions in individual nuclei from the region under study were reported in [6–9].

It should be noted that available experimental data on the energy dependence of radiative strength functions for $A \leq 100$ nuclei—these data predominantly come from experiments studying (p, γ) reaction—are obviously insufficient for systematic investigations in these realms, in sharp contrast to what we have in the region of $A \geq 100$ nuclei, where considerable advances have recently been made in studying the low-energy behavior of radiative strength functions owing to information efficiently extracted from data on radiative neutron capture. The situation is aggravated by the absence of experimental data on the level densities for nuclei under consideration in the excitation-energy range of interest and by the fact that the optical-model parame-

ters used in determining the radiative strength functions at low proton energies are questionable. It is difficult to compare radiative-strength-function values estimated on the basis of experimental data because different estimates for the same nuclei were often obtained with different values of the same parameters.

2. EXPERIMENTAL RESULTS AND THEIR ANALYSIS

In just the same way as in [1–5], the radiative strength functions are determined here by using the averaged intensities of primary gamma transitions to individual low-lying states excited in the nuclei under investigations in the (p, γ) reactions. For the target nuclei ^{56}Fe, ^{58}Fe, ^{60}Ni, ^{61}Ni, ^{62}Ni, and ^{64}Ni, the values of the energy release in the relevant (p, γ) reactions are $Q_0 = 6.02$, 7.37, 4.81, 5.87, 6.12, and 7.45 MeV, respectively. These Q_0 values are sufficiently high for the corresponding level density in compound nuclei to satisfy the conditions under which the statistical description is valid. That the thresholds for the (p, n) reactions on the above targets exceed 5.4, 3.1, 7.0, 3.1, 4.8, and 2.5 MeV, respectively, leaves a comparatively wide range of incident-proton energies at which the relevant investigations can be performed without exciting the neutron channel. The averaged intensities of primary gamma transitions were obtained from the spectra of high-energy gamma rays as measured by a pair spectrometer for proton energies from 1.5 to 3.0 MeV for $^{56, 58}$Fe targets, from 1.50 to 3.88 MeV for ^{60}Ni targets, from 2.21 to 2.43 MeV for ^{61}Ni targets, from 1.5 to 3.0 MeV for ^{62}Ni targets, and from 1.55 to 2.90 MeV for ^{64}Ni targets. Averaging over compound-nucleus states that is necessary for effectively suppressing Porter–Thomas fluctuations [10] and for achieving a satisfactory statistical accuracy was ensured by choosing target thicknesses in an optimal way and successively adding gamma-ray spectra measured at different energies with a shift equivalent to the target thickness.

According to statistical theory, the (p, γ) cross section averaged over compound-nucleus resonances can be represented in the form [11]

$$\sigma_{p,\gamma} = \frac{\lambda_p^2}{4\pi}\sum_J g(J) V_p V_\gamma \left(\sum_c V_c\right)^{-1}, \qquad (1)$$

where

$$V = T\left[1 + T\left(\sum_c T_c\right)^{-1}(W-1)\right]^{-1},$$

$$W = 1 + 2(1 + T^{1/2})^{-1};$$

λ_p is the proton wavelength; $g(J) = (2J + 1)/(2s + 1)/(2I + 1)$, I and s being the target-nucleus spin and the nucleon spin, respectively; T stands for the corresponding penetrability factors; and c is the channel index. For an even–even target nucleus, we have $g(J) = (2J + 1)/2$. Summation in Eq. (1) is performed over all the open reaction channels c and J^π compound-nucleus states allowed by relevant selection rules. The quantity W in expression (1) takes into account a correction for fluctuations that the cross section can develop because of a small number of open channels [11]. This correction may prove to be important at low energies. Expression (1) can be recast into the more compact form

$$\bar{\sigma}(p, \gamma_f) = \sum \sigma_\lambda \frac{T_{\gamma_f \lambda}}{T_\lambda}, \qquad (2)$$

where σ_λ is the cross section for the formation of the compound nucleus in the state λ, T_λ is the sum of all penetrability factors corresponding to open deexcitation channels for the state λ, and $T_{\gamma_f \lambda}$ is the penetrability factor for photons corresponding to primary transitions from the group of compound-nucleus states λ at energy E_γ to the final state f at energy $E_f = E_\lambda - E_\gamma$. For γ rays corresponding to transitions of multipole order L, the penetrability factor $T_{\gamma_f \lambda}$ can be expressed in terms of the radiative strength function $S_{\lambda_f}(E_\gamma)$ as [12]

$$T_{\gamma_f \lambda} = 2\pi S_{\lambda_f}(E_\gamma) E_\gamma^{2L+1}. \qquad (3)$$

The penetrability factor T_λ then assumes the form

$$T_\lambda = \sum_{l_{p'} j_{p'}} T_{l_{p'} j_{p'}} + \sum_{l_{n'} j_{n'}} T_{l_{n'} j_{n'}} + \sum \int_0^{E_\lambda} 2\pi \rho_J(E_\lambda - E_\gamma) E_\gamma^{2L+1} S_{\lambda_f}(E_\gamma) dE_\gamma, \qquad (4)$$

where $T_{l_{p'} j_{p'}}$ are the penetrability factors for protons in the output channel, $T_{l_{n'} j_{n'}}$ are the penetrability factors for the neutron channel, and $\rho_J(E_\lambda - E_\gamma)$ is the density of levels occurring at E_f and having a spin J.

The penetrability factors for protons were calculated with allowance for the results obtained in [13–21]. The use of a global systematics of the optical-potential parameters deduced from an analysis of the scattering of protons with energies above 8 MeV [13, 17] in calculations for energies below 4 MeV would hardly be reasonable, especially as the absorption potential can change sharply near closed shells [22]. Indeed, the detailed analysis of the cross sections for (p, γ) reactions and for the elastic and the inelastic scattering of low-energy protons on $^{54, 56}$Fe nuclei that was performed by Boukharouba *et al.* [15], who relied on the optical model, invoking dispersion theory and taking into account channel coupling and shell effects, revealed that the observed dependence of the imaginary part of the optical potential on the mass number for nuclei with A close to 60 can be attributed to changes that the filling of the shell induces in the density of

intermediate $2p1h$ states. In the present study, the optical-potential parameters were chosen in such a way as to ensure the best fit to data from [18–21, 23–25] on the cross sections for elastic and inelastic proton scattering and (p, γ) and (p, n) reactions on ^{56,58}Fe and $^{60–62,64}$Ni nuclei at incident proton energies below 4 MeV. The resulting parameters of the real part of the optical potential were virtually identical to those from [13–17], with exception of the diffuseness, which proved to be reduced. At the same time, the parameters of the imaginary part of the potential differ markedly from those in the global systematics. In particular, the imaginary part of the surface potential was taken in the form $W_s(E) = 3.85 + 0.72E$ MeV for the ^{56}Fe and in the form $W_s(E) = 5.6 – 0.25E$ MeV for the ^{58}Fe target nucleus. In just the same way as in [19], the imaginary part was used in the form $W_s(E) = 1.5(A – 58) + 0.5$ MeV for all nickel isotopes, despite the fact that experimental data on the inelastic scattering of low-energy protons by ^{60}Ni and ^{62}Ni nuclei are better approximated by the calculations with W_s from [13, 17]. The use of the parameters from [13, 17] in statistical calculations gives considerably overestimated values of the cross sections for the (p, γ) reaction on all stable nickel isotopes.

The level density in the nuclei under study, which is also an ingredient of the statistical description, was calculated within the back-shifted Fermi gas model. In these calculations, the level-density parameter a, the excitation-energy shift Δ allowing for nucleon pairing and shell effects, and the moment of inertia $\mathcal{J}$ were set to the values taken from [26] and presented in the table (versions 1 and 2). For the sake of comparison, the level density was also calculated by the phenomenological statistical method described in [27]. The parameter values used in this case are also presented in the table (version 3). A description of the level density was taken to be acceptable if it ensured a good fit of statistical calculations to experimental data over a wide range of excitation energies. The level densities calculated with the parameter values from the table are displayed in Fig. 1, along with experimental data. Circles in this figure represent data on the discrete section of the energy-level diagram up to an excitation energy of 5.5 MeV that were taken from [28, 29] for the ^{57,59}Co nuclei, from [30, 31] for the $^{61–63,65}$Cu nuclei, and from the NUDAT BNL database containing current results on these nuclei. For the ^{57}Co nucleus, squares show the data from [32], while the triangle corresponds to the results from [33]. For the ^{61}Cu nucleus, the square represents the data from [34]. For other nuclei, data for excitation energies above 5.5 MeV were taken from [35].

Specifying the form of the radiative strength function $S_{\lambda_f}(E_\gamma)$, one can now use expression (1) to calculate the intensities of direct gamma transitions to each individual low-lying state of the final nucleus. A comparison of the intensity calculated in this way with experimental data provides a criterion of the applicability of the form assumed for the radiative strength function. In this study, the radiative strength function appearing in Eq. (4) was specified either in a Lorentzian form or in the form obtained in various theoretical approaches. The quantity $S_{\lambda_f}[E_\gamma]$ entering into the coefficient $T_{\gamma_f\lambda}$ in the numerator on the right-hand side of Eq. (2) was chosen in such a way as to reproduce the measured absolute values of the partial (p, γ_f) cross section.

Parameters used in calculating the level density in the nuclei under study

Nucleus	Version	a, MeV^{-1}	Δ, MeV	$\mathcal{J}_{\text{rig}}$
^{57}Co	1	5.21	–0.41	0.5
	2	6.12	–0.20	1.0
	3	4.18	1.59	0.4
^{59}Co	1	5.50	–0.77	0.5
	2	6.31	–0.47	1.0
	3	3.06	1.56	0.4
^{61}Cu	1	5.03	–1.55	0.5
	2	5.99	–1.06	1.0
	3	4.41	1.54	0.4
^{62}Cu	1	6.48	0.97	0.5
	2	7.27	–1.07	1.0
	3	3.98	1.54	0.4
^{63}Cu	1	5.74	–0.96	0.5
	2	6.63	–0.67	1.0
	3	4.12	1.51	0.4
^{65}Cu	1	5.47	–1.00	0.5
	2	6.24	–0.77	1.0
	3	4.55	1.49	0.4
	4	3.94	1.49	0.4

Most frequently, $E1$ radiative strength functions are calculated (see, for example, [36–38] and references therein) within the approach that is based on Fermi liquid theory [39] and which was developed for spherical nonmagic nuclei. The main distinction between this method and that which relies on a Lorentz distribution is that, for $E_\gamma \longrightarrow 0$, the radiative strength function tends to a finite limit determined by the giant-resonance parameters E_0, Γ_0, and σ_0 and the nuclear temperature T in the final state. Here, we calculate radiative strength functions within the approach that was proposed in [40, 41] and which is also based on Fermi liquid theory, but which employs approximations somewhat differing from those in [39]; within this approach, it is considered that the energy dependence of the radiative strength function is affected by the shape of the GDR, whose width depends on excitation energy and on the nuclear temperature, and by the number of single-particle states that can be connected by transitions allowed by the Pauli exclusion principle. The number of such states depends on the transition energy and on the tem-

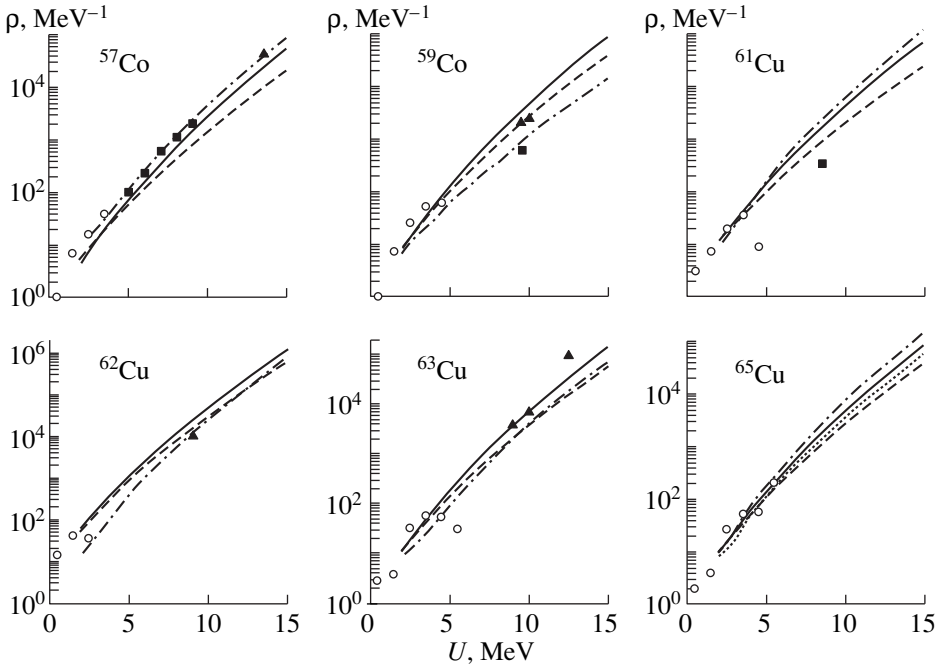

Fig. 1. Level densities in the nuclei under analysis versus excitation energy. In each panel, the dashed, the solid, the dash-dotted, and the dotted curve represent the results of the calculations with the parameter values presented in the table (versions 1–4, respectively). Experimental data were taken from [28–35] (for more details, see the main body of the text).

perature and the shell structure of the nucleus. Previously, we successfully used this approach to analyze experimental data on radiative strength functions for the dipole transitions in the ^{46}Ti [42], ^{69}Ga [43], ^{70}Ge [44], and ^{73,75}As [45] nuclei, which are pronouncedly deformed. However, it appeared to be less appropriate for describing experimental energy dependences of the radiative strength functions for the ^{85,87,89}Y nuclei [46] and especially for the ^{90}Zr nucleus [47]. For a GDR featuring two maxima, the $E1$ strength function treated within this approach can be represented as

$$S_\gamma^{E1} = 8.67\times10^{-8}\cdot 2\pi[1+\exp(-E_\gamma/T)]^{-1} \times\sum_{i=1}^{2}\frac{\sigma_i E_i^2\Gamma_{R(i)}(E_\gamma)}{(E_\gamma^2-E_i^2)^2+E_i\Gamma_{R(i)}(E_\gamma)}, \quad (5)$$

where

$$\Gamma_{R(i)}(E_\gamma) = \Gamma_i\rho_{2p-2h}(E_\gamma, T)/\rho_{2p-2h}(E_i, T)$$

and σ_i, E_i, and Γ_i are, respectively, the cross sections at the maxima, the positions of the GDR components, and their widths. Their values were chosen in such a way as to ensure the best fit of a Lorentz distribution to experimental data from [48, 49] on the cross sections for the (γ, n) reactions on ^{59}Co and ^{63}Cu nuclei. For want of experimental data on GDRs in the ^{57}Cu and ^{61,62,65}Cu nuclei, the radiative strength functions for these nuclei were calculated with the GDR parameters identical to those for the ^{59}Co and ^{63}Cu nuclei, respectively. The density of $2p$–$2h$ states, $\rho_{2p-2h}(E_\gamma, T)$, is governed both by the density of one-particle states and by the occupation numbers in the state that is populated after photon emission. In calculating $\rho_{2p-2h}(E_\gamma, T)$, we took into account of the shell structure of the spectrum of single-particle levels and the effect of the nuclear temperature T on the occupation numbers in these levels.

Since the single-particle $3s$ resonance at proton energies below the Coulomb barrier is excited in these nuclei, it is necessary to take into account the possible contribution of nonstatistical processes to the radiative strength functions that are associated with the effect of this resonance. The possible contribution of the valence capture mechanism involving the excitation of the quasistationary $3s$ and $2d$ states was estimated in [4]. The relevant contribution to the cross section was calculated within the semimicroscopic approach developed in [50]. In this approach, simple configurations are calculated on the basis of a single-particle model, while their coupling to complex configurations is taken into account within the optical model. It turned out that, near the maxima of the $3s$ and $2d$ resonances, the contribution of the valence mechanism to the capture cross section may be as large as 50%. At lower energies (6–10 MeV), the maximum contribution for $(3s + 2d) \longrightarrow 2p$ transitions can saturate 30 and 15% of the observed cross sections for ^{61}Cu and ^{63}Cu nuclei, respectively. The nonstatistical contribution is the most pronounced for the ^{61}Cu nucleus and decreases fast as the neutron shell is filled.

In order to estimate the contribution of the $M1$ transitions, we used the relation

$$S_\gamma^{E1}/S_\gamma^{M1} = 0.03A(E_\gamma^2+(\pi T)^2)/B_n^2 \quad (6)$$

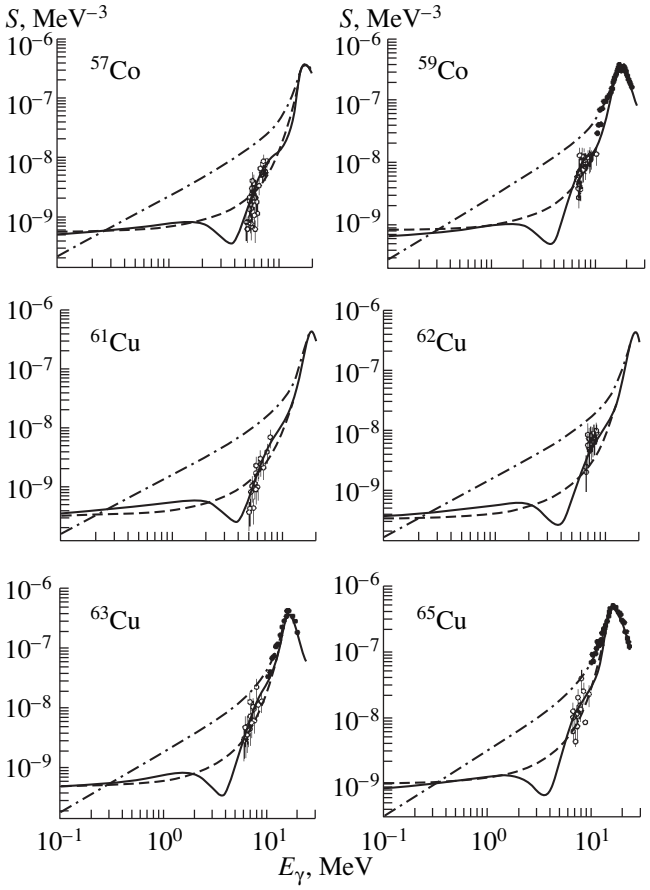

Fig. 2. Experimental and theoretical values of the radiative strength functions for primary gamma transitions in the nuclei under investigations. Open circles represent the radiative strength functions at E_p = 2.84, 2.82, 2.89, 2.30, 3.00, and 2.30 MeV for the ^{57}Co, ^{59}Co, ^{61}Cu, ^{62}Cu, ^{63}Cu, and ^{65}Cu, respectively. Closed circles correspond to data from [48, 49]. The theoretical results displayed in this figure are those that were calculated with a Lorentz distribution (dash-dotted curves) and those that were obtained on the basis of the statistical approach from [40, 41] with allowance for nuclear temperature (dashed curve) and nuclear temperature and the shell structure of nuclei (solid curves).

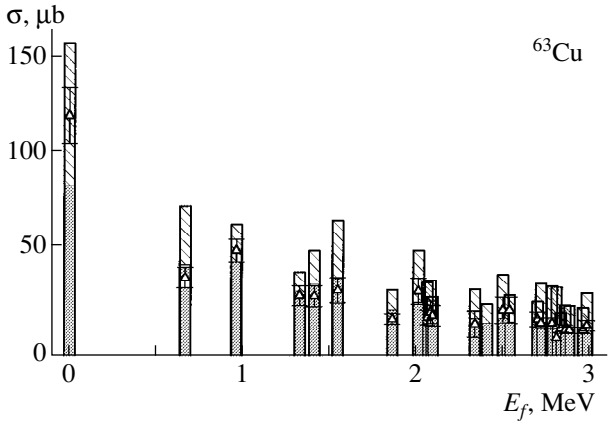

Fig. 3. Partial cross sections for the (p, γ_f) reaction on ^{62}Ni targets. The closed regions of the histograms correspond to the cross sections calculated with the radiative strength functions obtained on the basis of the statistical approach from [40, 41] with allowance for the shell structure and the temperature of the nucleus, while the shaded regions represent the cross sections calculated with the radiative strength functions in the Lorentzian form.

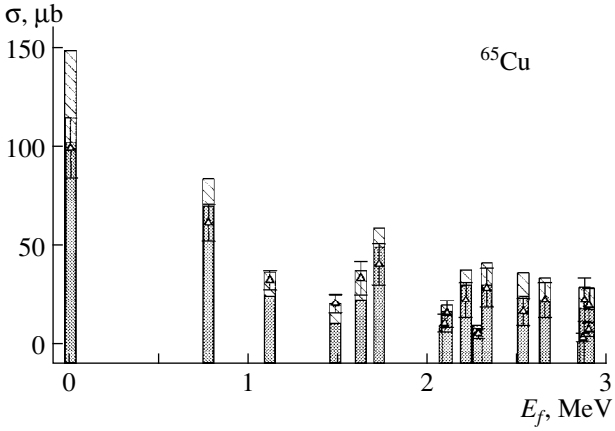

Fig. 4. As in Fig. 3, but for the (p, γ_f) reaction on ^{64}Ni targets.

(recall that B_n is the neutron binding energy, while T is the nuclear temperature in the final state), which was derived on the basis of the results obtained in [40] (for more details, see [42]). It should be noted that experimental data on $M1$ excitations in $1f_{7/2}$-shell nuclei suggest the suppression and a considerable fragmentation of the $M1$-resonance strength not only in relation to the predictions of the independent-particle model but also in relation to the predictions obtained within various versions of the random-phase approximation.

Figure 2 shows the radiative strength functions obtained from our analysis of experimental data on the partial cross sections for the (p, γ_f) reactions on ^{56,58}Fe and $^{60-62,64}$Ni targets at fixed proton energies. Experimental data near the GDR maxima were taken from [48, 49]. The dash-dotted, dashed, and solid curves represent the radiative strength functions derived theoretically on the basis of, respectively, a Lorentz distribution, Eq. (5) allowing only for temperature, and Eq. (5) allowing both for temperature and for the shell structure of the nucleus. In these calculations, the $M1$ contribution (not shown in Fig. 2) did not exceed 10–15% for various states of the nuclei being studied. For some cases, the measured partial cross sections for the relevant (p, γ_f) reactions are contrasted in Figs. 3 and 4 against the results of the calculations by Eq. (1) with various versions of the radiative strength functions. The closed regions of the histograms correspond to the cross sections calculated with the strength functions derived within the statistical approach [40, 41] that takes into account the shell structure and the nuclear temperature, while the shaded regions represent the

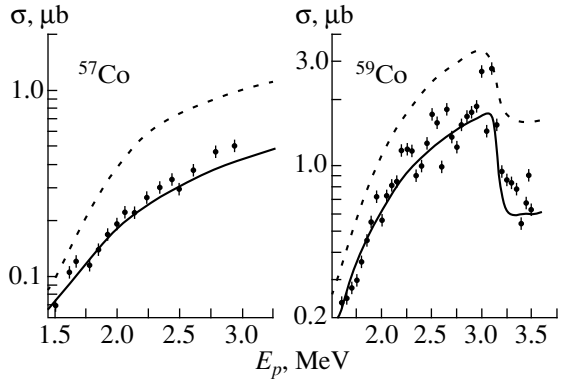

Fig. 5. Total cross sections for the (p, γ) reactions on $^{56, 58}$Fe targets: (dashed curves) results obtained with the radiative strength functions in the Lorentzian form and (solid curves) results obtained with the radiative strength functions calculated within the statistical approach developed in [40, 41]. The cross sections for the (p, γ) reactions were deduced on the basis of estimated experimental data from [22, 24] for ^{56}Fe targets and were taken from [25] for ^{58}Fe targets.

cross sections based on the radiative strength functions in a Lorentzian form. A similar comparison for the total cross sections as functions of the proton energy is illustrated in Figs. 5 and 6. The cross sections for the (p, γ) reactions were obtained on the basis of estimated experimental data from [22, 24] for ^{56}Fe targets and were borrowed from [25] for ^{58}Fe targets. It can be seen that the partial (p, γ_f) cross sections calculated with the radiative strength functions derived within the approach proposed in [40, 41] agree well with experimental data. The agreement between the calculated and measured values of the total (p, γ) cross sections is somewhat poorer in the proton-energy range under consideration. In all probability, this is because the total radiative widths are of crucial importance for calculating the total cross section; therefore, the degree of agreement depends on the accuracy of the radiative strength functions over the entire energy range. From Fig. 2, we can see that, over the entire photon energy range under study, the radiative strength functions cal-

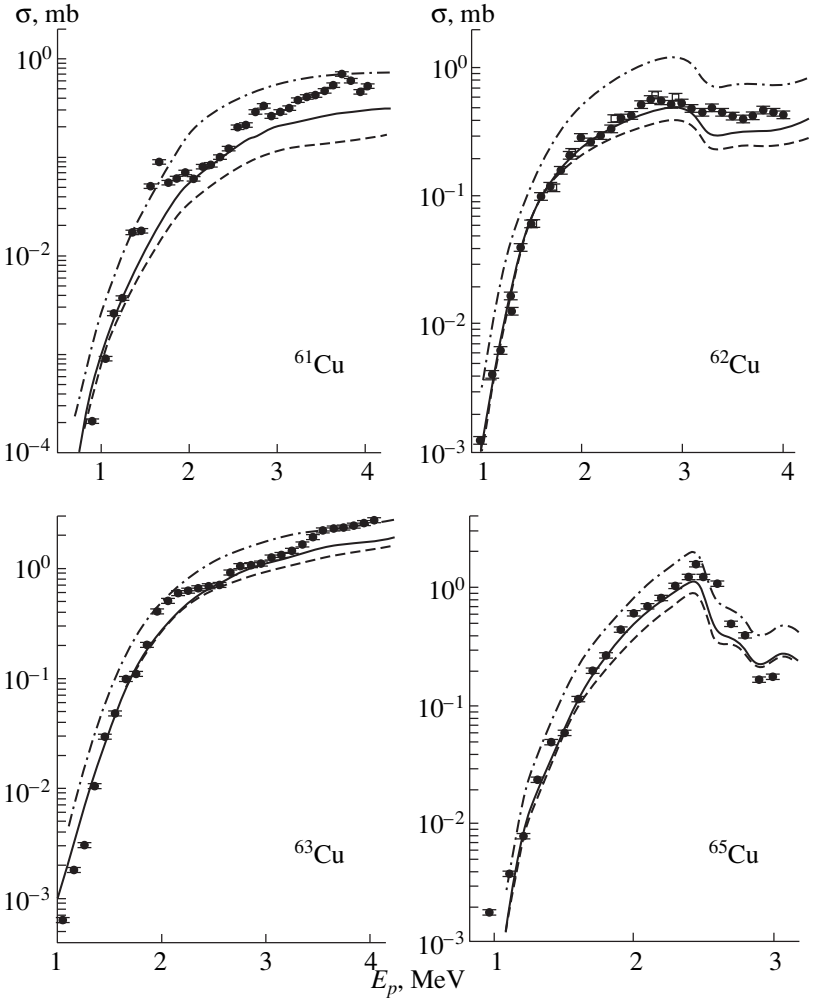

Fig. 6. Total cross sections for the (p, γ) reactions on $^{60–62, 64}$Ni targets. Experimental values were taken from [19–21]. The theoretical results displayed in this figure are those that were calculated with a Lorentz distribution (dash-dotted curves) and those that were obtained on the basis of the statistical approach from [40, 41] with allowance for nuclear temperature (dashed curve) and nuclear temperature and the shell structure of nuclei (solid curves).

culated in the approach from [40, 41] without use of adjustable parameters agree with experimental data both in shape and in magnitude. For the ^{59}Co and ^{65}Cu nuclei, which contain the largest number of valence neutrons among the cobalt and copper isotopes under consideration, the energy dependence of the radiative strength function is compatible with a Lorentz distribution as well.

If we pay no attention to the fact that an extrapolation of a Lorentz distribution to the low-energy region leads to considerably overestimated absolute values of the radiative strength functions for the ^{59}Co nucleus, it can be concluded that, by and large, the distribution of the $E1$ strength in the nuclei under investigation is in qualitative agreement with the energy dependence predicted by Soloviev *et al.* [51] for the $E1$ strength in heavier spherical nuclei. For A = 90–150 spherical nuclei, these authors calculated, within the quasiparticle–phonon model of the nucleus, the $E1$ strength functions over a wide excitation interval, including the GDR region. They also examined the GDR effect on the behavior of the radiative strength functions near the neutron binding energy. The results of further theoretical investigations along these lines were discussed in detail, for example, in [52]. On the basis of the conclusions drawn in [51], the observed reduction of the deviation from a Lorentz distribution in the $Z = 28 \pm 1$ nuclei with increasing number of valence neutrons can be attributed to the enhancement of the GDR effect on the radiative strength functions as the nuclei being considered recede from those with closed shells (for the latter, this effect is assumed to be insignificant) and to an increase in the excitation energy. The examples of ^{59}Co and ^{65}Cu nuclei excited in the (p, γ) reactions, which have the energy release of Q_0 = 7.4 MeV, the highest for the nuclei studied here, demonstrate that the closer the energy of direct gamma transitions to the GDR maximum, the better the agreement of a Lorentz distribution with experimental radiative strength functions, at least in shape.

It would be of interest to compare quantitatively our results with the radiative strength functions calculated within the semimicroscopic approach that was developed on [53] on the basis of the random-phase approximation and which allows for the single-particle continuum exactly and nucleon pairing approximately in describing doorway particle–hole configurations. In this approach, the coupling of doorway states forming GDRs to the complex configurations is taken into account directly at the low-energy GDR tail.

3. CONCLUSION

The absolute values and the energy dependences of the radiative strength functions below the neutron binding energy in the $^{57, 59}$Co and $^{61–63, 65}$Cu nuclei have been determined within a unified approach. It has been shown that the distribution of the $E1$ strength calculated within the statistical approach developed in [40, 41] on the basis on Fermi liquid theory agrees, without adjustable parameters, with experimental data over the entire photon-energy range under investigation both in shape and in absolute value. Only for the ^{59}Co and ^{65}Cu nuclei, which contain the largest number of valence neutrons among the cobalt and copper isotopes studied here, is the energy dependence of the radiative strength compatible with a Lorentz distribution as well. It has been assumed that this is due to the possible enhancement of the GDR effect on the radiative strength functions as the number of valence neutrons increases and to the fact that the energy dependence of the radiative strength functions for these nuclei was determined in the region closest to the GDR maximum because ^{59}Co and ^{65}Cu nuclei are excited in the (p, γ) reaction characterized by the highest energy release Q_0 for the nuclei investigated here.

ACKNOWLEDGMENTS

I am grateful to B. A. Nemashkalo and S. S. Ratkevich for stimulating discussions and assistance and to V. V. Varlamov for kindly placing photonuclear data at my disposal.

REFERENCES

1. K. Nilson, B. Erlandsson, and A. Marcinkowski, Nucl. Phys. A **391**, 61 (1982).
2. B. Erlandsoon, K. Nilson, and A. Marcinkowski, Nucl. Phys. A **348**, 1 (1980).
3. B. Erlandsson, K. Nilson, A. Maricinkowski, and J. Piotrowski, Z. Phys. A **293**, 43 (1979).
4. B. A. Nemashkalo, S. A. Pis'menetskiĭ, and V. E. Storizhko, Yad. Fiz. **36**, 280 (1982) [Sov. J. Nucl. Phys. **36**, 163 (1982)].
5. B. A. Nemashkalo, Yu. P. Mel'nik, V. E. Storizhko, and K. V. Shebeko, Yad. Fiz. **37**, 3 (1983) [Sov. J. Nucl. Phys. **37**, 1 (1983)].
6. B. A. Nemashkalo, S. S. Ratkevich, and I. D. Fedorets, in *Proceedings of the 47th International Conference on Nuclear Spectroscopy and Nuclear Structure, St. Petersburg, 1997*, pp. 159, 160.
7. S. S. Ratkevich, I. D. Fedorets, and B. A. Nemashkalo, in *Proceedings of the 49th International Conference on Nuclear Spectroscopy and Nuclear Structure, St. Petersburg, 1999*, p. 318.
8. I. I. Zalyubovskiĭ, S. S. Ratkevich, I. D. Fedorets, and B. A. Nemashkalo, in *Proceedings of the 48th International Conference on Nuclear Spectroscopy and Nuclear Structure, St. Petersburg, 1998*, p. 228.
9. I. I. Zalyubovskiĭ, S. S. Ratkevich, I. D. Fedorets, and B. A. Nemashkalo, in *Proceedings of the 49th International Conference on Nuclear Spectroscopy and Nuclear Structure, St. Petersburg, 1999*, p. 319.
10. C. E. Porter and R. G. Thomas, Phys. Rev. **104**, 483 (1956).
11. J. W. Tepel, H. M. Hofmann, and N. A. Weidenmüller, Phys. Lett. B **49B**, 1 (1974).

12. G. A. Bartholomew, E. D. Earle, A. J. Ferguson, *et al.*, Adv. Nucl. Phys. **7**, 229 (1973).
13. F. D. Becchetti and G. W. Greenlees, Phys. Rev. **182**, 1190 (1969).
14. S. Kailas and M. K. Mehta, in *Proceedings of the 2nd Indo–US Symposium on Nucl. Phys. Cyclotron and Intermediate Energy, Bombay, 1982*, Vol. 1, p. 505.
15. N. Boukharouba, C. E. Brient, S. M. Grimes, *et al.*, Phys. Rev. C **46**, 2375 (1992).
16. E. A. Romanovskiĭ, Doctoral Dissertation in Mathematics and Physics, Moscow (Moscow State Univ., 1981); E. A. Romanovsky, O. V. Bespalova, T. P. Kuchnina, *et al.*, Yad. Fiz. **61**, 37 (1998) [Phys. At. Nucl. **61**, 32 (1998)].
17. R. L. Varner, W. J. Thompson, T. L. McAbee, *et al.*, Phys. Rep. **201**, 57 (1991).
18. R. L. Hershberger, F. Gabbard, and C. E. Laird, in *Proceedings of the Fifth International Symposium on Capture Gamma-Ray Spectroscopy and Related Topics, Knoxville, 1984*, p. 692.
19. C. I. Tingwell, V. Y. Hansper, S. G. Tims, *et al.*, Nucl. Phys. A **496**, 127 (1989).
20. C. I. Tingwell, V. Y. Hansper, S. G. Tims, *et al.*, Nucl. Phys. A **480**, 162 (1988).
21. M. E. Sevior, L. W. Mitchell, M. R. Anderson, *et al.*, Aust. J. Phys. **36**, 463 (1983).
22. C. H. Johnson, A. Galonsky, and R. L. Kernell, Phys. Rev. C **20**, 2052 (1979).
23. G. A. Krivonosov *et al.*, Yad. Fiz. **24**, 461 (1976) [Sov. J. Nucl. Phys. **24**, 239 (1976)].
24. D. B. Nichols, R. G. Arns, H. J. Hausman, *et al.*, Phys. Rev. **183**, 945 (1969).
25. S. G. Times *et al.*, Nucl. Phys. A **563**, 473 (1993).
26. Yu. V. Sokolov, *Level Density in Nuclei* (Énergoatomizdat, Moscow, 1990).
27. A. S. Iljinov, M. V. Mebel, N. Bianchi, *et al.*, Nucl. Phys. A **543**, 517 (1992).
28. M. R. Bhat, Nucl. Data Sheets **67**, 195 (1992).
29. M. Coral and L. Baglin, Nucl. Data Sheets **69**, 733 (1993).
30. L. P. Ekstrom and J. Lyttkens, Nucl. Data Sheets **38**, 496 (1983).
31. M. M. King, Nucl. Data Sheets **60**, 337 (1990).
32. V. Mishra, N. Boukharouba, C. E. Brient, *et al.*, Phys. Rev. C **49**, 750 (1994); M. I. Svirin and G. N. Smirenkin, Yad. Fiz. **48**, 682 (1988) [Sov. J. Nucl. Phys. **48**, 437 (1988)].
33. T. Ericson and T. Mayer-Kuckuk, Annu. Rev. Nucl. Sci. **16**, 183 (1966).
34. J. Sziklai, T. Vass, J. A. Cameron, *et al.*, Phys. Rev. C **41**, 849 (1990).
35. M. Kicinska-Habior, K. A. Snover, C. A. Gossett, *et al.*, Phys. Rev. C **36**, 612 (1987).
36. F. Becvar, P. Cejnar, R. E. Chrien, and J. Kopecky, Phys. Rev. C **46**, 1276 (1992).
37. S. T. Boneva, É. V. Vasil'eva, V. D. Kulik, *et al.*, Fiz. Élem. Chastits At. Yadra **22**, 1433 (1991) [Sov. J. Part. Nucl. **22**, 698 (1991)].
38. O. T. Grudzevich, Yad. Fiz. **62**, 227 (1999) [Phys. At. Nucl. **62**, 192 (1999)].
39. S. G. Kadmenskiĭ, V. P. Markushev, and V. I. Furman, Yad. Fiz. **37**, 277 (1983) [Sov. J. Nucl. Phys. **37**, 165 (1983)].
40. V. K. Sirotkin, Yad. Fiz. **43**, 570 (1986) [Sov. J. Nucl. Phys. **43**, 362 (1986)].
41. V. K. Sirotkin and D. F. Zaretskiĭ, Izv. Akad. Nauk SSSR, Ser. Fiz. **52**, 984 (1988); D. F. Zaretskiĭ and V. K. Sirotkin, *Electromagnetic and Weak Interactions of Compound-Nucleus Levels* (Mosk. Inzh.-Fiz. Inst., Moscow, 1986).
42. I. I. Zalyubovskiĭ, B. A. Nemashkalo, S. S. Ratkevich, *et al.*, Yad. Fiz. **57**, 777 (1994) [Phys. At. Nucl. **57**, 727 (1994)].
43. S. S. Ratkevich, B. A. Nemashkalo, and I. D. Fedorets, Izv. Akad. Nauk, Ser. Fiz. **61**, 2039 (1997).
44. B. A. Nemashkalo, S. S. Ratkevich, V. K. Sirotkin, *et al.*, Yad. Fiz. **59**, 1925 (1996) [Phys. At. Nucl. **59**, 1857 (1996)].
45. S. S. Ratkevich, B. A. Nemashkalo, and I. D. Fedorets, Yad. Fiz. **60**, 804 (1997) [Phys. At. Nucl. **60**, 713 (1997)].
46. I. I. Zalyubovskiĭ, S. S. Ratkevich, I. D. Fedorets, and B. A. Nemashkalo, Izv. Akad. Nauk, Ser. Fiz. **61**, 178 (1997).
47. S. S. Ratkevich, B. A. Nemashkalo, and I. D. Fedorets, Izv. Akad. Nauk, Ser. Fiz. **61**, 2201 (1997).
48. R. A. Álvarez *et al.*, Phys. Rev. C **20**, 128 (1979).
49. V. V. Varlamov, N. G. Efimkin, B. S. Ishkhanov, *et al.*, Yad. Fiz. **58**, 387 (1995) [Phys. At. Nucl. **58**, 337 (1995)].
50. M. G. Urin, Fiz. Élem. Chastits At. Yadra **8**, 817 (1977) [Sov. J. Part. Nucl. **8**, 331 (1977)].
51. V. G. Soloviev, Ch. Stoyanov, and V. V. Voronov, Nucl. Phys. A **304**, 503 (1978).
52. V. G. Solov'ev, *Theory of Atomic Nuclei: Quasiparticles and Phonons* (Énergoatomizdat, Moscow, 1989; Institute of Physics, Bristol, 1992).
53. V. A. Rodin and M. G. Urin, Izv. Akad. Nauk, Ser. Fiz. **62**, 2106 (1998).

Translated by R. Tyapaev

Physics of Atomic Nuclei, Vol. 64, No. 1, 2001, pp. 57–61. Translated from Yadernaya Fizika, Vol. 64, No. 1, 2001, pp. 60–64.

NUCLEI
Theory

Change in the Structure of Colliding Deuterons

G. F. Filippov and V. N. Romanov

Bogolyubov Institute of Theoretical Physics, National Academy of Sciences of Ukraine, Metrologicheskaya ul. 14b, Kiev, 252143 Ukraine

Received September 15, 1999; in final form, February 22, 2000

Abstract—The effect of the fields of two colliding deuterons on the deuteron wave functions is investigated within the algebraic version of the resonating-group method. The problem of determining the continuum of the *K*-matrix elements at a given c.m. energy of the deuterons is formulated and solved on the basis of this approach. *© 2001 MAIK "Nauka/Interperiodica".*

1. INTRODUCTION

In investigating collisions of two deuterons within the standard version of the resonating-group method [1], the deuteron wave functions are assumed to be preset, so that attention is given primarily to determining the wave function of the relative motion of the deuterons.

Since deuteron systems are especially loose, it can be expected that, at small deuteron–deuteron distances, those about the range of nuclear forces, the deuteron wave functions are rearranged and that this rearrangement affects the character of the motion of the deuterons. By way of example, we indicate that, when two deuterons approach closely, each of them occurs in the attractive field generated by the other deuteron; as a result, the distance between the deuterons continues to decrease, which is accompanied by the growth of the kinetic energy of their relative motion. This growth is moderated, however, by the increase in the internal energy of the deuterons. In addition, the Coulomb repulsion of the deuterons begins to play a noticeable role in the energy balance, also suppressing the growth of the kinetic energy and even resulting in that, at extremely small distances, the growth in question gives way to a decrease.

The two-deuteron system chosen here is often studied on the basis of the Faddeev–Yakubovsky equations. However, we do not aim here at constructing an exact solution to these equations; considering a relatively simple system and nucleon–nucleon potentials typically used in the resonating-group method, we will try instead to find out whether the assumption that is conventionally made within this method and which consists in that the cluster wave functions do not change as the clusters approach one another and undergo a collision is justified and to establish simultaneously the conditions under which this assumption ceases to be valid. This question is quite pressing since the resonating-group method is usually used to analyze more complex nuclei, in which case the applicability of this method has not been proven rigorously, so that one needs some guidelines to judge the validity of the method.

In order to take into account, within the resonating-group method, the excitation of the deuterons during their collision, Kanada *et al.* [2] approximated the ground-state wave function of the deuteron and the wave functions of its excited states by orthogonal superpositions of three Gaussian functions. In this scheme, excited states simulate the continuous spectrum. However, their asymptotic behavior is fast descending, so that they do not reproduce deuteron breakup into two nucleons. At the same time, the polarization of the deuterons can be taken into account in this way if the distance between them is large. The same objective can be accomplished in multichannel calculations [3], where the deuteron–deuteron (*dd*) channel is supplemented with two binary channels, a proton–triton (*pt*) and a neutron–helium (n^3He) channel. Finally, the closed collective quadrupole channel, which extends the dynamical description of the deuteron–deuteron interaction, was taken into account in [4, 5], along with the binary channels.

Meanwhile, the question of the role of the three-particle (*dnp*) and the four-particle (2*p*2*n*) channel in the four-nucleon system remained unanswered in [2–5]. The coupling of these channels to the deuteron–deuteron channel leads to the reactions $dd \longrightarrow dpn$ and $dd \longrightarrow 2p2n$. A description of these reactions could furnish a basis for qualitatively understanding multiparticle reactions and for quantitatively assessing their cross sections; so far, these issues have not been studied in sufficient detail.

The algebraic version of the resonating-group method [6, 7] provides a conventional framework for taking into account dynamical variables that are responsible for changes in the deuteron structure and for performing a consistent analysis of the process of a deuteron–deuteron collision. In order to implement this, the harmonic-oscillator basis of the single-channel approximation is extended via the inclusion of those states that reproduce the excitation of deuteron systems

when they approach each other and even their breakup as the result of a collision event.

Our objective here is to formulate, within the algebraic version of the resonating-group method, a new approach to describing the deuteron–deuteron interaction in order to analyze and, if necessary, to remove errors that emerge from the choice of an approximate expression for the wave function of the deuteron ground state; to take into account the contribution to deuteron polarization from the direct interaction of the deuteron nucleons; to demonstrate the character of changes in the states of the deuterons as they approach each other; and to describe both elastic deuteron–deuteron collisions and the breakup of one or two deuterons as the result of a deuteron–deuteron collision.

2. EXPANSION COEFFICIENTS AND SET OF EQUATIONS OF THE ALGEBRAIC VERSION OF THE RESONATING-GROUP METHOD

By using the representation of a harmonic-oscillator basis and by expanding the resonating-group-method expression for the wave function Ψ of the two-deuteron system [6, 7] in the infinite series,

$$\Psi = \sum_{n_1=0}^{\nu}\sum_{n_2=0}^{\nu}\sum_{n=0}^{\infty} C_{n_1n_2n}\hat{A}[\phi_{n_1}(1)\phi_{n_2}(2)f_n], \qquad (1)$$

we arrive at the problem of seeking the expansion coefficients $C_{n_1n_2n}$. Let us recall the notation used in (1): $\hat{A}$ is the antisymmetrization operator; n_1 and n_2 are the numbers of quanta of the basis functions $\phi_{n_1}(1)$ and $\phi_{n_2}(2)$ of the first and the second deuteron, respectively; and n is the number of quanta of the wave function f_n describing the relative motion of the deuterons. In practice, we have to restrict ourselves to a finite number of basis functions $\phi_{n_1}(1)$ and $\phi_{n_2}(2)$, assuming that $n_1, n_2 \le \nu$. To avoid encumbering the presentation with details that do not affect the fundamental aspects of the formulation of the problem, we will restrict ourselves to basis states characterized by zero orbital angular momentum and neglect the Coulomb interaction of the protons. The second limitation can be removed. In addition, we will assume that the total spin S of the two deuterons is zero and that there are no noncentral forces.

For the coefficients $C_{n_1n_2n}$, the set of equations of the algebraic version of the resonating-group method has the form

$$\sum_{n_1=0}^{\nu}\sum_{n_2=0}^{\nu}\sum_{n=0}^{\infty}\langle\tilde{n}_1\tilde{n}_2\tilde{n}|\hat{H}-E|n_1n_2n\rangle C_{n_1n_2n} = 0, \qquad (2)$$
$$\tilde{n}_1, \tilde{n}_2 = 0, 1, 2, \ldots, \nu; \quad \tilde{n} = 0, 1, 2, \ldots, \infty.$$

Within this framework, the matrix elements

$$\langle\tilde{n}_1\tilde{n}_2\tilde{n}|\hat{H}-E|n_1n_2n\rangle$$

between the harmonic-oscillator basis functions are constructed in the standard way by using generating functions. However, the problem of closing the set of Eqs. (2)—that is, the problem of going over from an infinite number of equations in the set to a finite set of equations requires a dedicated discussion.

Following the general idea of the algebraic version of the resonating-group method, we must first determine the asymptotic behavior of the coefficients $C_{n_1n_2n}$. For $n \ge n_0$ and $n_0 \gg 1$, they are expressed in terms of an a priori unknown K matrix. Suppose that

$$\bar{C}_{n_1n_2n} = C_{n_1n_2n}$$

if $n \ge n_0$.

Instead of (2), we then obtain the set of equations

$$\sum_{n_1=0}^{\nu}\sum_{n_2=0}^{\nu}\sum_{n=0}^{n_0-1}\langle\tilde{n}_1\tilde{n}_2\tilde{n}|\hat{H}-E|n_1n_2n\rangle C_{n_1n_2n}$$
$$+\sum_{n_1=0}^{\nu}\sum_{n_2=0}^{\nu}\sum_{n=n_0}^{\infty}\langle\tilde{n}_1\tilde{n}_2\tilde{n}|\hat{H}-E|n_1n_2n\rangle\bar{C}_{n_1n_2n} = 0, \qquad (3)$$
$$\tilde{n}_1, \tilde{n}_2 = 0, 1, 2, \ldots, \nu; \quad \tilde{n} = 0, 1, 2, \ldots, n_0.$$

As long as the energy E of the relative motion of colliding deuterons is higher than the deuteron binding energy ε but lower than 2ε, $n_0(\nu+1)^2$ coefficients $C_{n_1n_2n}$ for $n \le n_0$ and the K-matrix elements are unknown quantities to be found by solving the set of Eqs. (3). The relation between the coefficients $\bar{C}_{n_1n_2n}$ and the K-matrix elements will be deduced in the next section.

3. ASYMPTOTIC BEHAVIOR OF THE COEFFICIENTS $C_{n_1n_2n}$ FOR $n \gg 1$

For mass, length, and energy units, we use the nucleon mass m, the oscillator length r_0, and $\hbar^2/mr_0^2$, respectively. By way of example, we indicate that, if E is the energy of the two-neutron system and if ε is the deuteron binding energy, the possible values of the momentum k of the ruptured neutron–proton pair obey the condition

$$\frac{1}{2}k^2 \le E - \varepsilon$$

for $E \le 2\varepsilon$.

At all finite values of ν, in which case the numbers of terms in the sums over n_1 and n_2 are bounded, expression (1) can be interpreted as a wave packet representing a superposition of bound states and continuum states of the first and the second deuteron.

Let $C^0_{n_1}$ be the Fourier coefficients for the wave function $\psi_0(1)$ of the deuteron ground state,

$$\psi_0(1) = \sum_{n_1=0}^{\infty} C^0_{n_1}\phi_{n_1}(1), \tag{4}$$

and let $C^k_{n_1}$ be the Fourier coefficients for the wave function $\psi_k(1)$ of a continuum state characterized by the momentum k,

$$\psi_k(1) = \sum_{n_1=0}^{\infty} C^k_{n_1}\phi_{n_1}(1). \tag{5}$$

These coefficients must be defined as solutions to the wave equation for the deuteron and are normalized to the delta function of k,

$$\sum_{n_1=0}^{\infty} C^k_{n_1}C^{k'}_{n_1} = \delta(k-k'). \tag{6}$$

The wave packet (1) is then projected onto states (4) and (5) in a conventional way; if $n \geq n_0$ and if, in addition, $n_0 \gg 1$, this yields the following relations for the asymptotic coefficients $\bar{C}_{n_1n_2n} = C_{n_1n_2n}$:

$$B_n(0k) = \sum_{n_1=0}^{\nu}\sum_{n_2=0}^{\nu} \bar{C}_{n_1n_2n}C^0_{n_1}C^k_{n_2}, \tag{7}$$

$$B_n(00) = \sum_{n_1=0}^{\nu}\sum_{n_2=0}^{\nu} \bar{C}_{n_1n_2n}C^0_{n_1}C^0_{n_2}. \tag{8}$$

The value of the positive integer ν determines the number of discrete nodes k_i [it is equal to $\nu(\nu+2)$] at which, with the aid of the K-matrix representation, we must specify the coefficients $B_n(0k_i)$, setting

$$B_n(0k_i) = K_{0k_i}N_{1/2}(\sqrt{2E-2\varepsilon-k_i^2}\sqrt{4n+3}), \tag{9}$$

$$\begin{aligned} B_n(00) &= J_{1/2}(\sqrt{2E}\sqrt{4n+3}) \\ &\quad - K_{00}N_{1/2}(\sqrt{2E}\sqrt{4n+3}), \end{aligned} \tag{10}$$

where K_{00} and K_{0k_i} are K-matrix elements. By using relation (8), together with the expressions for $B_n(0k_i)$, where $i = 1, 2, \ldots, \nu$, we can derive $(\nu+1)^2$ equations relating the coefficients $\bar{C}_{n_1n_2n}$ at $n \geq n_0 \gg 1$ to the K-matrix elements K_{00}, K_{0k_i}, and $K_{k_ik_j}$, which are of interest to us, and to Bessel and Neumann functions and eventually close up the set of linear algebraic equations of the algebraic version of the resonating-group method.

An alternative form of the coefficients $\bar{C}_{n_1n_2n}$ that involves an integral with respect to the momentum k and which highlights the fact that we are dealing with continuum states can be represented as

$$\begin{aligned} \bar{C}_{n_1n_2n} &= A^{00}_{n_1n_2}\sqrt{2}(E)^{1/4}(J_{1/2}(\sqrt{2E}\sqrt{4n+3}) \\ &\quad - K_{00}N_{1/2}(\sqrt{2E}\sqrt{4n+3})) + \int A^{0k}_{n_1n_2}K_{0k}\sqrt{2}(2E \\ &\quad - 2\varepsilon - k^2)^{1/4}N_{1/2}(\sqrt{2E-2\varepsilon-k^2}\sqrt{4n+3})dk, \end{aligned} \tag{11}$$

where

$$A^{00}_{n_1n_2} = C^0_{n_1}C^0_{n_2}, \quad A^{0k}_{n_1n_2} = C^0_{n_1}C^k_{n_2}, \quad 0 \leq n_1,\ n_2 \leq \infty.$$

In this case, the continuum states for the relative motion of two deuterons are normalized to a delta function of the relevant momentum $\sqrt{2(2E-2\varepsilon-k^2)}$.

4. COEFFICIENTS $C_{n_1n_2n}$ AT SMALL VALUES OF n

Small values of n correspond to small deuteron–deuteron distances, where the deuteron wave functions are affected most strongly by the deuteron–deuteron field. In order to describe changes in the deuteron states at this stage, we consider the expansion

$$\sum_{n_1=0}^{\nu}\sum_{n_2=0}^{\nu} C_{n_1n_2n}\phi_{n_1}(1)\phi_{n_2}(2)$$

at fixed n. By applying an orthogonal transformation, we can recast this expansion into the alternative form

$$\begin{aligned} &\sum_{n_1=0}^{\nu}\sum_{n_2=0}^{\nu} C_{n_1n_2n}\phi_{n_1}(1)\phi_{n_2}(2) \\ &= \sum_{\alpha=1}^{\nu+1}\lambda_\alpha(n)\sum_{p=0}^{\nu}B^\alpha_p(n)\phi_p(1)\sum_{q=0}^{\nu}B^\alpha_q(n)\phi_q(2), \end{aligned} \tag{12}$$

where λ_α are eigenvalues of the symmetric matrix $\|C_{n_1n_2n}\|$ of dimensions $(\nu+1)\times(\nu+1)$ with a given value n (recall that the total spin is $S = 0$) and B^α_p ($p = 0, 1, 2, \ldots, \nu$) are its eigenvectors.

From Eq. (12), it follows that two deuterons (both simultaneously) can be in one of the $\nu+1$ states

$$\psi_{n,\alpha} = \sum_{p=0}^{\nu} C^\alpha_p(n)\phi_p. \tag{13}$$

The wave functions for these states depend on n and, hence, change with n. The probability $W(n, \alpha)$ that

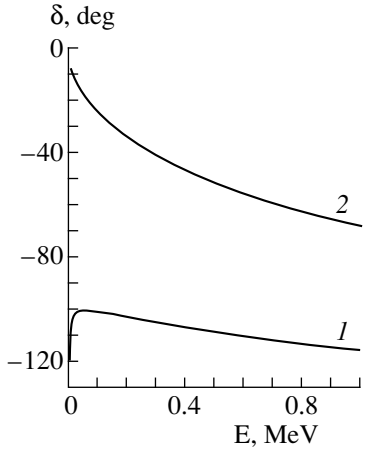

Fig. 1. Phase shift δ for elastic deuteron–deuteron scattering as a function of the c.m. energy of the relative motion of the deuterons in the (curve *1*) ν = 0 and the (curve *2*) ν = 6 approximation.

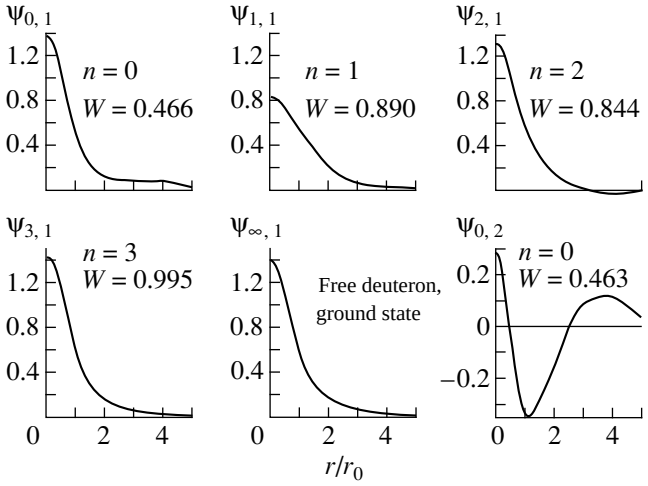

Fig. 2. Radial dependences of the wave functions $\psi_{0,1}$, $\psi_{1,1}$, $\psi_{2,1}$, $\psi_{3,1}$, $\psi_{\infty,1}$, and $\psi_{0,2}$ as obtained by diagonalizing the matrices of the coefficients for colliding deuterons.

the deuterons are in the state specified by Eq. (13) is given by

$$W(n, \alpha) = \frac{\lambda_\alpha^2(n)}{\sum_{\alpha'} \lambda_{\alpha'}^2(n)}. \qquad (14)$$

5. RESULTS OF THE CALCULATIONS

Within the algebraic version of the resonating-group method, the phase shift $\delta(E)$ for elastic deuteron–deuteron scattering, the eigenvalues $\lambda_\alpha(n)$, and the eigenvectors $\{B_p^\alpha\}$ were calculated here in the region of energies E from zero to the deuteron-breakup threshold. In this calculation, we used the Minnesota nucleon–nucleon potential [8] and set the oscillator radius to $r_0 = 1.82$ fm. We assumed that $\nu = 6$. The phase shifts calculated at $\nu = 5$ and $\nu = 6$ differ by less than one percent.

The behavior of the phase shift $\delta(E)$ is illustrated in Fig. 1. The behavior of the phase shift $\delta_0(E)$ at $\nu = 0$ and $r_0 = 1.5$ fm is also shown in Fig. 1. The latter phase shift increases fast with increasing above-threshold energy, achieves a maximum, and then begins to decrease slowly. This behavior suggests a negative value of the scattering length and the occurrence of a narrow resonance at the energy value where the phase shift has a maximal derivative. As to the phase shift $\delta(E)$, it decreases monotonically; therefore, the corresponding scattering length is positive, and a moderately shallow bound state must occur under the threshold.

A drastic change in the behavior of the phase shift as ν increases from zero to seven can be explained in the following way. At $\nu = 0$, the harmonic-oscillator basis states involved in the calculation give only one bound state in the system of two interacting deuterons. As a matter of fact, this is the ^{4}He ground state, which governs the behavior of the phase shift $\delta_0(E)$. According to our calculations, its energy reckoned from the threshold for alpha-particle breakup into four nucleons is –25.6 MeV (–25.1 MeV if this energy is reckoned from the threshold for alpha-particle breakup into two deuterons). But if $\nu = 6$, the energy of the ground bound state changes insignificantly (this energy is now equal to –28.7 MeV if it is reckoned from the threshold of the complete breakup of the alpha particle and 24.6 MeV if it is reckoned from the threshold for the alpha-particle breakup into two deuterons); however, there arises a second bound state occurring much more closely to the threshold for breakup into two deuterons than the ground state. This is reason why the behavior of the phase shift $\delta(E)$ differs significantly from the behavior of $\delta_0(E)$.

We note from the outset that, in fact, the ^{4}He nucleus has only one bound state, but there is a 0^+ resonance above the threshold for ^{4}He breakup through the *pt* channel and below the threshold for breakup through the n^3He channel. In the approximation being considered, these channels are both closed, so that the resonance becomes a bound state. The results of our calculations indicate that the deuteron–deuteron channel plays an important role in the formation of the 0^+ resonance state in ^{4}He both in the case of the $\nu = 0$ approximation, where this state is above the deuteron–deuteron threshold, and in the case of the $\nu = 6$ approximation, where it goes below this threshold.

Let us now address the question of changes in the structure of the deuteron functions as the deuterons approach each other. Figure 2 displays the graphs of the eigenfunctions $\psi_{n,\alpha}$ at $\alpha = 1$ and $E = 1$ MeV, which have the highest weight $W(n, \alpha)$, and the graph of the function $\psi_{0,2}$. For all nonzero values of n, $W(n, 1)$ is

slightly less than unity; however, $W(0, 1) = 0.466$ and $W(0, 2) = 0.463$. At the first stage of the approach, the root-mean-square deuteron radius decreases with decreasing n (by almost 33% at $n = 2$); further, it begins to grow and, at $n = 0$, proves to be 32% greater than its original value of 1.453 fm. Any variation in the deuteron radii with respect to the optimal original value is accompanied by a decrease in the deuteron binding energy and, hence, by deuteron excitation. This reduces the contribution of the kinetic energy of the relative motion of the deuterons to the total energy balance. In the case where the energy of 9.6 MeV corresponds to the $\alpha = 2$, $n = 0$ excited states of weight $W(0, 2) = 0.463$, this contribution decreases by 12.84 MeV.

Similar conclusions are valid for the $E = 2$ MeV version calculated on the basis of the same code.

6. CONCLUSIONS

In analyzing inelastic processes accompanying collisions between deuterons of energies in excess of their breakup threshold, we have to deal with wave packets whose expansion furnishes information about effective cross sections for elastic and inelastic scattering. We have proposed a new computational scheme. On the basis of this scheme, we have been able to find the *K*- or the *S*-matrix elements for transitions into continuum states at a fixed energy of two interacting deuterons. We have derived a closed finite set of algebraic equations; by solving this set, we have obtained the relevant *K*-matrix elements representing continuous functions of the energy of deuterons broken up in a collision event. The results of the calculations for this *K* matrix will be presented elsewhere.

The phase shift for elastic deuteron–deuteron scattering has been calculated for the case where the energy of the relative motion of two deuterons does not exceed the deuteron-breakup threshold. The behavior of the wave functions of deuterons approaching each other has been investigated at small distances between the deuterons. It is the Fourier coefficients in the expansion of the wave function in the harmonic-oscillator basis that contain information about this behavior. We have set forth and implemented an approach that makes it possible to extract such data and to determine the character of the variations in the deuteron wave function.

The deformation of the deuteron wave functions affects significantly the behavior of the deuteron–deuteron phase shift; this is directly seen from the data in Fig. 1. To a considerable extent, this effect is due to the features of the system under investigation. Had we taken no account of the deformation, we would have obtained an above-threshold deuteron–deuteron resonance and the phase-shift behavior corresponding to this resonance. Upon the inclusion of the deformation of the deuteron wave functions, however, the resonance sinks below the threshold for deuteron–deuteron breakup, and the character of the phase-shift behavior changes. It now corresponds to the presence of a relatively shallow bound state under the threshold.

This phenomenon can also occur in more complicated systems investigated within the resonating-group method, where the inclusion of the deformation of the cluster wave functions, which strengthens the interaction between the clusters, results in the emergence of a resonance that is not observed if the deformation is not taken into account or if the resonance transforms into a bound state.

REFERENCES

1. K. Wildermuth and Y. Tang, *A Unified Theory of the Nucleus* (Vieweg, Wiesbaden, 1977; Mir, Moscow, 1980).
2. H. Kanada, T. Kaneko, and Y. C. Tang, Phys. Rev. C **43**, 371 (1991).
3. V. S. Vasilevskiĭ, I. Yu. Rybkin, and G. F. Filippov, Yad. Fiz. **51**, 112 (1990) [Sov. J. Nucl. Phys. **51**, 71 (1990)].
4. G. F. Filippov, V. S. Vasilevskiĭ, M. Bruno, *et al.*, Yad. Fiz. **51**, 1551 (1990) [Sov. J. Nucl. Phys. **51**, 978 (1990)].
5. V. S. Vasilevsky, G. F. Filippov, F. Arickx, *et al.*, J. Phys. G **18**, 1227 (1992).
6. G. F. Filippov, V. S. Vasilevskiĭ, and L. L. Chopovskiĭ, Fiz. Élem. Chastits At. Yadra **15**, 1338 (1984) [Sov. J. Part. Nucl. **15**, 600 (1984)].
7. G. F. Filippov, Riv. Nuovo Cimento **9**, 1 (1989).
8. D. R. Thompson, M. LeMere, and Y. C. Tang, Nucl. Phys. A **286**, 53 (1977).

Translated by A. Isaakyan

Physics of Atomic Nuclei, Vol. 64, No. 1, 2001, pp. 62–67. Translated from Yadernaya Fizika, Vol. 64, No. 1, 2001, pp. 65–71.

ELEMENTARY PARTICLES AND FIELDS
Experiment

Universality of Multifragmentation of Residual Nuclei Produced in High-Energies Nucleus–Nucleus Interactions

A. Abd-Elhafiez[1)], V. Sh. Navotny[2)], G. I. Orlova, V. V. Uzhinskii[3)], and M. M. Chernyavski

Lebedev Institute of Physics, Russian Academy of Sciences, Leninskiĭ pr. 53, Moscow, 117924 Russia

Received September 16, 1999; in final form, February 15, 2000

Abstract—Experimental data on the multifragmentation of residual nuclei produced in the krypton interactions with photoemulsion nuclei at 0.9 GeV per projectile nucleon are presented and compared with similar data on fragmentation from experiments where gold nuclei of energy 10.7 GeV per nucleon appear as projectiles. It is shown for the first time that there exist two modes of nuclear multifragmentation, those where less (first mode) or more (second mode) than half of nucleons are knocked out of the incident nucleus. Residual nuclei that have close masses and which are produced in various reactions accompanied by the knock-on of more than half of nucleons of the initial nucleus fragment in nearly the same way. In addition, evidence for a radial flux of spectator fragments is obtained for the first time in the decay of residual nuclei of krypton projectiles. © *2001 MAIK "Nauka/Interperiodica".*

1. INTRODUCTION

Interesting experimental results on the multifragmentation of nuclei at low and intermediate energies have been obtained in recent years. A radial spherically symmetrical flux of fragments with kinetic energies proportional to their masses was observed in central collisions of gold nuclei [1–5]. This is inconsistent with the assumption that nuclear multifragmentation has a statistical character. A radial flux of spectator fragments in the rest frame of the fragmenting nucleus was found in studying the interaction of gold nuclei of energy 10.7 GeV per projectile nucleon with photoemulsion nuclei [6, 7]. According to estimates presented in [5], the energy of this radial motion is 30 to 50% of the available energy. At the same time, evidence for invariability of the isotope temperature of fragmenting nuclei over a wide excitation-energy range as obtained from experiments at the ALADIN facility [8] is considered to suggest the occurrence of a first-order (liquid–gas) transition and a statistical character of nuclear multifragmentation. Finally, the experimental result of the INDRA Collaboration [9], who found that the isotopic composition of fragmentation products is independent of the masses of fragmenting nuclei at the same excitation energy, is indicative of a spinodal instability of residual nuclei. Thus, the current experimental situation is rather intricate; more precisely, a theoretical interpretation of the existing data presents a challenging problem.

We assume that the problem can be resolved by studying the fragmentation of comparatively light systems (the aforementioned studies analyzed the fragmentation of heavy nuclei). As a matter of fact, the well-known statistical model of multifragmentation (SMM) of nuclei [10, 11] was used to describe the fragmentation of both heavy nuclei (see [10]) and the nuclear residues of oxygen [12]. The no less popular model of quantum molecular dynamics [13], as well as the model of antisymmetrized molecular dynamics [14], either incorporating mean-field effects, is generally used to study the interactions of light nuclei. Hence, there is a range of nuclei where both approaches are applicable. Here, we present experimental data on the multifragmentation of residual nuclei produced in the interactions between krypton nuclei with an energy of 0.9 GeV per nucleon and photoemulsion nuclei.

First and foremost, we will address the most interesting dependence of the multiplicity of intermediate-mass fragments (IMF) with charges $3 \le Z_F \le 30$ on the mass of the fragmenting system. This multiplicity is estimated in terms of the "bound"-charge value

$$Z_{\text{bound}} = \sum_F Z_F, \quad Z_F \ge 2,$$

or

$$Z_{\text{b3}} = \sum_F Z_F, \quad Z_F \ge 3.$$

We further consider intrinsic features of fragmenting systems, such as the mean charge of the heaviest fragment and the asymmetry in the system of fragments. The basic results are summarized in the Conclusion.

[1)] Atomic Energy Authority, Nuclear Research Centre, Cairo, Egypt.
[2)] Institute for Physics and Technology, Uzbek Academy of Sciences, ul. Timiryazeva 2b, 700084 Tashkent, Republic of Uzbekistan.
[3)] Joint Institute for Nuclear Research, Dubna, Moscow oblast, 141980 Russia.

2. EXPERIMENTAL SAMPLE

Stacks of NIKFI BR-2 nuclear photoemulsion were irradiated with ^{84}Kr nuclei accelerated to 1 GeV per projectile nucleon at the SIS/GSI accelerator and with ^{197}Au nuclei accelerated to 10.7 GeV per projectile nucleon at the BNL/AGS accelerator. The sensitivity of the photoemulsion was not poorer than 30 grains per 100 μm for singly charged particles with minimum ionization. In order to analyze the interactions of krypton with nuclear photoemulsion, we selected events where the incident energy of krypton nuclei was within the interval 0.8–0.95 GeV per projectile nucleon, in which case the mean energy of krypton nuclei was about 0.9 GeV per projectile nucleon.

All interactions were found by means of fast–slow scanning along the track (the scanning in the forward direction was fast, while the scanning in the backward direction was slow), with the rate of fast scanning precluding any discrimination in event selection. The slow scanning was carried out to find events where the projectile nucleus suffered neither significant modifications nor deflection. Upon the removal of electromagnetic-dissociation events and events of purely elastic scattering from the sample of interactions under study, there remained 677 events of krypton–photoemulsion interactions and 1057 events of gold–photoemulsion interactions.

Under the conditions of our experiment, spectator fragments with charge $Z_F = 2$ were identified visually. The ionization along the tracks of these particles is constant over a large distance and is equal to $g/g_0 \approx 4$, where g_0 is the minimum ionization along the track of a relativistic singly charged particle. Fragments with charge $Z_F \geq 3$ were also identified visually; the ionization along the track of such fragments exceeds that of doubly charged fragments. In order to determine the charges of $Z_F \geq 3$ fragments, the δ-electron density was measured over a distance not less than 10 mm; the calibration was performed by using the primary track of a known charge and $Z_F = 2$ fragments. The accuracy of a charge determination was not poorer than 3 charge units for $Z_F > 40$ fragments and ±1 for $Z_F < 20$ fragments.

Relativistic particles having emission angles in the region $\theta < \theta_0$ were taken to be singly charged spectator fragments. The value θ_0 was determined from the relation

$$\sin\theta_0 = (0.2\ \text{GeV}/c)/p_0,$$

where p_0 is the projectile momentum in GeV/c per nucleon.

The polar (θ) and the azimuthal (φ) angle were measured for all charged particles in each event found by means of scanning.

The transverse momenta of the spectator fragments were determined as

$$|p_T| = 2Z_F p_0 \sin\theta, \qquad (1)$$

where Z_F is the fragment charge and p_0 is the momentum per projectile nucleon. The ratio A_F/Z_F for the fragments was assumed to be equal to 2. The mean relative error in determining the transverse momenta of the fragments did not exceed 7%.

It should be noted that, at high energies—in contrast to what occurs at low and intermediate energies—the target- and projectile-fragmentation regions are distinctly separated for multiply charged fragments (see Fig. 7 and Fig. 1 from [15] and [16], respectively). The probability of compound-nucleus formation is assumed to be small. Therefore, the problem of separating target- and projectile-nucleus fragments is simplified. The velocity of the nuclear fragments of the projectile are assumed to coincide in absolute values with the projectile velocity, and it is on the basis of this assumption that we proposed the definition in (1). Obviously, it is violated for deep-inelastic collisions, where fragments lose a considerable fraction of their longitudinal momentum. However, we cannot take this circumstance into account for want of relevant experimental information and because of special features of photoemulsion experiments.

The greatest uncertainty in estimating the fragment momenta is associated with the assumption that the number of protons (P) is identical to the number of neutrons (N) in nuclear fragments. For example, relation (1) underestimates the transverse momenta for heavy nuclei, where $N > P$. When applied to doubly charged fragments, which involve a certain fraction of ^{3}He nuclei, relation (1) overestimates the transverse momenta on average. As was shown in [17], a 10% admixture of ^{3}He nuclei to $Z = 2$ fragments leads to a 1% increases in the variance of the transverse-momentum distribution of doubly charged fragments (from 162 to 164 MeV/c); naturally, this cannot distort the conclusions of our study.

Under the conditions of photoemulsion experiments, a dedicated experimental procedure is required for identifying the fragments of target nuclei, but it was not used in our case. Therefore, our data refer to projectile fragments identified by the photoemulsion procedure. In photoemulsion devoted to high-energy interactions (at $E \geq 1$ GeV per projectile nucleon), projectile fragments are usually dubbed spectator fragments. We will follow this tradition, sometimes omitting the "spectator" modifier.

3. MULTIPLICITIES OF INTERMEDIATE-MASS FRAGMENTS AS FUNCTIONS OF THE MASS OF A RESIDUAL NUCLEUS

It is obvious that, at a fixed mass of the residual nucleus, the mean multiplicity of intermediate-mass fragments, $\langle N_{\text{IMF}}\rangle$, increases with excitation energy. At higher excitation energies, however, the production of light fragments becomes dominant, so that $\langle N_{\text{IMF}}\rangle$ must decrease. It is precisely such a dependence that was

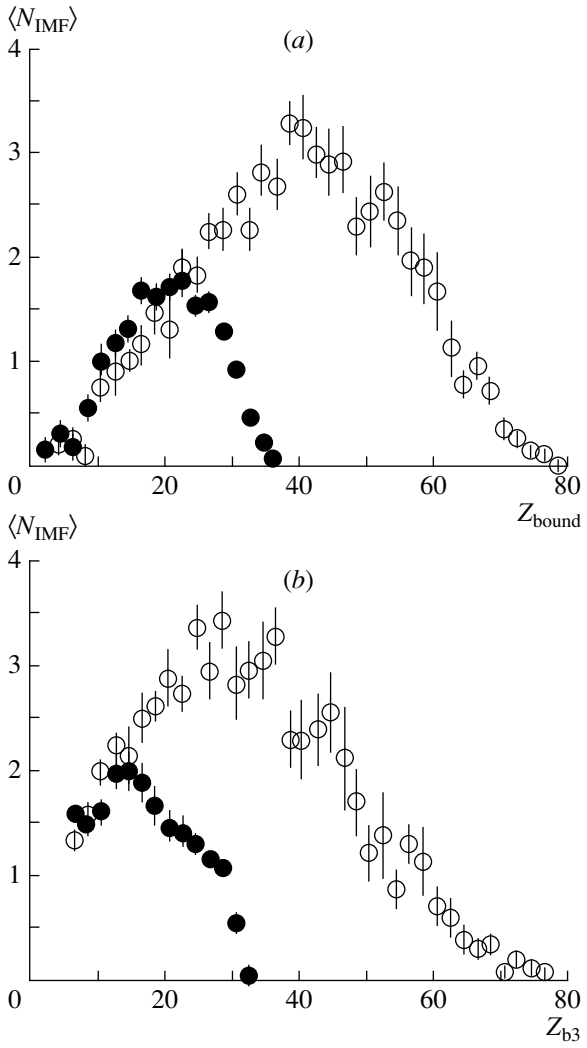

Fig. 1. Multiplicity of intermediate-mass fragments as a function of the bound charge (*a*) Z_{bound} or (*b*) Z_{b3}: (closed circles) data on the interactions between krypton nuclei of energy 0.9 GeV per projectile nucleon and photoemulsion nuclei and (open circles) data on the interactions between gold nuclei of energy 10.7 GeV per projectile nucleon and photoemulsion nuclei.

established by the ALADIN Collaboration [18–20], who studied the multifragmentation of residual nuclei produced in the interactions between gold nuclei with an energy of 600 MeV per projectile nucleon and various targets. In that case, the quantity Z_{bound}, including the charges of alpha particles, was used as a measure of the residual-nucleus mass. Since alpha particles can be produced at the stage of preequilibrium decay, Botvina *et al.* [21] proposed using another quantity, Z_{b3}. That $\langle N_{IMF}\rangle$ as a function of Z_{bound} or Z_{b3} showed no variations in response to changes in the target-nucleus mass is the most interesting result. Since the aforementioned dependence is determined primarily by the relationship between the excitation energy and the residual-nucleus mass, it can be concluded that gold-projectile nuclear residues that have the same mass and which were produced in different reactions have close excitation energies. Our data in Fig. 1 permit refining this observation.

Our results for $\langle N_{IMF}\rangle$ as a function of Z_{bound} and Z_{b3} are shown in Fig. 1 (closed circles), along with relevant data for gold projectiles of energy 10.7 GeV per nucleon [6, 7] (open circles). It can be seen that the data on the fragmentation of gold and krypton residual nuclei are close at $Z_{bound} \le 22$ and $Z_{b3} \le 16$. Although errors in our experimental data are quite large, we can say that, at the same value of Z_{bound}, the number of product IMFs is slightly greater in the fragmentation of residual nuclei of krypton projectiles than in the fragmentation of residual nuclei of gold projectiles. At the same time, the points virtually coincide at $Z_{b3} \le 16$ for the two types of interaction when the variable Z_{b3} is used. This suggests that, at high energies, residual nuclei that are produced in the interactions of different systems, but which have the same mass, have close excitation energies if more than half of nucleons are knocked out of the initial nuclei at the fast stage of the interactions.

It is noteworthy that, as Z_{b3} decreases, the IMF multiplicity grows sharply around the Z_{b3} value of 30. In all probability, this is due to the threshold nature of nuclear multifragmentation. The evaporation of nucleons and light nuclei is obviously dominant at low excitation energies. The channels of multifragment decay open up at higher excitation energies. It is not clear whether this occurs smoothly or abruptly at some threshold value. Because of large errors in the data on the fragmentation of residual nuclei of gold projectiles, it is difficult to pinpoint changes in the behavior of the multiplicity at large Z_{b3}. A vaster statistical sample is necessary for this. The data of the ALADIN collaboration have the required statistical significance for $Z_{b3} \ge 70$, but they seem to be plagued by methodological uncertainties. We deem that, with the aim of establishing the threshold character of nuclear multifragmentation, it would be of interest to perform a more careful investigation of the IMF multiplicity at large Z_{b3} values.

4. INTRINSIC FEATURES OF A DECAYING SYSTEM AS A FUNCTION OF Z_{bound} AND Z_{b3}

Investigation of the heaviest fragments in events yielded a completely unexpected result. Figure 2 shows the mean charge of the heaviest fragment in an event as a function of Z_{bound} and Z_{b3}. For the interactions of krypton nuclei with photoemulsion nuclei, a change in the behavior of $\langle Z_{max}\rangle$ as a function of Z_{b3} is clearly seen at $Z_{b3} \sim 15$. A similar change is also observed in the data on the fragmentation of residual nuclei of gold projectiles, but it is not so pronounced. The effect is smeared when use is made of the variable Z_{bound}. We approximated the bound-charge dependence of $\langle Z_{max}\rangle$ by linear functions in various regions of the bound-charge values ($\langle Z_{max}\rangle = a + bx$, $x = Z_{bound}, Z_{b3}$). The results of this fit, which are quoted in Table 1, corroborate visual observations. For the various projectile species, the parame-

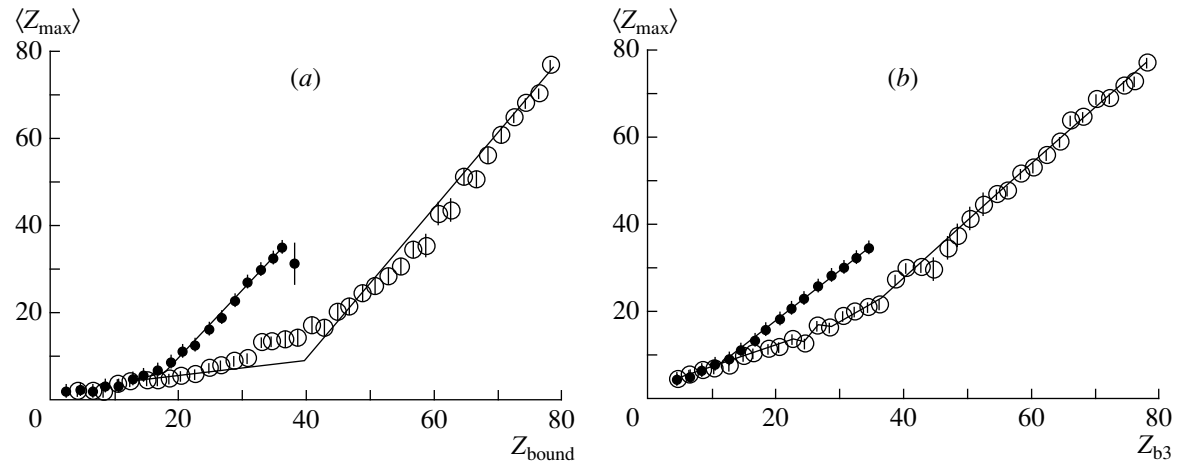

Fig. 2. Mean charge of the heaviest fragment in events as a function of the bound charge. The notation is identical to that in Fig. 1.

ters of the fit agree within two standard deviations if Z_{b3} is less than half the charge of the initial nucleus. At larger values of the bound charge, the parameters are not close. The quality of the fit in terms of the variable Z_{bound} is much poorer: the χ^2 value is greater.

The bound-charge dependence of $\langle Z_{max}\rangle$ was also approximated by the piecewise smooth functions

$$\langle Z_{max}\rangle = \begin{cases} a_1 + \dfrac{a_2 - a_1}{x_2 - x_1}(x - x_1), & x \le x_2, \\ a_2 + \dfrac{a_3 - a_2}{x_3 - x_2}(x - x_2), & x > x_2, \end{cases}$$

where $x = Z_{bound}$ or Z_{b3}. The fitted values of the parameters in this approximation are given in Table 2. In Fig. 2, the resulting approximations are represented by solid lines. It can be seen that the position of the kink (x_2 value) corresponds to a value below half the charge of the initial nucleus and that the χ^2 values are smaller when use is made of the variable Z_{b3}.

In summary, we can conclude that residual nuclei that are formed upon the removal of less than half of nucleons from the initial nucleus and those that are formed upon the removal of more than half of nucleons fragment differently. In order to investigate this point in greater detail, we define the asymmetry A_{12} for each event as

$$A_{12} = \frac{Z_1 - Z_2}{Z_1 + Z_2},$$

where Z_1, Z_2, etc., are the fragment charges arranged in decreasing order ($Z_1 \ge Z_2 \ge Z_3 \ldots$, $Z_1 \equiv Z_{max}$).

The data in Fig. 3, which shows the mean asymmetry in events versus Z_{bound} and Z_{b3}, are compatible with the above statement. It can be seen that the mean asymmetry $\langle A_{12}\rangle$ as a function of Z_{b3} is virtually constant for $Z_{b3} \le 15$ and that it grows sharply with increasing Z_{b3}. Thus, $Z_{b3} \le 15$ events are characterized by a low decay asymmetry, while $Z_{b3} > 15$ events are highly asymmetric in this respect. A similar behavior can be traced in the fragmentation of heavier systems.

In terms of the variable Z_{bound}, it is difficult to decide conclusively that there exist two modes of fragmentation of residual nuclei of krypton projectiles. In the data on the fragmentation of heavier systems, the mean asymmetry $\langle A_{12}\rangle$ behaves differently at Z_{bound} values above and below the projectile charge. At small Z_{bound} values, the mean asymmetry $\langle A_{12}\rangle$ takes very similar values for the different fragmenting systems.

On the whole, we can conclude that there are at least two types of nuclear multifragmentation.

5. FRAGMENT ENERGIES AS FUNCTIONS OF Z_{bound}

According to the statistical model of nuclear multifragmentation, the kinetic energy of fragments in the rest frame of the fragmenting nucleus is determined by the charge of the residual nucleus; therefore, a decrease in Z_{bound} is expected to be accompanied by a decrease in

Table 1. Fitted values of the parameters in a linear-function approximation of $\langle Z_{max}\rangle$ versus the bound charge

Projectile nucleus	Bound-charge interval	a	b	χ^2/NDF
Kr	Z_{b3} = 3–15	1.8 ± 0.2	0.57 ± 0.04	5.1/6
Au	Z_{b3} = 3–37	2.2 ± 0.1	0.50 ± 0.02	10.5/17
Kr	Z_{b3} = 16–35	–4.3 ± 0.6	1.13 ± 0.02	5.4/10
Au	Z_{b3} = 42–79	–26.8 ± 2.3	1.34 ± 0.03	6.0/19
Kr	Z_{bound} = 2–15	1.5 ± 0.1	0.19 ± 0.02	19/7
Au	Z_{bound} = 2–37	0.4 ± 0.1	0.28 ± 0.01	49/17
Kr	Z_{bound}= 22–37	–23.4 ± 1.6	1.63 ± 0.05	57/9
Au	Z_{bound}= 54–79	–74.5 ± 4.1	1.92 ± 0.06	47/13

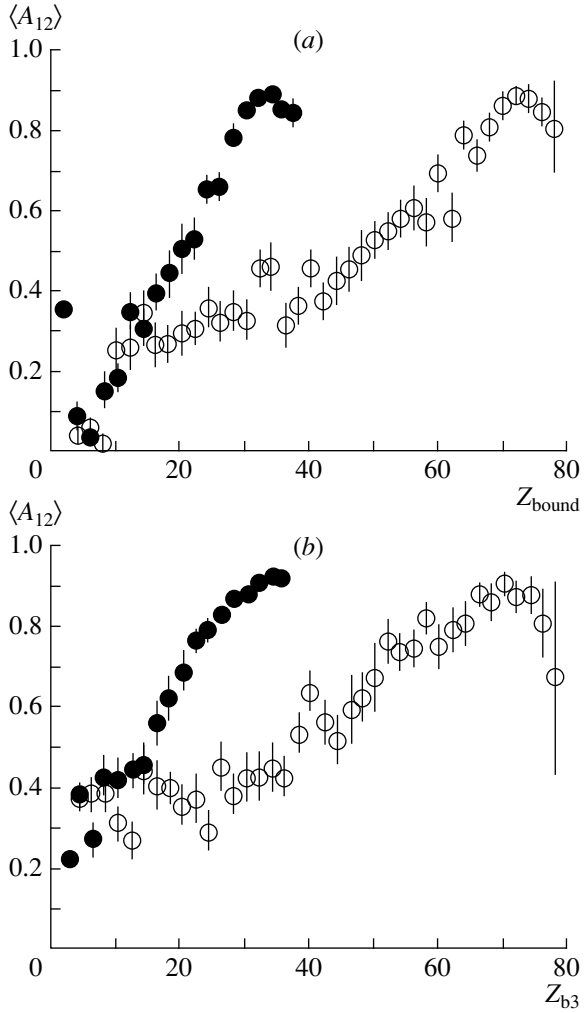

Fig. 3. Mean asymmetry in events as a function of the bound charge. The notation is identical to that in Fig. 1.

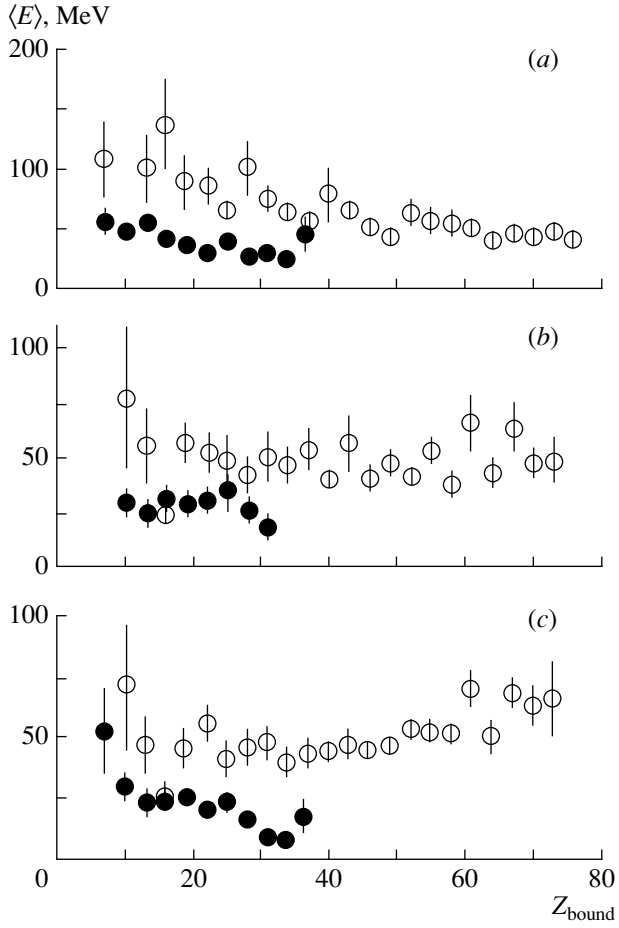

Fig. 4. Estimated mean kinetic energies of fragments in the rest frame of the fragmenting nucleus for (*a*) doubly charged fragments, (*b*) Z_F = 3–5 fragments, and (*c*) intermediate-mass fragments. The notation for the points is identical to that in Fig. 1.

the fragment energy [22]. In order to go over from the laboratory frame to the rest frame of the fragmenting nucleus, we used the Galilean transformation in the form described in detail by Adamovich *et al*. [6]. Under the assumption of isotropic decay, the mean kinetic energy of a fragment and its mean transverse momentum are related by the equation

$$\langle E\rangle = \frac{3}{2}\frac{\langle p_T^2\rangle}{4Z_F m_N},$$

where p_T is the fragment transverse momentum, Z_F is the fragment charge, and m_N is the nucleon mass.

Figure 4 shows data on the mean kinetic energies of $Z_F \geq 2$ fragments in events where the number of multiply charged fragments is greater than or equal to three. The kinetic energies of the fragments of krypton nuclei do not show any tendency to decrease with decreasing residual-nucleus masses at $Z_{\text{bound}} \leq 25$. Moreover, they are virtually constant in this region of Z_{bound}. A similar pattern is observed in fragmentation of gold nuclei.

Table 2. Fitted values of the parameters in a piecewise-linear-function approximation of $\langle Z_{\max}\rangle$ versus the bound charge

Nucleus	Bound charge	a_1	x_1	a_2	x_2	a_3	x_3	χ^2/NDF
Kr	Z_{b3}	3.58	3	8.0 ± 0.6	11.3 ± 0.6	34.5	34.5	14/16
Au	Z_{b3}	3.58	3	18.2 ± 0.7	32.5 ± 0.9	77.5	78.5	18/38
Kr	Z_{bound}	2.00	2	5.0 ± 0.3	16.6 ± 0.4	35.2	36.0	37/18
Au	Z_{bound}	2.00	2	9.3 ± 0.3	39.3 ± 0.5	78.5	80.0	150/38

This suggests the presence of a radial flux of fragments. According to our data, the energy of the radial flux depends on the projectile mass.

6. CONCLUSION

Experimental data on the fragmentation of residual nuclei formed in the interactions between krypton projectiles with an energy of 0.9 GeV per nucleon and photoemulsion nuclei have been presented.

It has been shown that the residual nuclei fragment in nearly the same way, irrespective of the projectile mass, if the bound charge does not exceed half the charge of the initial nucleus.

Evidence for the threshold character of nuclear multifragmentation and for the existence of the projectile-mass dependence of the radial flux of fragments has been obtained.

The observed experimental regularities have been disclosed most vividly when the variable Z_{b3} has been used as a measure of the residual-nucleus mass.

Further theoretical and experimental investigations into the fragmentation of intermediate-mass nuclei would be of interest.

ACKNOWLEDGMENTS

We are grateful to the EMU-01/12 Collaboration for kindly placing at our disposal their experimental data on the fragmentation of residual nuclei of gold projectiles.

The work of some of us was supported by the Russian Foundation for Basic Research (project no. 99-02-17757).

REFERENCES

1. S. C. Jeong *et al.*, Phys. Rev. Lett. **72**, 3468 (1994).
2. W. C. Hsi *et al.*, Phys. Rev. Lett. **73**, 3367 (1994).
3. M. A. Lisa *et al.*, Phys. Rev. Lett. **75**, 2662 (1995).
4. FOPI Collab. (G. Poggi *et al.*), Nucl. Phys. A **586**, 755 (1995).
5. FOPI Collab. (W. Reisdorf *et al.*), Nucl. Phys. A **612**, 493 (1997).
6. EMU-01 Collab. (M. I. Adamovich *et al.*), Z. Phys. A **359**, 277 (1997).
7. V. Sh. Navotny and V. V. Uzhinskii, Yad. Fiz. **61**, 671 (1998) [Phys. At. Nucl. **61**, 598 (1998)]; K. G. Gulamov, V. Sh. Navotny, and V. V. Uzhinskii, Yad. Fiz. **62**, 581 (1999) [Phys. At. Nucl. **62**, 533 (1999)].
8. J. Pochodzalla *et al.*, Phys. Rev. Lett. **75**, 1040 (1995).
9. INDRA Collab. (M. F. Rivet *et al.*), Preprint No. IPNO-DRE-98-08 (IPN, Orsay, 1998).
10. J. P. Bondorf *et al.*, Phys. Rep. **257**, 134 (1995).
11. D. H. E. Gross, Rep. Prog. Phys. **53**, 605 (1990).
12. A. S. Botvina *et al.*, Z. Phys. A **345**, 413 (1993); V. V. Glagolev *et al.*, Yad. Fiz. **61**, 2132 (1998) [Phys. At. Nucl. **61**, 2021 (1998)].
13. J. Aichelin, Phys. Rep. **202**, 233 (1991).
14. A. Ono and H. Horiuchi, Phys. Rev. C **53**, 2958 (1996); A. Ono, Phys. Rev. C **59**, 853 (1999).
15. A. M. Baldin, Fiz. Élem. Chastits At. Yadra **8**, 429 (1977) [Sov. J. Part. Nucl. **8**, 175 (1977)].
16. KLMM Collab. (M. L. Cherry *et al.*), Phys. Rev. C **52**, 2652 (1995).
17. EMU-01 Collab. (M. I. Adamovich *et al.*), Phys. Lett. B **338**, 397 (1994).
18. J. Hubele *et al.*, Z. Phys. A **340**, 263 (1991).
19. J. Hubele *et al.*, Phys. Rev. C **46**, R1577 (1992).
20. P. Kreutz *et al.*, Nucl. Phys. A **556**, 672 (1993).
21. A. S. Botvina *et al.*, Nucl. Phys. A **584**, 737 (1995).
22. S. Yu. Shmakov *et al.*, Yad. Fiz. **58**, 1735 (1995) [Phys. At. Nucl. **58**, 1635 (1995)].

Translated by E. Kozlovskiĭ

Physics of Atomic Nuclei, Vol. 64, No. 1, 2001, pp. 68–73. Translated from Yadernaya Fizika, Vol. 64, No. 1, 2001, pp. 72–77.

ELEMENTARY PARTICLES AND FIELDS
Theory

Chiral Anomaly in $K\gamma \longrightarrow K\pi$ Reactions

R. N. Rogalyov*
Institute for High Energy Physics, Protvino, Moscow oblast, 142284 Russia
Received January 10, 2000; in final form, May 10, 2000

Abstract—Implications of the chiral anomaly for the cross sections of the reactions $K^+\gamma \longrightarrow K^+\pi^0$, $K^0\gamma \longrightarrow K^0\pi^0$, $K^+\gamma \longrightarrow K^0\pi^+$, and $K^0\gamma \longrightarrow K^+\pi^-$ are investigated. Near the threshold, the contribution of the chiral anomaly dominates the cross sections for the first and the second reaction. These cross sections are compared with the cross sections for the third and the fourth reaction, which receive no contribution from the chiral anomaly. Prospects for an experimental study of the $KK\pi\gamma$ vertex in the Coulomb production of π mesons by a K-meson beam are discussed. *© 2001 MAIK "Nauka/Interperiodica".*

1. INTRODUCTION

The concept of a chiral anomaly is taken to mean a violation of classical chiral symmetry at the quantum level. Such a breakdown of symmetry occurs in theories featuring chiral fermions—in particular, in the Standard Model. Phenomenological implications of the chiral anomaly for strong, electromagnetic, and weak semileptonic processes involving pseudoscalar mesons can be deduced from the functional [1]

$$S[U,\ell,r]_{\mathrm{WZW}} = -\frac{iN_c}{240\pi^2}\int d\sigma^{ijklm}\langle\Sigma_i^L\Sigma_j^L\Sigma_k^L\Sigma_l^L\Sigma_m^L\rangle - \frac{iN_c}{48\pi^2}\int d^4x\varepsilon_{\mu\nu\alpha\beta}(W(U,\ell,r)^{\mu\nu\alpha\beta} - W(\mathbf{1},\ell,r)^{\mu\nu\alpha\beta}), \quad (1)$$

which must be included in the action of chiral perturbation theory (ChPT). The first integral on the right-hand side of Eq. (1) must be taken over five-dimensional space whose boundary is four-dimensional Minkowski space; the indices i, j, k, l, and m run the values from 1 to 5; σ^{ijklm} is a relevant volume element; μ, ν, α, and β are the indices in Minkowski space; and N_c is the number of colors ($N_c = 3$). The functional in (1), also known as the Wess–Zumino–Witten (WZW) action, is expressed in terms of the meson fields as

$$W(U,\ell,r)^{\mu\nu\alpha\beta} = \left\langle U\ell_\mu\ell_\nu\ell_\alpha U^\dagger r_\beta + \frac{1}{4}U\ell_\mu U^\dagger r_\nu U\ell_\alpha U^\dagger r_\beta + iU\partial_\mu\ell_\nu\ell_\alpha U^\dagger r_\beta + i\partial_\mu r_\nu U\ell_\alpha U^\dagger r_\beta - i\Sigma_\mu^L\ell_\nu U^\dagger r_\alpha U\ell_\beta + \Sigma_\mu^L U^\dagger\partial_\nu r_\alpha U\ell_\beta - \Sigma_\mu^L\Sigma_\nu^L U^\dagger r_\alpha U\ell_\beta + \Sigma_\mu^L\ell_\nu\partial_\alpha\ell_\beta + \Sigma_\mu^L\partial_\nu\ell_\alpha\ell_\beta - i\Sigma_\mu^L\ell_\nu\ell_\alpha\ell_\beta + \frac{1}{2}\Sigma_\mu^L\ell_\nu\Sigma_\alpha^L\ell_\beta - i\Sigma_\mu^L\Sigma_\nu^L\Sigma_\alpha^L\ell_\beta\right\rangle - (L \longleftrightarrow R), \quad (2)$$

where

$$\Sigma_\mu^L = U^\dagger\partial_\mu U,\ \Sigma_\mu^R = U\partial_\mu U^\dagger,\ U = \exp(i\Phi\sqrt{2}/F),$$

$$\Phi = \begin{pmatrix} \frac{\pi^0}{\sqrt{2}} + \frac{\eta^8}{\sqrt{6}} + \frac{\eta^0}{\sqrt{3}} & \pi^+ & K^+ \\ \pi^- & -\frac{\pi^0}{\sqrt{2}} + \frac{\eta^8}{\sqrt{6}} + \frac{\eta^0}{\sqrt{3}} & K_0 \\ K^- & \bar{K}_0 & -\frac{2\eta^8}{\sqrt{6}} + \frac{\eta^0}{\sqrt{3}} \end{pmatrix};$$

$$r_\mu = A_\mu\begin{pmatrix} \frac{2}{3} & 0 & 0 \\ 0 & -\frac{1}{3} & 0 \\ 0 & 0 & -\frac{1}{3} \end{pmatrix};$$

$$\ell_\mu = r_\mu + \frac{eW_\mu^+}{\sqrt{2}\sin\theta_{\mathrm{W}}}\begin{pmatrix} 0 & V_{ud} & V_{us} \\ 0 & 0 & 0 \\ 0 & 0 & 0 \end{pmatrix} + \frac{eW_\mu^-}{\sqrt{2}\sin\theta_{\mathrm{W}}}\begin{pmatrix} 0 & 0 & 0 \\ V_{ud}^* & 0 & 0 \\ V_{us}^* & 0 & 0 \end{pmatrix}; \quad (3)$$

$F = 93$ MeV; and $(L \longleftrightarrow R)$ stands for the interchanges $U \longleftrightarrow U^\dagger$, $\ell_\mu \longleftrightarrow r_\mu$, and $\Sigma_\mu^L \longleftrightarrow \Sigma_\mu^R$.

* e-mail: rogalyov@mx.ihep.su

Substituting definitions (3) into expression (2), we derive all terms stemming from the chiral anomaly that appear in the effective Lagrangian for the aforementioned processes. Here, we are interested in the terms in this Lagrangian that describe photon interaction with three pseudoscalar mesons:[1)]

$$\mathcal{L}_{\mathrm{WZW}}^{3P\gamma} = \frac{ie}{4\pi^2 F^3}\varepsilon^{\mu\nu\alpha\beta}A_\beta\Big((\partial_\mu\pi^+\partial_\nu\pi^- + \partial_\mu K^+\partial_\nu K^- + \partial_\mu K^0\partial_\nu\bar{K}^0)\partial_\alpha\pi^0 + \frac{\sqrt{3}}{3}(\partial_\mu\pi^+\partial_\nu\pi^- + \partial_\mu K^+\partial_\nu K^- - 3\partial_\mu K^0\partial_\nu\bar{K}^0)\partial_\alpha\eta^8 + \frac{\sqrt{6}}{3}(\partial_\mu\pi^+\partial_\nu\pi^- + \partial_\mu K^+\partial_\nu K^-)\partial_\alpha\eta^0\Big). \quad (4)$$

The $\gamma\pi^0\pi^+\pi^-$ and $\gamma\eta\pi^+\pi^-$ vertices were studied theoretically in [3, 4] and experimentally in the Coulomb production of π^0 and η mesons at the IHEP accelerator [5, 6].

An experimental study of anomalous vertices involving K mesons is of particular interest because of their role in the WZW action (1). To obtain deeper insight into the role of the K mesons, we assume, for the time being, that there are no K mesons in the low-energy effective Lagrangian (this would be the case if the s quark were heavy).

In a hypothetical world featuring only two light quarks, any effective meson Lagrangian respects not only the symmetries of the underlying QCD Lagrangian but also some additional symmetries—for example, the parity of the number of Goldstone bosons is conserved in this hypothetical world. In this case, one of the rules for constructing an effective theory—any effective theory must satisfy all symmetries of the respective underlying theory and only them—is violated. Note that the simplest reaction that respects all symmetries of the QCD Lagrangian and only them is $K^+K^- \longrightarrow \pi^+\pi^0\pi^-$ [1].

Moreover, the important conclusion that the coefficient of Lagrangian (1) can take only integral values (in units of $1/240\pi^2$) was deduced under the assumption that the manifold of Goldstone bosons coincides with the $SU(3)$ group (this is equivalent to the existence of three light quarks).

However, manifestations of the chiral anomaly in reactions featuring the K mesons have received little attention. The only case where it was considered is the calculation of the anomalous contribution to nonleptonic weak interactions [7].[2)] [7]. Unfortunately, the amplitudes of such processes depend on additional parameters; therefore, the chiral-anomaly contribution proper is hidden and can be isolated only under some auxiliary assumptions.

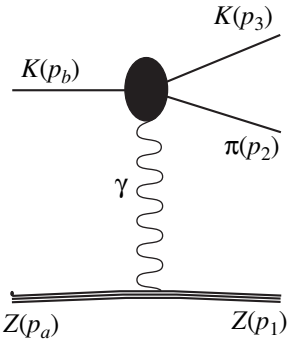

Fig. 1. Kinematics of the Coulomb productions of π mesons on a beryllium nucleus: $q = p_a - p_1$, $t_1 = q^2$, $s_2 = (p_2 + p_3)^2$, $t_2 = (p_b - p_3)^2$, and $s = (p_a + p_b)^2 \approx M_Z^2 + 2M_Z E$.

Here, we study the manifestations of the chiral anomaly in the strong and electromagnetic interactions of the strange particles. Since such manifestations cannot be observed in meson decays, we consider the amplitudes of the $K\gamma \longrightarrow K\pi$ scattering processes, which can be studied experimentally in the Coulomb production of π mesons by a K-meson beam (Fig. 1).

The behavior of the $K\gamma \longrightarrow K\pi$ amplitude in the chiral limit is completely determined by the anomalous WZW Lagrangian (1), whereas, at the physical values of the meson masses and $\sqrt{s} \sim 0.9$ GeV, it is determined by the contribution of the 1^{--} resonances. A similar statement is valid for the reactions $\pi\gamma \longrightarrow \pi\pi$ and $\pi\gamma \longrightarrow \eta\pi$, whose amplitudes were calculated in [3] (see also [4]) by using the Kawarabayashi–Suzuki–Riazuddin–Fayyazuddin (KSRF) relations and anomalous Ward identities.

We calculate the amplitudes of the reaction $K\gamma \longrightarrow K\pi$ on the basis of the Bando–Kugo–Yamawaki model [8, 9], which represents a version of the vector-meson-dominance model based on a Lagrangian that generates the KSRF relations and the anomalous Ward identities.

2. BANDO–KUGO–YAMAWAKI MODEL

The Bando–Kugo–Yamawaki model is a natural extension of ChPT to the interactions between the pseudo-Goldstone 0^{-+} mesons (P) and the vector 1^{--} mesons (V). Within this model, the vector mesons originate from a dynamical breakdown of hidden gauge symmetry in the CHPT Lagrangian. The normal-sector Lagrangian of the Bando–Kugo–Yamawaki model has the form

$$\mathcal{L}_{\mathrm{norm}} = -F^2\langle p_\mu p_\mu\rangle - 2F^2\langle(v_\mu - igV_\mu - ie\mathcal{B}_\mu)^2\rangle - \frac{1}{2}\langle V_{\mu\nu}^2\rangle, \quad (5)$$

[1)]Strictly speaking, expression (1) was deduced for the case of the $SU(3)$ [instead of $U(3)$] group. A generalization of the action functional (1) to the case of the $U(3)$ group by naively considering the η^0 meson among the pseudo-Goldstone bosons was used in [2].

[2)]The action functional (1) itself describes only the strong, electromagnetic, and semileptonic weak interactions of the pseudoscalar mesons.

where

$$\mathcal{B} = A_\mu Q, \quad Q = \mathrm{diag}\left(\frac{2}{3}, -\frac{1}{3}, -\frac{1}{3}\right);$$

A_μ is the electromagnetic field; here and below, angular brackets denote evaluation of the trace over the $SU(3)$ indices; and

$$p_\mu = \frac{1}{2}(\xi^\dagger\partial_\mu\xi + \partial_\mu\xi\xi^\dagger),$$

$$v_\mu = \frac{1}{2}(\xi^\dagger\partial_\mu\xi - \partial_\mu\xi\xi^\dagger), \quad \xi = \exp\left(\frac{i\Phi}{F\sqrt{2}}\right).$$

The first term in this Lagrangian coincides with the ChPT Lagrangian. The Lagrangian in (5) is invariant under the transformations

$$\begin{aligned}\xi &\longrightarrow g_L\xi h^{-1}(\xi, g_L, g_R),\\ \xi^\dagger &\longrightarrow g_R\xi^\dagger h^{-1}(\xi, g_L, g_R),\end{aligned} \tag{6}$$

which are defined in such way that $v_\mu \longrightarrow hv_\mu h^{-1} - \partial_\mu h h^{-1}$. The field V_μ describing the vector mesons is introduced as the compensating field for these transformations [see the second term in the expression (5)], and its kinetic term is generated dynamically [9].

The mass matrix in Lagrangian (5) is determined by the quadratic form

$$\mathcal{L}_{\mathrm{mass}} = 2F^2\left(g^2V_\mu^aV_\mu^a + \sqrt{2}egQ^aV_\mu^aA_\mu + \frac{2}{3}e^2A_\mu A_\mu\right),$$

where $Q^a = \langle\lambda^a, Q\rangle$ and $V_\mu^a = \sqrt{2}\,\langle\lambda^a, V_\mu\rangle$. A diagonalization of this matrix gives rise to the mixing of the fields V_μ^3 and V_μ^8 with the field A_μ. The eigenstates of the mass matrix that are associated with the mixing of the fields under consideration have the form

$$R'_\mu = -\frac{1}{2}V_\mu^3 + \frac{\sqrt{3}}{2}V_\mu^8,$$

$$\mathcal{R}_\mu = -\frac{1}{g'}\left(g\left(\frac{\sqrt{3}}{2}V_\mu^3 + \frac{1}{2}V_\mu^8\right) + \sqrt{\frac{2}{3}}eA_\mu\right),$$

$$\mathcal{A}_\mu = -\frac{1}{g'}\left(-\sqrt{\frac{2}{3}}e\left(\frac{\sqrt{3}}{2}V_\mu^3 + \frac{1}{2}V_\mu^8\right) + gA_\mu\right).$$

The masses of the fields R'_μ and $\mathcal{R}_\mu$ are, respectively, $2Fg$ and $2Fg'$, where $g' = \sqrt{g^2 + 2e^2/3}$, and the massless field $\mathcal{A}_\mu$ describes the physical photon. In what follows, we neglect terms of order e^2 since $e \ll g$. In this approximation, the mass term of the field V_μ and the vertex of the γ–V transition are given by

$$\frac{m_V^2}{2}V_\mu^aV_\mu^a + eg_VA_\mu\sum_{a=\rho^0,\omega,\phi}V_\mu^aQ^a, \tag{7}$$

where

$$\rho_\mu^0 = V_\mu^3, \quad \omega_\mu = \sqrt{\frac{2}{3}}V_\mu^0 + \frac{1}{\sqrt{3}}V_\mu^8,$$

$$\phi_\mu = \frac{1}{\sqrt{3}}V_\mu^0 - \sqrt{\frac{2}{3}}V_\mu^8; \quad Q_{\rho^0} = 1,$$

$$Q_\omega = \frac{1}{3}, \quad Q_\phi = -\frac{\sqrt{2}}{3},$$

$$m_V = 2Fg, \tag{8}$$

$$g_V = m_VF\sqrt{2}. \tag{9}$$

Formulas (8) and (9) are, respectively, the first and the second KSRF relation; they determine the numerical value of the constant of the VPP interaction, $g = 4.9$, and the constant of the γ–V transitions, $g_V \sim (325\ \mathrm{MeV})^2$.

The interaction Lagrangian describing anomalous-parity processes has the form [8]

$$\mathcal{L}_{\mathrm{anom}} = \mathcal{L}_{\mathrm{WZW}} - \frac{i}{16\pi^2}\left(c\mathcal{L}_1 + (3+c)\mathcal{L}_2 + \frac{3}{2}\mathcal{L}_4 - \frac{3}{2}\mathcal{L}_6\right), \tag{10}$$

where

$$\mathcal{L}_1 = \varepsilon^{\mu\nu\alpha\beta}\langle L_\mu L_\nu L_\alpha R_\beta - R_\mu R_\nu R_\alpha L_\beta\rangle,$$

$$\mathcal{L}_2 = \varepsilon^{\mu\nu\alpha\beta}\langle L_\mu R_\nu L_\alpha R_\beta\rangle,$$

$$\mathcal{L}_4 = \varepsilon^{\mu\nu\alpha\beta}\langle ig(\partial_\mu V_\nu - \partial_\nu V_\mu + ig[V_\mu, V_\nu]) \times (L_\alpha R_\beta - R_\alpha L_\beta)\rangle,$$

$$\mathcal{L}_6 = \varepsilon^{\mu\nu\alpha\beta}\langle i(F_{\mu\nu}^L L_\alpha R_\beta - F_{\mu\nu}^R R_\alpha L_\beta)\rangle$$

and

$$L_\mu = \xi^\dagger\partial_\mu\xi - igV_\mu - i\xi^\dagger\ell_\mu\xi,$$

$$R_\mu = -\partial_\mu\xi\xi^\dagger - igV_\mu - i\xi r_\mu\xi^\dagger,$$

$$F_{\mu\nu}^L = \xi^\dagger(\partial_\mu\ell_\nu - \partial_\nu\ell_\mu + i[\ell_\mu, \ell_\nu])\xi,$$

$$F_{\mu\nu}^R = \xi(\partial_\mu r_\nu - \partial_\nu r_\mu + i[r_\mu, r_\nu])\xi^\dagger.$$

The coefficient c in expression (10) is a free parameter; the lowest order terms in the expansion of Lagrangian (10) in the fields are independent of c and are given by the expression

$$\mathcal{L}_{\mathrm{anom}} = \frac{i\sqrt{2}}{16\pi^2}(3iPVV + 2PPP\gamma), \tag{11}$$

where

$$PPP\gamma = \varepsilon^{\mu\nu\alpha\beta}\langle r_\mu\partial_\nu\Phi\partial_\alpha\Phi\partial_\beta\Phi\rangle,$$

$$PVV = \varepsilon^{\mu\nu\alpha\beta}\langle(V_\mu\partial_\nu V_\alpha + \partial_\mu V_\nu V_\alpha)\partial_\beta\Phi\rangle.$$

The Lagrangian in (10) possesses the following properties:

(i) It meets the requirements of the principle of vector-meson dominance for the $P\gamma\gamma$ vertices. This means that decays of the $P \longrightarrow \gamma\gamma$ type are necessarily mediated by the PVV vertex and that, in the total Lagrangian, there are no $P\gamma\gamma$ and $PV\gamma$ vertices. It should be emphasized that the behavior of the amplitudes in the chiral limit coincides with that predicted by the WZW Lagrangian (1), this coincidence being due to the KSRF relations (8) and (9).

(ii) It adequately describes the decay $\omega \longrightarrow 3\pi$. According to this model, this decay of the ω meson proceeds in two stages: $\omega \longrightarrow \rho\pi \longrightarrow \pi\pi\pi$; Therefore, the $PPPV$ vertex does not appear in the Lagrangian. The principle of vector-meson dominance for the $PPPV$ vertices does not agree with experimental data [8, 10].

3. RESULTS OF THE CALCULATIONS

The expressions for the amplitudes of $K\gamma \longrightarrow K\pi$ reactions can be derived from the interaction Lagrangians (5) and (10). The relevant diagrams are shown in Fig. 2. The result has the form

$$A_{K\gamma\to K\pi} = -\frac{ie}{16\pi^2 F^3}\varepsilon^{\mu\nu\alpha\beta}q^\mu p_b^\nu p_2^\alpha \epsilon^\beta \times\left(C_0 + \frac{C_s M_{K^*}^2}{s - M_{K^*}^2 + i\Gamma_{K^*}\sqrt{s}} + \frac{C_t M_\rho^2}{t - M_\rho^2} + \frac{C_u M_{K^*}^2}{u - M_{K^*}^2}\right), \quad (12)$$

where ϵ is the photon polarization vector, while q, p_b, and p_2 are the momenta of, respectively, the photon, the initial K meson, and the π meson (see Fig. 1). The coefficients C_0, C_s, C_t, and C_u for specific processes are presented in Table 1.

Here, the unitarization of the amplitude is achieved in the simplest way, by adding the imaginary term $i\Gamma_V\sqrt{s}$ to the denominators of the vector-meson propagators. We neglect the widths of the t-channel and u-channel resonances because we consider the behavior of the amplitudes only in the s channel.

Let us denote by $I(s)$ the integral of the square of the absolute value of the parenthetical expression on the right-hand side of Eq. (12); that is,

$$I(s) = \int_{t_-}^{t_+}\left|C_0 + \frac{C_s M_{K^*}^2}{s - M_{K^*}^2 + i\Gamma_{K^*}\sqrt{s}} + \frac{C_t M_\rho^2}{t - M_\rho^2} + \frac{C_u M_{K^*}^2}{u - M_{K^*}^2}\right|^2 dt, \quad (13)$$

where t_+ and t_- are the kinematical limits. The cross section for the reaction $K\gamma \longrightarrow K\pi$ then has the form

$$\sigma = \frac{1}{1024\pi^4}\frac{\alpha}{F^6}\frac{I(s_2)}{(s_2 - m_K)^2}.$$

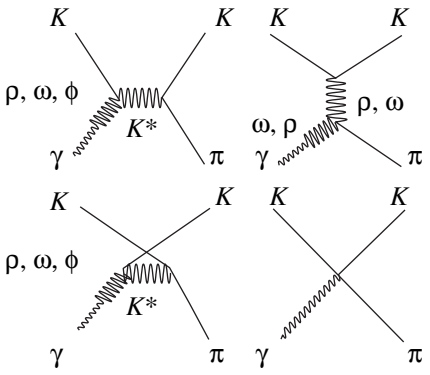

Fig. 2. Tree diagrams contributing to the amplitude of the reaction $K\gamma \longrightarrow K\pi$.

Cross sections of this type can be studied in the Coulomb production of π mesons by a K-meson beam. The kinematical variables used to describe these reactions are defined in Fig. 1. We consider the cross section for the scattering into the following kinematical domain:

$$-(50\ \text{MeV})^2 < t_1 < -\frac{(s_2 - m_K^2)^2}{4E_K^2}, \qquad (m_K + m_\pi)^2 < s_2 < 0.6\ \text{GeV}^2. \quad (14)$$

Here, E_K is the energy of the K-meson beam; the constraint $t_1 > -(50\ \text{MeV})^2$ is introduced in order to isolate the Coulomb production of π mesons (Fig. 1) from

Table 1. Coefficients C_0, C_s, C_t, and C_u from Eq. (12)

Reaction	C_0	C_s	C_t	C_u
$K^+\gamma \longrightarrow K^+\pi^0$	2	1	4	1
$K^+\gamma \longrightarrow K^0\pi^+$	0	$\sqrt{2}$	$\sqrt{2}$	$-2\sqrt{2}$
$K^0\gamma \longrightarrow K^0\pi^0$	2	2	2	2
$K^0\gamma \longrightarrow K^+\pi^-$	0	$-2\sqrt{2}$	$\sqrt{2}$	$\sqrt{2}$

Table 2. Values characterizing the near-threshold behavior of the cross section $d\sigma/ds_2$ in Eq. (17)

Reaction	σ, nb	C, nb/GeV^3	$s_2^{\max}$, GeV^2
$K^+\gamma \longrightarrow K^+\pi^0$	81	1.0×10^5	0.55
$K^+\gamma \longrightarrow K^0\pi^+$	20	2.9×10^2	0.40
$K^0\gamma \longrightarrow K^0\pi^0$	165	1.6×10^5	0.45
$K^0\gamma \longrightarrow K^+\pi^-$	99	2.6×10^3	0.45

Note: Here, σ is the cross section for scattering in the kinematical domain (14); the energy threshold corresponds to $s_2 = 0.396\ \text{GeV}^2$; and $s_2^{\max}$ is the s value 2 bounding the domain of validity of Eq. (17).

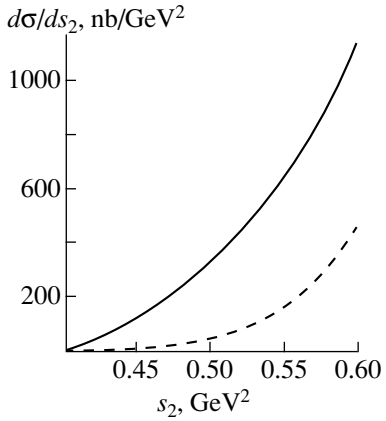

Fig. 3. Cross sections for Coulomb scattering on a beryllium nucleus as functions of $s_2 = (p_K^{\text{out}} + p_\pi)^2$ at the beam energy of 40 GeV in the near-threshold region: (solid curve) $K^+Z \longrightarrow K^+\pi^0 Z$ and (dashed curve) $K^+Z \longrightarrow K^0\pi^+ Z$. Here and in Figs. 4 and 5, the square of the momentum transfer to the nucleus satisfies the kinematical constraint $|t_1| < (50\ \text{MeV})^2$.

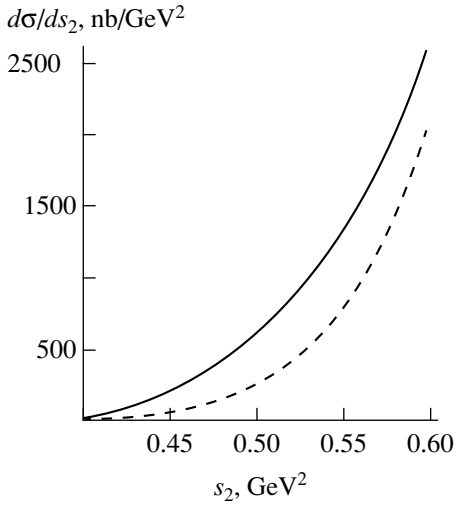

Fig. 4. Cross sections for Coulomb scattering on s beryllium nucleus as functions of $s_2 = (p_K^{\text{out}} + p_\pi)^2$ at the beam energy of 40 GeV in the near-threshold region: (solid curve) $K^0Z \longrightarrow K^0\pi^0 Z$ and (dashed curve) $K^0Z \longrightarrow K^+\pi^- Z$.

π-meson production governed by the other mechanisms [6]; the constraint $s_2 < 0.6\ \text{GeV}^2$ is imposed to exclude the resonance region; the remaining two boundaries have a kinematical origin.

Using the equivalent-photon approximation, we express the cross section for the Coulomb production of π mesons on a nucleus in terms of the cross section for the reaction $K\gamma \longrightarrow K\pi$ as

$$\frac{d\sigma}{ds_2 dt_2 dt_1} = \frac{Z^2\alpha}{\pi}\frac{|t_1 - t_1^{\min}|}{t_1^2}\frac{1}{s_2 - m_K^2}\frac{d\sigma_{K\gamma\to K\pi}}{dt_2}. \quad (15)$$

Upon integration with respect to t_1 over the domain determined by the constraints in (14), we arrive at

$$\frac{d\sigma}{ds_2} = \frac{Z^2\alpha^2}{(2\pi)^5}\frac{1}{32F^6}\left(\ln\frac{4E^2Q^2}{(s_2 - m_K^2)^2} - 1 + \frac{(s_2 - m_K^2)^2}{4E^2Q^2}\right) \times \frac{I(s_2)}{(s_2 - m_K^2)^3}. \quad (16)$$

The chiral anomaly reveals itself in the behavior of the cross sections under study in the vicinity of the point $s = t = u = 0$, where the amplitude in (12) is determined by Lagrangian (4). The chiral anomaly contributes to the amplitudes of the reactions $K^+\gamma \longrightarrow K^+\pi^0$ and $K^0\gamma \longrightarrow K^0\pi^0$, but it does not contribute to the amplitudes of the reactions $K^+\gamma \longrightarrow K^0\pi^+$ and $K^0\gamma \longrightarrow K^+\pi^-$. This is clearly demonstrated in Figs. 3 and 4, which display the near-threshold behavior of the relevant cross sections.

Near the threshold, the behavior of the cross section can be described by the formula

$$\frac{d\sigma_{K\gamma\to K\pi}}{ds_2} = C(s_2 - (m_K + m_\pi)^2)^{3/2}, \quad (17)$$

where the coefficients C for the specific reactions are quoted in Table 2. The energy ranges where expression (17) provides a good approximation to the cross sections and the total cross sections for π-meson production on a beryllium nucleus at an incident-kaon energy of about 40 GeV in the kinematical domain

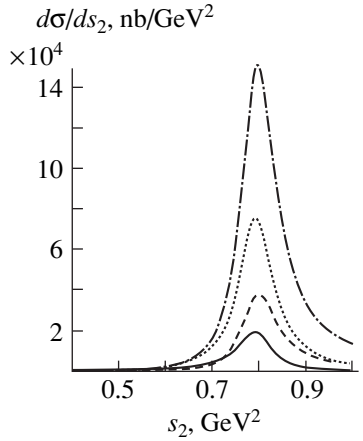

Fig. 5. Cross sections for Coulomb scattering on a beryllium nucleus as functions of $s_2 = (p_K^{\text{out}} + p_\pi)^2$ at the beam energy of 40 GeV in the resonance region: (solid curve) $K^+Z \longrightarrow K^+\pi^0 Z$, (dashed curve) $K^+Z \longrightarrow K^0\pi^+ Z$, (dotted curve) $K^0Z \longrightarrow K^0\pi^0 Z$, and (dash-dotted curve) $K^0Z \longrightarrow K^+\pi^- Z$.

specified by (14) are also given in Table 2. The energy dependence of the cross section is described by a complicated function since the first term in the expansion offers a good approximation only in the immediate vicinity of the threshold.

Over the resonance region, the theoretical cross sections behave in a conventional way (Fig. 5).

4. CONCLUSION

The characteristic behavior of the differential cross section (15) at small $|t_1|$ (so-called Coulomb peak) makes it possible to isolate the Coulomb production of π mesons against the background of other production mechanisms [11]; the Coulomb production is dominant at $|t_1| < (50\ \text{MeV})^2$. Owing to this, it is possible to study experimentally $K^+\gamma \longrightarrow K^+\pi^0$, $K^0\gamma \longrightarrow K^0\pi^0$, $K^+\gamma \longrightarrow K^0\pi^+$, and $K^0\gamma \longrightarrow K^+\pi^-$. The near-threshold behavior of the first and the second process is determined by the chiral anomaly, but the chiral anomaly does not contribute to the amplitudes of the third and the fourth process. As a consequence, the theoretical cross sections for the first and the second process are 10–100 times larger than the cross sections for the third and the fourth process over the entire near-threshold region. The proposed measurements of the cross sections under consideration may provide a unique source of experimental information about the coefficients of the $KK\pi\gamma$ vertices in Lagrangian (4) and about manifestations of the chiral anomaly in strong and electromagnetic processes involving K mesons. Such measurements would allow us to check the validity of the vector-meson-dominance model [9] in the anomalous sector.

ACKNOWLEDGMENTS

I am grateful to V. F. Obraztsov, Yu. P. Guz, and A. M. Zaĭtsev for stimulating discussions.

REFERENCES

1. E. Witten, Nucl. Phys. B **223**, 422 (1983).
2. L. I. Ametller, in *The Second DAΦNE Physics Handbook*, Ed. by L. Maiani, G. Pancheri, and N. Paver (INFN–LNF, Frascati, 1995), p. 427.
3. S. Rudaz, Phys. Lett. B **145B**, 281 (1984); T. D. Cohen, Phys. Lett. B **233**, 467 (1989).
4. B. R. Holstein, Phys. Rev. D **53**, 4099 (1996); E. P. Venugopal and B. R. Holstein, Phys. Rev. D **57**, 4397 (1998).
5. Y. M. Antipov *et al.*, Phys. Rev. D **36**, 21 (1987).
6. D. V. Amelin *et al.*, Preprint No. 98-62, IFVÉ (Institute of High Energy Physics, Protvino, 1998).
7. G. Ecker, J. Kambor, and D. Wyler, Nucl. Phys. B **394**, 101 (1993); G. Ecker, H. Neufeld, and A. Pich, Nucl. Phys. B **413**, 321 (1994).
8. T. Fujiwara *et al.*, Prog. Theor. Phys. **73**, 926 (1985).
9. M. Bando, T. Kugo, and K. Yamawaki, Phys. Rep. **164**, 217 (1988).
10. J. Bijnens, Int. J. Mod. Phys. A **8**, 3045 (1993).
11. L. G. Landsberg, in *Proceedings of the XXI International Workshop on High Energy Physics and Field Theory, Protvino, 1998*, p. 97.

Translated by R. Rogalyov

Physics of Atomic Nuclei, Vol. 64, No. 1, 2001, pp. 74–83. Translated from Yadernaya Fizika, Vol. 64, No. 1, 2001, pp. 78–87.

ELEMENTARY PARTICLES AND FIELDS
Theory

Asymptotic Behavior of Amplitudes for Longitudinal-Leptoquark Processes and Structure of the Scalar Sector in the Minimal Model Involving Four-Color Symmetry

A. V. Povarov* and A. D. Smirnov**

Yaroslavl State University, ul. Sovetskaya 14, Yaroslavl, 150000 Russia

Received September 7, 1999; in final form, January 24, 2000

Abstract—Within the minimal model based on the four-color symmetry of quarks and leptons of the Pati–Salam type, the asymptotic behavior of amplitudes for processes involving longitudinal leptoquarks (and W or Z' bosons) is investigated, together with the mechanism according to which the growth of these amplitudes at high energies is suppressed by scalar fields. It is shown that, within the Higgs mechanism of mass generation and of the mass splitting of quarks and leptons, the four-color symmetry of quarks and leptons requires that scalar-leptoquark doublets, scalar-gluon doublets, and an extra color-singlet scalar doublet exist in addition to the standard Higgs doublet. © *2001 MAIK "Nauka/Interperiodica"*.

1. INTRODUCTION

Searches for possible versions of new physics beyond the Standard Model (SM) that are induced by higher symmetries (supersymmetry, left–right symmetry, etc.) represent one of the currently popular lines of investigations into elementary-particle physics. Among symmetries possibly existing in nature, there is the four-color symmetry of quarks and leptons that treats leptons as a fourth color [1]. From this symmetry, it follows that there must exist new particles, vector leptoquarks, with masses on the order of the mass scale at which this symmetry is broken. It should be noted that, in models featuring four-color symmetry, it is natural to assume the existence of scalar leptoquarks—such particles were phenomenologically introduced and analyzed in a number of studies (see, for example, [2, 3]). But if the scalar leptoquarks are introduced phenomenologically, it is not clear whether the existence of such particles is an inevitable consequence of four-color symmetry. It would be of interest to clarify the role of the scalar leptoquarks in the theory being discussed and to find out what particles, other than vector leptoquarks, are mandatory in the presence of four-color symmetry.

In this study, we give answers to these questions by investigating the asymptotic behavior of longitudinal-leptoquark amplitudes and by considering suppression of their undesirable growth at high energies by the contributions from new scalar particles. It is well known from [4–6] that the contribution of the longitudinal components of massive gauge fields to the amplitudes for processes involving such fields grows with energy. In the total amplitude, the leading terms cancel out by virtue of the gauge-invariant structure of the interaction, while the remaining growing contributions must be suppressed by the contributions from scalar particles. In the SM, the growth of amplitudes for processes involving longitudinal W and Z bosons is suppressed by the standard Higgs particle. By investigating the asymptotic behavior of amplitudes for longitudinal-leptoquark processes, we show here what scalar particles are required for suppressing the growth of these amplitudes within the minimal model featuring the four-color symmetry of quarks and leptons of the Pati–Salam type if it is the Higgs mechanism that is responsible for mass generation and for the splitting of the quark and lepton masses [7, 8].

2. CONTRIBUTION OF THE GAUGE SECTOR TO THE $\bar{l}_2 Q_2 \longrightarrow VV\bar{V}$ AMPLITUDE

Among extensions of the SM that involve four-color symmetry, the minimal version of four-color quark–lepton symmetry considered here (see [7, 8]) is the most economical one in the number of new gauge fields. It is based on the $SU_V(4) \times SU_L(2) \times U_R(1)$ group as the minimal group that combines the symmetry of the SM and the four-color symmetry of quarks and leptons. Upon a spontaneous breakdown, this group generates, in addition to the SM gauge fields, two triplets $V^{\pm}_{\alpha\mu}$ ($\alpha = 1, 2, 3$) of massive vector leptoquarks with charges of $\pm 2/3$ and an extra massive neutral Z' boson.

The interaction of the vector leptoquarks and of the Z and Z' bosons with the fermions can be described in

* e-mail: povarov@univ.uniyar.ac.ru
** e-mail: asmirnov@univ.uniyar.ac.ru

the model-independent form

$$\mathcal{L}_\Psi^V = \frac{g_4}{\sqrt{2}}(V_{\alpha\mu}J_{\alpha\mu}^V + \text{h.c.}), \tag{1}$$

$$\mathcal{L}_\Psi^{\text{NC}} = -Z_\mu J_\mu^Z - Z'_\mu J_\mu^{Z'}, \tag{2}$$

where

$$\begin{aligned} J_{\alpha\mu}^V &= \bar{Q}_{pa\alpha}\gamma_\mu(g_{aV} + g_{aA}\gamma_5)_{pq}l_{qa}, \\ J_\mu^{Z,Z'} &= \bar{f}_{pa}\gamma_\mu(v_{f_{pa}}^{Z,Z'} + a_{f_{pa}}^{Z,Z'}\gamma_5)f_{pa}. \end{aligned} \tag{3}$$

Here, $f_{pa} = \{Q_{pa\alpha}, l_{pa}\} \equiv \Psi_{paA}$; $A = \alpha, 4$, $\alpha = 1, 2, 3$ being the $SU_c(3)$ color index; $p, q = 1, 2, 3, \ldots$ stand for the generation number; and $a = 1, 2$ is the $SU_L(2)$ index.

Since the basis quark and lepton fields $Q_{pa\alpha}^{'L,R}$ and $l_{pa}^{'L,R}$ can generally be expressed in terms of the physical fields $Q_{pa\alpha}^{L,R}$ and $l_{pa}^{L,R}$ as the superpositions

$$\begin{aligned} Q_{pa\alpha}^{'L,R} &= \sum_q (A_{Q_a}^{L,R})_{pq}Q_{qa\alpha}^{L,R}, \\ l_{pa}^{'L,R} &= \sum_q (A_{l_a}^{L,R})_{pq}l_{qa}^{L,R}, \end{aligned} \tag{4}$$

where $A_{f_a}^{L,R}$ are unitary matrices, the constants g_{aA} and g_{aV} appearing in (3) are matrices in the generation indices.

In addressing the question of what scalar particles are required for implementing spontaneously broken four-color symmetry, we begin by examining the amplitude for the process

$$\bar{l}_{p2}Q_{q2\alpha} \longrightarrow V_\beta V_\gamma \bar{V}_\delta, \tag{5}$$

where l_{p2} and $Q_{q2\alpha}$ are, respectively, the down leptons and quarks of the p and q generations and $\alpha, \beta, \gamma, \delta = 1, 2, 3$ are the $SU_c(3)$ color indices of the quarks and the leptoquarks. The diagrams for this process that are due to the gauge sector are shown in Fig. 1.

With increasing c.m. energy ε of colliding particles, the amplitude for the process in (5) involving transverse gauge bosons decreases in proportion to $1/\varepsilon$. Each of the longitudinal leptoquarks generates an additional power of growth in the energy ε, with the result that nondecreasing terms of the second, the first, and the zeroth order in ε appear in the amplitude featuring three longitudinal leptoquarks. In the total amplitude, the leading second-order terms cancel out, so that the resulting amplitude contains nondecreasing terms of the first and the zeroth order in ε.

According to our calculations, the amplitude for the process in (5) involving three longitudinal leptoquarks

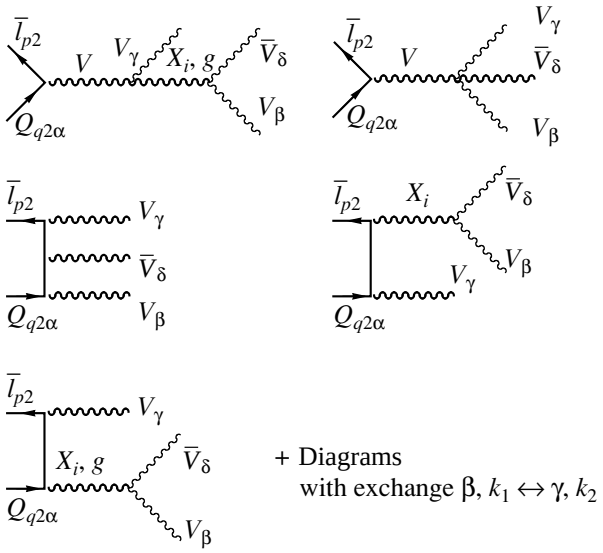

Fig. 1. Diagrams representing the contribution to the amplitude for the process $\bar{l}_{p2}Q_{q2\alpha} \longrightarrow V_\beta V_\gamma \bar{V}_\delta$ from the gauge sector.

is given by

$$\begin{aligned} &M^{(\text{gauge})}(\bar{l}_{p2}Q_{q2\alpha} \longrightarrow V_\beta V_\gamma \bar{V}_\delta) \\ &= (M_0^{(\text{gauge})} + M_\Delta^{(\text{gauge})})\delta_{\alpha\gamma}\delta_{\beta\delta} \\ &+ (\beta, k_1 \leftrightarrow \gamma, k_2) + o(1/\varepsilon), \end{aligned} \tag{6}$$

$$M_{0,\Delta}^{(\text{gauge})} = \frac{g_4^3}{4\sqrt{2}m_V^3}\bar{l}_{p2}(-p_2)(A_{0,\Delta}^{\text{gauge}})_{pq}Q_{q2\alpha}(p_1), \tag{7}$$

$$\begin{aligned} A_0^{\text{gauge}} &= -\frac{1}{p^2}\left[4m_V^2\hat{k}_3 + 2\frac{\sum_i m_{X_i}^2 g_{X_iVV}^2}{g_4^2}(\hat{k}_2 - \hat{k}_3)\right]\overset{+}{g}_{2+} \\ &+ 2\Big[-\hat{k}_3(\overset{+}{g}_{2+}g_{2+} - 1) \\ &+ \left(1 - \frac{m_V^2}{k_2k_3}\right)(\hat{k}_2 - \hat{k}_3)\left(V_{l_{2^+}} + \frac{1}{2}\right)\Big]\overset{+}{g}_{2+} \\ &+ \frac{\hat{k}_2 - \hat{k}_3}{k_2k_3}\frac{\sum_i m_{X_i}^2 g_{X_iVV}(g_{X_iVV}\overset{+}{g}_{2+} + V_{l_{2^+}}^{X_i}\overset{+}{g}_{2+} - \overset{+}{g}_{2+}V_{Q_{2^+}}^{X_i})}{g_4^2} \\ &+ 2\left(\frac{m_V^2}{k_2k_3} - 1\right)(\hat{k}_2 - \hat{k}_3)\overset{+}{g}_{2-}\left(V_{Q_{2^+}} - \frac{1}{6}\right), \end{aligned} \tag{8}$$

$$A_\Delta^{\text{gauge}} = \frac{1}{p^2}\left[4pk_3 + 2\frac{\sum_i m_{X_i}^2 g_{X_iVV}^2}{g_4^2}\frac{p(k_2-k_3)}{m_V^2}\right]\Delta_{2-}$$
$$-\left(\frac{\hat{k}_1}{p_1k_1}+\frac{\hat{k}_2}{p_2k_2}\right)\Delta_{2+}g_{2-}\Delta_{2-} + \frac{1}{p_2k_2}[\hat{k}_3(\Delta_{2-}M_{Q_2}$$
$$+ M_{l_2}\Delta_{2+}) + \hat{k}_2\hat{k}_3\Delta_{2-}](\overset{+}{g}_{2+}g_{2+}-1)$$
$$+\frac{1}{p_1k_1}\left[\left(-\hat{k}_3(\overset{+}{g}_{2+}g_{2+}-1)+(\hat{k}_2-\hat{k}_3)\left(V_{l_2+}+\frac{1}{2}\right)\right)\right. \quad (9)$$
$$\times(\Delta_{2+}M_{Q_2}+M_{l_2}\Delta_{2-}) + \left(-(\hat{k}_2-\hat{k}_3)\hat{k}_1\left(V_{l_2+}+\frac{1}{2}\right)\right.$$
$$\left.\left.+\hat{k}_3\hat{k}_1(\overset{+}{g}_{2+}g_{2+}-1)\right)\Delta_{2-}\right] + \frac{1}{p_2k_1}[(M_{Q_2}^2-M_{l_2}^2)$$
$$\times(\hat{k}_2-\hat{k}_3)\overset{+}{g}_{2-} + \hat{k}_1(\hat{k}_2-\hat{k}_3)\Delta_{2-}]\left(V_{Q_2+}-\frac{1}{6}\right).$$

Here, $\bar{l}_{p2}(-p_2)$ and $Q_{q2\alpha}(p_1)$ are, respectively, the lepton and the quark bispinors; m stands for the masses of the corresponding particles; p_1 and p_2 are, respectively, the antilepton and the quark 4-momenta; $p = p_1 + p_2 = k_1 + k_2 + k_3$; and k_1, k_2, and k_3 and β, γ, and δ are the 4-momenta and the $SU_c(3)$ indices of the vector leptoquarks. The coupling-constant matrices appearing in Eqs. (8) and (9) are expressed in terms of the constants in (3) as

$$(g_{a\pm})_{pq} = (g_{aV} \pm \gamma_5 g_{aA})_{pq},$$
$$(V_{f_{a\pm}}^{X_i})_{pq} = \delta_{pq}(v_{f_{pa}}^{X_i} \pm \gamma_5 a_{f_{pa}}^{X_i}),$$
$$(V_{f_{a\pm}})_{pq} = \delta_{pq}\sum_i g_{X_iVV}(v_{f_{pa}}^{X_i} \pm \gamma_5 a_{f_{pa}}^{X_i})/g_4^2,$$

where g_{X_iVV} is the coupling constant for the interaction of the field $X_i = (A_\mu, Z_\mu, Z'_\mu)$, $i = 1, 2, 3$, with the vector leptoquarks and g_4^2 is the gauge constant of the fourth leptoquark vertex.

The nondecreasing parts of the amplitude in (6) involve two terms, $M_0^{(\text{gauge})}$ and $M_\Delta^{(\text{gauge})}$. Of these, the first is independent of the fermion mass, while the second depends on the quark and lepton masses through the equality

$$\Delta_{a\pm} = \overset{+}{g}_{a\pm}M_{Q_a} - M_{l_a}\overset{+}{g}_{a\mp}, \quad (10)$$

where $(M_{Q_a})_{pq} = m_{Q_{pa}}\delta_{pq}$ and $(M_{l_a})_{pq} = m_{l_{pa}}\delta_{pq}$ are the diagonal quark and lepton mass matrices. In the particular case where the leptoquark current in (3) is of a vector character and is diagonal, expressions (10) are proportional to the difference of the lepton and quark masses. In the minimal model of four-color quark–lepton symmetry, the constants appearing in (8) and (9) can be represented as

$$g_{aV,A} = g_4(K_a^L \pm K_a^R)/2, \quad (11)$$
$$g_{X_iVV} = (2/3)|e|\{1, -t_W(c - s/\sigma), t_W(s + c/\sigma)\}, \quad (12)$$

where g_4 is the $SU_V(4)$ gauge constant; $K_a^{L,R} = (A_{Q_a}^{L,R})^+ A_{l_a}^{L,R}$ are unitary matrices in the generation indices; $t_W = \tan\theta_W$, θ_W being the weak-mixing (Weinberg) angle; $c = \cos\theta$ and $s = \sin\theta$, θ being the $Z - Z'$ mixing angle; and $\sigma = s_W s_s/\sqrt{1 - s_W^2 - s_s^2}$, with $s_{W,s} = \sin\theta_{W,s}$, θ_s being the strong-mixing angle [7, 8].

By taking into account expressions (11) and (12) and the constants in (3), which are determined by the structure of the neutral currents of the minimal model of four-color quark–lepton symmetry [7, 8], we obtain

$$\overset{+}{g}_{a\pm}g_{a\pm} = I, \quad V_{l_a\pm} = -I/2, \quad V_{Q_a\pm} = I/6,$$
$$g_{X_iVV} + V_{l_a\pm}^{X_i} - V_{Q_a\pm}^{X_i} = 0. \quad (13)$$

Simplifying expressions (8) and (9) with the aid of these equalities, we arrive at

$$A_0^{\text{gauge}} = -\frac{1}{p^2}\left[4m_V^2\hat{k}_3 + 2\frac{\sum_i m_{X_i}^2 g_{X_iVV}^2}{g_4^2}(\hat{k}_2-\hat{k}_3)\right]\overset{+}{g}_{2+}, \quad (14)$$

$$A_\Delta^{\text{gauge}} = \frac{1}{p^2}\left[4pk_3 + 2\frac{\sum_i m_{X_i}^2 g_{X_iVV}^2}{g_4^2}\frac{p(k_2-k_3)}{m_V^2}\right]\Delta_{2-} \quad (15)$$
$$-\left(\frac{\hat{k}_1}{p_1k_1}+\frac{\hat{k}_2}{p_2k_2}\right)\Delta_{2+}g_{2-}\Delta_{2-}.$$

3. SCALAR SECTOR AND YUKAWA INTERACTION

The nondecreasing gauge-sector contributions determined by Eqs. (6), (7), (14), and (15) must be suppressed by the relevant contributions from scalar fields responsible for the generation of fermion and gauge-boson masses. Among these fields, there is the SM scalar doublet $\Phi_a^{(\text{SM})}$, $a = 1, 2$. In the presence of four-color symmetry, it can either be an invariant with

respect to the $SU_V(4)$ group or have a more complicated structure.

For the first case, it can be shown that, following a spontaneous breakdown of symmetry, its Yukawa interaction with the $SU_V(4)$-invariant fermion current leads to a relation of the form $\Delta_{a\pm} = 0$ for the quark and lepton masses. With allowance for Eq. (10), this relation means for the general case that the product of the masses of the up (down) leptons is equal to the product of the masses of the corresponding quarks; in the particular case of $K_a^L = K_a^R = I$, this means that the quarks and leptons have equal masses in each generation. However, this is at odds with experimental data both in the former and in the latter case. At first glance, it seems that the quark and lepton masses could be split by introducing, in an ad hoc manner, the $SU_V(4)$-invariant SM doublet $\Phi^{(SM)}$ that involves the 15th component of the fermion scalar current and which violates the $SU_V(4)$ symmetry of the Yukawa coupling; however, the calculations show that, in the asymptotic expression, this gives no way to ensure cancellation of the quark- and lepton-mass-dependent part of the amplitude $M_\Delta^{(\text{gauge})}$. The commonly adopted approach to the generation of the quark and lepton masses assumes that, at large scales, the quarks and leptons have zero or equal masses, but that, at the SM scale, their running masses split, taking values close to the experimental ones. Within this approach, it is necessary, however, to solve a nontrivial problem of ensuring sizable splitting of the quark and lepton masses (by way of example, this splitting is about $m_t = 175$ GeV for the third generation).

An alternative approach was proposed in [7, 8]. It is based on the Higgs mechanism of splitting of the quark and lepton masses. In this approach, the multiplet of the fields $\Phi_{ja}^{(3)}$ ($j = 1, 2, \ldots, 15$) transforming according to the (15, 2, 1) representation of the $SU_V(4) \times SU_L(2) \times U_R(1)$ group is introduced in addition to the $SU_V(4)$-invariant scalar doublet $\Phi_a^{(2)}$ ($a = 1, 2$). The Yukawa coupling of these multiplets to the fermions generates arbitrary quark and lepton masses; as will be shown below, the remaining physical scalar fields ensure suppression of the undesirable growth of the amplitude for the process in (5). In this case, the SM Higgs doublet $\Phi_a^{(SM)}$ has a more complicated structure, appearing to be a superposition of the doublets $\Phi_a^{(2)}$ and $\Phi_{15,a}^{(3)}$. The multiplets $\Phi_A^{(1)}$, $A = 1, 2, 3, 4$, and $\Phi_j^{(4)}$ transforming according to the (4,1,1) and (15,1,0) representations of the $SU_V(4) \times SU_L(2) \times U_R(1)$ group are used to generate vector-leptoquark and Z'-boson masses.

The scalar multiplets of the minimal version of four-color quark–lepton symmetry can be represented in the form

$$(4, 1, 1)\colon \Phi^{(1)} = \begin{pmatrix} S_\alpha^{(1)} \\ \dfrac{\eta_1 + \chi^{(1)} + i\omega^{(1)}}{\sqrt{2}} \end{pmatrix},$$

$$(1, 2, 1)\colon \Phi_a^{(2)} = \delta_{a2}\frac{\eta_2}{\sqrt{2}} + \phi_a^{(2)},$$

$$(15, 2, 1)\colon \Phi_a^{(3)} = \begin{pmatrix} (F_a)_{\alpha\beta} & S_{a\alpha}^{(+)} \\ S_{a\beta}^{(-)} & 0 \end{pmatrix} + \Phi_{15,a}^{(3)} t_{15},$$

$$(15, 1, 0)\colon \Phi^{(4)} = \begin{pmatrix} F_{\alpha\beta}^{(4)} & S_\alpha^{(4)}/\sqrt{2} \\ S_\beta^{*(4)}/\sqrt{2} & 0 \end{pmatrix} + (\eta_4 + \chi^{(4)})t_{15},$$

where $\Phi_{15,a}^{(3)} = \delta_{a2}\eta_3 + \phi_{15,a}^{(3)}$; η_1, η_2, η_3, and η_4 are vacuum expectation values; t_{15} is the 15th generator of the $SU_V(4)$ group; $a = 1, 2$ is the $SU_L(2)$ index; and $\alpha, \beta = 1, 2, 3$ are the $SU_c(3)$ color indices.

The multiplet $\Phi^{(3)}$ contains two doublets of the scalar leptoquarks $S_{a\alpha}^{(\pm)}$ with hypercharges $Y_{S^{(\pm)}}^{(SM)} = 1 \pm 4/3$; eight doublets of the scalar gluons F_{ja}, $j = 1, 2, \ldots, 8$ with $Y^{(SM)} = 1$; and the doublet $\Phi_{15,a}^{(3)}$, which is mixed with the doublet $\Phi_a^{(2)}$, forming the SM doublet $\Phi^{(SM)}$ and an additional doublet Φ':

$$\Phi^{(SM)} = \begin{pmatrix} \Phi_1^{(SM)} \\ \dfrac{\eta + \chi^{(SM)} + i\omega}{\sqrt{2}} \end{pmatrix}, \quad \Phi' = \begin{pmatrix} \Phi_1' \\ \dfrac{\chi' + i\omega'}{\sqrt{2}} \end{pmatrix}.$$

Here, $\eta = \sqrt{\eta_2^2 + \eta_3^2} = (\sqrt{2}\,G_F)^{-1/2} \approx 250$ GeV is the SM vacuum expectation value.

In addition to the SM Goldstone modes $\Phi_1^{(SM)}$ and ω, there are also the Goldstone modes $\omega^{(1)}$ and

$$S_0 = \left[-\frac{\eta_1}{2}S^{(1)} + \sqrt{\frac{2}{3}}\left(\eta_3\frac{S_2^{(+)} + S_2^{*(-)}}{\sqrt{2}} + \eta_4 S^{(4)}\right)\right] \Big/ \sqrt{\frac{\eta_1^2}{4} + \frac{2}{3}(\eta_3^2 + \eta_4^2)}, \tag{16}$$

which are associated with the breakdown of four-color symmetry.

The leptoquark fields entering into S_0 can be represented as a superposition of the Goldstone mode S_0 and

the physical fields S_1, S_2, and S_3 with an electric charge of 2/3 that are orthogonal to S_0 as

$$S_2^{(+)} = \sum_k C_k^{(+)} S_k, \quad \overset{*}{S}{}_2^{(-)} = \sum_k C_k^{(-)} S_k,$$
$$S^{(1)} = \sum_k C_k^{(1)} S_k, \quad S^{(4)} = \sum_k C_k^{(4)} S_k, \tag{17}$$

where $C_k^{(\pm)}$, $C_k^{(1)}$, and $C_k^{(4)}$ ($k = 0, 1, 2, 3$) are elements of the 4×4 unitary matrix of scalar-leptoquark mixing.

In the unitary gauge, the Goldstone modes are eliminated:

$$\Phi_1^{(\mathrm{SM})} = 0, \quad \omega = 0, \quad \omega^{(1)} = 0, \quad S_0 = 0.$$

For physical fields, we then have the SM Higgs field $\chi^{(\mathrm{SM})}$, the extra $SU_c(3)$-color-singlet doublet Φ', two triplets of the up leptoquarks $S_{1\alpha}^{(+)}$ and $S_{1\alpha}^{(-)}$ with electrical charges of 5/3 and 1/3, three scalar leptoquarks $S_{k\alpha}$ ($k = 1, 2, 3$) with an electrical charge of 2/3, eight doublets of the scalar gluons $F_{j,a}$, the octet of the scalar gluons $F_j^{(4)}$, and the $SU_c(3)$ color-singlet fields $\chi^{(1)}$ and $\chi^{(4)}$.

The scalar fields that have the $SU_L(2)$-doublet origin interact with the fermions. The corresponding Yukawa Lagrangian generally has the form [7, 8]

$$\mathscr{L}_\Psi^{\mathrm{Yukawa}} = -\overline{\Psi}{}'^L_{paA}[(h_b)_{pq}\phi_a^{(2)b}\delta_{AB} + (h'_b)_{pq}\phi_{ia}^{(3)b}(t_i)_{AB}]\Psi'^R_{qbB} + \mathrm{h.c.}, \tag{18}$$

where $\Psi'^{L,R}_{paA} = \{Q'^{L,R}_{pa\alpha}, l'^{L,R}_{pa}\}$; $\phi_a^{(2)2} = \Phi_a^{(2)}$; $\phi_a^{(2)1} = \varepsilon_{ac}(\Phi_c^{(2)})^*$; $\phi_{ia}^{(3)2} = \Phi_{ia}^{(3)}$; and $\phi_{ia}^{(3)1} = \varepsilon_{ac}(\Phi_{ic}^{(3)})^*$, $i = 1, 2, \ldots, 15$; t_i stands for the generators of the $SU_V(4)$ group; ε_{ac} is an antisymmetric symbol; and h_b and h'_b are arbitrary matrices.

Following spontaneous symmetry breaking treated with allowance for $\Phi^{(2)}$–$\Phi_{15}^{(3)}$ mixing and diagonalization of the mass matrices by using relation (4), the Lagrangian (18) gives the fermion mass term and the Lagrangian $\mathscr{L}_\Psi^{\mathrm{int}}$ describing the interaction of the fermion and scalar fields in the form

$$\mathscr{L}_\Psi^{\mathrm{int}} = \mathscr{L}_{\chi^{(\mathrm{SM})}ff} + \mathscr{L}_{\Phi' ff} + \mathscr{L}_{FQQ} + \mathscr{L}_{SQl},$$

$$\mathscr{L}_{\chi^{(\mathrm{SM})}ff} = -\frac{\chi^{(\mathrm{SM})}}{\eta}(\bar{Q}_a M_{Q_a} Q_a + \bar{l}_a M_{l_a} l_a),$$

$$\mathscr{L}_{\Phi' ff} = \mathscr{L}_{\chi' ff} + \mathscr{L}_{\omega' ff} + \mathscr{L}_{\Phi'_1 ff},$$

$$\mathscr{L}_{\chi' ff} + \mathscr{L}_{\omega' ff} = \frac{\chi' - i\omega'(\tau_3)_{aa}}{\eta}\frac{1}{2\sin 2\beta}$$

$$\times\{\bar{Q}_a^L[(1-2\cos 2\beta)M_{Q_a} + K_a^L M_{l_a}^+ K_a^R]Q_a^R$$

$$+ \bar{l}_a^L[(-1-2\cos 2\beta)M_{l_a} + 3K_a^{+L} M_{Q_a} K_a^R]l_a^R\} + \mathrm{h.c.},$$

$$\mathscr{L}_{\Phi'_1 ff} = \frac{1}{\sqrt{2}\sin 2\beta}\frac{\Phi'_1}{\eta}\left\{\bar{Q}_1\left[\frac{1-\gamma_5}{2}\right.\right.$$

$$\times((1-2\cos 2\beta)C_Q M_{Q_2} + C_Q K_2^L M_{l_2}^+ K_2^R)$$

$$\left.-\frac{1+\gamma_5}{2}((1-2\cos 2\beta)M_{Q_1} C_Q + K_1^R M_{l_1}^+ K_1^L C_Q)\right]Q_2$$

$$+\bar{l}_1\left[\frac{1-\gamma_5}{2}(-(1+2\cos 2\beta)C_l M_{l_2} + 3C_l^+ K_2^L M_{Q_2} K_2^R)\right.$$

$$\left.+\frac{1+\gamma_5}{2}((1+2\cos 2\beta)M_{l_1} C_l - 3^+ K_1^R M_{Q_1} K_1^L C_l)\right]l_2\Bigg\}$$

$$+\mathrm{h.c.},$$

$$\mathscr{L}_{FQQ} = \mathscr{L}_{F_2Q_1Q_1} + \mathscr{L}_{F_2Q_2Q_2} + \mathscr{L}_{F_1Q_1Q_2},$$

$$\mathscr{L}_{F_2Q_1Q_1} \tag{19}$$

$$= -\sqrt{3}\frac{1}{\eta\sin\beta}\left\{\bar{Q}_{1\alpha}\frac{1+\gamma_5}{2}\overset{+}{M}_1(t_j)_{\alpha\beta}Q_{1\beta}F_{2j} + \mathrm{h.c.}\right\},$$

$$\mathscr{L}_{F_2Q_2Q_2}$$

$$= -\sqrt{3}\frac{1}{\eta\sin\beta}\left\{\bar{Q}_{2\alpha}\frac{1-\gamma_5}{2}M_2(t_j)_{\alpha\beta}Q_{2\beta}F_{2j} + \mathrm{h.c.}\right\},$$

$$\mathscr{L}_{F_1Q_1Q_2} = -\sqrt{3}\frac{1}{\eta\sin\beta}\left\{\bar{Q}_{1\alpha}\left[\frac{1-\gamma_5}{2}C_Q M_2\right.\right.$$

$$\left.\left.-\frac{1+\gamma_5}{2}\overset{+}{M}_1 C_Q\right](t_j)_{\alpha\beta}Q_{2\beta}F_{1j} + \mathrm{h.c.}\right\},$$

$$\mathscr{L}_{SQl} = \mathscr{L}_{SQ_a l_a} + \mathscr{L}_{S_1^{(+)}Q_1 l_2} + \mathscr{L}_{S_1^{(-)}l_1 Q_2},$$

$$\mathscr{L}_{SQ_a l_a} = -\sqrt{\frac{3}{2}}\frac{1}{\eta\sin\beta}\left\{\bar{Q}_{a\alpha}\left[\left(\frac{1-\gamma_5}{2}M_a K_a^R\right.\right.\right.$$

$$\left.+\frac{1+\gamma_5}{2}\overset{+}{M}_a K_a^L\right)\frac{S_{2\alpha}^{(+)} + \overset{*}{S}{}_{2\alpha}^{(-)}}{2} + (\tau_3)_{aa}\left(-\frac{1-\gamma_5}{2}M_a K_a^R\right.$$

$$\left.\left.\left.+\frac{1+\gamma_5}{2}\overset{+}{M}_a K_a^L\right)\frac{S_{2\alpha}^{(+)} - \overset{*}{S}{}_{2\alpha}^{(-)}}{2}\right]l_a + \mathrm{h.c.}\right\},$$

$$\mathcal{L}_{S_1^{(+)}Q_1l_2} = -\sqrt{\frac{3}{2}}\frac{1}{\eta\sin\beta}\left\{\bar{Q}_{1\alpha}\left[\frac{1-\gamma_5}{2}C_Q M_2 K_2^R - \frac{1+\gamma_5}{2}M_1 K_1^L C_l\right] l_2 S_{1\alpha}^{(+)} + \text{h.c.}\right\},$$

$$\mathcal{L}_{S_1^{(-)}l_1Q_2} = -\sqrt{\frac{3}{2}}\frac{1}{\eta\sin\beta}\left\{\bar{l}_1\left[-\frac{1+\gamma_5}{2}K_1^R M_1 C_Q + \frac{1-\gamma_5}{2}C_l K_2^L M_2\right] Q_{2\alpha} S_{1\alpha}^{(-)} + \text{h.c.}\right\},$$

where $M_a = M_{Q_a} - K_a^L M_{l_a} K_a^R$, $(F_a)_{\alpha\beta} = \sqrt{2}\,F_{aj}(t_j)_{\alpha\beta}$, C_Q is the Cabibbo–Kobayashi–Maskawa matrix, C_l is the matrix analogous to it in the lepton sector, and β is the $\Phi^{(2)}$–$\Phi_{15}^{(3)}$ mixing angle ($\tan\beta = \eta_3/\eta_2$).

4. CONTRIBUTION OF THE SCALAR SECTOR TO THE $\bar{l}_2 Q_2 \longrightarrow VV\bar{V}$ AMPLITUDE AND CANCELLATION OF DIVERGENCES

The contribution of the scalar sector to the amplitude for the process in (5) is described by the diagrams in Fig. 2. The expressions for the required three-particle interactions of scalar and gauge fields are presented in the Appendix. By using the notation analogous to that in Eqs. (6) and (7), the contribution of these diagrams can be represented as the sum of the contributions of the individual fields $\chi^{(SM)}$, χ', F_{2j}, and S_k of the doublet origin; that is,

$$A_{0,\Delta}^{\text{scalar}} = A_{0,\Delta}^{\chi^{(SM)}} + A_{0,\Delta}^{\chi'} + A_{0,\Delta}^{F_2} + A_{0,\Delta}^{S}. \tag{20}$$

For the above contributions, our calculations yield

$$A_0^{\chi^{(SM)}} = \frac{1}{g_4^2}\frac{1}{p^2}\left[-2\sum_\chi g_{\chi VV}^2\hat{k}_1 + g_{F^{(4)}VV}^2\left(\frac{\hat{k}_1}{3} - \hat{k}_2\right)\right]\overset{+}{g}_{2+}, \tag{21}$$

$$A_\Delta^{\chi^{(SM)}} = \frac{1}{g_4^2}\left\{\frac{g_{\chi^{(SM)}VV}}{\eta}\left(\frac{\hat{k}_1}{p_2k_1}\Delta_{2+}M_{Q_2} - \frac{\hat{k}_1}{p_1k_1}M_{l_2}\Delta_{2-} - 2\Delta_{2-}\right) + \frac{1}{m_V^2p^2}\left[2\sum_\chi g_{\chi VV}^2 k_1p + g_{F^{(4)}VV}^2\left(-\frac{k_1p}{3} + k_2p\right)\right]\Delta_{2-}\right\}, \tag{22}$$

$$A_0^{\chi'} = -\frac{1}{g_4^2}\frac{1}{p^2}2g_{\chi'VV}^2\hat{k}_1\overset{+}{g}_{2+}, \tag{23}$$

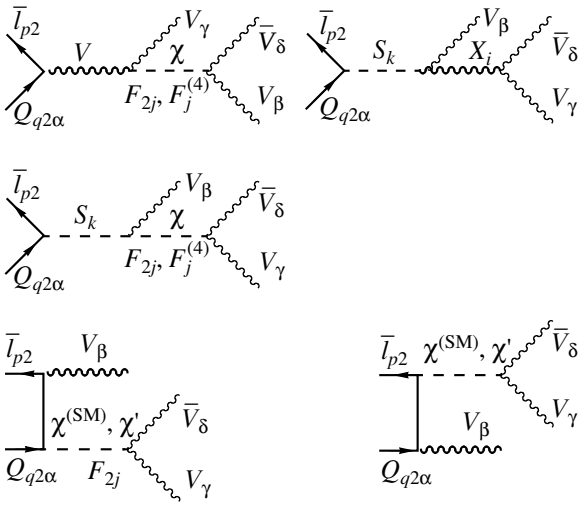

Fig. 2. Diagrams representing the contribution to the amplitude for the process $\bar{l}_{p2}Q_{q2\alpha} \longrightarrow V_\beta V_\gamma \bar{V}_\delta$ from the scalar sector of the model based on the minimal version of four-color quark–lepton symmetry.

$$A_\Delta^{\chi'} = \frac{1}{g_4^2}\left\{-g_{\chi'VV}\frac{\eta}{4\eta_2\eta_3}\left[8\left(1 - \frac{\eta_3^2}{\eta^2}\right)\Delta_{2-} - \frac{\hat{k}_1}{p_1k_1}\left(4\frac{\eta_3^2}{\eta^2}M_{l_2}\Delta_{2-} + 3\Delta_{2+}g_{2-}\Delta_{2-}\right) + \frac{\hat{k}_1}{p_2k_1}\left(4\frac{\eta_3^2}{\eta^2}\Delta_{2+}M_{Q_2} - \Delta_{2+}g_{2-}\Delta_{2-}\right)\right] + 2g_{\chi'VV}^2\frac{1}{m_V^2p^2}k_1p\Delta_{2-}\right\}, \tag{24}$$

$$A_0^{F_2} = \frac{1}{g_4^2}\frac{1}{p^2}g_{F_2^{(1)}VV}^2\left(\frac{\hat{k}_1}{3} - \hat{k}_2\right)\overset{+}{g}_{2+}, \tag{25}$$

$$A_\Delta^{F_2} = \frac{1}{g_4^2}\left\{\frac{g_{F_2^{(1)}VV}}{\eta_3}\sqrt{\frac{3}{2}}\frac{1}{2}\left[-\frac{4}{3}\Delta_{2-} + \left(-\frac{\hat{k}_1}{3p_2k_1} + \frac{\hat{k}_2}{p_2k_2}\right)\Delta_{2+}g_{2-}\Delta_{2-}\right] - \frac{g_{F_2^{(1)}VV}^2}{m_V^2p^2}\left(\frac{k_1p}{3} - k_2p\right)\Delta_{2-}\right\}, \tag{26}$$

$$A_0^S = 0,$$

$$A_\Delta^S = -4\sqrt{\frac{3}{2}}\frac{1}{g_4^3p^2\eta_3}\left\{\sum_k U_{1k}\left[\sum_\chi g_{\chi VV}g_{\chi S_kV}k_1p - \sum_F g_{FVV}g_{FS_kV}\left(-\frac{k_1p}{3} + k_2p\right)\right]\right. \tag{27}$$

$$-\sum_i g_{X_iVV} g_{X_iS_kV} \frac{1}{2}(k_1k_2 - k_1k_3)\Big]\Delta_{2-} \qquad (28)$$
$$+\sum_i g_{X_iVV} g_{X_iS_3V} \frac{1}{2}(k_1k_2 - k_1k_3)$$
$$\times\gamma_5(\overset{+}{g}_{2-}M_{Q_2} - M_{l_2}\overset{+}{g}_{2-})\Big\},$$

where $\chi = \{\chi^{(SM)}, \chi', \chi^{(1)}, \chi^{(4)}\}$ and $F = \{F_2^{(1)}, F^{(4)}, F_2^{(2)}\}$ are the octets of real neutral scalar gluons, $F_2 = (F_2^{(1)} + iF_2^{(2)})/\sqrt{2}$, and $U_{1k} = (C_k^{(+)} + C_k^{(-)})/\sqrt{2}$.

By analyzing the contributions given by Eqs. (21)–(28), we note that the contribution $A_\Delta^{\chi^{(SM)}}$ from the SM Higgs particle $\chi^{(SM)}$ [see Eq. (22)] does not involve second-order terms in $\Delta_{2\pm}$ of the type of the last term in Eq. (15). In the case of quarks and leptons with arbitrary masses, this contribution is insufficient for cancellation of the gauge-sector contribution in the asymptotic region. Second-order terms of this type are contained in the contributions $A_\Delta^{\chi'}$ and $A_\Delta^{F_2}$ from the extra doublet and octet of down scalar gluons [see Eqs. (24) and (26)]. An analysis reveals, however, that these contributions are also insufficient for the aforementioned cancellation; only together with the scalar-leptoquark contribution (28) do these fields ensure the required cancellation of the gauge amplitude.

For the total contribution from the scalar sector to the amplitude for the process in (5), the inclusion of the coupling constants appearing in Eqs. (21)–(28) (see Appendix) does indeed yield

$$A_0^{\text{scalar}} = \frac{1}{p^2}\Big[4g_4^2\hat{k}_3\Big[\frac{\eta_1^2}{4} + \frac{2}{3}(\eta_3^2 + \eta_4^2)\Big] + \frac{g_4^2\eta_1^2}{2}(\hat{k}_2 - \hat{k}_3)\Big]\overset{+}{g}_{2+} + \ldots, \qquad (29)$$

$$A_\Delta^{\text{scalar}} = -\frac{1}{p^2}\Bigg[4pk_3\frac{g_4^2\Big[\frac{\eta_1^2}{4} + \frac{2}{3}(\eta_3^2 + \eta_4^2)\Big]}{m_V^2} + \frac{g_4^2\eta_1^2}{2}\frac{p(k_2 - k_3)}{m_V^2}\Bigg] + \Big(\frac{\hat{k}_1}{p_1k_1} + \frac{\hat{k}_2}{p_2k_2}\Big)\Delta_{2+}g_{2-}\Delta_{2-} \qquad (30)$$
$$+\frac{4}{m_V^2}\Big[g_4^2\Big(\frac{\eta_1^2}{4} + \frac{2}{3}(\eta_3^2 + \eta_4^2)\Big) - m_V^2\Big]\Delta_{2-},$$

where the ellipsis stands for the omitted immaterial terms, whose contribution to the amplitude is of order $1/\varepsilon$.

Taking into account the relations

$$m_V^2 = g_4^2\Big(\frac{\eta_1^2}{4} + \frac{2}{3}(\eta_3^2 + \eta_4^2)\Big),$$
$$\sum_i \frac{m_{X_i}^2 g_{X_iVV}^2}{g_4^2} = \frac{g_4^2\eta_1^2}{4},$$

which are predicted by the model, we can show that the contributions given by (29) and (30) exactly cancel the corresponding contributions (14) and (15) from the gauge sector. For this cancellation to occur, one needs, in addition to the SM Higgs field $\chi^{(SM)}$, the scalar leptoquarks $S_{k\alpha}$ ($k = 1, 2, 3$) with a charge of 2/3; the octet of down scalar gluons F_{2j}; the octet of scalar gluons $F_j^{(4)}$; and the extra fields χ', $\chi^{(1)}$, and $\chi^{(4)}$.

5. AMPLITUDE FOR THE PROCESS $\bar{Q}_1Q_2 \longrightarrow V\bar{V}W$ AND ROLE OF THE UPPER COMPONENTS OF SCALAR DOUBLETS

In order to clarify the role of other scalar fields, it is necessary to consider processes involving longitudinal leptoquarks and W and Z' bosons in the final state. By way of example, we indicate that, in order to reveal the role of the up components of the scalar doublets, it is sufficient to consider the amplitude of the process

$$\bar{Q}_{p1\alpha}Q_{q2\beta} \longrightarrow V_\gamma\bar{V}_\delta W, \qquad (31)$$

where $Q_{p1\alpha}$ and $Q_{q2\beta}$ are the up and down quarks of p and q generations, while α, β, γ, and $\delta = 1, 2, 3$ are the $SU_c(3)$ color indices of the quarks and leptoquarks.

The calculation of the gauge-sector contribution to the color-singlet part of the amplitude for the process in (31) within the minimal version of four-color quark–lepton symmetry yields

$$M^{(\text{gauge})} = \frac{g_4^2g_2\delta_{\gamma\delta}}{4\sqrt{2}m_V^2m_W}\frac{1}{\sqrt{3}} \times\sum_\alpha \bar{Q}_{p1\alpha}(-p_1)(A_0^{\text{gauge}} + A_\Delta^{\text{gauge}})_{pq}Q_{q2\alpha}(p_2) + o(1/\varepsilon), \qquad (32)$$

$$A_0^{\text{gauge}} = 0,$$

$$A_\Delta^{\text{gauge}} = C_Qg_{2-}\Delta_{2-}(1 - \gamma_5) - \overset{+}{\Delta}_{1+}\overset{+}{g}_{1+}C_Q(1 + \gamma_5) + \Big(\frac{\hat{k}_2}{2p_1k_2} + \frac{\hat{k}_3}{2p_2k_3}\Big)\overset{+}{\Delta}_{1-}\overset{+}{C}_l\Delta_{2-}(1 - \gamma_5) - \frac{\hat{k}_2}{2p_1k_2}\overset{+}{\Delta}_{1-}\Delta_{1-}C_Q(1 + \gamma_5) - \frac{\hat{k}_3}{2p_2k_3}C_Q\overset{+}{\Delta}_{2-}\Delta_{2-}(1 + \gamma_5) \qquad (33)$$

$$+\frac{\hat{k}_1}{2p_1k_1}(M_{Q_1}C_Q(1-\gamma_5)-C_QM_{Q_2}(1+\gamma_5))g_{2-}\Delta_{2-}$$

$$+\frac{\hat{k}_1}{2p_2k_1}\overset{+}{\Delta}_{1-}\overset{+}{g}_{1-}(C_QM_{Q_2}(1-\gamma_5)-M_{Q_1}C_Q(1+\gamma_5)),$$

where k_1, k_2, and k_3 are the 4-momenta of the W boson and vector leptoquarks.

The scalar-sector contribution to the amplitude for the process in (31) is described by the diagrams in Fig. 3. In the case of the color-singlet initial state, the above contribution can be represented in the form

$$A_0^{\text{scalar}} = 0, \tag{34}$$

$$\begin{aligned}A_\Delta^{\text{scalar}} &= (2C_Qg_{2-}\Delta_{2-}-C_Q\overset{+}{\Delta}_{2+}\overset{+}{g}_{2+}-g_{1-}\overset{+}{C}_l\Delta_{2-})(1-\gamma_5)\\ &+(\overset{+}{\Delta}_{1+}C_l\overset{+}{g}_{1+}+g_{1-}\Delta_{1-}C_Q-2g_{1-}\Delta_{1-}c_Q)(1+\gamma_5)\\ &-\left(\frac{\hat{k}_2}{2p_1k_2}+\frac{\hat{k}_3}{2p_2k_3}\right)\overset{+}{\Delta}_{1-}\overset{+}{C}_l\Delta_{2-}(1-\gamma_5)\\ &+\frac{\hat{k}_2}{2p_1k_2}\overset{+}{\Delta}_{1-}\Delta_{1-}C_Q(1+\gamma_5)\\ &+\frac{\hat{k}_3}{2p_2k_3}C_Q\overset{+}{\Delta}_{2-}\Delta_{2-}(1+\gamma_5)\end{aligned} \tag{35}$$

$$+\frac{\hat{k}_1}{2p_1k_1}(-M_{Q_1}C_Q(1-\gamma_5)+C_QM_{Q_2}(1+\gamma_5))g_{2-}\Delta_{2-}$$

$$+\frac{\hat{k}_1}{2p_2k_1}g_{1+}\Delta_{1+}(-C_QM_{Q_2}(1-\gamma_5)+M_{Q_1}C_Q(1+\gamma_5))$$

$$-C_Qg_{2-}\Delta_{2-}(1-\gamma_5)+g_{1-}\Delta_{1-}\overset{+}{g}_{1+}C_Q(1+\gamma_5).$$

With allowance for the identities

$$g_{a-}\Delta_{a-}(1\pm\gamma_5) = \overset{+}{\Delta}_{a+}\overset{+}{g}_{a+}(1\pm\gamma_5),$$
$$g_{1\pm}\overset{+}{C}_l = C_Qg_{2\pm},$$

expression (35) exactly cancels the corresponding gauge-sector contribution (33). Appropriate calculations for the color-octet initial state also lead to analogous cancellations in the amplitude for the process in (31).

We note that the diagrams in Fig. 3 involve, in addition to the fields $\chi^{(\text{SM})}$ and χ' and the down gluons F_{2j}, which appear in the diagrams in Fig. 2, the up components of the scalar leptoquarks $S_{1\alpha}^{(\pm)}$, of the scalar gluons F_{1j}, and of the extra doublet Φ_1', whose contributions are necessary for the above cancellations; the contributions of the scalar gluons do not vanish only in the case of the octet initial state.

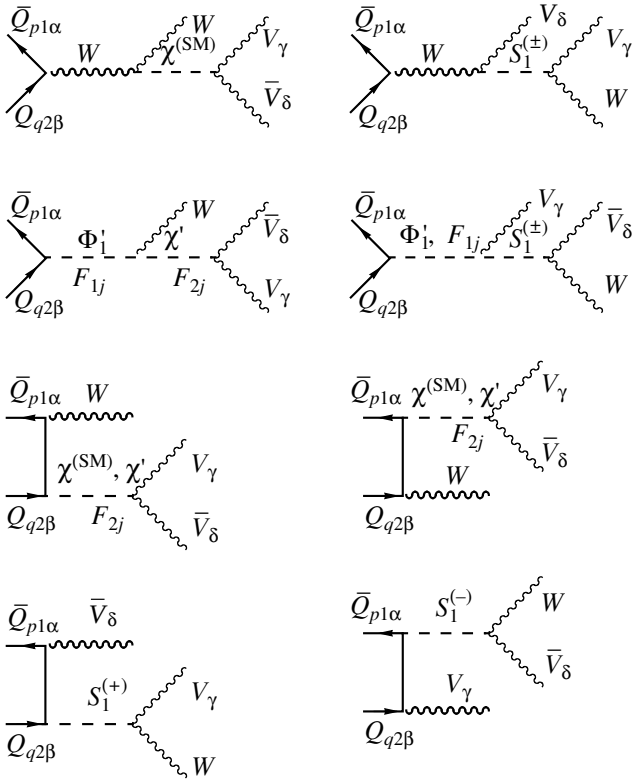

Fig. 3. Diagrams representing the contribution to the amplitude for the process $\bar{Q}_{p1\alpha}Q_{q2\beta} \longrightarrow V_\gamma\bar{V}_\delta W$ from the scalar sector of the model based on the minimal version of four-color quark–lepton symmetry.

Finally, our analysis performed along similar lines for the amplitude of the process

$$\bar{Q}_{p2\alpha}Q_{q2\beta} \longrightarrow V_\gamma\bar{V}_\delta Z' \tag{36}$$

reveals that the imaginary part ω' of the down component of the doublet Φ' is necessary for suppressing the growth of the amplitude for this process.

6. CONCLUSION

In summary, our calculations and analysis of the asymptotic behavior of amplitudes for processes involving longitudinal leptoquarks (and W or Z' bosons) within the minimal four-color-symmetry model have demonstrated that, in addition to the SM doublet $\Phi_a^{(\text{SM})}$, the doublets of scalar leptoquarks $S_{a\alpha}^{(\pm)}$, the doublets of scalar gluons F_{aj} ($j = 1, 2, \ldots, 8$), and an extra color-singlet scalar doublet Φ_a' must inevitably arise in the case of four-color symmetry if the Higgs mechanism is responsible for the generation of quark and gluon masses and for the splittings of these masses. In the presence of mass-split quarks and leptons, the particles listed immediately above are necessary for suppressing the high-energy growth of the longitudi-

nal-leptoquark amplitudes and appear to be some kind of a price that has been paid for the Higgs mechanism of the aforementioned splitting. We note that the couplings of these particles to the fermions are proportional to the ratio of the fermion masses to the SM vacuum expectation value [see Eqs. (19)] and are therefore quite small. At the same time, the scalar leptoquarks and scalar gluons can contribute significantly to the parameters S, T, and U of radiative corrections and can prove to be relatively light [9]. A further investigation of the properties of these particles is of interest in our opinion.

ACKNOWLEDGMENTS

This work was supported in part by the Ministry for Higher Education of the Russian Federation within the program Universities of Russia—Fundamental Research (project no. 1157).

APPENDIX

For the sake of reference, we present here three-particle Lagrangians and the couplings of the gauge fields A_μ, Z_μ, Z'_μ, W_μ, and $V_{\alpha\mu}$ to the scalar fields within the minimal version of four-color quark–lepton symmetry (we have used these Lagrangians and couplings in calculating of the amplitudes for the processes investigated in the present study). We have

$$L_{\chi VV} = g_{\chi VV}\chi\overset{*}{V}_{\alpha\mu}V_{\alpha\mu},$$
$$\chi = \{\chi^{(\mathrm{SM})}, \chi', \chi^{(1)}, \chi^{(4)}\},$$
$$g_{\chi VV} = \left\{\frac{4}{3}g_4^2\eta_3\sin\beta, \frac{4}{3}g_4^2\eta_3\cos\beta, g_4^2\frac{\eta_1}{2}, \frac{4}{3}g_4^2\eta_4\right\}; \quad \text{(A.1)}$$

$$L_{\chi^{(\mathrm{SM})}ZZ} + L_{\chi^{(\mathrm{SM})}Z'Z'} + L_{\chi^{(\mathrm{SM})}ZZ'} = \frac{e^2}{4s_\mathrm{W}^2c_\mathrm{W}^2}\eta\chi^{(\mathrm{SM})}(Z_{1\mu} + \sigma Z_{2\mu})^2, \quad \text{(A.2)}$$

$$L_{\chi^{(1)}Z_2Z_2} = \frac{e^2}{4c_\mathrm{W}^2}(s_\mathrm{W}/\sigma + \sigma/s_\mathrm{W})^2\eta_1\chi^{(1)}Z_{2\mu}Z_{2\mu}, \quad \text{(A.3)}$$
$$Z_{1\mu} = Z_\mu c - Z'_\mu s, \quad Z_{2\mu} = Z_\mu s + Z'_\mu c,$$

where, $c = \cos\theta$ and $s = \sin\theta$, θ being the Z–Z' mixing angle;

$$L_{\chi S_n^{(2/3)}V} = ig_{\chi S_n^{(2/3)}V}[(\chi\partial_\mu\overset{*}{S}{}^{(2/3)}_{n\alpha} - \partial_\mu\chi\overset{*}{S}{}^{(2/3)}_{n\alpha})V_{\alpha\mu} - \text{h.c.}],$$
$$S_{n\alpha}^{(2/3)} = \{S_{2\alpha}^{(+)}, \overset{*}{S}{}_{2\alpha}^{(-)}, S_\alpha^{(1)}, S_\alpha^{(4)}\}, \quad n = 1, 2, 3, 4,$$
$$g_{\chi^{(\mathrm{SM})}S_2^{(+)}V} = g_{\chi^{(\mathrm{SM})}\overset{*}{S}{}_2^{(-)}V} = g_4\sin\beta/\sqrt{3}, \quad \text{(A.4)}$$

$$g_{\chi' S_2^{(+)}V} = g_{\chi'\overset{*}{S}{}_2^{(-)}V} = g_4\cos\beta/\sqrt{3},$$
$$g_{\chi^{(1)}S_2^{(1)}V} = -g_4/2, \quad g_{\chi^{(4)}S^{(4)}V} = \sqrt{2/3}g_4;$$
$$L_{X_i^0S_n^{(2/3)}V} = g_{X_i^0S_n^{(2/3)}V}X_{i\mu}^0(\overset{*}{S}{}_{n\alpha}^{(2/3)}V_{\alpha\mu} + \text{h.c.}),$$
$$g_{X_i^0S_{1,2}^{(2/3)}V} = -\frac{2}{3\sqrt{3}}|e|g_4\eta_3\left\{1, \frac{1}{s_\mathrm{W}c_\mathrm{W}}\left(\mp\frac{3}{2} - s_\mathrm{W}^2\right),\right.$$
$$\left.\frac{1}{s_\mathrm{W}c_\mathrm{W}}\left(\mp\frac{3}{2}\sigma + \frac{s_\mathrm{W}^2}{\sigma}\right)\right\}, \quad \text{(A.5)}$$

$$g_{X_i^0S^{(1)}V} = \frac{1}{3}|e|g_4\eta_1\left\{1, -t_\mathrm{W}, -\frac{t_\mathrm{W}}{2\sigma} - \frac{3}{2}\frac{\sigma}{s_\mathrm{W}c_\mathrm{W}}\right\},$$
$$g_{X_i^0S^{(4)}V} = -\frac{2}{3}\sqrt{2/3}|e|g_4\eta_4\{1, -t_\mathrm{W}, t_\mathrm{W}/\sigma\},$$

where $X_{i\mu}^0 = \{A_\mu, Z_{1\mu}, Z_{2\mu}\}$;

$$L_{X_i^0F_2F_2} = ig_{X_i^0F_2F_2}X_{i\mu}^0(\partial_\mu\overset{*}{F}_{2j}F_{2j} - \text{h.c.}), \quad \text{(A.6)}$$

$$L_{X_i^0\omega'\chi'} = g_{X_i^0\omega'\chi'}X_{i\mu}^0(\partial_\mu\omega'\chi' - \omega'\partial_\mu\chi'), \quad \text{(A.7)}$$

where $g_{X_i^0F_2F_2} = g_{X_i^0\omega'\chi'} = (|e|/2s_\mathrm{W}c_\mathrm{W})\{0, 1, \sigma\}$;

$$L_{FVV} = g_{FVV}F_j\overset{*}{V}_{\alpha\mu}(t_j)_{\alpha\beta}V_{\beta\mu},$$
$$F_j = \{F_{2j}^{(1)}, F_j^{(4)}, F_{2j}^{(2)}\}, \quad j = 1, 2, \ldots, 8, \quad \text{(A.8)}$$
$$g_{FVV} = \{2\sqrt{2/3}g_4^2\eta_3, 2\sqrt{2/3}g_4^2\eta_4, 0\},$$

where $F_{2j} = (F_{2j}^{(1)} + iF_{2j}^{(2)})/\sqrt{2}$;

$$L_{F_1S_1^{(+)}V} = ig_4[(\partial_\mu\overset{*}{S}{}_{1\alpha}^{(+)}F_{1j} - \overset{*}{S}{}_{1\alpha}^{(+)}\partial_\mu F_{1j})(t_j)_{\alpha\beta}V_{\beta\mu} - \text{h.c.}], \quad \text{(A.9)}$$

$$L_{F_1S_1^{(-)}V} = ig_4[(\partial_\mu S_{1\alpha}^{(-)}\overset{*}{F}_{1j} - S_{1\alpha}^{(-)}\partial_\mu\overset{*}{F}_{1j})(t_j)_{\alpha\beta}V_{\beta\mu} - \text{h.c.}], \quad \text{(A.10)}$$

$$\sum_F L_{FS_kV} = i\sum_F g_{FS_kV}[(\partial_\mu\overset{*}{S}_{k\alpha}F_j - \overset{*}{S}_{k\alpha}\partial_\mu F_j)(t_j)_{\alpha\beta}V_{\beta\mu} - \text{h.c.}], \quad \text{(A.11)}$$

where $g_{FS_kV} = \{g_4(\overset{*}{C}{}_k^{(+)} + \overset{*}{C}{}_k^{(-)})/\sqrt{2}, g_4\overset{*}{C}{}_k^{(4)}, ig_4(\overset{*}{C}{}_k^{(+)} - \overset{*}{C}{}_k^{(-)})/\sqrt{2}\}$;

$$L_{W\Phi'_1\chi'} = -ig_2/2[W_\mu^{(+)}(\partial_\mu \overset{*}{\Phi}{}'_1\chi' - \overset{*}{\Phi}{}'_1\partial_\mu\chi') - \text{h.c.}], \quad \text{(A.12)}$$

$$L_{WF_1F_2} = -ig_2/\sqrt{2}[W_\mu^{(+)}(\partial_\mu \overset{*}{F}_{1j}F_{2j} - \overset{*}{F}_{1j}\partial_\mu F_{2j}) - \text{h.c.}], \quad \text{(A.13)}$$

$$L_{WSV} = \sqrt{2/3}g_2g_4\eta_3[(-W_\mu^{(+)*}S_{1\alpha}^{(+)} + \overset{*}{W}{}_\mu^{(+)}S_{1\alpha}^{(-)})V_{\alpha\mu} + \text{h.c.}], \quad \text{(A.14)}$$

$$L_{\Phi'_aS_a^{(+)}V} = i\sqrt{2/3}g_4\cos\beta[(\Phi'_a\partial_\mu \overset{*}{S}{}_{a\alpha}^{(+)} - \partial_\mu\Phi'_a\overset{*}{S}{}_{a\alpha}^{(+)})V_{\alpha\mu} - \text{h.c.}], \quad \text{(A.15)}$$

$$L_{\Phi'_aS_a^{(-)}V} = i\sqrt{2/3}g_4\cos\beta[(\overset{*}{\Phi}{}'_a\partial_\mu S_{a\alpha}^{(-)} - \partial_\mu\overset{*}{\Phi}{}'_aS_{a\alpha}^{(-)})V_{\alpha\mu} - \text{h.c.}]. \quad \text{(A.16)}$$

REFERENCES

1. J. C. Pati and A. Salam, Phys. Rev. D **10**, 275 (1974).
2. W. Buchmüller, R. Rückl, and D. Wyler, Phys. Lett. B **191**, 442 (1987).
3. J. L. Hewett and T. G. Rizzo, Phys. Rev. D **56**, 5709 (1997).
4. E. B. Bogomol'nyĭ, V. I. Zakharov, and L. B. Okun', in *Proceedings of the First School in Physics at the Institute of Theoretical and Experimental Physics* (Atomizdat, Moscow, 1973), p. 49.
5. A. I. Vaĭnshteĭn and I. B. Khriplovich, Yad. Fiz. **13**, 198 (1971) [Sov. J. Nucl. Phys. **13**, 111 (1971)].
6. L. B. Okun, *Leptons and Quarks* (Nauka, Moscow, 1981; North-Holland, Amsterdam, 1984).
7. A. D. Smirnov, Phys. Lett. B **346**, 297 (1995).
8. A. D. Smirnov, Yad. Fiz. **58**, 2252 (1995) [Phys. At. Nucl. **58**, 2137 (1995)].
9. A. D. Smirnov, Phys. Lett. B **431**, 119 (1998).

Translated by A. Isaakyan

Physics of Atomic Nuclei, Vol. 64, No. 1, 2001, pp. 84–97. Translated from Yadernaya Fizika, Vol. 64, No. 1, 2001, pp. 88–100.

ELEMENTARY PARTICLES AND FIELDS
Theory

Koba–Nielsen–Olesen Scaling

A. I. Golokhvastov*
Joint Institute for Nuclear Research, Dubna, Moscow oblast, 141980 Russia
Received July 27, 1999

Abstract—A correct version of Koba–Nielsen–Olesen (KNO) scaling is described in detail for multiplicity distributions. Some statements on the violation of KNO scaling that are based on an erroneous interpretation of experimental data are discussed. An accurate comparison with data is presented for the distributions of negatively charged particles originating from electron–positron annihilation at $\sqrt{s}$ = 3–161 GeV, from inelastic proton–proton collisions at $\sqrt{s}$ = 2.4–62 GeV, and from nucleus–nucleus collisions at p_{lab} = 4.5–520 GeV/c per projectile nucleon. Data on proton–antiproton interactions at $\sqrt{s}$ = 546 GeV are also considered. © *2001 MAIK "Nauka/Interperiodica".*

1. MULTIPLICITY DISTRIBUTIONS

Usually, multiplicity distributions are among the first experimental data obtained at any new accelerator. In an inelastic collision of two primary particles, the multiplicity distribution determines the probability of an event as a function of the number of secondaries of a specific type that are produced in this event; that is, $P_n = \sigma_n/\sigma_{\text{inel}}$, where σ_n is the cross section for the production of n such particles, while $\sigma_{\text{inel}} = \sum_0^\infty \sigma_n$ is the total cross section for the inelastic interaction of primary particles.

Among distributions of this type, those with respect to all charged particles are studied more frequently than others. However, the procedure where charged mesons produced, for example, in proton–proton interactions are added to the number of protons that survived the interaction does not seem natural. But for nucleus–nucleus collisions, where there may occur protons that did not suffer inelastic interaction, such a procedure appears to be still stranger.

Moreover, charge conservation leads to a trivial nonuniformity in such a distribution, say, in electron–positron annihilation, where there is no odd probabilities. At the same time, such probabilities appear in a bounded rapidity (for instance) interval and even may become commensurate with even probabilities, provided that this interval is sufficiently narrow.

In order to circumvent such problems, we will consider the multiplicity distributions of negatively charged hadrons (in practice, π^- mesons, with a small admixture of K^- mesons) in electron–positron annihilation [1–13], as well as in inelastic proton–proton [14–41] and nucleus–nucleus [42–45] interactions. Data for nucleus–nucleus interactions are often presented precisely for negatively charged particles, because it is easier to count them than nuclear fragments.

In interactions of the first two types, the number of all charged particles in an event, n_{ch}, is unambiguously related to the corresponding number of negatively charged particles, n_{neg}; that is,

$$n_{\text{ch}} = 2n_{\text{neg}} \quad \text{for } e^+e^- \text{ and } n_{\text{ch}} = 2n_{\text{neg}} + 2 \quad \text{for } pp. \quad (1)$$

In the following, the number of negatively charged particles is denoted merely by n.

2. ASYMPTOTIC KOBA–NIELSEN–OLESEN SCALING

On the basis of some physical considerations Koba–Nielsen–Olesen (KNO) formulated the statement that the shape of the multiplicity distribution is independent of primary energy (KNO scaling) [46]. Earlier, Polyakov drew the same conclusion from different considerations [47]. In contrast to the statement itself, its theoretical grounds were not confirmed by experimental data, so that KNO scaling remained an empirical fact.

Figure 1 illustrates the meaning of this statement, which was formulated for very high energies. Since such energies correspond to very high multiplicities, the multiplicity distributions appear as continuous functions in this case. Figure 1*a* shows the possible shapes of these functions for various primary energies. The area under each curve is equal to unity since it represents the sum of all probabilities: $\int P_n dn = \sum P_n = 1$. The mean multiplicity $\langle n \rangle = \sum nP_n = \int nP_n dn$ grows with energy. Each curve can be contracted linearly along the horizontal direction in proportion to some of its horizontal dimensions—for example, the mean value $\langle n \rangle$ (as in Fig. 1*b*), the most probable value, or the FWHM—and extended along the vertical direc-

* e-mail: golokhv@lhe17.jinr.dubna.su

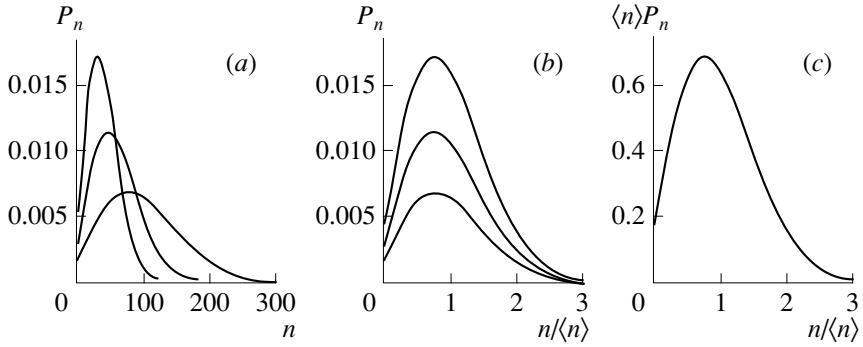

Fig. 1. Definition of the concept of similarity of continuous functions (KNO scaling). Normalized functions (*a*) are similar if upon a linear contraction of each of them along the horizontal direction in proportion to some of its horizontal dimensions—for example, $\langle n\rangle$ (*b*)—and a linear extension along the vertical direction in the same proportion (*c*) they coincide at each point.

tion in the same proportion for the area under the curve to remain eventually unchanged (Fig. 1*c*). The KNO scaling then states that the curves will coincide at each point [48]; that is,

$$\langle n\rangle P_n = \Psi\left(\frac{n}{\langle n\rangle}\right), \tag{2}$$

where $\Psi(z)$ is a function that is independent of energy and which is normalized by the conditions

$$\int_0^\infty \Psi(z)dz = 1 \quad \text{and} \quad \int_0^\infty z\Psi(z)dz = 1. \tag{3}$$

The first equality in (3) follows from the fact that the sum of all probabilities is unity, while the second results from the contraction of the functions P_n to the extent that the mean value of each of these reduces to unity. Equation (2) imposes no constraints on the form of the function $\Psi(z)$, with the exception of those in (3)—it merely represents the concept of similarity for continuous normalized functions.

In Eq. (2), the scale parameter $\langle n\rangle$ can be replaced by any other quantity that is linear in n and which characterizes the horizontal dimension of the function P_n—for example, the square root of the variance (standard deviation), $D_2 \equiv [\sum(n - \langle n\rangle)^2 P_n]^{1/2}$; a different central moment raised to the corresponding power, $D_q \equiv [\sum(n - \langle n\rangle)^q P_n]^{1/q}$; or the absolute moment $\langle n^q\rangle^{1/q} \equiv (\sum n^q P_n)^{1/q}$. All of these vary with energy in proportion to one another, provided that the asymptotic KNO scaling $\langle n\rangle \propto \langle n^q\rangle^{1/q} \propto D_q$ holds [see Eqs. (10) and (11) below].

The scaling relation in (2) is a particular case of a weaker symmetry for which the identity of the distribution shapes is verified only upon bringing both the mean values and the widths in coincidence (by making a shift along the horizontal direction and by changing the scale in proportion to D_2, respectively) [49]:

$$P_n = \frac{1}{D_2} F\left(\frac{n - \langle n\rangle}{D_2}\right). \tag{4}$$

The scaling relation in (4) can also be represented in the form [50]

$$P_n = \frac{1}{\langle n\rangle - \alpha(\sqrt{s})} f\left(\frac{n - \alpha(\sqrt{s})}{\langle n\rangle - \alpha(\sqrt{s})}\right) \tag{5}$$

(here, α is an energy-dependent quantity) by means of the substitution $\alpha \equiv \langle n\rangle - \eta D_2$, where η = const.

In contrast to the KNO scaling that is specified by Eq. (2) and which involves only one free parameter dependent on energy (for example, $\langle n\rangle$), the scaling specified by Eq. (4) or Eq. (5) has two free parameters that are independent of each other and which are functions of energy (for example, $\langle n\rangle$ and D_2). In this sense, the latter resembles the approximation of multiplicity distributions by a binomial distribution [51, 52], which also involves two such parameters.

3. INTRINSIC CONTRADICTION

At currently available accelerator energies, the quantity P_n cannot be considered as a continuous function: by way of example, we indicate that, in proton–proton interactions, $\langle n\rangle \sim 2$ at $p_{\text{lab}} = 100$ GeV/c and $\langle n\rangle \sim 5$ and 13 at $\sqrt{s}$ = 60 and 546 GeV, respectively. In this case, Eq. (2) is intrinsically contradictory, irrespective of its physical substantiation—mathematically, it is inconsistent with the normalization condition $\sum_0^\infty P_n = 1$ [53].

This contradiction becomes obvious when we inspect closely the data in Fig. 2*a*. According to Eq. (2), the operation inverse to that depicted in Fig. 1 must be implemented in order to obtain some multiplicity distribution for a given $\langle n\rangle$ from the continuous universal function $\Psi(z)$ in Fig. 2*a*; that is, it is necessary to choose the scale $z_0 = 1/\langle n\rangle$ along the z axis, in which case the probability P_n will be equal to the area of a

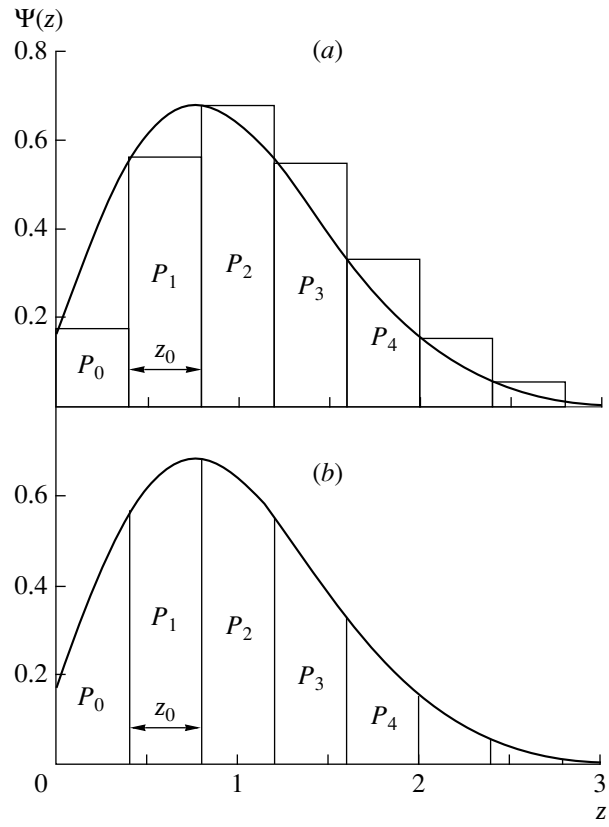

Fig. 2. Derivation of a discrete multiplicity distribution from a continuous normalized universal function $\Psi(z)$ according to (*a*) the recipe $P_n = 1/\langle n\rangle \cdot \Psi(n/\langle n\rangle)$ (in this case, the sum of the areas of the rectangles is not equal to the area under the curve; that is, $\sum P_n \neq 1$) and (*b*) the correct recipe [in this case, the probability P_n is equal to the area under the curve in the interval between nz_0 and $(n+1)z_0$]; here, $\sum P_n = 1$, but $z_0 \neq 1/\langle n\rangle$.

rectangle whose upper vertex lies on the curve $\Psi(z)$ at the point $z = nz_0 = n/\langle n\rangle$. The height of this rectangle is $\langle n\rangle P_n$, while its base is $1/\langle n\rangle$.

For $z_0 \longrightarrow 0$ ($\langle n\rangle \longrightarrow \infty$), the sum of the areas of all rectangles (total probability), the area under the curve, is equal to unity. This sum cannot remain unchanged, however, with increasing z_0 (that is, with decreasing energy). A numerical integration becomes overly crude in this case. The distribution in Fig. 2*a* approximately corresponds to 100 GeV/*c* in proton–proton interactions. The distribution of all charged particles has the same shape, apart from a change in the notation for partial probabilities according to Eq. (1): $P_0 \longrightarrow P_2$, $P_1 \longrightarrow P_4$, etc.

A change in the normalization of the function $\Psi(z)$ would involve introducing an energy dependence in $\Psi(z)$ with the result that the input hypothesis would be abandoned. Of course, KNO scaling was formulated as an approximate regularity; however, it is desirable to establish the extent to which it holds. For this, one has either to treat it accurately or to quantify the distortions introduced by incorrectness of the mathematical procedure used.

Thus, it is necessary to define similarity of discrete functions prior to experimentally testing the hypothesis of similarity of multiplicity distributions. The concept of similarity must be intrinsically consistent for $\langle n\rangle \sim 1$ and must correspond to the asymptotic form in (2) for $\langle n\rangle \longrightarrow \infty$.

4. CORRECT KNO SCALING

A possible procedure for correctly deducing various multiplicity distributions from one universal function $\Psi(z)$ is illustrated in Fig. 2*b*, where the probability P_n is equal to the area under the curve in the interval of width z_0. It can be seen that the sum of the probabilities is always obtained to be equal to unity and that, for $z_0 \longrightarrow 0$, Fig. 2*a* coincides with Fig. 2*b*. This statement can be represented as [53]

$$P_n = \int_{nz_0}^{(n+1)z_0} \Psi(z)dz. \qquad (6)$$

The normalization conditions in (3) for the function $\Psi(z)$ remain in force, but $\langle n\rangle$ is not equal to $1/z_0$ here; it can be obtained in this case only from the multiplicity distribution, in just the same way as other statistical moments.

From Fig. 2*b*, it follows that, knowing the experimental multiplicity distribution at some energy value, one can deduce the relevant distribution at the energy value corresponding to z_0' twice as great as z_0, the neighboring areas being summed in this case: $P_n' = P_{2n} + P_{2n+1}$. The same procedure can be repeated for $z_0'' = 3z_0$: $P_n'' = P_{3n} + P_{3n+1} + P_{3n+2}$, etc. In Figs. 3 and 4, the points obtained in this way from ISR data [40] are compared with data at lower energies. It can be seen that they agree down to the lowest energies.

For the sake of comparison, we note that the equalities $P_n' = 2P_{2n}$, $P_n'' = 3P_{3n}$, etc., follow from Eq. (2). In this case, we generally have $\sum P_n' \neq 1$ and $\sum P_n'' \neq 1$.

We further recast Eq. (6) into an alternative form by introducing the continuous parameter $m \equiv z/z_0$, which fills gaps on the discrete axis n in Fig. 1*a* and which should have been introduced prior to deriving Eq. (2) in order to avoid integration with respect to the discrete parameter n [53]:

$$P_n = \int_n^{n+1} P(m)dm, \qquad (7)$$

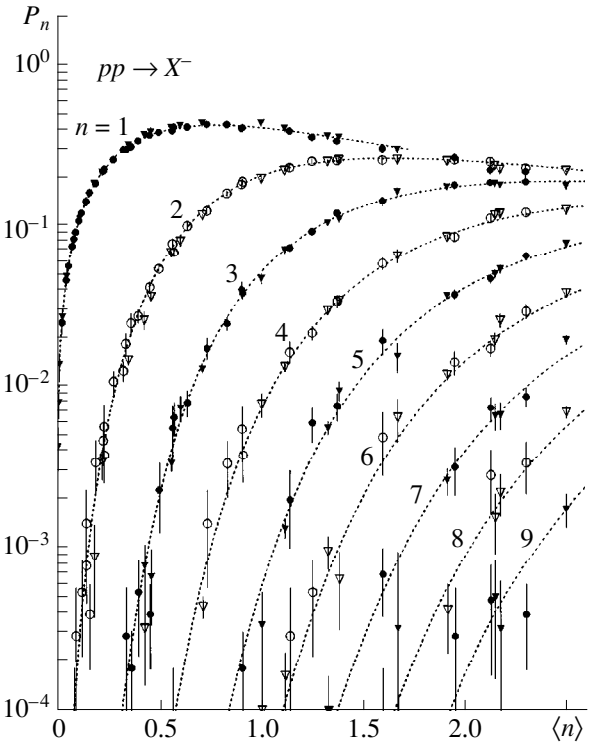

Fig. 3. Experimental multiplicity distributions of negatively charged particles, along with theoretical ones computed on the basis of distributions obtained experimentally at higher energies by using the equations $P_n^{'} = P_{2n} + P_{2n+1}$, $P_n^{''} = P_{3n} + P_{3n+1} + P_{3n+2}$, etc.—see Fig. 2*b*. The curves were calculated by formula (6) for the functions $\Psi^{pp}(z)$ given by Eqs. (19) and (20) (visually, they are indistinguishable). Closed and open inverted triangles represent experimental data at energies in the range 1.7–147 GeV/*c*, while closed and open circles illustrate results computed on the basis of ISR data.

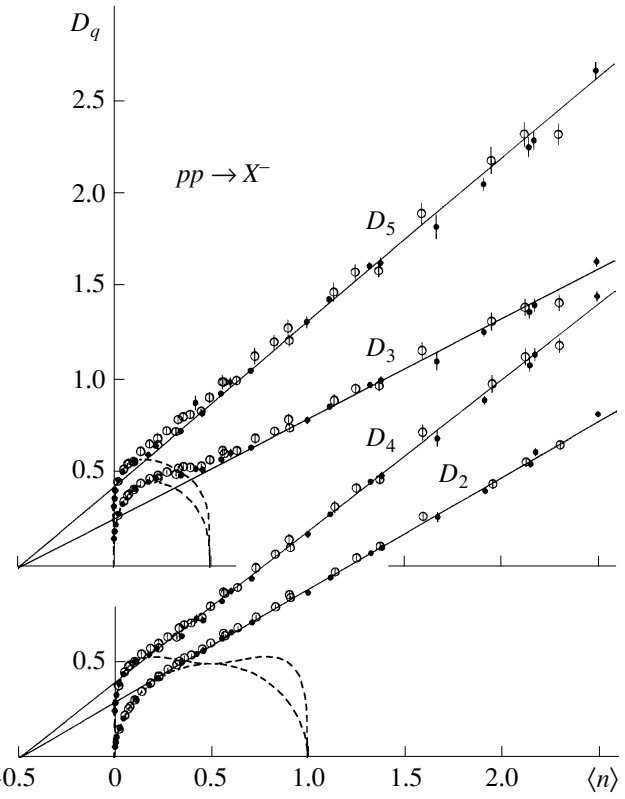

Fig. 4. Central moments $D_q \equiv (\sum (n - \langle n \rangle)^q P_n)^{1/q}$ as functions of $\langle n \rangle$. Even and odd moments are offset by unity. The Wróblewski straight lines specified by Eq. (14) are presented in the figure. Dashed curves show lower bounds on D_q (at a given $\langle n \rangle$ value, the quantity D_q attains a minimum when only two neighboring probabilities P_n do not vanish [54]). Closed circles represent experimental data at energies in the range 1.7–147 GeV/*c*, while open circles illustrate results computed on the basis of ISR data.

$$P(m) \equiv \frac{1}{\langle m \rangle} \Psi\left(\frac{m}{\langle m \rangle}\right), \quad \langle m \rangle \equiv \int_0^\infty m P(m) dm = 1/z_0. \quad (8)$$

Thus, the discrete distribution P_n can be represented in the form of a histogram of the continuous KNO-invariant function $P(m)$.

Within this formulation, the concept of similarity retains its former meaning; that is, it refers to continuous functions exclusively. Here, only the procedure changes according to which we obtain discrete multiplicity distributions from them. Instead of the intrinsically contradictory prescription that we actually used in Eq. (2), we now have at our disposal the correct prescription (7):

$$P_n = P(m)|_{m=n}. \quad (9)$$

The continuous KNO-invariant function $P(m)$ possesses simple properties, which were previously assigned to the discrete function P_n, but that led to confusing results. The absolute and central statistical moments of the function $P(m)$ are proportional to its mean value $\langle m \rangle$ raised to the corresponding power ($z \equiv m/\langle m \rangle$):

$$\frac{\langle m^q \rangle}{\langle m \rangle^q} \equiv \frac{1}{\langle m \rangle^q} \int_{-\infty}^{\infty} m^q P(m) dm = \int_{-\infty}^{\infty} z^q \Psi(z) dz = \text{const}, \quad (10)$$

$$\frac{\mu_q}{\langle m \rangle^q} \equiv \int_{-\infty}^{\infty} \frac{(m - \langle m \rangle)^q}{\langle m \rangle^q} P(m) dm = \int_{-\infty}^{\infty} (z-1)^q \Psi(z) dz = \text{const}. \quad (11)$$

In order to obtain multiplicity distributions, Parry and Rotelli [55, 56] used a formula close to that in Eq. (7). A physical model of such histogramming was considered in [55].

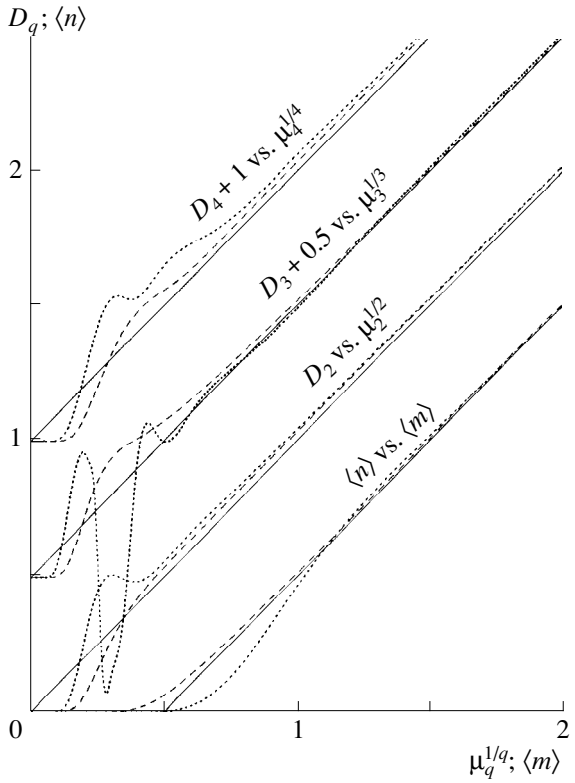

Fig. 5. Various parameters of the discrete function P_n versus the corresponding parameters of the continuous function $P(m)$ for the approximations of $\Psi(z)$ that describe (dotted curves) electron–positron annihilation according to Eqs. (18) and (20) and (dashed curve) proton–proton interactions according to Eqs. (19) and (20). Solid straight lines correspond to the approximate formulas (12) and (13). The values of D_3 and D_4 are shifted upward by 0.5 and 1, respectively.

5. APPROXIMATE IMPLICATIONS

At not overly small $\langle n\rangle$, we find from Eqs. (7) and (8) that

$$\begin{aligned}\langle m\rangle &= \int_0^\infty mP(m)dm = \sum_n \int_n^{n+1} mP(m)dm \\ &\approx \sum_n (n+0.5)\int_n^{n+1} P(m)dm \\ &= \sum_n (n+0.5)P_n = \langle n\rangle + 0.5,\end{aligned} \tag{12}$$

a result that can also be observed by inspecting Fig. 2*b* more closely—the center of gravity of each P_n bin occurs approximately at $z = (n + 0.5)z_0$ rather than at $z = nz_0$ [57].

For the approximations of $\Psi(z)$ that are shown in Fig. 6 and which describe electron–positron annihilation and proton–proton interactions, Fig. 5 (lower curves) shows the precise $\langle m\rangle$ dependences of $\langle n\rangle$ that were obtained on the basis of Eqs. (7) and (8). It can be seen that, for proton–proton interactions, the approximation in (12) holds quite accurately from $\langle n\rangle \sim 0.2$, which corresponds to $p_{\text{lab}} \sim 4$ GeV/c.

An approximate relation between the central moments of a continuous and a discrete function is still simpler, since the additional term 0.5 in n and $\langle n\rangle$ cancels out, so that we have

$$\begin{aligned}\mu_q &= \sum_n \int_n^{n+1} (m - \langle m\rangle)^q P(m)dm \\ &\approx \sum_n (n - \langle n\rangle)^q \int_n^{n+1} P(m)dm = D_q^q\end{aligned} \tag{13}$$

(see Fig. 5). Therefore, the strict proportionality relation $\mu_q^{1/q} \propto \langle m\rangle$ for the functions $P(m)$ (11) leads to an approximate formula for P_n [58, 59]:

$$D_q \propto (\langle n\rangle + 0.5). \tag{14}$$

Upon going over to all charged particles according to relation (1) for proton–proton interactions, we arrive at empirical Wróblewski straight lines [60, 61]:

$$D_q^{\text{ch}} \propto (\langle n_{\text{ch}}\rangle - 1). \tag{15}$$

In Fig. 4, these straight lines are presented according to Eq. (14). When the correct formula (6) was not known, it was believed that these straight lines are indicative of a violation of KNO scaling, since they do not go through the origin of coordinates.

From Eqs. (7), (8), and (12), we also approximately have [58]

$$P_n \approx P(m)|_{m = n + 0.5} \approx \frac{1}{\langle n\rangle + 0.5}\Psi\left(\frac{n + 0.5}{\langle n\rangle + 0.5}\right). \tag{16}$$

For electron–positron annihilation and proton–proton interactions, Fig. 6 shows examples of distributions with respect to these coordinates. Upon going over to all charged particles according to relation (1) for proton–proton interactions, it follows from (16) that, in this case, there arises improved KNO scaling that assumes the form

$$P_{n_{\text{ch}}} = \frac{1}{\langle n_{\text{ch}}\rangle - 1}\Psi\left(\frac{n_{\text{ch}} - 1}{\langle n_{\text{ch}}\rangle - 1}\right) \tag{17}$$

and which was proposed in [60, 61].

For all charged particles in electron–positron annihilation, the relations that are obtained from (14), (16), and (1) differ from (15) and (17) only by the reversal of all minus signs.

6. ELECTRON–POSITRON ANNIHILATION AND PROTON–PROTON INTERACTIONS

Figures 7 and 8 display the ratios $(\langle n\rangle + 0.5)/D_2$ and D_q/D_2 for electron–positron annihilation at $\sqrt{s}$ = 3–161 GeV and for proton–proton interactions at $\sqrt{s}$ =

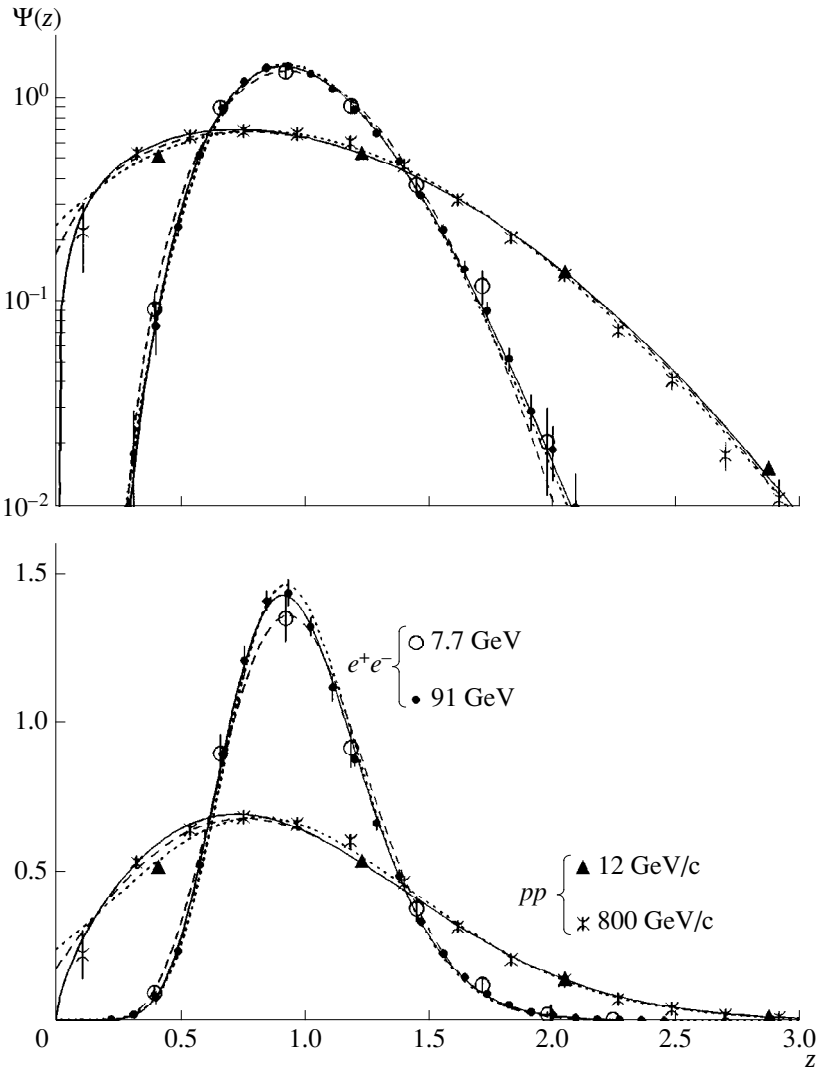

Fig. 6. Examples of multiplicity distributions of negatively charged particles from electron–positron annihilation and proton–proton interactions (on a logarithmic and on a linear scale). The distributions are plotted here in the coordinates $z = (n + 0.5)/(\langle n\rangle + 0.5)$ and $\Psi = (\langle n\rangle + 0.5)P_n$ of the improved KNO scaling (16). The solid, dashed, and dotted curves represent, respectively, the functions Ψ_1 [as given by Eq. (18) for electron–positron annihilation and by Eq. (19) for proton–proton interactions], Ψ_2 [as given by Eq. (18) for electron–positron annihilation and by Eq. (19) for proton–proton interactions], and Ψ_3 [as given by Eq. (20) both for electron–positron annihilation and for proton–proton interactions].

2.4–62 GeV (p_{lab} = 2–2000 GeV/c), as well as for proton–antiproton interactions at $\sqrt{s}$ = 546 GeV. From Eq. (14), it follows that, in contrast to the moments C_q (see below), these quantities must fast approach a plateau with increasing energy.

In mathematical statistics, the quantity D_2^2 is referred to as a variance, while $(D_3/D_2)^3$ and $[(D_4/D_2)^4 - 3]$ are called a skewness and a kurtosis [62], respectively. In the physics of multiparticle production, these quantities are usually used without relevant powers.

The curves in Figs. 7 and 8 were computed on the basis of Eq. (6) by using the functions $\Psi(z)$ represented in Fig. 6. For electron–positron annihilation, the first two functions are given by (see [6, 11] and [59, 63], respectively)

$$\Psi_1^{ee}(z) = a_1 z^{c_1}\exp(-b_1 z);$$
$$\Psi_2^{ee}(z) = a_2(z-c_2)^3\exp[-b_2(z-c_2)^2] \quad (18)$$

[for $z < c_2$, we have $\Psi_2^{ee}(z) \equiv 0$]. The free parameters were set to c_1 = 11 and c_2 = 0.2, while the results obtained for the coefficients from the normalization conditions (3) are a_1 = 223 367, $b_1 = c_1 + 1 = 12$, a_2 = 15.2, and b_2 = 2.76.

For proton–proton interactions, the analogous functions are (see [64] and [58, 59, 61, 65], respectively)

$$\Psi_1^{pp}(z) = a_1 z^{c_1}\exp(-b_1 z^2),$$
$$\Psi_2^{pp}(z) = a_2(z+c_2)\exp[-b_2(z+c_2)^2], \quad (19)$$

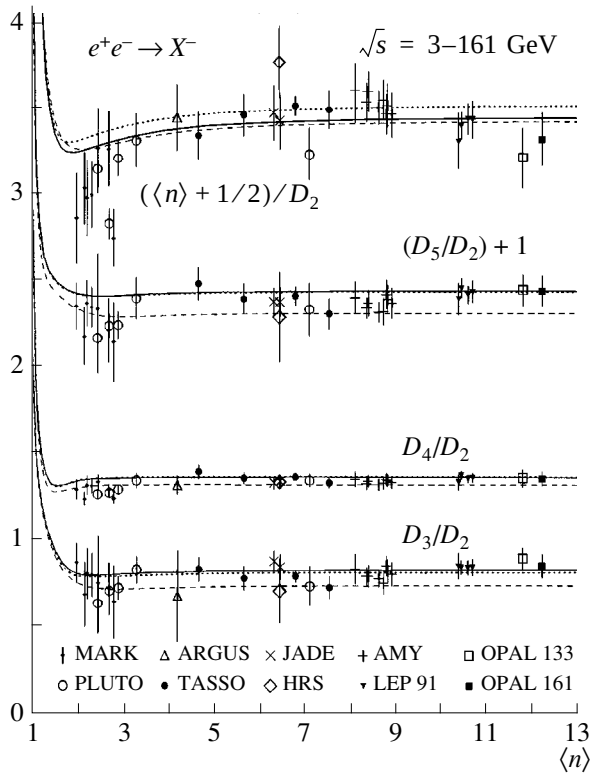

Fig. 7. Ratios of the moments of the multiplicity distributions of negatively charged particles from electron–positron annihilation ($D_q \equiv [\sum(n - \langle n\rangle)^q P_n)]^{1/q}$). The quantity D_5/D_2 is shifted upward by unity. The displayed curves were computed on the basis of the improved KNO scaling specified by Eq. (6). In these calculations, use was made of the approximations Ψ_1^{ee} (18), Ψ_2^{ee} (18), and Ψ_3^{ee} (20) (the results are depicted by, respectively, solid, dashed, and dotted curves), and the probability P_0 was set to zero (since it was not measured experimentally).

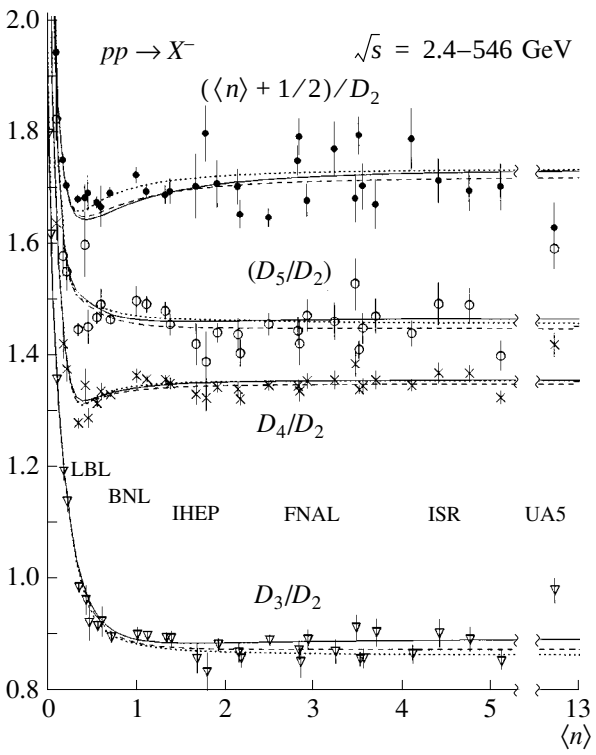

Fig. 8. Ratios of the moments of the multiplicity distributions of negatively charged particles from proton–proton interactions ($D_q \equiv [\sum(n - \langle n\rangle)^q P_n)]^{1/q}$). The displayed curves were computed on the basis of the improved KNO scaling specified by Eq. (6). In these calculations, use was made of the approximations Ψ_1^{pp} (19), Ψ_2^{pp} (19), and Ψ_3^{pp} (20) (the results are depicted by, respectively, solid, dashed, and dotted curves).

where $c_1 = 0.66$ and $c_2 = 0.14$ and where the values that the normalization conditions (3) yield for the relevant coefficients are $a_1 = 1.19$, $b_1 = 0.62$, $a_2 = 1.25$, and $b_2 = 0.62$.

The third function $\Psi(z)$ has the same form both for electron–positron annihilation and for proton–proton interactions [66, 67]:

$$\Psi_3(z) = \frac{N}{\sqrt{2\pi}\sigma}\frac{1}{z+c}\exp\left(-\frac{[\ln(z+c)-\mu]^2}{2\sigma^2}\right). \quad (20)$$

Of the four parameters appearing in (20), c, μ, N, and σ, two are free, while the remaining two are related by the conditions in (3). Specifically, we have $N = 1$, $\mu = 0.43$, $\sigma = 0.18$, and $c = 0.56$ for electron–positron annihilation and $N = 1.06$, $\mu = 1.638$, $\sigma = 0.121$, and $c = 4.25$ for proton–proton interactions [67].

We emphasize that, in contrast to the energy-dependent parameters from Section 2, all the parameters that were presented immediately above and which determine the specific form of the function $\Psi(z)$ have no bearing on the statement of KNO scaling.

Despite the significant distinctions between the analytic expressions for the functions $\Psi_{1,2,3}$, all three groups of curves in Fig. 7 (and in Fig. 8 as well) are quite close. They are also close in Figs. 9 and 10, which display the normalized moments $C_q \equiv \langle n^q\rangle/\langle n\rangle^q$ for the same data. The quantities C_q do not reach a plateau even at the ISR energy. From Eq. (16), it can be seen that the moments $\langle(n + 0.5)^q\rangle/\langle n + 0.5\rangle^q$ could approach a plateau sufficiently fast.

In computing our curves for electron–positron annihilation, the quantity P_0 was set to zero, since it has not yet been measured in experiments (the remaining P_n were normalized to unity), but this is of importance only at the lowest energies. As a result, the moments C_q fall sharply in Fig. 9 for $\langle n\rangle \longrightarrow 1$. Apart from this, the curves for electron–positron annihilation (Figs. 7, 9) behave in just the same way as those for proton–proton interactions, no distinctions other than those in magni-

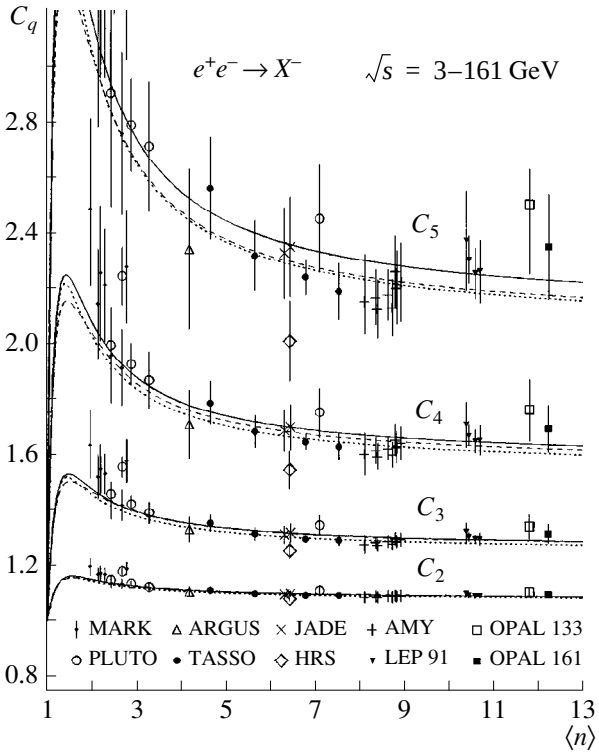

Fig. 9. Normalized moments of the multiplicity distributions of negatively charged particles from electron–positron annihilation ($C_q \equiv \langle n^q \rangle / \langle n \rangle^q$, where $\langle n^q \rangle \equiv \sum n^q P_n$). The displayed curves were computed on the basis of the improved KNO scaling specified by Eq. (6). In these calculations, use was made of the approximations Ψ_1^{ee} (18), Ψ_2^{ee} (18), and Ψ_3^{ee} (20) (the results are depicted by, respectively, solid, dashed, and dotted curves), and the probability P_0 was set to zero (since it was not measured experimentally). The latter leads to a dip on the curves when $\langle n \rangle \longrightarrow 1$.

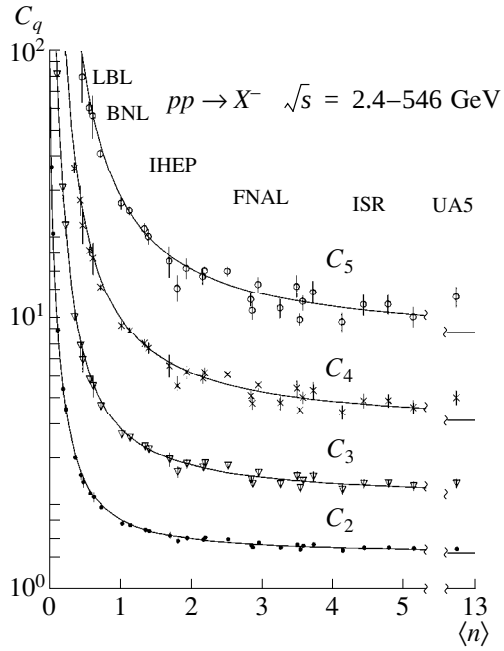

Fig. 10. Normalized moments of the multiplicity distributions of negatively charged particles from proton–proton interactions ($C_q \equiv \langle n^q \rangle / \langle n \rangle^q$, where $\langle n^q \rangle \equiv \sum n^q P_n$). The displayed curves were computed on the basis of the improved KNO scaling specified by Eq. (6). In these calculations, use was made of the functions $\Psi^{pp}(z)$ given by (19) and (20) (visually, the corresponding curves are indistinguishable).

tude being observed. This behavior is determined by histogramming in Eqs. (6) and (7), but it is independent of the specific form of the function $\Psi(z)$.

Usually, various approximations of the function $\Psi(z)$ have no physical validation (see, however, [68, 69])—at least, their interpretation has nothing to do with histogramming in Eqs. (6) and (7). However, the use of these approximations makes it possible to see how the experimental points must behave if the correct KNO scaling holds.

7. S$\bar{p}p$S DATA

The S$\bar{p}p$S [41] points (data from the UA5 experiment at $\sqrt{s}$ = 546 GeV) in Figs. 8 and 10 were obtained via the same transition from all charged particles to negatively charged particles [which is specified in Eqs. (1)] as in the case of proton–proton interactions—that is, under the assumption that, at each multiplicity value, the number of leading protons and antiprotons in proton–antiproton interactions is equal, on average, to the number of protons in proton–proton interactions.

It can be seen from Eqs. (1) that, in electron–positron annihilation, the normalized moments for all charged particles, $C_q^{\mathrm{ch}} \equiv \langle n_{\mathrm{ch}}^q \rangle / \langle n_{\mathrm{ch}} \rangle^q$, are equal to the corresponding moments for negatively charged particles. In proton–proton interactions, there is no such equality because of the shift of two in Eq. (1). Figure 11 displays these moments for proton–proton interactions. The curves were computed by using the distributions of all charged particles as obtained according to Eq. (1). These distributions in turn were rescaled from the distributions obtained for negatively charged particles on the basis of the same functions $\Psi(z)$ given by Eqs. (19) and (20). From a comparison of the curves in Figs. 10 and 11, it can be seen that they do not reach a plateau even at the S$\bar{p}p$S energy (at sufficiently high energies, the moments C_q must coincide with C_q^{ch}).

The data in Figs. 8, 10, and 11 exhibit evidence for a violation of KNO scaling in the UA5 experiment—experimental points do not lie on the curve. At the same time, these figures show points that occur off the curve beyond a greater number of standard deviations than the UA5 points do—for example, these are data from [32] at p_{lab} = 147 GeV/c ($\langle n \rangle \simeq 2.5$, $\langle n_{\mathrm{ch}} \rangle \simeq 7$). Fre-

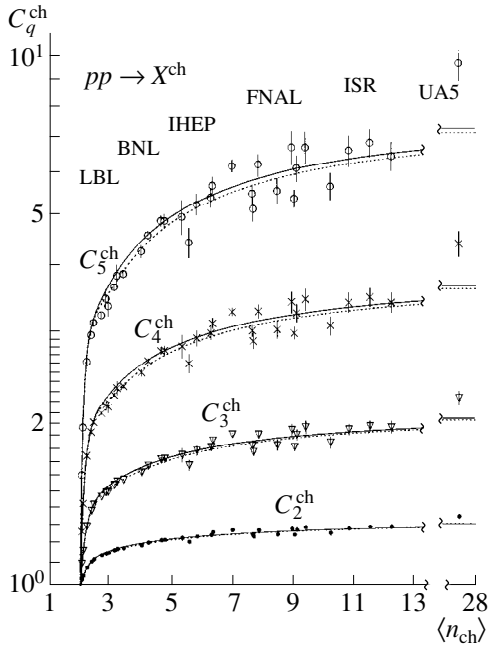

Fig. 11. Normalized moments of the multiplicity distributions of all charged particles in proton–proton interactions ($C_q^{ch} \equiv \langle n_{ch}^q \rangle / \langle n_{ch} \rangle^q$, where $\langle n_{ch}^q \rangle \equiv \sum n_{ch}^q P_{n_{ch}}$). The displayed curves were computed by relying on the improved KNO scaling specified by Eq. (6) for the distributions of negatively charged particles and by implementing a subsequent transition to all charged particles according to Eq. (1). The functions Ψ^{pp} given by (19) and (20) were substituted into Eq. (6) (visually, the resulting curves are virtually indistinguishable).

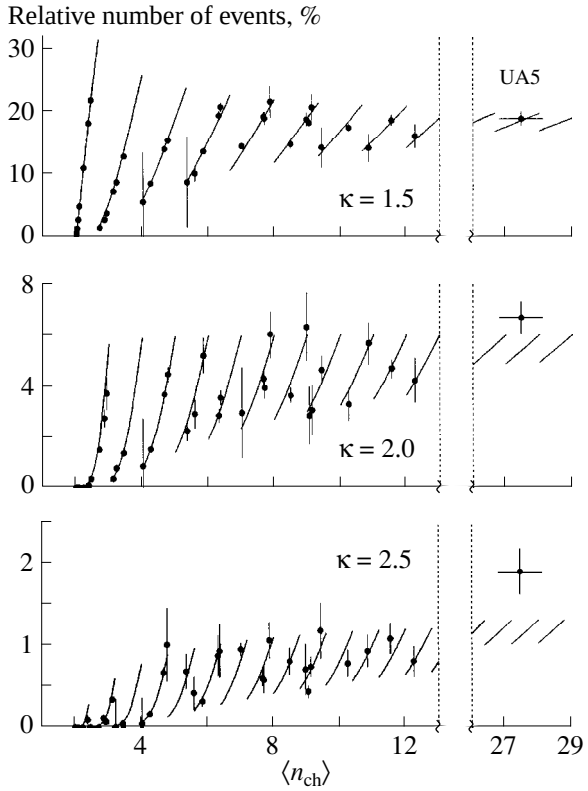

Fig. 12. Percentage of events where the multiplicity of charged particles exceeds the mean multiplicity by a preset factor ($\kappa = 1.5, 2.0, 2.5$). The curves were computed by relying on the improved KNO scaling specified by Eq. (6) for the distributions of negatively charged particles and by subsequently performing a transition to all charged particles according to Eq. (1). The functions Ψ^{pp} given by Eqs. (19) and (20) were substituted into Eq. (6) (visually, the resulting curves are indistinguishable). As the mean multiplicity of all charged particles, $\langle n_{ch} \rangle$, becomes greater, the curve in question undergoes discontinuities when the current multiplicity falls below $\kappa \langle n_{ch} \rangle$.

quently, graphs illustrating invariability of the moments C_q^{ch} up to the ISR energy and their sharp growth at the $S\bar{p}pS$ energies (see Fig. 11), which is associated with a violation of KNO scaling, are plotted precisely from this energy.

In Fig. 10, however, which is actually equivalent to Fig. 11, the UA5 points lie even below the points at 147 GeV/*c* (and below the majority of the remaining points). As a matter of fact, a violation of the correct KNO scaling for negatively charged particles is suggested here exclusively by the occurrence of the points off the curves.

Figure 12 shows the percentage of events whose multiplicity exceeds the mean multiplicity by a preset factor ($\kappa = 1.5, 2.0, 2.5$) [41]. Of course, the relevant curve representing the above percentage cannot be as smooth as that in [41]. The discontinuities correspond to those points at which, as $\langle n_{ch} \rangle$ is increased, the quantity $\kappa \langle n_{ch} \rangle$ becomes greater than a current even integer since one more partial probability $P_{n_{ch}}$ drops out of the percentage in question [59].

It should be emphasized that only the partial cross sections for inelastic proton–proton interactions are meant here. Multiplicity distributions in non-single-diffraction interactions not involving events having some specific topology—for example, events where all charged particles are emitted into the same hemisphere (in the c.m. frame) or events characterized by a low multiplicity and by the presence of an energetic leading charged particle—are discussed quite often. It is the impossibility to introduce similar experimental criteria at different energies (rather than the arbitrariness of such criteria at a given energy value) that generates poorly controllable uncertainties.

8. NUCLEUS–NUCLEUS INTERACTIONS

As a rule, multiplicity distributions in elementary-particle distributions are normalized to an inelastic cross section—that is, the cross section for the production of at least one new particle ($P_n = \sigma_n/\sigma_{inel}$). In the case of a normalization to the total cross section, which includes the elastic-scattering cross section, there

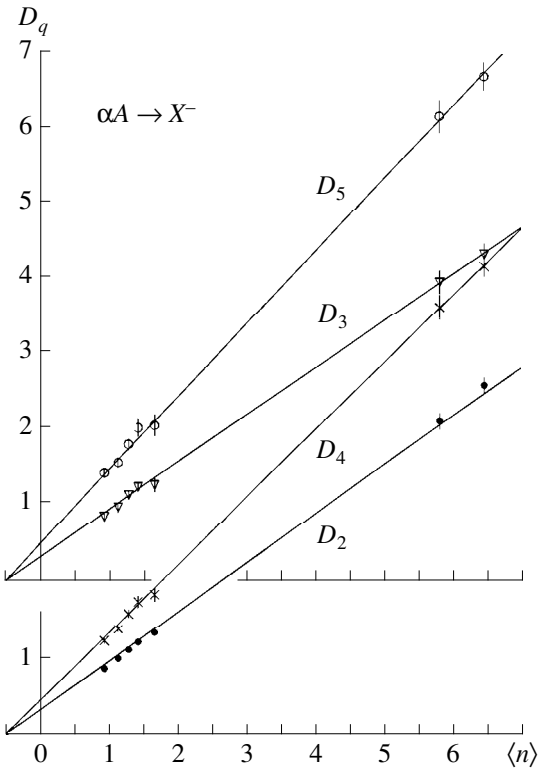

Fig. 13. Moments $D_q \equiv (\sum (n - \langle n \rangle)^q P_n)^{1/q}$ as functions of $\langle n \rangle$ for the multiplicity distributions of negatively charged particles in αα interactions at $\sqrt{s}$ = 26 and 31 GeV per nucleon and in αLi^6, αC, αNe, and αCu interactions at p_{lab} = 4.5 GeV/c per nucleon. The Wróblewski straight lines, $D_q \propto (\langle n \rangle + 0.5)$, are drawn through the points. The even and odd moments are offset by two units.

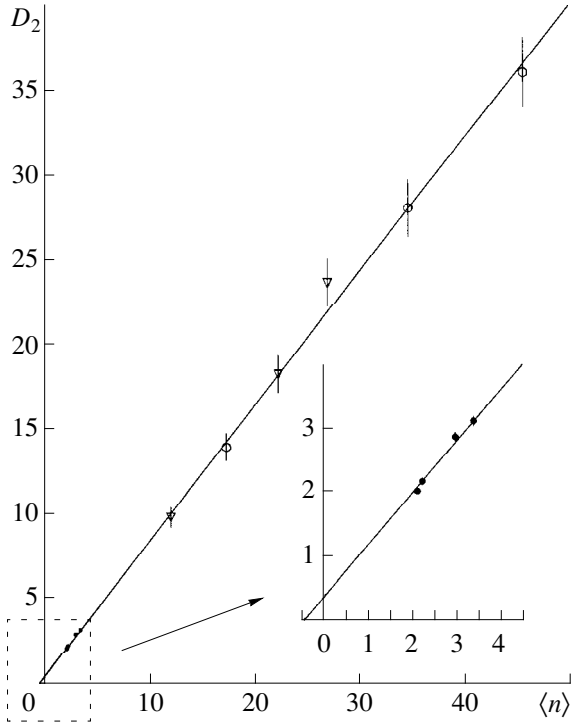

Fig. 14. Moment $D_2 \equiv (\sum (n - \langle n \rangle)^2 P_n)^{1/2}$ as a function of $\langle n \rangle$ for the multiplicity distributions of negatively charged particles in ONe, OCu, and OAu interactions at (▽) 60 and (○) 200 GeV per nucleon and in CNe, CSi, CCu, and CZr interactions at (●) 3.7 GeV/c per nucleon. A part of the figure close to the origin of coordinates is shown in the inset on an enlarged scale. The Wróblewski straight line, $D_2 \propto (\langle n \rangle + 0.5)$ (14), is drawn through the points.

would arise a peak in the zeroth bin (P_0). With increasing energy, this peak would grow in relation to the remaining bins because the fraction of elastic-scattering cross section is virtually independent of energy and because the inelastic-scattering cross section is distributed over an ever increasing number of channels that correspond different multiplicity values—that is to say, it is not necessary, in the case of such a normalization, to verify the hypothesis of the scaling of distributions. In comparing a complete theory with experimental data, it makes no difference what distribution is used, but the theory of soft processes in strong interactions has yet to be developed.

In nucleus–nucleus reactions, one could use various cross sections for a normalization—for example, the meson-production cross section σ_{pr}; the reaction cross section σ_{re}, which includes σ_{pr} and the cross section for the quasielastic breakup of nuclei; and the inelastic-scattering cross section σ_{inel}, which includes σ_{re} and the cross section for nuclear excitation. For the distributions of negatively charged particles, they differ only by the presence of the cross section σ_0. On the basis of the same considerations on the absences of an enhance-

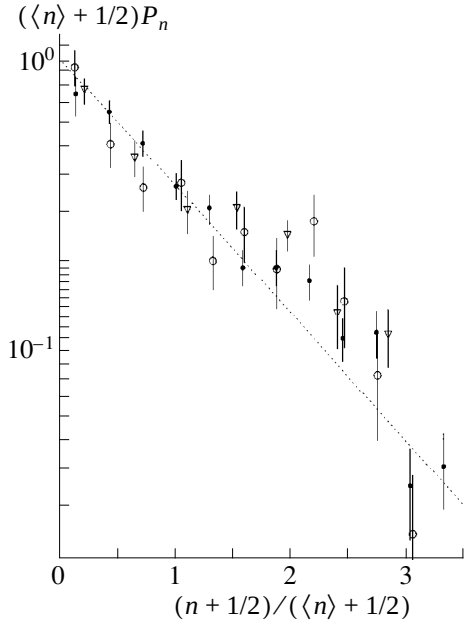

Fig. 15. Multiplicity distributions in (●) CCu interactions at 3.7 GeV per nucleon and in OCu interactions at (▽) 60 and (○) 200 GeV per nucleon in the coordinates of the improved KNO scaling specified by Eq. (16). It can be seen that these distributions have very similar shapes. The dotted line corresponds to $\Psi(z) = \exp(-z)$.

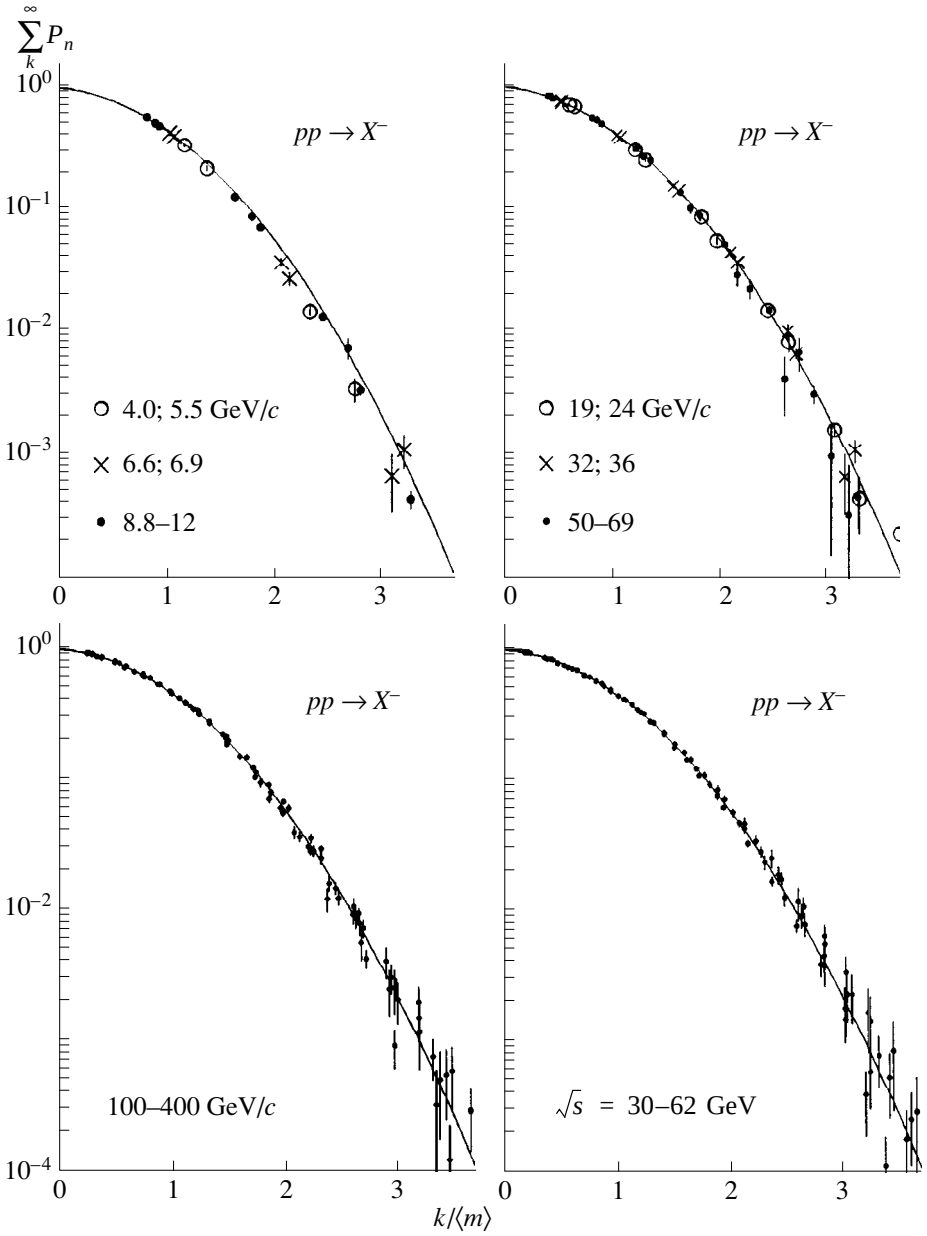

Fig. 16. Integrated multiplicity distributions of negatively charged particles, $\sum_k^\infty P_n$, in proton–proton interactions at various energy values versus $k/\langle m \rangle$ [see Eq. (21)]. The approximate formula $\langle m \rangle = \langle n \rangle + 0.5$ (12) is used to determine the mean value $\langle m \rangle$. The curves for $\Phi(z)$ were computed on the basis of the approximations $\Psi^{pp}(z)$ given by (19) and (20) (visually, the resulting curves are indistinguishable).

ment in the zeroth channel, it would be natural to normalize multiplicity distributions in nucleus–nucleus reactions to σ_{pr} [42].

For alpha-particle interactions with various nuclei at an alpha-particle momentum of 4.5 GeV/c per nucleon (which corresponds to the kinetic energy of 3.7 GeV per nucleon [42]), D_q as a function of $\langle n \rangle$ for the case of normalization to σ_{pr} is displayed in Fig. 13, along with data on $\alpha\alpha$ interactions at c.m. energies of 26.3 and 31.2 GeV per nucleon (the corresponding energies of one alpha particle in the rest frame of the second alpha particle are 370 and 520 GeV per nucleon [44]). The points are well consistent with the Wróblewski straight lines $D_q \propto (\langle n \rangle + 0.5)$, confirming once again that expression (14) is more fundamental than expression (15). We note that, in contrast to what occurs in proton–proton interactions and in electron–positron annihilation, there is no unambiguous relation between these expressions in nucleus–nucleus interactions. At an energy of 3.7 GeV per nucleon, targets are not lighter than ^{6}Li, but it can be seen from the figure that all the points pre-

sented here lie on straight lines—that is, the shape of the multiplicity distributions depends only slightly on the target nucleus in the present case [42].

Data on the interactions of carbon nuclei of energy 3.7 GeV per nucleon with various nuclei [43] are given in Fig. 14, along with oxygen-nucleus data at energies 60 and 200 GeV per nucleon [45]. It can be seen that all points lie on the same straight line. The same points at 3.7 GeV per nucleon, along with the same Wróblewski straight line, which intersects, as in Fig. 13, the abscissa at the point $\langle n\rangle = -0.5$, in perfect agreement with Eq. (14), are shown in the inset on an enlarged scale.

In the coordinates of the improved KNO scaling (16), Fig. 15 illustrates a direct comparison of the multiplicity distributions in CCu collisions at 3.7 GeV per nucleon and OCu collisions at 60 and 200 GeV per nucleon. The shapes of the distributions are seen to agree within the errors. This shape differs markedly from the shape of the corresponding distributions in electron–positron annihilation and proton–proton interactions (Fig. 6).

9. INTEGRAL REPRESENTATION

Equation (7) can be represented in the integral form

$$\sum_{n=k}^{\infty} P_n = \int_k^{\infty} P(m)\,dm = \int_{k/\langle m\rangle}^{\infty} \Psi\left(\frac{m}{\langle m\rangle}\right) d\left(\frac{m}{\langle m\rangle}\right) = \Phi\left(\frac{k}{\langle m\rangle}\right). \quad (21)$$

A similar accumulated (integrated) probability is often used in statistics instead of its discrete and contentious derivatives given by the functions P_n and $P(m)$ [62] (see also [64]).

The integrated probability $\Phi(k/\langle m\rangle)$ is related to the function $\Psi(z)$ by the equation

$$\Phi(z) = \int_z^{\infty} \Psi(z)\,dz \quad \text{or} \quad \Psi(z) = -\frac{d}{dz}\Phi(z) \quad (22)$$

and satisfies the conditions $\Phi(0) = 1$ and $\int_0^{\infty} \Phi(z)dz = 1$, which follow from (3) [58]. It should be noted that the function $\Phi(z)$ defined by Eqs. (21) and (22) coincides with that in [53, 57], but it differs in sign from that in [58].

The probabilities P_n are calculated from $\Phi(z)$ in a simpler way than from $\Psi(z)$ in (6):

$$P_n = \Phi(nz_0) - \Phi(nz_0 + z_0). \quad (23)$$

Since the quantity $\sum_k^{\infty} P_n$ in (21) is a function of only one variable $k/\langle m\rangle$ [57], the multiplicity distributions at different energies can be associated with one curve representing $\Phi(z)$. Figure 16 shows data on proton–proton interactions in terms of these coordinates. The approximation specified by Eq. (12) is used for $\langle m\rangle$. The $\Phi(z)$ curves correspond to the functions $\Psi^{pp}(z)$ in Eqs. (19) and (20) (visually, they are indistinguishable).

At very low energies, where only P_0 and P_1 do not vanish, scaling formulated correctly must hold automatically—in the case being discussed, points lie exactly on the curve, irrespective of the form of the function $\Psi(z)$ used. This is clear from the fact that $\langle n\rangle \equiv P_1$ in the present case—that is the distribution is specified entirely by one value $\langle n\rangle$. These points are not shown in the figure.

10. CONCLUSION

A comparison of the predictions of correct KNO scaling (also known as KNO-G scaling) with experimental data was performed in [11, 66] (e^+e^-), [67] (e^+e^-, pp), [34, 58] (π^+p, K^+p, pp), [70, 71] (νA, $\bar{\nu}A$, μA), [72] (e^+p), and [73] (AA) as well. It has no theoretical validation at present, but there are many models that predict asymptotic KNO scaling.

To conclude, we note that the recipe in Eq. (6) for deducing discrete multiplicity distributions from a continuous probability function is far from new. If the function $\Psi(z) = \exp(-z)$ (see Fig. 15) is substituted into Eq. (6), we arrive at

$$P_n = \int_{nz_0}^{(n+1)z_0} e^{-z}dz = (1 - e^{-z_0})e^{-nz_0} \left[= \frac{\langle n\rangle^n}{(\langle n\rangle + 1)^{n+1}}\right]. \quad (24)$$

It is the procedure that was used by Planck [74] in quantizing a continuous Maxwell probability distribution ($z = E/kT$, $z_0 = h\nu/kT$) in one of the formulations of a quantum hypothesis in order to obtain the spectrum of heat radiation. Here, P_n is the multiplicity distribution of thermal photons of frequency ν.

The result in (24) expressed in terms of $\langle n\rangle = \sum nP_n = [\exp(z_0) - 1]^{-1}$ (bracketed expression), a Bose–Einstein distribution, is often used to derive a negative binomial distribution in order to describe multiplicity distributions [51, 52].

In alternative formulations of the heat-radiation problem, a Boltzmann spectrum is usually quantized by means of the recipe specified by Eq. (9): $P_n' = P(m)|_{m=n} \propto \exp(-E/kT)$, where $E = nh\nu$; after that, the quantities P_n' are normalized to unity: $P_n = \exp(-nh\nu/kT)/\sum \exp(-nh\nu/kT$. Nonetheless, the result coincides with that in (24) because, for $\Psi(z) = \exp(-z)$—and only for this function—the ratio $P_n/P(m)$ is independent of n at $m = n$.

The mean number of photons (phonons) of frequency ν in the Planck spectrum, $\langle n\rangle = [\exp(z_0) - 1]^{-1} = [\exp(h\nu/kT) - 1]^{-1}$, at large $\langle n\rangle$ values is related to the corresponding mean value of the Boltzmann spectrum, $\langle m\rangle = 1/z_0 = kT/h\nu$, by the same approximate equality $\langle m\rangle \approx \langle n\rangle + 0.5$ (12), which is independent of the form of the function $\Psi(z)$. The dependence at small $\langle n\rangle$ values, which is analogous to that represented by the lower curves in Fig. 5, can be found, for example, in [75].

Irrespective of its physical substantiation in [74], the mathematical procedure specified by Eq. (24) follows from the Born–Kramers quantization rule [76, 77] (see also [78]), a general principle that was formulated just on the eve of the advent of quantum mechanics and which provides a recipe for obtaining discrete quantum-mechanical quantities from the corresponding continuous classical quantities. Using the notation adopted here, taking into account the sign in the present definition (22) of the function $\Phi(z)$, and considering that, in our case, the index n is already reserved for other purposes, we can formulate this principle as follows: a discrete quantity P_l associated with the quantum states l and $l + \tau$ is $P_l = \Phi(l) - \Phi(l + \tau)$ [see Eq. (23)], where $\Phi(z)$ is obtained from the equality $-\tau[\partial\Phi(z)/\partial z] = \tau\Psi(z) = P(m)$ [see Eqs. (8) and (22)], with $P(m)$ being a classical analog of the quantum quantity P_l [76, 77].

REFERENCES

1. 3–7 GeV: J. L. Siegrist *et al.*, Phys. Rev. D **26**, 969 (1982) (references [1–13] contain data on electron–positron annihilation).
2. 3.6–44 GeV: W. Braunschweig *et al.*, Z. Phys. C **45**, 193 (1989).
3. 5–31 GeV: M. Althoff *et al.*, Z. Phys. C **22**, 307 (1984).
4. 10 GeV: H. Albrecht *et al.*, Z. Phys. C **54**, 13 (1992).
5. 12–35 GeV: W. Bartel *et al.*, Z. Phys. C **20**, 187 (1983).
6. 29 GeV: M. Derrick *et al.*, Phys. Rev. D **34**, 3304 (1986).
7. 52–61 GeV: H. W. Zheng *et al.*, Phys. Rev. D **42**, 737 (1990).
8. 91 GeV: R. Barate *et al.*, Phys. Rep. **294**, 1 (1998).
9. 91 GeV: P. Abreu *et al.*, Z. Phys. C **50**, 185 (1991).
10. 91 GeV: B. Adeva *et al.*, Z. Phys. C **55**, 39 (1992).
11. 91 GeV: P. D. Acton *et al.*, Z. Phys. C **53**, 539 (1992).
12. 133 GeV: G. Alexander *et al.*, Z. Phys. C **72**, 191 (1996).
13. 161 GeV: K. Ackerstaff *et al.*, Z. Phys. C **75**, 193 (1997).
14. 1 to 2 GeV/*c*: F. Shimizu *et al.*, Nucl. Phys. A **386**, 571 (1982) (references [14–41] contain data on inelastic proton–proton scattering).
15. 2.2 GeV/*c*: A. M. Eisner *et al.*, Phys. Rev. B **138**, 670 (1965).
16. 2.8 GeV/*c*: E. Pickup *et al.*, Phys. Rev. **125**, 2091 (1962).
17. 3.7 GeV/*c*: E. L. Hart *et al.*, Phys. Rev. **126**, 747 (1962).
18. 4 GeV/*c*: L. Bodini *et al.*, Nuovo Cimento A **58**, 475 (1968).
19. 5.5 GeV/*c*: G. Alexander *et al.*, Phys. Rev. **154**, 1284 (1967).
20. 6.6 GeV/*c*: E. R. Gellert, Preprint No. LBL-749, LBL (Berkeley, 1972).
21. 6.9 GeV/*c*: S. Danieli *et al.*, Nucl. Phys. B **27**, 157 (1971).
22. 8.8 GeV/*c*: C. N. Booth *et al.*, Phys. Rev. D **27**, 2018 (1983).
23. 10 GeV/*c*: S. P. Almeida *et al.*, Phys. Rev. **174**, 1638 (1968).
24. 12, 24 GeV/*c*: V. Blobel *et al.*, Nucl. Phys. B **69**, 454 (1974).
25. 19 GeV/*c*: H. Boggild *et al.*, Nucl. Phys. B **27**, 285 (1971).
26. 32 GeV/*c*: M. Yu. Bogolyubskiĭ *et al.*, Yad. Fiz. **46**, 1680 (1987).
27. 36 GeV/*c*: I. V. Boguslavskiĭ *et al.*, Preprint No. 110134, OIYaI (Joint Institute for Nuclear Research, Dubna, 1976).
28. 50 GeV/*c*: V. V. Ammosov *et al.*, Phys. Lett. B **42B**, 519 (1972).
29. 60 GeV/*c*: C. Bromberg *et al.*, Phys. Rev. D **15**, 64 (1977).
30. 69 GeV/*c*: V. V. Babintsev *et al.*, Preprint No. M-25, IFVÉ (Institute for High Energy Physics, Protvino, 1976).
31. 100 GeV/*c*: W. M. Morse *et al.*, Phys. Rev. D **15**, 66 (1977).
32. 147 GeV/*c*: D. Brick *et al.*, Phys. Rev. D **25**, 2794 (1982).
33. 205 GeV/*c*: S. Barish *et al.*, Phys. Rev. D **9**, 2689 (1974).
34. 250 GeV/*c*: M. Adamus *et al.*, Z. Phys. C **32**, 475 (1986).
35. 300 GeV/*c*: A. Firestone *et al.*, Phys. Rev. D **10**, 2080 (1974).
36. 360 GeV/*c*: J. L. Bailly *et al.*, Z. Phys. C **23**, 205 (1984).
37. 400 GeV/*c*: R. D. Kass *et al.*, Phys. Rev. D **20**, 605 (1979).
38. 405 GeV/*c*: C. Bromberg *et al.*, Phys. Rev. Lett. **31**, 1563 (1973).
39. 800 GeV/*c*: R. Ammar *et al.*, Phys. Lett. B **178**, 124 (1986).
40. 30–60 GeV: A. Breakstone *et al.*, Phys. Rev. D **30**, 528 (1984).
41. 546 GeV: G. J. Alner *et al.*, Phys. Rep. **154**, 247 (1987).
42. V. D. Aksinenko *et al.*, Nucl. Phys. A **324**, 266 (1979).
43. V. D. Aksinenko *et al.*, Nucl. Phys. A **348**, 518 (1980).
44. W. Bell *et al.*, Phys. Lett. B **128B**, 349 (1983).
45. A. Bamberger *et al.*, Phys. Lett. B **205**, 583 (1988).
46. Z. Koba, H. B. Nielsen, and P. Olesen, Nucl. Phys. B **40**, 317 (1972).
47. A. M. Polyakov, Zh. Éksp. Teor. Fiz. **59**, 542 (1970) [Sov. Phys. JETP **32**, 296 (1970)].
48. Z. Koba, CERN–JINR School of Physics, CERN 73-12 (1973).
49. O. Czyżewski and K. Rybicki, Nucl. Phys. B **47**, 633 (1972).
50. M. Blažek, Z. Phys. C **32**, 309 (1986).
51. A. Giovannini, Nuovo Cimento A **15**, 543 (1973).
52. W. J. Knox, Phys. Rev. D **10**, 65 (1974).

53. A. I. Golokhvastov, Yad. Fiz. **27**, 809 (1978) [Sov. J. Nucl. Phys. **27**, 430 (1978)].
54. L. F. Zhirkov *et al.*, Yad. Fiz. **31**, 199 (1980) [Sov. J. Nucl. Phys. **31**, 105 (1980)].
55. G. V. Parry and P. Rotelli, Preprint No. IC/73/3 (Triest, 1973).
56. G. V. Parry and P. Rotelli, Lett. Nuovo Cimento **7**, 649 (1973).
57. A. I. Golokhvastov, Yad. Fiz. **30**, 253 (1979) [Sov. J. Nucl. Phys. **30**, 128 (1979)].
58. R. Szwed and G. Wrochna, Z. Phys. C **29**, 255 (1985).
59. A. I. Golokhvastov, Preprint No. E2-87-484, OIYaI (Joint Institute for Nuclear Research, Dubna, 1987).
60. A. Wróblewski, Acta Phys. Pol. B **4**, 857 (1973).
61. A. J. Buras *et al.*, Phys. Lett. B **47B**, 251 (1973).
62. W. T. Eadie *et al.*, *Statistical Methods* (North-Holland, Amsterdam, 1971).
63. S. Barshay and Y. Yamaguchi, Phys. Lett. B **51B**, 376 (1974).
64. G. Bozoki *et al.*, Nuovo Cimento A **64**, 881 (1969).
65. R. Szwed, Preprints IFD/3/86, IFD/5/86 (Warsaw, 1986).
66. R. Szwed and G. Wrochna, Z. Phys. C **47**, 449 (1990).
67. M. Gazdzicki *et al.*, Mod. Phys. Lett. A **6**, 981 (1991).
68. R. Szwed *et al.*, Mod. Phys. Lett. A **5**, 1851 (1990).
69. G. Wrochna, Preprints IFD/5/90, IFD/9/90 (Warsaw, 1990).
70. J. T. Jones *et al.*, Z. Phys. C **54**, 45 (1992).
71. N. Schmitz, Int. J. Mod. Phys. A **8**, 1993 (1993).
72. S. Aid *et al.*, Z. Phys. C **72**, 573 (1996).
73. R. Szwed, Preprint IFD/6/89 (Warsaw, 1989).
74. M. Planck, *Sitzungsber* (Acad. Wiss., Berlin, 1914; Nauka, Moscow, 1975).
75. Ch. Kittel, *Thermal Physics* (Wiley, New York, 1969; Nauka, Moscow, 1977), Chap. 15.
76. M. Born, Z. Phys. **26**, 379 (1924).
77. M. Jammer, *The Conceptual Development of Quantum Mechanics* (McGraw-Hill, New York, 1967; Nauka, Moscow, 1985), Chap. 4.3.
78. I. E. Tamm, *Collection of Works* (Nauka, Moscow, 1975), Vol. 1, p. 146; Vol. 2, p. 311.

Translated by A. Isaakyan

Physics of Atomic Nuclei, Vol. 64, No. 1, 2001, pp. 9–16. Translated from Yadernaya Fizika, Vol. 64, No. 1, 2001, pp. 11–18.

NUCLEI
Experiment

Statistical Properties of Deexcitation of Fragments Originating from the Spontaneous Fission of ^{252}Cf

O. T. Grudzevich

Institute of Atomic Power Engineering, Obninsk, Kaluga oblast, 249020 Russia

Received September 20, 1999; in final form, March 3, 2000

Abstract—A method of parametrizing radiative strength functions for electric dipole transitions is used to calculate the spectra of photons emitted by fragments originating from the spontaneous fission of ^{252}Cf nuclei. The LDPL-98 library of parameters, which contains data for 2000 nuclei, is composed for performing relevant calculations. It is shown that the use of this method leads to regular agreement with experimental data—that the structure and the energy dependence of the spectra are reproduced without varying parameters suggests a statistical character of fission-fragment deexcitation. © *2001 MAIK "Nauka/Interperiodica".*

1. INTRODUCTION

It was shown in [1] that radiative strength functions that characterize electric dipole transitions and which are usually used in various calculations can be modified with allowance for experimental data on transitions between discrete levels. The proposed modification of the Kadmensky–Markushev–Furman (KMF) method [2], which takes into account quasiparticle fragmentation, involved using the temperature of the transition final state as an adjustable parameter (the approach relying on this procedure will henceforth be referred to as the KMF method employing an adjustable temperature, or merely the KMF–AT method). Strictly speaking, the KMF method is applicable only in the case of compound-state deexcitation—that is, for primary photons. Despite the conclusions drawn in [3], the question of whether the method in question is applicable to multistep gamma transitions has yet to be clarified. Therefore, the KMF–AT version can be considered as an attempt at adapting the KMF method to the problem of calculating the spectra of secondary photons. Of many possible means for taking into account the observed intensities of transitions between discrete levels, use was made of the simplest one, that which assumes a constant temperature at all stages of the multicascade process. The KMF–AT method was tested by applying it to isomeric cross sections for neutron-induced and photonuclear reactions and to gamma spectra for (n, $xn\gamma$) reactions. Within the analysis on the basis of the proposed parametrization, it turned out that the computed gamma-ray spectra regularly comply with experimental data and that, sometimes, the resulting description of the cross sections for the excitation of high-spin isomers is radically improved in this way.

In the present study, the experimental database used in a comparison with the results of relevant calculations is extended via the inclusion of the spectra of gamma rays emitted from the fragments of ^{252}Cf spontaneous fission. The objective pursued here is to test the applicability of the statistical model of the nucleus to describing the emission properties of fission fragments.

2. COMPUTATIONAL PROCEDURE

Of the ingredients of the statistical model that are involved in the calculation of the radiative deexcitation of excited nuclei, two are of prime importance. These are the density of nuclear levels characterized by the excitation energy U and the total angular momentum J, $\rho(U, J)$, and the radiative strength functions $f_{XL}(E_\gamma)$ for X-type gamma rays of multipole order L and energy E_γ. As a rule, the parameters of the models underlying the calculation of $\rho(U, J)$ and f_{XL} are determined by fitting experimental data on the density of neutron resonances and on photoabsorption cross sections, respectively. Therefore, it can be believed that the predicted level densities are reliable up to excitation energies of 8 to 10 MeV and that the predicted strength functions f_{E1} are quite accurate for photon energies in the range 10–20 MeV. However, the deexcitation of excited nuclei is accompanied by a copious emission of soft photons (E_γ = 1–3 MeV), so that it is necessary to extrapolate relevant strength functions to this energy region. It is well known that the predictions of different approaches to calculating f_{E1} at low energies can differ by orders of magnitude even when these predictions rely on the same values of the giant-dipole-resonance parameters. A feature peculiar to the KMF-AT approach is that, by choosing the parameter T, it is possible to reproduce the maximum values of f_{E1} that are observed in the properties of transitions between discrete levels. It is assumed that the spectra observed in specific reactions are formed by the most intense transitions. The reasons behind the existence of a distinct step of maximum values of the observed strength functions in the region $E_\gamma <$ 2 MeV for nuclei differing in character (superallowed transitions) [1] have yet to be clarified.

1063-7788/01/6401-0009$21.00

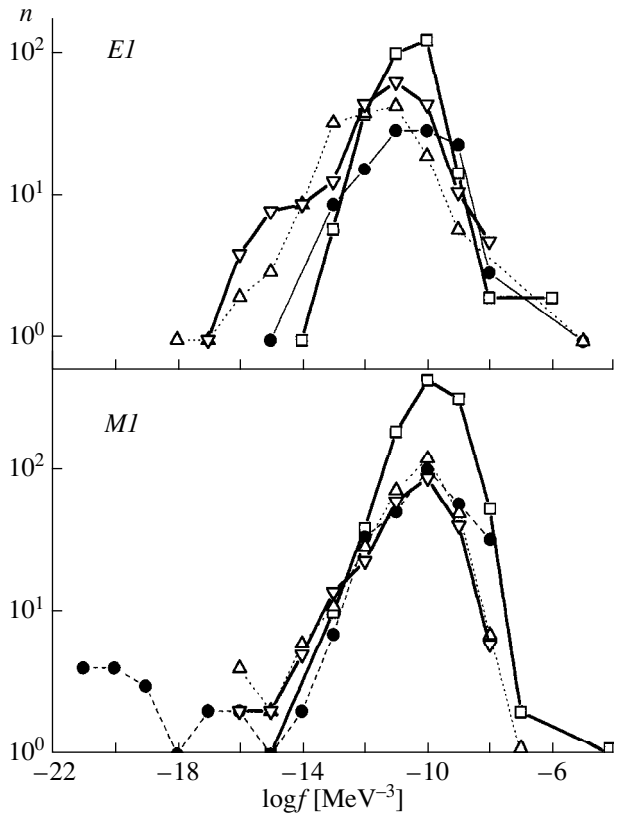

Fig. 1. Distribution of strength functions for $E_\gamma < 2$ MeV electric and magnetic dipole transitions (n stands for the number of transitions). Points represent experimental data from [4] for the mass-number ranges (open boxes) 45–84, (closed circles) 85–105, (open triangles) 106–145, and (open inverted triangles) 145–165.

The distributions of experimental strength functions for dipole transitions [4] are displayed in Fig. 1 for various intervals of mass numbers. For all mass regions of nuclear emitters and for transitions of both types, there exists a distinct upper limit on the quantities $f_{E,M1}$ that corresponds to superallowed dipole transitions. One can also clearly see transitions characterized by various mean logarithms of strength functions—special-type splitting of distributions that becomes more pronounced with increasing mass number. Statistically significant values of $f_{E,M1}$ lie between 10^{-15} and 10^{-8} MeV^{-3}. In this case, any procedure for averaging giant distinctions will result in mean values $\langle f_{E,M1}\rangle$ that are commensurate with the maximum values $f_{E,M1}^{\max}$. In the present study, we make use of the KMF method, which describes the observed values $f_{E1}^{\max}$.

The number of photons (multiplicity) $S_\gamma(Z, A, U, E_\gamma)dE_\gamma$ of energy E_γ between E_γ and $E_\gamma + dE_\gamma$ that are emitted by a (Z, A) nucleus excited to the energy U is calculated on the basis of the cascade–evaporation model (CEM) by using the expressions from [1]. The number of photons per fission event that are emitted by fragments belonging to the mass range between A_1 and A_2 can be calculated with the aid of the relation

$$S_\gamma(E_\gamma)dE_\gamma = \sum_i Y_i \int_0^{U_m} S_\gamma(Z_i, A_i, U, E_\gamma) f(U) dU dE_\gamma, \quad (1)$$

where Y_i is the independent yield of the (Z, A) fragment prior to neutron emission, while $f(U)$ is the excitation-energy distribution of primary populations. Summation is performed over all fragments in the specified mass range. The quantity obtained by formula (1) will be referred to as the spectrum of photons. In order to calculate the spectrum of neutrons, we can make use of a similar expression.

The total number of photons, μ, and the total number of neutrons, ν, that are emitted by fragments of mass A are determined by integrating the corresponding multiplicities and by subsequently performing summation (with a relevant weight) of the independent yields over all nuclei of given mass:

$$\mu, \nu(A) = \sum_Z Y(Z, A) \int_0^{U_m} f(U) dU \int_0^{E_m} S_{\gamma, n}(Z, A, U, E) dE. \quad (2)$$

2.1. Input Data for Relevant Calculations: LDPL Library

Theoretical calculations of the decays of fission fragments with allowance for total-angular-momentum and parity conservation are extremely cumbersome. In implementing such calculations, it is necessary to invoke vast arrays of input data—first of all, data on the features of excitations, such as level densities and diagrams of discrete levels. The situation is further aggravated if neutron-excess nuclei appear as fragments—the point is that, in the majority of cases, there is no experimental information about the density of neutron resonances in such nuclei.

In this connection, it is necessary to mention a formidable work performed by the international group of experts who created, under the aegis of the International Atomic Energy Agency, a library of input data for theoretical calculations of cross sections for nuclear reactions [5]. Unfortunately, this library covers only those nuclei for which there is information on the density of neutron resonances; moreover, the recommended file of data on discrete levels, which was composed on the basis of the compilation presented in [6], contains some conceptual and technical errors.

A new version of the library of the parameters of the level density and of the diagram of discrete levels, LDPL-98, was created in order to provide inputs for calculations of cross sections and spectra associated

with transformations of nuclei far from the stability band. In composing this library, which covers data on 2000 nuclei, full advantage was taken of the possibilities offered by the generalized model of superfluid nuclei, which allows for shell, collective, and superfluid effects. The version of this model for computing level densities [7] requires presetting four quantities: $\tilde{a}$, the asymptotic level-density parameter; δ, the effective correction for even–odd distinctions; δW, the shell correction; and ω_{2^+}, the quadrupole-phonon energy identified with the energy of the first $J^\pi = 2^+$ level in even–even nuclei. The last two are determined from experimental data that have no bearing on the level density. Shell corrections are computed on the basis of the liquid-drop model of the nucleus by using experimental values of nuclear masses. The effective correction for even–odd distinctions in the level density is determined by fitting the calculated excitation-energy dependences of the number of levels to experimental data on discrete levels. This is the point where merits of the generalized model of superfluid nuclei manifest themselves most clearly. On one hand, the result is weakly dependent on the asymptotic level-density parameter, so that one can make use of available diagrams of discrete levels if there are no data on the density of neutron resonances. On the other hand, the resulting values are described satisfactorily by simple systematics [7], so that this systematics can be employed in those cases where the diagram of discrete levels is not known or where it is insufficiently reliable. The asymptotic level-density parameter is satisfactorily described by the dependence $\tilde{a} = 0.073A + 0.115A^{2/3}$, and we can hope to predict reliably this quantity for nuclei whose experimental level densities are not known. The reliability of the LDPL-98 data for fission fragments is discussed below.

For the majority of fission fragments, the experimental photoabsorption cross sections are unavailable, so that the systematics of the giant-dipole-resonance parameters must used in the calculations. The existing data on the energies E_r, widths Γ_r, and maximum cross sections σ_r [8], as deduced from the description of experimental data of the photoabsorption cross sections on the basis of the Lorentz formula, are presented in Fig. 2. A satisfactory description of these parameters can be obtained by means of the systematics

$$\begin{aligned} \sigma_r &= 0.085A^{5/3}\ (\text{mb}), \\ E_r &= 51A^{1/4}\ (\text{MeV}), \\ \Gamma_r &= 6.1 - 0.012A\ (\text{MeV}). \end{aligned} \tag{3}$$

In deriving expressions (3), we disregarded resonance splitting for strongly deformed nuclei. It can be seen that the entire body of available data can be described by simple relations to within 50%. This means that, by using the representations in (3), the strength functions in the energy range 10–20 MeV can be computed to approximately the same degree of precision.

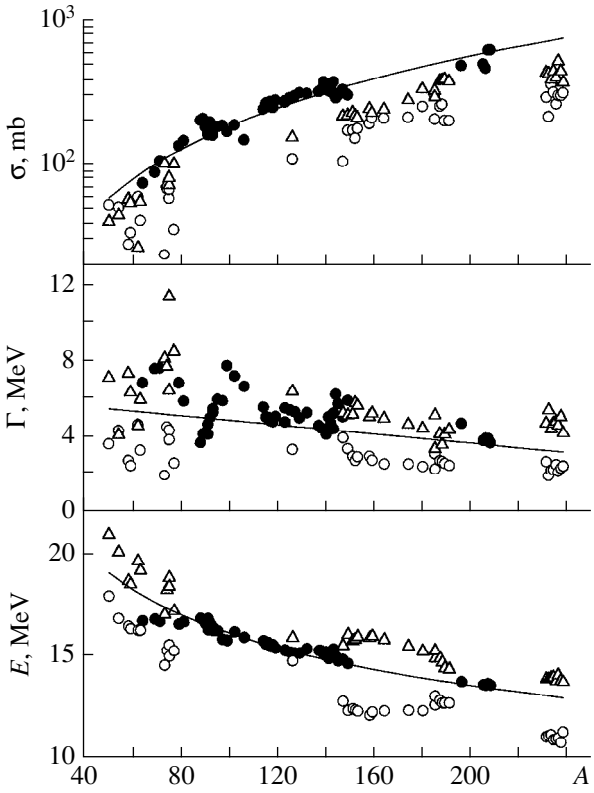

Fig. 2. Parameters of giant dipole resonances for A = 50–240 nuclei (energies, widths, and maximal cross sections). Points represent a fit of a Lorentzian dependence to the experimental photoabsorption cross sections [8] for (closed circles) monoresonances and (open circles and triangles) split resonances. Curves illustrate the results of the calculations by formulas (3).

2.2. Excitation Energies of Fragments

The level density and the radiative strength functions do not exhaust factors that control the shape of the spectrum of radiation from a fragment: this spectrum also depends on the mean excitation energy of a primary fragment and on the total-angular-momentum distribution of fragment population. From a theoretical analysis and from the experience gained in calculating the spectra, it follows that the last functional affects the results only slightly even at low excitation energies; therefore, we will use a distribution where the populations are proportional to the level density at a given value of the total angular momentum, $\rho(U, J)$. It should be emphasized that additional checks upon such a distribution are required when it is used to describe the isomeric ratios for fragments.

The mean values of fragment excitation energies, $\langle U \rangle$, will be determined by comparing the results of the calculations for mean numbers of neutrons, $\nu(A)$, by formula (2) with experimental data presented in [9].

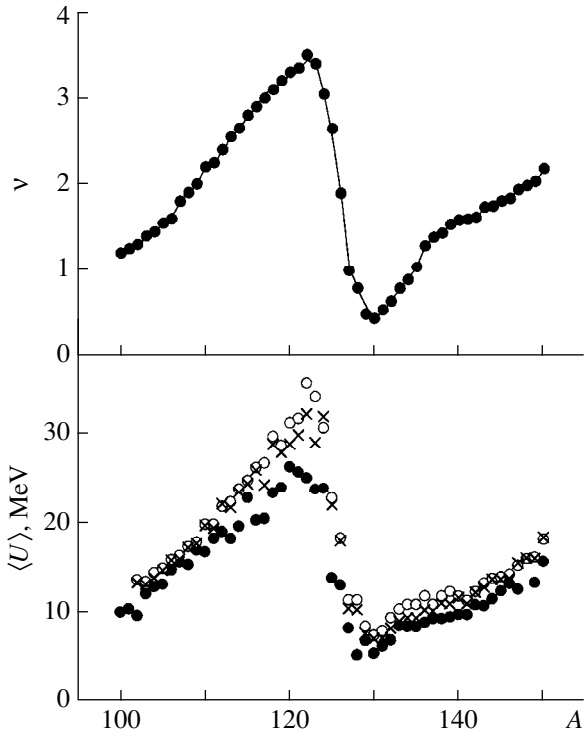

Fig. 3. Mean excitation energies $\langle U \rangle$ of fragments with mass number A and mean number of neutrons, ν. Points represent (closed circles) experimental data from [9], (open circles) results obtained from a fit to the observed values of ν(A), and (crosses) results deduced from the balance of the computed mean radiation energies. The solid curve corresponds to the result of the relevant fit.

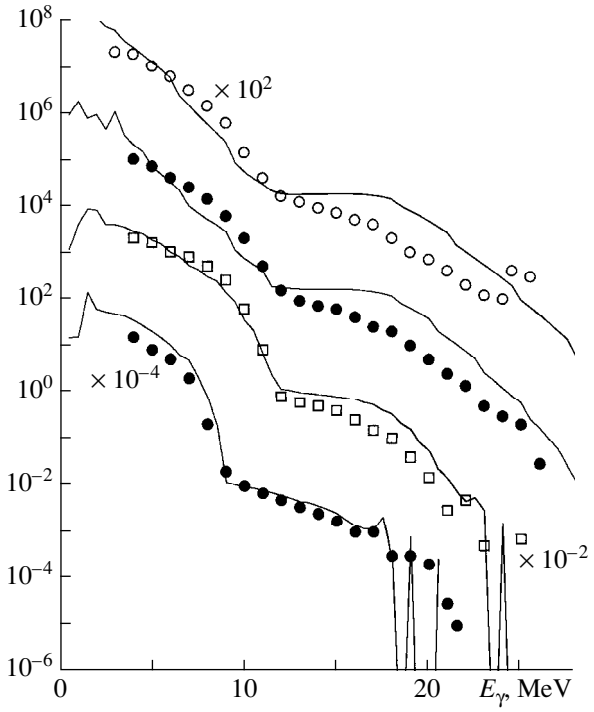

Fig. 4. Spectra of photons (in μb/MeV) from the reaction $\alpha + {}^{48}\mathrm{Ti} = {}^{52}\mathrm{Cr}$ at alpha-particle energies of 12, 17, 24, and 28 MeV (from bottom to top). Points represent experimental data from [11], while curves illustrate the results of the calculations.

The yields of fragments preceding prompt fission neutrons were borrowed from [10], while the spectra of fission neutrons for excitation energies from 0 to 80 MeV were computed on the basis of the Hauser–Feshbach formalism with the parameter values from the LDPL-98 library. The calculations were performed for nuclei whose yields vary between the maximum value $Y_{\max}(A)$ and the value that is one-tenth as great as that. For the fragment mass numbers in the interval A = 102–150, the list of nuclei that meet this criterion includes 123 species.

The values of $\langle U \rangle$ that were determined from a fit to the observed values of ν(A) are displayed in Fig. 3, along with the results obtained in [9], where the mean values that the excitation energy has prior to neutron emission were determined from the mean-energy-balance equation

$$\langle U \rangle = \nu(\langle B_n \rangle + \langle E_n \rangle) + \langle E_\gamma \rangle, \qquad (4)$$

where $\langle E_n \rangle$ is the mean neutron energy, $\langle B_n \rangle$ is the mean neutron binding energy, and $\langle E_\gamma \rangle$ is the mean energy carried away by photons. The approximation $\langle E_\gamma \rangle \approx B_n/2$ was used in [9]. It should be recalled that, although the experimental values of ν and $\langle E_n \rangle$ are used in Eq. (4), it can lead to errors in $\langle U \rangle$.

From Fig. 3, it can be seen that the results obtained by three methods for the mean excitation energies of primary fragments are quite consistent over the entire mass interval with the exception of the region A = 110–125. The distinctions in this region, which sometimes become as large as 12 MeV, may be due to the use of the approximation $\langle E_\gamma \rangle \approx B_n/2$ in [9]. That the $\langle U \rangle_1$ values obtained in the present study from a fit to ν_{expt} are in reasonably good agreement with $\langle U \rangle_2$ as computed by formula (4) with the aid of the evaluated values of $\langle E_n \rangle$ and $\langle E_\gamma \rangle$ nevertheless suggests that the method proposed here for extracting mean excitation energies of primary fragments is preferable. In view of this, the ensuing calculations will rely on $\langle U \rangle_1$ values.

A considerable number of fragments may prove to be excited to U = 20–35 MeV (see Fig. 3). This circumstance must be taken into account in estimating the quality of the description of the hard section of the observed spectra, since the uncertainties in calculating the level density increase as one moves away on the excitation energy scale from nuclei for which the level density was studied experimentally. To illustrate the situation where the flaws in describing level densities become obvious, the calculated spectra of gamma rays from the reaction $\alpha + {}^{48}\mathrm{Ti} = {}^{52}\mathrm{Cr}$ are contrasted in Fig. 4 against the spectra measured in [11] at various energies of incident alpha particles. The soft section of each spectrum is determined by the level density after parti-

cle emission, which leads to the formation of a residual nucleus at low excitation energies. The step in the right-hand section of the spectrum is associated with primary photons that originate from the decay of a compound nucleus and which compete with particles of nonzero mass. Thus, the probability of high-energy-photon emission is determined not only by the relevant strength function but also by the level density at the corresponding high value of the excitation energy. By way of example, we indicate that, in response to the growth of E_α from 12 to 28 MeV, the excitation energy changes from 20 to 35 MeV. It is obvious that a systematic bias can arise in the spectrum computed with the level density extrapolated from the neutron binding energy (8–10 MeV) to 35 MeV. In the case being considered, the level density is overestimated at high excitation energies. At the same time, it can be shown that, at $E_\alpha = 12$ and 17 MeV, the hard sections of the spectra are reproduced quite faithfully, which indicates that, within the generalized model of superfluid nuclei, the level density is extrapolated quite reliably by 10–15 MeV upward on the excitation-energy scale.

As to the reaction $^{19}F + {}^{27}Al = {}^{46}Ti$ (see Fig. 5), the primary excitations of ^{46}Ti that are generated in it occur at 40 to 60 MeV. It can be seen that, even at a minimal value of U, there are sizable discrepancies in the hard sections of the spectra and that, with increasing excitation energy, these discrepancies grow.

Thus, the step in the soft sections of the spectra, which is associated with the decay of the nucleus initially produced in a highly excited state, can be a source of information about the density of nuclear levels at high excitation energies. The uncertainties in the radiative strength functions are minimal in this region of radiated energies, because there are comprehensive data on the photoabsorption cross sections at these energies.

At relevant excitation energies of the fragments, the values of the level-density parameter a from the LDPL-98 library, which are used in the calculations, become commensurate with the data from [9] in Fig. 6. However, a direct comparison of these quantities is not quite correct because the different approaches to calculating level densities were used in the two cases. Since the collective enhancement of the level density is taken into account in our approach, the a values in the two models must be close for nuclei where collective effects are small (that is, for magic nuclei). For nuclear species far off magic ones, the inclusion of collective effects reduces the parameter a. From Fig. 6, it can be seen that, in the mass range $A = 125$–135 (region of the doubly magic nucleus ^{132}Sn), the parameter values from the LDPL-98 agree, both in absolute value and in the shape of the mass number dependence, with data from [9], which were obtained by fitting the experimental spectra of neutrons originating from fission fragments. This clearly demonstrates that data from the LDPL-98 library are quite reliable and that the generalized model

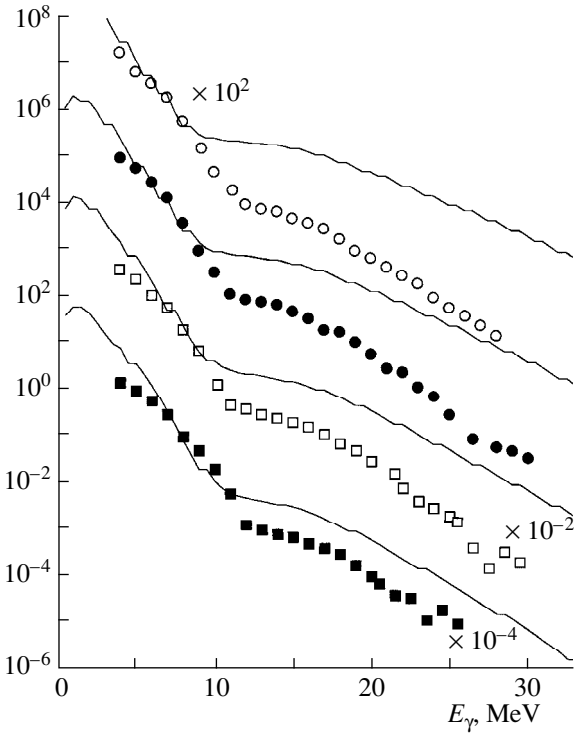

Fig. 5. Spectra of photons (in μb/MeV) from the reaction $^{19}F + {}^{27}Al = {}^{46}Ti$ at projectile energies of 30, 40, 50, and 60 MeV (from bottom to top). Points represent experimental data from [11], while curves illustrate the results of the calculations.

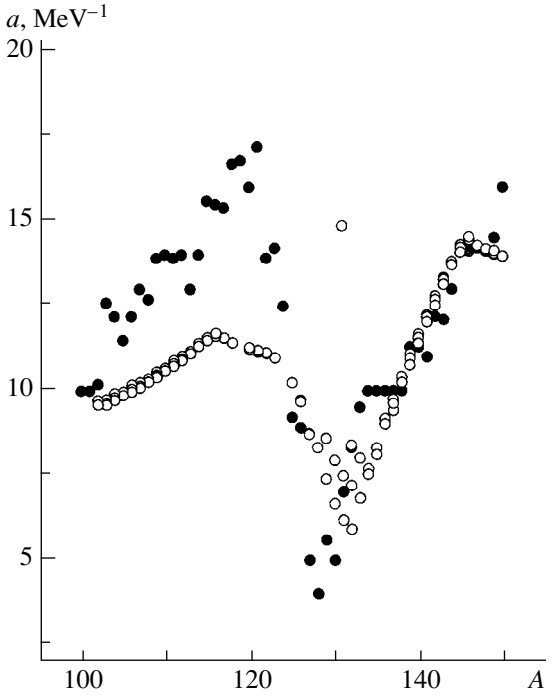

Fig. 6. Level-density parameters for fragments originating from the spontaneous fission of ^{252}Cf versus the mass number: (closed circles) data from [9] and (open circles) level-density parameters according to the systematics from [7] for relevant excitation energies.

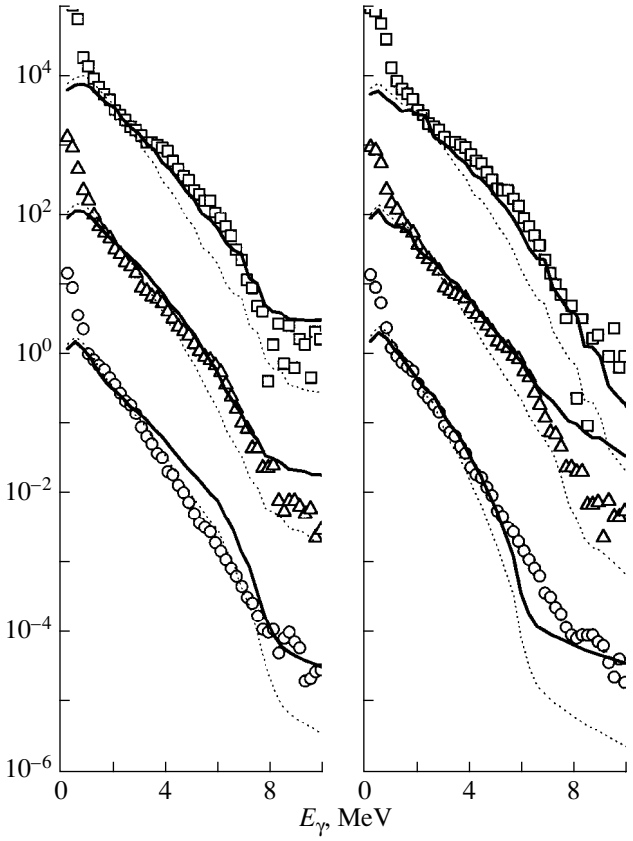

Fig. 7. Spectra (in arbitrary units) of photons emitted by (right panel) heavy fragments formed in the spontaneous fission of ^{252}Cf and (left panel) the complementary light fragments. Open symbols represent experimental data from [12] for the following ranges of heavy-fragment (light-fragment) masses: (boxes) 126–130 (122–126), (triangles) 134–138 (114–118), and (circles) 142–146 (106–110). Solid and dashed curves illustrate the results of the calculations that employ the radiative strength functions f_{E1} found, respectively, on the basis of the KMF–AT method and on the basis of the Lorentzian dependence.

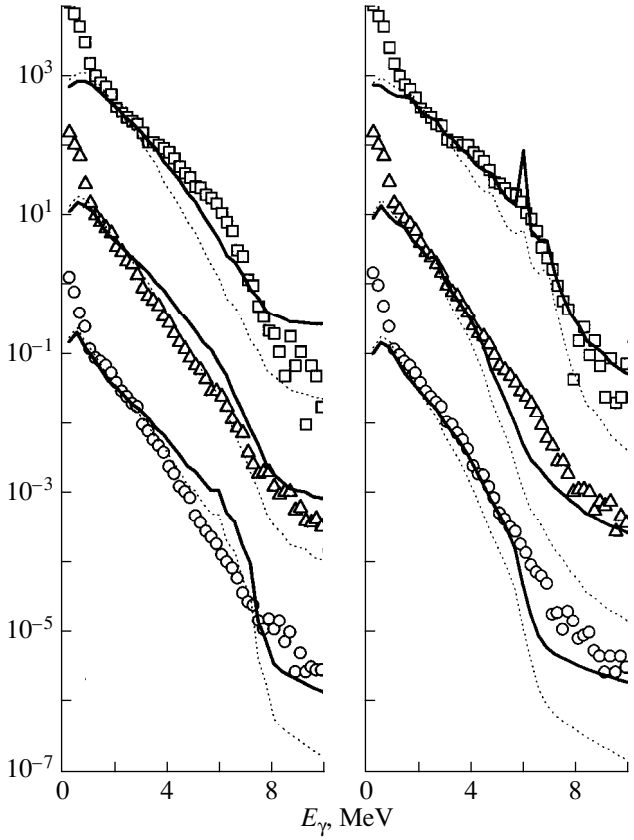

Fig. 8. As in Fig. 7, but for the fragment-mass ranges 130–134 (118–122), 138–142 (110–114), and 146–150 (102–106).

of superfluid nuclei furnishes accurate predictions for the level densities in nuclei far off the stability band. That collective effects are taken into account in this model explains the discrepancy for A = 110–120 fragments.

3. RESULTS OF THE CALCULATIONS

One feature that is peculiar to the experimental spectra of photons from fragments produced in the spontaneous fission of ^{252}Cf and which was comprehensively discussed in [12] is that the shape of the spectrum for A = 126–136 fragments differs from that for fragments having different masses (Figs. 7, 8). Indeed, the spectra of fragments in the vicinity of the doubly magic nucleus ^{132}Sn exhibit a considerable excess of photons with energies in the interval 3–8 MeV. This fact was explained in [9], where it was shown on the basis of an analysis of neutron spectra that the level-density parameters of nuclei in the region of the doubly magic nucleus ^{132}Sn have a pronounced shell structure (see Fig. 6). Another feature of the measured spectra is that the spectrum of photons from a heavy fragment is quite similar to the spectrum of photons from the complementary light fragment (Fig. 9). This may tentatively be associated with inability to identify unambiguously the source of radiation in the experiment reported in [12].

In the context of the present study, the point of prime interest is that of testing agreement between the slope of experimental photon spectra from [12] and the slope of the theoretical spectra constructed by using two methods for evaluating strength functions for electric dipole transitions, the KMF–AT method and the method relying on a Lorentzian dependence. The calculated spectra for various intervals of the mass of a heavy fragment and the mass of the complementary light fragment are displayed in Figs. 7 and 8, along with the relevant experimental data from [12]. It can easily be seen that, by using the KMF–AT method for calculating strength functions, one achieves more acceptable agreement between the experimental and calculated slopes of the spectra, especially for heavy fragments. Among the cases considered here, the most representative changes are observed in the intervals A = 126–130, 142–146, 138–142, and 146–150. It is noteworthy that,

in the intervals A = 126–130 and 130–134 near a doubly magic fragment, an excess of photons with energies in the range 3–8 MeV is faithfully reproduced without any additional effort.

Taking into account the aforementioned special feature of the method of measurements, we perform a further analysis on the basis of a comparison of data for complementary fragments with the corresponding calculated spectra in the form of mean values with weights proportional to the yields of the heavy and light fragments (see Fig. 9). This comparison reveals an additional uncertainty caused by the possible distinctions between the observed and the calculated fragment-mass dependence of photon multiplicities—in other words, by uncertainties in the normalization of the calculated spectra. From Fig. 9, it can be seen that the resulting description of the observed photon spectra is satisfactory in the energy region $E_\gamma \geq 1$ MeV for all fragment masses. The distinctions that still remain can easily be removed by varying the normalization factors in the computed spectra for complementary fragments since the required forms are embedded in the components constituting the eventual spectra (see Figs. 7, 8).

It is worth noting that, in all cases considered here (Figs. 7–9), the calculated spectra always fall short of experimental values for low radiation energies ($E_\gamma <$ 1 MeV). If, despite the complicated energy dependence of the detector efficiency in this interval, the experimental data are reliable for it, an analysis of the discrepancies could furnish interesting information about the properties of excited states of fission fragments. For example, it would be possible to estimate the contribution of rotational degrees of freedom to the formation of the initial fragment spins, since the enhancement of gamma-decay probabilities in transitions between the members of rotational bands, which was disregarded in the calculations, appears to be the most natural explanation of the observed discrepancies. In this connection, it would be useful to improve the mass resolution of the spectra [12].

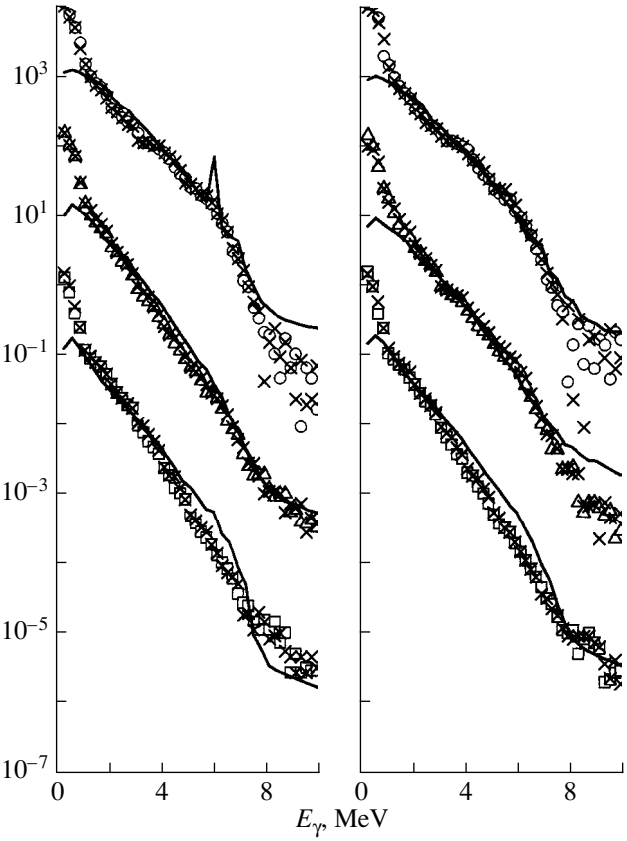

Fig. 9. Data (in arbitrary units) on the spectra of photons emitted by fragments originating from ^{252}Cf fission. Open symbols represent experimental data from [12] for various ranges of heavy-fragment masses (for each kind of symbol, data for the first and the second range are displayed on the left and on the right panel, respectively): (circles) 130–134 and 126–130, (triangles) 138–142 and 134–138, and (boxes) 146–150 and 142–146. Crosses represent data for the complementary light fragments. Curves illustrate the results of the calculations that were performed for various pairs of fragments and which employ data from the LDPL-98 library and the radiative strength functions f_{E1} as determined on the basis of the KMF–AT method.

4. CONCLUSION

A theoretical analysis of the spectra of photons from the fragments produced in the spontaneous fission of ^{252}Cf has been performed. The LDPL-98 library of parameters, which contains data on the level densities and on the diagrams of levels for 2000 nuclei, has been composed for relevant calculations. The excitation energies of primary fragments have been extracted, and the reliability of the resulting values has been tested. It has been shown that, within the statistical model of the nucleus, the observed spectra can be satisfactorily reproduced by using the $E1$ radiative strength functions as obtained by the KMF–AT method, which takes into account experimental data on the properties of transitions between discrete levels. It has been conjectured that the reasons behind the discrepancies between the observed and computed spectra are associated with the uncertainties in the level densities at high excitation energies and with the enhancement of the intensities of transitions between the members of rotational bands.

ACKNOWLEDGMENTS

I am indebted to W.I. Furman and A.A. Goverdovski for discussions, comments, and advice that stimulated this research.

REFERENCES

1. O. T. Grudzevich, Yad. Fiz. **62**, 227 (1999) [Phys. At. Nucl. **62**, 192 (1999)].
2. S. G. Kadmenskiĭ, V. P. Markushev, and V. I. Furman, Yad. Fiz. **37**, 277 (1983) [Sov. J. Nucl. Phys. **37**, 165 (1983)].

3. J. Kopecky and M. Uhl, Phys. Rev. C **41**, 1941 (1990).
4. ENSDF, prod. INSDDN, maint. NNDC, BNL, USA (file as 1996).
5. IAEA-TECDOC-1034, Vienna, 1998.
6. NUDAT database, version 23 Feb. 1996, maint. NNDC, BNL, USA.
7. O. T. Grudzevich, A. V. Ignatyuk, and A. V. Zelenetsky, in *Proceedings of the International Conference on Nuclear Data for Science and Technology, Mito, Japan, 1988*, p. 1221.
8. S. S. Dietrich and B. L. Berman, At. Data Nucl. Data Tables **38**, 199 (1988).
9. C. Budtz-Jorgensen and H. Knitter, Nucl. Phys. A **490**, 307 (1988).
10. A. C. Wahl, At. Data Nucl. Data Tables **39**, 1 (1988).
11. G. Feldman, K. A. Snover, J. A. Behr, *et al.*, Phys. Rev. C **47**, 1436 (1993).
12. F. J. Hambsch, J. Aarle, and R. Vogt, in *Proceedings of the XIII Meeting on Physics of Nuclear Fission, Obninsk, 1995*, p. 27.

Translated by A. Isaakyan

Physics of Atomic Nuclei, Vol. 64, No. 1, 2001, pp. 98–102. From Yadernaya Fizika, Vol. 64, No. 1, 2001, pp. 101–105.

ELEMENTARY PARTICLES AND FIELDS
Theory

Leading/Nonleading Charm-Production Asymmetry in $\Sigma^- p$ Interactions*

O. I. Piskounova

Lebedev Institute of Physics, Russian Academy of Sciences, Leninskiĭ pr. 53, Moscow, 117924 Russia

Received November 17, 1999

Abstract—The asymmetry between the spectra of leading and nonleading charmed mesons that was measured in $\Sigma^- A$ interactions at p_L = 340 GeV/c in the WA89 experiment is described within the Model of Quark–Gluon Strings (QGS model also known as QGSM) under the assumption that there is a fraction of charmed sea quark–antiquark pairs (intrinsic charm) in an interacting hyperon. It is shown that the asymmetries between D^-- and D^+-meson spectra and between D_s^-- and D_s^+-meson spectra can be approximated by QGSM curves obtained with the same string-fragmentation parameter, $a_1 = 10$, and the same intrinsic-charm fraction, $\delta_{c,\bar{c}} = 0.01$, as those that were used in describing D_s^-/D_s^+-meson asymmetry of $\pi^- A$ experiments in previous studies. The asymmetry between the spectra of Λ_c and $\bar{\Lambda}_c$ that was measured in $\Sigma^- A$ collisions at p_L = 600 GeV/c in the E781 experiment is also described within this scheme. The QGSM results are compared with the results of the calculations in the next-to-leading approximation of perturbative QCD that were performed by other authors. © *2001 MAIK "Nauka/Interperiodica".*

1. INTRODUCTION

The asymmetries between the spectra of D^- and D^+ mesons and between the spectra of D_s^- and D_s^+ mesons were measured in $\Sigma^- A$ interactions at p_L = 340 GeV/c in the WA89 experiment [1]. It is of interest to compare these asymmetries with those obtained in the $\pi^- A$ experiments [2, 3] in order to understand the influence of the quark composition of beam particles on productions of heavy-flavored particles and to extract some specific features of the spectra of strange–charmed mesons due to the presence of a strange valence quark in the Σ^- hyperon. The difference between the spectra ($x \equiv x_F = 2p_\parallel/\sqrt{s}$) of leading and nonleading particles was discussed recently, and several theoretical models explained successfully the asymmetry as an effect that is due to the interplay of the quark contents of the projectile and the quark content of the product hadron. Charmed mesons containing ordinary quarks of the same type as beam particles have a higher average value of x. The asymmetry defined as

$$A(x) = \frac{dN^{D^-}/dx - dN^{D^+}/dx}{dN^{D^-}/dx + dN^{D^+}/dx}, \qquad (1)$$

is a function that grows with x. There are two different theoretical approaches to describing this effect. The first one is based on perturbative QCD. It takes into account the recombination of intrinsic-charm quarks with the valence quarks of the projectile as the origin of asymmetry [4]. Other phenomenological models exploit the properties of fragmentation functions in order to insert asymmetry. We will not discuss here the details of recombination models, but we are going to concentrate on a nonperturbative approach known as the Model of Quark–Gluon Strings (QGS model also known as QGSM) [5]. This model describes well the leading/nonleading charm asymmetry for $\pi^- p$ experiments [6].

2. QUARK DISTRIBUTIONS IN THE QGSM

The cross section for the inclusive production of D mesons is represented as the sum over n-Pomeron cylinder diagrams:

$$f_1 = x\frac{d\sigma^D}{dx}(s, x) = \int E\frac{d^3\sigma^D}{d^3p}d^2p_\perp = \sum_{n=0}^{\infty}\sigma_n(s)\varphi_n^D(s, x). \qquad (2)$$

Here, the function $\varphi_n^D(s, x)$ is the particle distribution in the configuration of n cut cylinders, and σ_n is the probability of this process. The parameter of the supercritical Pomeron used here is $\Delta_P = \alpha_P(0) - 1 = 0.12$. The

* This article was submitted by the author in English.

detailed formulas for σ_n and φ_n^D in pp interactions can be found in [7].

The distribution functions for the case of $\Sigma^- p$ collisions are given by

$$\varphi_n^D(s,x) = a_0^D\{F_q^{(n)}(x_+)F_{qq}^{(n)}(x_-) + F_{qq}^{(n)}(x_+)F_q^{(n)}(x_-) + 2(n-1)F_{q_{\text{sea}}}^{(n)}(x_+)F_{q_{\text{sea}}}^{(n)}(x_-)\}, \quad (3)$$

where a_0^D is the density parameter of quark–antiquark chain fragmentation into a given type of mesons.

The particle distribution on each side of the chain can be built on the account of the quark contents of the beam particle ($x_+ = (x + \sqrt{x^2 + x_\perp^2})/2$, $x_\perp = 2m_\perp/\sqrt{s}$) and of the target particle ($x_- = (x - \sqrt{x^2 + x_\perp^2})/2$):

$$\begin{aligned} F_q^{(n)}(x_+) &= \frac{1}{3}F_s^{(n)}(x_+) + \frac{2}{3}F_d^{(n)}(x_+), \\ F_{qq}^{(n)}(x_+) &= \frac{1}{3}F_{dd}^{(n)}(x_+) + \frac{2}{3}F_{ds}^{(n)}(x_+), \\ F_q^{(n)}(x_-) &= \frac{1}{3}F_d^{(n)}(x_-) + \frac{2}{3}F_u^{(n)}(x_-), \\ F_{qq}^{(n)}(x_-) &= \frac{1}{3}F_{uu}^{(n)}(x_-) + \frac{2}{3}F_{ud}^{(n)}(x_-). \end{aligned} \quad (4)$$

Each $F_i(x_\pm)$ is constructed as the convolution

$$F_i(x_\pm) = \int_{x_\pm}^1 f_{\Sigma^-}^i(x_1)\frac{x_\pm}{x_1}\mathcal{D}_i^D\left(\frac{x_\pm}{x_1}\right)dx_1, \quad (5)$$

where $f^i(x_1)$ is the structure function of the ith quark that has an energy fraction x_1 in the interacting hadron and $\mathcal{D}_i^D(z)$ is the fragmentation function for the transition of this quark into the considered type of D or D_s mesons.

The structure functions of quarks in an interacting proton were described in [7]. In the case of the hyperon, they depend on the parameter of the Regge trajectory of the φ meson ($s\bar{s}$) because of the presence of an s quark in Σ^-; that is,

$$\begin{aligned} f_{\Sigma^-}^d(x_1) &= C_d^{(n)}x_1^{-\alpha_R(0)}(1-x_1)^{\alpha_R(0)-2\alpha_N(0)+\alpha_\varphi(0)+n-1}, \\ f_{\Sigma^-}^{dd}(x_1) &= C_{dd}^{(n)}x_1^{\alpha_R(0)-2\alpha_N(0)}(1-x_1)^{-\alpha_\varphi(0)+n-1}, \\ f_{\Sigma^-}^{ds}(x_1) &= C_{ds}^{(n)}x_1^{\alpha_R(0)-2\alpha_N(0)+\alpha_R(0)-\alpha_\varphi(0)}(1-x_1)^{-\alpha_R(0)+n-1}, \\ f_{\Sigma^-}^{s}(x_1) &= C_s^{(n)}x_1^{-\alpha_R(0)}(1-x_1)^{\alpha_R(0)-2\alpha_N(0)+\alpha_R(0)-\alpha_\varphi(0)+n-1}, \end{aligned} \quad (6)$$

where $\alpha_\varphi(0) = 0$. The constants $C_i^{(n)}$ are determined by the normalization conditions

$$\int_0^1 f_i(x_1)dx_1 = 1.$$

3. FRAGMENTATION FUNCTIONS

For the quark and diquark chains, the fragmentation functions are constructed according to the rules proposed in [8]. The following favored fragmentation function for transitions into D_s^- mesons is written for the strange valence quark:

$$\mathcal{D}_s^{D_s^-}(z) = \frac{1}{z}(1-z)^{-\alpha_\psi(0)+\lambda}(1 + a_1^{D_s}z^2). \quad (7)$$

Here, $\lambda = 2\alpha'_{D^*}(0)\overline{p_{\perp D^*}^2}$, and $\alpha_\psi(0)$ is the parameter of the Regge trajectory of ψ mesons ($c\bar{c}$). The additional factor $(1 + a_1^{D_s}z^2)$ provides the parametrization [9] of the probability of heavy-quark production in the interval from $z = 0$ to $z \longrightarrow 1$. The values of the constant $a_1^{D_s}$ will be discussed below.

The function for the nonleading fragmentation of the d-quark chain is

$$\mathcal{D}_d^{D^+}(z) = \frac{1}{z}(1-z)^{-\alpha_R(0)+\lambda+2(1-\alpha_R(0))+\Delta_\psi}, \quad (8)$$

where $\alpha_R(0) = 0.5$ and $\Delta_\psi = \alpha_R(0) - \alpha_\psi(0)$. The function of the nonleading fragmentation of the diquark chain has the form

$$\mathcal{D}_d^{D_s^-}(z) = \frac{1}{z}(1-z)^{-\alpha_\varphi(0)+\lambda+2(1-\alpha_R(0))+\Delta_\psi}. \quad (9)$$

The following fragmentation function corresponds to the version of the diquark fragmentation into D_s^- mesons:

$$\mathcal{D}_{ds}^{D_s^-}(z) = \frac{1}{2z}(1-z)^{\alpha_R(0)-2\alpha_N(0)+\lambda+\Delta_\psi}(1 + a_1^{D_s}z^2) + \frac{1}{2z}(1-z)^{\alpha_R(0)-2\alpha_N(0)+\lambda+\Delta_\varphi+\Delta_\psi+1}. \quad (10)$$

4. THE ASYMMETRY-SUPPRESSION CAUSES

Some fractions of sea quark pairs in the hyperon, $d\bar{d}$ and $s\bar{s}$, must be taken into account since they suppress the leading/nonleading asymmetry. The structure functions for ordinary quark pairs in the quark sea of the hyperon can be written in the same way as the

valence-quark distributions:

$$f_{\Sigma^-}^{d,\bar{d}}(x_1) = C_{d,\bar{d}}^{(n)} x_1^{-\alpha_R(0)} (1-x_1)^{\alpha_R(0)-2\alpha_N(0)+\Delta_\varphi+n-1+2(1-\alpha_R(0))}. \quad (11)$$

Here, sea quarks and antiquarks have an additional power term $2[1-\alpha_R(0)]$ corresponding to the quark distribution of the two-Pomeron diagram including one sea quark pair.

The structure function for strange sea quarks obeys the same rules; that is,

$$f_{\Sigma^-}^{s,\bar{s}}(x_1) = C_{s,\bar{s}}^{(n)} \delta_{s,\bar{s}} x_1^{-\alpha_\varphi(0)} \times (1-x_1)^{\alpha_R(0)-2\alpha_N(0)+\Delta_\varphi+n-1+2(1-\alpha_R(0))}, \quad (12)$$

where $\Delta_\varphi = \alpha_R(0) - \alpha_\varphi(0)$ and $\delta_{s,\bar{s}} = 0.25$ (see [10]).

The fragmentation function for the transition of a strange sea quark (or antiquark) into D_s mesons has the following form for mesons of both charges:

$$\mathcal{D}_{s,\bar{s}}^{D_s^-}(z) = \frac{1}{z} z^{1-\alpha_\varphi(0)} (1-z)^{-\alpha_\varphi(0)+\lambda+2(1-\alpha_R(0))+\Delta_\psi}. \quad (13)$$

The additional fragmentation parameter $a_f^{D_s}$ is equal to the fragmentation parameter for D mesons.

5. INTRINSIC-CHARM DISTRIBUTION

Since we have taken into account the $d\bar{d}$ and $s\bar{s}$ fraction in the quark sea of the hyperon, some fraction of charmed sea quarks must be considered as well. This small heavy-quark admixture plays an important role owing to its strong impact on the difference between the leading and nonleading charmed-meson spectra.

The structure function for charmed sea quarks is similar to the distribution of strange sea quarks; that is,

$$f_{\Sigma^-}^{c,\bar{c}}(x_1) = C_{c,\bar{c}}^{(n)} \delta_{c,\bar{c}} x_1^{-\alpha_\psi(0)} \times (1-x_1)^{\alpha_R(0)-2\alpha_N(0)+\Delta_\varphi+\Delta_\psi+n-1+2(1-\alpha_R(0))}, \quad (14)$$

where $\delta_{c,\bar{c}}$ is the weight of the charm admixture to the quark sea of the hyperon. In fact, it should not necessarily be equal to the charmed-quark fraction in the quark sea of the pion [6]. This is the only parameter that we can vary for Σ^- interaction after the best fit to pion experimental data that was obtained before. The value of $\delta_{c,\bar{c}}$ can be estimated in describing the WA89 data on D_s- and D-meson asymmetries. It should be expressed in units of $\sqrt{a_0^D}$ for the reasons of correct normalization [see Eq. (3)]. The same was done in estimating the charmed-quark fraction in the quark sea of the pion. This factor will be omitted to simplify the representation of $\delta_{c,\bar{c}}$. The value of a_0^D is universal for each sort of beam particles and is approximately equal to 3×10^{-4} for D-meson production [9].

The fragmentation functions for D mesons are given by

$$\mathcal{D}_{c,\bar{c}}^{D^-,D^+}(z) = \frac{1}{z} z^{1-\alpha_\psi(0)} (1-z)^{-\alpha_R(0)+\lambda}. \quad (15)$$

For D_s mesons, we have

$$\mathcal{D}_{c,\bar{c}}^{D_s^-,D_s^+}(z) = \frac{1}{z} z^{1-\alpha_\psi(0)} (1-z)^{-\alpha_\varphi(0)+\lambda}. \quad (16)$$

6. $\Lambda_c/\bar{\Lambda}_c$ ASYMMETRY

The asymmetry between the spectra of Λ_c and $\bar{\Lambda}_c$ that was measured in $\Sigma^- A$ collisions can easily be obtained by means of nearly the same calculations as those described above. What is of importance here is that the leading Λ_c baryon is formed from the single d quark of the projectile particle. No diquark from the Σ^--hyperon participates in the production of a leading charmed baryon. This allows us to take the results of our calculation for D-meson production at $p_L = 600$ GeV/c and to compare them with the $\Lambda_c/\bar{\Lambda}_c$ asymmetry measured in $\Sigma^- A$ collisions in the E781 experiment [11]. The parameter a_1 means in this case a parametrization parameter for the density of Λ_c in the fragmentation of a uc-diquark string; it can differ from the a_1 value taken for D-meson production. The energy of the interaction must also be changed. The parameter of the intrinsic-charm fraction, $\delta_{c,\bar{c}}$, must have the same value as that for D-meson calculations because one does not know which leading particles are produced.

It should be realized that the reasonings about $\Lambda_c/\bar{\Lambda}_c$ asymmetry are given here only to illustrate the simple quark-counting approach within the QGSM. Complete calculations of the spectra of Λ_c and $\bar{\Lambda}_c$ will be carried out in this model on the basis of data available from various beam experiments.

7. FINAL PLOTS AND COMPARISON

The main parameter of the QGSM scheme that is responsible for leading/nonleading charm asymmetry is a_1. It is the parametrization parameter of the leading fragmentation-function dependence on $z \longrightarrow 1$. The fraction of charmed sea quarks, $\delta_{c,\bar{c}}$, is the second parameter in these calculations that makes the asymmetry lower because of equal numbers of D^+ and D^- mesons produced by each sea-charmed-quark pair. Two sets of this couple of parameters were chosen in describing data on $\pi^- A$ interactions: $a_1 = 4$, $\delta_{c,\bar{c}} = 0$ and

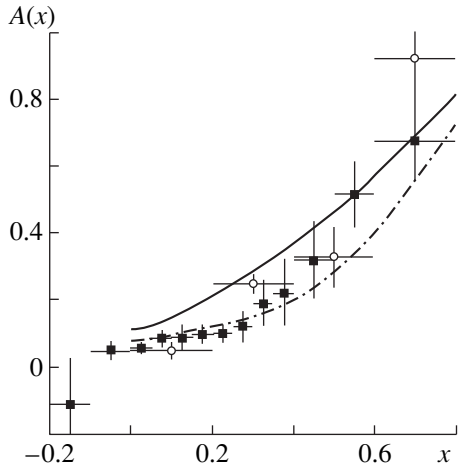

Fig. 1. Asymmetries between D^- and D^+ spectra according to the (closed squares) E791 [2] and (open circles) WA92 [4] experiments and relevant QGSM curves for (solid curve) $a_1 = 10$ and $\delta_{c,\bar{c}} = 0.05$ and (dash-dotted curve) $a_1 = 4$ and $\delta_{c,\bar{c}} = 0$.

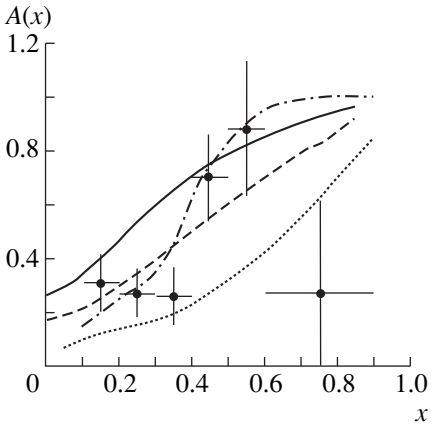

Fig. 2. D^-/D^+ asymmetry according to (closed circles) the WA89 measurements [1] and relevant theoretical calculations: (solid curve) QGSM results at $a_1 = 10$ and $\delta_{c,\bar{c}} = 0.01$, (dashed curve) QGSM results at $a_1 = 4$ and $\delta_{c,\bar{c}} = 0$, (dash-dotted curve) results from [12], and (dotted curve) results corresponding to $A(x)$ predicted in [13].

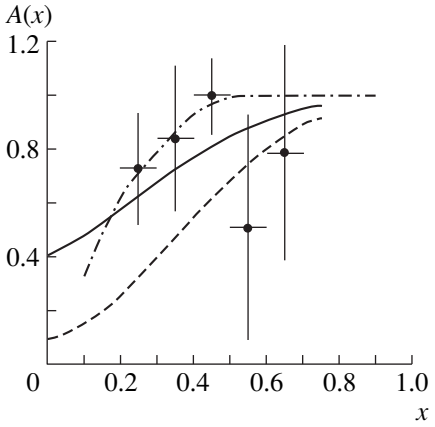

Fig. 3. D_s^-/D_s^+ asymmetry according to the WA89 measurements [1]. The notation for the theoretical curves is identical to that in Fig. 2.

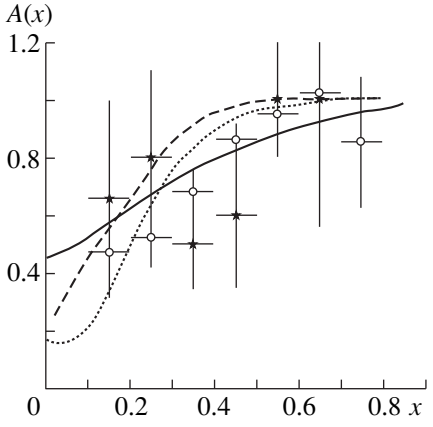

Fig. 4. Asymmetry between Λ_c and $\bar{\Lambda}_c$ spectra according to the (open circles) E781 [11] and (closed stars) WA89 [1] measurements and relevant theoretical calculations: (solid curve) QGSM results for $a_1 = 25$ and $\delta_{c,\bar{c}} = 0.01$, (dashed curve) results from [12], and (dotted curve) results corresponding to $A(x)$ predicted in [14].

$a_1 = 10$, $\delta_{c,\bar{c}} = 0.05$. We consider here these two values of a_1, taking $\delta_{c,\bar{c}}$ to be more or less a free parameter.

Two curves displayed in Fig. 1 represent fits to data from the E791 and WA92 pion-beam experiments [2, 3] with the two parameter sets discussed above. Data of the WA89 experiment are described in Figs. 2 and 3 with the same value of the parameter a_1. It should be noted that a smaller fraction of charmed sea quarks was taken into account (actually, the value of $\delta_{c,\bar{c}} = 0.01$ was used to describe both the D^-/D^+ and the D_s^-/D_s^+ asymmetry in $\Sigma^- A$ interactions instead of $\delta_{c,\bar{c}} = 0.05$ in the case of pion beam in the E791 experiment).

The resulting curves obtained in several theoretical models [12, 13] are also shown in these figures.

The asymmetry between the spectra of Λ_c and $\bar{\Lambda}_c$ that was measured in $\Sigma^- A$ collisions at $p_L = 600$ GeV/c [11] is shown in Fig. 4. It is fitted with the D-meson asymmetry curve calculated in the QGSM with a larger value of parameter a_1 ($a_1 = 25$) and with the same value of the parameter $\delta_{c,\bar{c}}$ ($\delta_{c,\bar{c}} = 0.01$). This preliminary calculation provides a good description of the data of

both the E781 and the WA89 experiment, as was expected for the reasons mentioned in Section 6.

8. CONCLUSIONS

There are several conclusions derived from the calculations discussed in this article:

(1) Data of the WA89 experiment on the charm-production asymmetry can be described within the QGSM with the same asymmetry-parameter value of $a_1 = 10$ as E791 data for $\pi^- A$ interactions and with a nonzero fraction of charmed sea quarks.

(2) Only a preliminary choice can be made between the case of $\delta_{c,\bar{c}} = 0$ and the case of a nonzero value of the fraction of $c\bar{c}$ sea quarks. More statistically reliable data from baryon-beam experiments are required for drawing a definitive conclusion.

(3) The D^-/D^+ and D_s^-/D_s^+ asymmetries measured with a Σ^- beam are more sensitive to the weight of charmed quark pairs in the quark sea of the interacting hyperon ($\delta_{c,\bar{c}} = 0.01$) than could be seen in π^--beam interaction ($\delta_{c,\bar{c}} = 0.05$).

(4) The D_s^-/D_s^+ asymmetry is higher than the D^-/D^+ asymmetry, because strange quark pairs suppressing the asymmetry in D_s production have a lower weight in the quark sea of the hyperon than ordinary $d\bar{d}$ pairs, which cause the suppression of D^-/D^+-meson asymmetry.

(5) Data of the E781 experiment on charmed-baryon-production asymmetry can be preliminarily described within the QGSM with the asymmetry-parameter value of $a_1 = 25$ for Λ_c density in d-quark-string fragmentation. The asymmetry between the spectra of Λ_c and $\bar{\Lambda}_c$ that was measured in $\Sigma^- A$ collisions grows more slowly with x_F than in the predictions within other approaches.

(6) The two charmed-meson asymmetries have nonzero values at $x_F = 0$ in these calculations at the WA89 energy and decrease with increasing energy.

ACKNOWLEDGMENTS

I am grateful to Prof. A.B. Kaidalov, Prof. H.-W. Siebert, Prof. J. Pochodzalla, and Dr. E.A. Chudakov for numerous stimulating discussions and to my colleagues in the Particle Physics Laboratory of the Max-Planck-Institut in Heidelberg for their hospitality during the time when the basic points of the article were discussed.

This work was supported by Deutsche Forschungsgemeinschaft [grant no. 436 RUS 113/332/O(R)].

REFERENCES

1. WA89 Collab. (M. I. Adamovich *et al.*), Eur. Phys. J. C **8**, 593 (1999).
2. E791 Collab. (E. M. Aitala *et al.*), Phys. Lett. B **411**, 230 (1997).
3. WA92 Collab. (M. I. Adamovich *et al.*), Nucl. Phys. B **495**, 3 (1997).
4. R. Vogt and S. J. Brodsky, Nucl. Phys. B **438**, 261 (1995); T. Gutiérrez and R. Vogt, Nucl. Phys. B **539**, 189 (1999).
5. A. B. Kaidalov, Phys. Lett. B **116B**, 459 (1982).
6. O. I. Piskounova, Nucl. Phys. B, Proc. Suppl. **50**, 179 (1996); Yad. Fiz. **60**, 513 (1997) [Phys. At. Nucl. **60**, 439 (1997)]; hep-ph/9904208.
7. O. I. Piskounova, Preprint No. 140, FIAN (Lebedev Institute of Physics, USSR Academy of Sciences, 1987).
8. A. B. Kaĭdalov, Yad. Fiz. **45**, 1450 (1987) [Sov. J. Nucl. Phys. **45**, 902 (1987)].
9. O. I. Piskounova, Yad. Fiz. **56** (8), 176 (1993) [Phys. At. Nucl. **56**, 1094 (1993)].
10. A. B. Kaĭdalov and O. I. Piskunova, Yad. Fiz. **41**, 1278 (1985) [Sov. J. Nucl. Phys. **41**, 816 (1985)].
11. SELEX Collab. (J. Russ *et al.*), in *Proceedings of ICHEP, Vancouver, 1998*; M. Iori *et al.*, hep-ex/9910039.
12. A. K. Likhoded and S. R. Slabospitsky, Yad. Fiz. **60**, 1097 (1997) [Phys. At. Nucl. **60**, 981 (1997)].
13. G. H. Arakelyan, Yad. Fiz. **61**, 1682 (1998) [Phys. At. Nucl. **61**, 1570 (1998)].
14. G. H. Arakelyan, hep-ph/9906544.